
Search for electroweakinos using the ATLAS detector



LUDWIG-MAXIMILIANS-UNIVERSITY MUNICH
FACULTY OF PHYSICS

DISSERTATION

Eric Schanet

April 2021

Suche nach Elektroweakinos mit dem ATLAS Detektor



LUDWIG-MAXIMILIANS-UNIVERSITÄT MÜNCHEN
FAKULTÄT FÜR PHYSIK

DISSERTATION

Eric Schanet

April 2021

Erstgutachterin: PD Dr. Jeanette Lorenz

Zweitgutachter: Prof. Dr. Wolfgang Dünnweber

There is a particularly common and—at least until recently—widely believed seafarers' tale which may be heard everywhere from the most noisome seafront dives to the elegant drawing rooms of the ship-owning aristocracy. This is ‘supersymmetry’. It is a seductive story. It offers many things to the excitable traveller, and one of the things it offers is Dark Matter.

Let us hope that new experiments … will soon reveal new physics beyond the Standard Model. Perhaps it will look something like the possibilities discussed, but let us hope that it will take us beyond the beyonds imagined by theorists.

May we live in interesting times

Zusammenfassung

Obwohl das Standardmodell der Teilchenphysik eine außerordentlich erfolgreiche Theorie darstellt, deuten einige Beobachtungen auf die Existenz neuer Physik jenseits dessen was im Rahmen des Standardmodells erklärt werden kann hin. Supersymmetrie ist der Oberbegriff für eine Klasse von Theorien, die einige der offenen Fragen des Standardmodells erklären könnten. Sie sagt die Existenz von supersymmetrischen Partnern für jedes Teilchen des Standardmodells voraus und könnte, unter anderem, einen Teilchenkandidaten für dunkle Materie liefern.

Diese Arbeit stellt eine Suche nach supersymmetrischen Teilchen, die über die elektroschwache Wechselwirkung paarproduziert werden, vor. Endzustände mit einem Lepton, fehlender Transversalenergie und einem Higgs Boson, welches in zwei b -Quarks zerfällt, werden untersucht. Insgesamt werden 139 fb^{-1} an Daten aus Proton-Proton Kollisionen berücksichtigt, welche mit dem ATLAS Detektor bei einer Schwerpunktsenergie von $\sqrt{s} = 13 \text{ TeV}$ im Run 2 des Large Hadron Colliders aufgezeichnet wurden. Ein, auf einer Likelihood-Methode basierender, simultaner Fit in allen Suchregionen wird verwendet, um hohe Sensitivität zu möglichst vielen kinematischen Bereichen im untersuchten Parameterraum zu gewährleisten.

Keine signifikante Abweichung von den Standardmodellvorhersagen wird in den Daten beobachtet, weshalb die Ergebnisse in einem vereinfachten Modell für Paarproduktion von Elektroweakinos interpretiert werden. Für leichteste Neutralinos mit Massen von $\lesssim 100 \text{ GeV}$ ($\approx 250 \text{ GeV}$), können leichteste Charginos und zweitleichteste Neutralinos mit Massen bis zu 740 GeV (600 GeV) ausgeschlossen werden.

Da heutige Teilchenphysik-Experimente aufgrund ihrer Komplexität und Größenordnung nicht trivial reproduzierbar sind, gleichzeitig aber eine Vielzahl an Modellen für Physik jenseits des Standardmodells existiert, wird ein besonderes Augenmerk auf die technische Durchführbarkeit einer Neuinterpretation der Suche gelegt. Die volle Likelihood-Funktion der Suche wird veröffentlicht und eine vollständig reproduzierbare Umsetzung der Suche anhand Container-Technologie und parametrisierter Job-Vorlagen wird diskutiert. Mit Hinblick auf rechenintensive Neuinterpretationen in hoch-dimensionalen Parameterräumen wird eine Methode eingeführt, um die Likelihood-Funktionen von ATLAS Suchen nach Supersymmetrie zu nähern. Mit Hilfe dieser Methode wird schlussendlich eine Neuinterpretation der Suche in einem Unterraum einer 19-dimensionalen Menge von vollständigeren supersymmetrischen Modellen durchgeführt und deren Ergebnisse diskutiert.

Abstract

Despite the success of the Standard Model of Particle Physics, a number of hints suggest the existence of new physics beyond the scope of phenomena that can be explained in the theoretical framework of the Standard Model. One class of theories that could be able to explain some of the open questions of the Standard Model is Supersymmetry. It introduces supersymmetric partners to each of the Standard Model particles, and could, for example, provide a candidate for Dark Matter.

This thesis presents a search for electroweak production of supersymmetric particles in events with one lepton, missing transverse momentum and a Higgs boson decaying into two b -quarks. The search analyses 139 fb^{-1} of proton–proton collision data at a centre-of-mass energy of $\sqrt{s} = 13\text{ TeV}$, recorded by the ATLAS detector at the Large Hadron Collider. A likelihood-based simultaneous fit in all search regions is introduced in order to achieve sensitivity to a large variety of kinematic regimes. No significant deviation from the Standard Model predictions is seen in data in any of the search regions. The results are subsequently interpreted in a simplified model for electroweakino pair-production. Lightest chargino and next-to-lightest neutralino masses of 740 GeV (600 GeV) can be excluded for lightest neutralino masses of $\lesssim 100\text{ GeV}$ ($\approx 250\text{ GeV}$).

Given that today’s particle physics experiments are not easily reproducible and a large number of phenomenologically viable models for physics beyond the Standard Model exist, special focus is put on the reusability and reinterpretability of the search. The full likelihood function of the search is published in a readily available format, and a fully reusable implementation of the search using containerised workflows with parameterised job templates is provided. In light of conceptually interesting but computationally challenging reinterpretations in high-dimensional model spaces, a method for generically approximating the likelihood functions of ATLAS searches for Supersymmetry is introduced and validated. Using this approach, a reinterpretation of the search in a subspace of a 19-dimensional set of more complete supersymmetric models is performed and its results are discussed.

Contents

I	Fundamental concepts	3
1	Theory	5
1.1	The Standard Model of particle physics	5
1.1.1	Particle content of the Standard Model	6
1.1.2	The Standard Model as a gauge theory	7
1.1.3	Renormalisation and divergencies	17
1.2	Supersymmetry	18
1.2.1	Shortcomings of the Standard Model	18
1.2.2	Supersymmetric Algebra	22
1.2.3	Supermultiplets	23
1.2.4	Supersymmetric Lagrangian	24
1.2.5	The Minimal Supersymmetric Standard Model	26
1.2.6	The phenomenological MSSM	30
1.2.7	Simplified models	31
1.3	Search for electroweakinos	33
1.3.1	Production of electroweakinos at the Large Hadron Collider	33
1.3.2	Models used within this work	34
2	Experiment	37
2.1	The Large Hadron Collider	37
2.1.1	Pile-up	39
2.1.2	Luminosity and data-taking	41
2.2	ATLAS Experiment	42
2.2.1	Coordinate system	44
2.2.2	Magnet system	44

2.2.3	Inner detector	45
2.2.4	Calorimeters	47
2.2.5	Muon spectrometer	49
2.2.6	Forward detectors	51
2.2.7	Trigger and data acquisition system	51
2.2.8	Monte Carlo simulation	52
3	Statistical data analysis	57
3.1	The likelihood function	57
3.2	Parameter estimation	59
3.3	Statistical tests	60
3.4	CL_s approach	63
3.5	Asimov dataset	64
3.6	Sensitivity estimation	64
II	The 1-lepton analysis	67
4	Analysis overview	69
4.1	Search for electroweakinos in the 1ℓ final state	69
4.2	Standard Model backgrounds	70
4.3	Monte Carlo samples	71
4.3.1	Signal samples	71
4.3.2	Background samples	72
4.4	Object definitions	73
4.4.1	Tracks and vertices	73
4.4.2	Electrons and Photons	74
4.4.3	Muons	75
4.4.4	Jets	76
4.4.5	Flavour tagging	77
4.4.6	Missing transverse momentum	78
4.5	Overlap removal	78
4.6	Analysis variables	79
4.7	Trigger strategy	83
4.8	Event cleaning	84

5 Signal region optimisation	87
5.1 Optimisation methods	87
5.1.1 Multidimensional cut scan	87
5.1.2 N-1 plots	89
5.1.3 Scans using asymptotic formulae	89
5.2 Optimisation for the 1ℓ search	90
5.2.1 Starting from benchmark signal points	90
5.2.2 Towards final signal regions	92
5.3 Signal region definitions	94
6 Background estimation	101
6.1 General strategy	101
6.1.1 Transfer factor approach	101
6.1.2 Analysis blinding	102
6.1.3 Data versus Monte Carlo plots	103
6.2 Control regions	103
6.3 Validation regions	108
7 Systematic uncertainties	111
7.1 Experimental uncertainties	111
7.1.1 Pile-up reweighting and luminosity	111
7.1.2 Triggers	112
7.1.3 Leptons	112
7.1.4 Jets	112
7.1.5 Flavour tagging	113
7.1.6 Missing transverse energy	113
7.2 Theoretical uncertainties	113
7.2.1 Background	115
7.2.2 Signal	116
7.3 Impact on signal regions	116
8 Results	119
8.1 Background-only fit results	119
8.1.1 Results in the control regions	119

8.1.2	Results in the validation regions	121
8.1.3	Results in the signal regions	123
8.2	Interpretation	128
8.2.1	Model-independent upper limits	128
8.2.2	Model-dependent exclusion limits	128
8.3	Discussion	130
III	Reinterpretation	133
9	Preservation and reusability	135
9.1	The case for reinterpretations	135
9.1.1	Motivation	135
9.1.2	Approaches for reinterpretations	136
9.2	Public full likelihood	138
9.3	Full analysis preservation using containerised workflows	139
9.3.1	Software preservation	139
9.3.2	Processing steps preservation	140
9.3.3	Workflow preservation	140
9.4	Truth-level analysis	141
9.4.1	Truth-level selection	141
9.4.2	Truth smearing	143
9.5	Validation of the truth-level analysis	145
9.5.1	Validation in loose preselection	145
9.5.2	Validation in signal regions	145
9.5.3	Validation using likelihood	145
10	Simplified likelihoods	149
10.1	Motivation	149
10.2	Building simplified likelihoods	151
10.3	Computational performance	154
10.4	Physics performance	155
10.5	Limitations	156
10.6	Outlook and future prospects	159

11 Reinterpretation in the pMSSM	161
11.1 Motivation	161
11.2 Model sampling and processing	162
11.2.1 Sampling	162
11.2.2 Selection and processing	163
11.2.3 Event generation	163
11.2.4 Truth-level analysis	164
11.3 Phenomenology of the LSP	164
11.4 Impact of the search on the pMSSM	165
11.4.1 Impact on electroweakino masses	165
11.4.2 Impact on pMSSM parameters	170
11.4.3 Impact on dark matter relic density	172
11.5 Discussion	173
IV Summary and Outlook	175
12 Conclusions	177
V Appendix	181
Appendix A	183
A.1 Additional information on signal region optimisation	183
A.2 Background estimation	192
Appendix B	195
B.1 Truth smearing	195
B.2 Simplified likelihood results	199
Appendix C	205
C.1 Phenomenology of the LSP	205
C.2 Impact on electroweakinos	208
C.3 Impact on pMSSM parameters	208
C.4 Impact on dark matter relic density	210
Bibliography	215

Introduction

Particle physics studies the fundamental constituents and interactions of matter with the ultimate goal of uncovering the laws of nature that govern the most fundamental building blocks of the universe. Over the course of more than a century, fundamental physics has continuously pushed the frontiers of knowledge, reaching ever-smaller length-scales on which the fundamental interactions of the building blocks of matter can be understood. The resulting theoretical framework, the Standard Model of particle physics (SM), provides answers to some of the deepest questions that can be asked about the universe and is the most fundamental, experimentally validated description of nature known to date.

Particle physics finds itself, however, at an interesting crossroad. On the one hand, the SM is very successful in describing nature at its smallest scales and—with the discovery of the Higgs boson in 2012 [1, 2]—has recently been experimentally completed. Through various particle physics experiments, the precision and predictive power of the SM have been tested to an unprecedented level, finding no significant deviations in experimental data so far. On the other hand, however, a number of cosmological observations as well as flavour and precision electroweak measurements are putting increasing pressure on the SM. For example, although the existence of dark matter (DM) is nowadays well-established, it cannot be suitably described within the theoretical framework of the SM. Over the course of the last decades, it has become increasingly clear that the SM is an effective theory, and thus only a low-energy approximation to a more fundamental theory of nature.

A plethora of theories aiming to explain the shortcomings of the SM exist. One class of such theories is Supersymmetry (SUSY), extending the SM by associating supersymmetric partners to the SM particles. SUSY could, for example, be able to provide a candidate particle for DM or explain some of the tensions observed in electroweak precision measurements. Up until the discovery of the Higgs boson, the theory and experimental communities in particle physics were in a state of *symbiosis* with a clear pathway to follow: validating and completing the SM. This is, however, no longer the case and experimental particle physics faces an era where a large number of models for beyond the Standard Model (BSM) physics can be thought of, but no clear indication of where to start looking is available.

Although theoretical arguments suggest that supersymmetric particles could exist at the energies accessible with the Large Hadron Collider (LHC), no such particles have been found so far. Up until recently, searches for SUSY have, however, mostly focused on the production of the supersymmetric partners of quarks and gluons through the strong interaction. With the second run of the LHC recently come to an end, an unprecedented amount of proton–proton collision data has been recorded by the LHC experiments and is available for physics analysis. This

allows to search for supersymmetric particles produced through the electroweak interaction that have previously not been accessible due to their low theoretical production rates, compared to those produced through the strong interaction.

Due to their complexity and lifetimes approaching half a century, experiments like the ATLAS detector at the LHC are in general not easily repeatable and thus severely challenge the scientific method. This precarious situation, coupled with the wide landscape of BSM models available to search for, requires efforts to not only preserve searches for BSM physics, but make them fully reusable in the context of new, additional BSM models.

This thesis presents a search for the supersymmetric partners of the SM Higgs and gauge bosons, collectively referred to as *electroweakinos*. The search uses 139 fb^{-1} of proton–proton collision data recorded at a centre-of-mass energy of 13 TeV with the ATLAS detector. It is embedded in a larger effort within the ATLAS collaboration, searching for SUSY in the context of a variety of theoretical models. The present work is divided into four main parts. In part I, the fundamental concepts necessary for the remainder of the thesis are presented. This includes a theoretical introduction to the SM and SUSY, followed by a description of the experimental setup, concluding with a discussion of the statistical concepts used. Part II introduces the aforementioned search for electroweakinos and discusses its results using 139 fb^{-1} of proton–proton collision data recorded by ATLAS. In part III, preservation and reusability efforts are presented, aiming to make the search readily available to reinterpretation efforts inside as well as outside of the ATLAS collaboration. Furthermore, a method for approximating the statistical models of SUSY searches is introduced and validated in chapter 10. These efforts culminate in a reinterpretation of the search in a subspace of a 19-dimensional set of more complete supersymmetric scenarios, the results of which are discussed in chapter 11. Finally, the thesis concludes with a brief summary in part IV.

Part I

Fundamental concepts

Chapter 1

Theory

The Standard Model of particle physics (SM), introduced in the following section, is a theoretical framework providing a description of nature on the level of elementary particles. Although experimentally well-validated, a number of open questions are left unanswered by the SM. For this reason, the second part of this chapter introduces Supersymmetry, a class of theories that could provide answers to some of these open questions. As searching for Supersymmetry will be the guiding thread for the greater part of this thesis, this chapter will highlight the phenomenological consequences of supersymmetric theories. The mathematical description in the following sections largely follows Refs. [3, 4] for the SM and Refs. [5, 6] for Supersymmetry.

1.1 The Standard Model of particle physics

By the end of the 1920s, quantum mechanics and general relativity had been relatively well established, and the consensus among physicists was that matter is composed of nuclear atoms consisting of electrons and protons. During the 1930s, a multitude of new experimental discoveries and theoretical puzzles excited physicists in, among others, three important directions of research: nuclear physics, cosmic rays and relativistic quantum mechanics [7]. At this time, open questions in these fields included, e.g., the continuous spectrum of the β -decay, the nature of cosmic rays, or the negative energy states in Dirac's relativistic electron theory. As a result of these directions ultimately flowing together, the following decades saw elementary particle physics, emerge as a new field of research.

Since these early times of particle physics, significant progress has been made in describing nature at the subatomic scale. Today, a century later, the resulting theoretical framework, the SM, is the most fundamental, experimentally validated theory of nature known to mankind. It provides an extremely precise description of the interactions of elementary particles and has been experimentally tested to an unprecedented level of accuracy. Given the remarkable success of the SM, it is not surprising that its history is paved with numerous awards for both experimental and theoretical work. In 1964, the Nobel prize was awarded to Feynman, Schwinger and Tomonaga for their fundamental work on quantum electrodynamics (QED), a quantum field theory allowing the precise calculation of fundamental processes like, e.g., the anomalous magnetic moment of the electron that is known to a relative experimental

Table 1.1: Names, electric charges and masses (rounded to three significant digits if known to that precision) of all observed fermions in the SM [9]. The symbols used in the following are indicated in parentheses after the particle names.

	generation	particle	electric charge [e]	mass
leptons	1	electron (e)	-1	511 keV
		electron neutrino (ν_e)	0	< 1.1 eV
	2	muon (μ)	-1	106 MeV
		muon neutrino (ν_μ)	0	< 0.19 MeV
	3	tau (τ)	-1	1.78 GeV
		tau neutrino (ν_τ)	0	< 18.2 MeV
quarks	1	up (u)	$\frac{2}{3}$	2.16 MeV
		down (d)	$-\frac{1}{3}$	4.67 MeV
	2	charm (c)	$\frac{2}{3}$	1.27 GeV
		strange (s)	$-\frac{1}{3}$	93 MeV
	3	top (t)	$\frac{2}{3}$	173 GeV
		bottom (b)	$-\frac{1}{3}$	4.18 GeV

uncertainty of 2.3×10^{-10} [8]. In 1979, Glashow, Weinberg and Salam were awarded the Nobel prize for their work towards electroweak unification. The most prominent recent progress is undoubtedly the discovery of the Higgs boson, not only resulting in the Nobel prize being awarded to Englert and Higgs, but also completing the SM, roughly 50 years after the existence of the Higgs boson had been postulated.

1.1.1 Particle content of the Standard Model

Apart from the experimentally non-vanishing neutrino masses, the SM successfully describes ordinary matter as well as their interactions, namely the electromagnetic, weak and strong interactions, leaving gravity as the only fundamental force not described within the SM. The particles in the SM are classified into two main categories, depending on their spin. Particles with half-integer spin follow the Fermi-Dirac statistics and are called *fermions*. As they are subject to the Pauli exclusion principle, they make up ordinary matter. Particles with integer spin are called *bosons*, follow Bose-Einstein statistics and mediate the fundamental interactions.

Fermions are further divided into leptons and quarks, that each come in three generations with increasing masses[†]. Each of the three electrically charged leptons is associated to a corresponding neutral neutrino (more on this association in chapter section 1.1.2). While the SM assumes massless neutrinos, the observation of neutrino oscillations [10] implies the existence of at least two massive neutrinos. By extending the SM to allow non-vanishing neutrino masses, neutrino oscillations can be introduced through lepton generation mixing, described by the Pontecorvo–Maki–Nakagawa–Sakata (PMNS) matrix [11]. Apart from an electric charge, the six quarks also carry a colour charge, of which three types exist: *red*, *green* and *blue* as well as their respective anti-colours. The mixing in the quark sector through the weak interaction can be described by the Cabibbo–Kobayashi–Maskawa (CKM) matrix [12, 13]. Finally, each

[†] Neutrinos might not exist in a normal mass hierarchy but could also have an inverted mass hierarchy.

Table 1.2: Names, electric charges and masses (rounded to three significant digits if known to that precision) of all observed bosons in the SM [9]. The symbols used in the following are indicated in parentheses after the particle names.

particle	spin	electric charge [e]	mass
photon (γ)	1	0	0
gluon (g)	1	0	0
W^\pm	1	± 1	80.4 GeV
Z^0	1	0	91.2 GeV
Higgs boson (h)	0	0	125 GeV

fermion comes with its own anti-particle with same mass and spin, but inverted charge-like quantum numbers[†]. All fermions in the SM are listed in table 1.1.

The fundamental forces described by the SM are propagated by bosons with spin-1. The photon γ couples to electrically charged particles and mediates the electromagnetic interaction. As the photon is massless, the electromagnetic force has infinite range. The strong force is mediated by gluons carrying one unit of colour and one unit of anti-colour. Due to colour-confinement, colour charged particles like quarks and gluons cannot exist as free particles and instead will form colour-neutral bound states. Although nine gluon states would theoretically be possible, only eight of them are realised in nature—the colour-singlet state $\frac{1}{\sqrt{3}}(|r\bar{r}\rangle + |g\bar{g}\rangle + |\bar{b}b\rangle)$ would result in long-range strong interactions, which have not been observed. Finally, the weak force is mediated by a total of three bosons, two charged W^\pm bosons and a neutral Z boson[§]. The mediators of the weak force are massive, resulting in a finitely ranged interaction. They gain their masses through the Higgs mechanism (discussed in chapter section 1.1.2). All bosons known to the SM are listed in table 1.2.

1.1.2 The Standard Model as a gauge theory

Formally, the SM is a collection of a special type of quantum field theories (QFTs), called gauge theories. In the same way that quantum mechanics is the quantisation of dynamical fields of particles, QFT is the application of quantum mechanics to dynamical systems of fields, providing a uniform description of quantum mechanical particles and classical fields, while including special relativity.

In classical mechanics, the fundamental quantity is the action S , which is the time integral of the Lagrangian L , a functional characterising the state of a system of particles in terms of generalised coordinates q_1, \dots, q_n . In field theory, the Lagrangian can be written as spatial integral of a Lagrangian density $\mathcal{L}(\phi_i, \partial_\mu \phi_i)$, which is a function of fields ϕ_i and their spacetime derivatives $\partial_\mu \phi_i$. In the following, the Lagrangian density \mathcal{L} will simply be referred to as the

[†] The exact nature of anti-neutrinos is still an open question and ties into whether or not the neutrino mass matrix contains non-vanishing Majorana mass terms.

[§] Due to the electroweak unification, offering a unified description of the electromagnetic and weak interactions in the SM, the Z boson technically has an electromagnetic component and thus is not a *pure* mediator of the weak interaction. Electroweak unification will be discussed in section 1.1.2.

Lagrangian. The action can then be written as

$$S = \int L dt = \int \mathcal{L}(\phi_i, \partial_\mu \phi_i) d^4x. \quad (1.1)$$

Using the principle of least action $\delta S = 0$, the equation of motions for each field are given by the Euler-Lagrange-equation,

$$\partial_\mu \left(\frac{\partial \mathcal{L}}{\partial (\partial_\mu \phi_i)} \right) - \frac{\partial \mathcal{L}}{\partial \phi_i} = 0. \quad (1.2)$$

As opposed to the Hamiltonian formalism, the Lagrange formulation of field theory is especially well suited for the relativistic dynamics in particle physics, as it exhibits explicit Lorentz-invariance [4]. This is a direct consequence of the principle of least action, since Lorentz-transformed extrema in the action will still be extrema for Lorentz-invariant Lagrangians.

Symmetries are of central importance in the SM. As Emmy Noether has famously shown in 1918 for classical mechanics, every continuous symmetry of the action has a corresponding conservation law [14]. In the context of classical field theory, each generator of a continuous internal or spacetime symmetry transformation leads to a conserved current, and thus to a conserved charge. In QFTs, quantum versions of Noether's theorem, called Ward–Takahashi identities [15, 16] for Abelian theories and Slavnov–Taylor identities [17–19] for non-Abelian theories relate the conservation of quantum currents and charge-like quantum numbers to continuous symmetries of the Lagrangian.

From a theoretical point of view, the SM is a non-Abelian gauge theory based on the symmetry group

$$SU(3)_C \otimes SU(2)_L \otimes U(1)_Y,$$

where $U(n)$ ($SU(n)$) describes (special) unitary groups, i.e. the Lie groups of $n \times n$ unitary matrices (with determinant 1, if special). $SU(3)_C$ generates quantum chromodynamics (QCD), describing the interaction of particles with colour charge C through exchange of gluons, and $SU(2)_L \otimes U(1)_Y$ generates the electroweak interaction. Here, the subscript Y represents the weak hypercharge, while L indicates that $SU(2)_L$ only couples to left-handed particles (right-handed antiparticles).

Feynman diagrams

Transitioning from classical field theory to quantum field theory is typically done through either canonical quantisation or the usage of the path integral formalism. As only the simplest field theories can be solved analytically, i.e. those containing only free fields and no interactions, perturbation theory is used for calculating scattering cross sections and decay rates for any QFT containing interactions. Any transition matrix can then be written as a series expansion in the coupling constant, with each term represented by Feynman diagrams.

Using appropriate Feynman rules dictating the possible vertices (representing interactions between fields) and propagators (representing the propagation of fields), an infinite number of Feynman diagrams can be written down. All possible combinations of propagators and vertices (i.e. all possible Feynman diagrams) that can be used to connect given incoming and outgoing

particles then represent the full perturbation series. Only the lowest order in the series is considered at leading order (LO), the next-lowest at next-to-leading order (NLO), and so on.

Gauge principle

The gauge principle is fundamental to the SM and dictates that the existence of gauge fields is directly related to symmetries under local gauge transformations. QED, being the simplest gauge theory, can be taken to illustrate this important principle. The free Dirac Lagrangian for a single, non-interacting fermion with mass m is given by

$$\mathcal{L}_{\text{Dirac}} = \bar{\psi} (i\gamma^\mu \partial_\mu - m) \psi, \quad (1.3)$$

where ψ is a four-component complex spinor field, $\bar{\psi} = \psi^\dagger \gamma^0$, and γ^μ with $\mu = 0, 1, 2, 3$ are the Dirac matrices with the usual anticommutation relations generating a matrix representation of the Dirac algebra

$$\{\gamma^\mu, \gamma^\nu\} \equiv \gamma^\mu \gamma^\nu + \gamma^\nu \gamma^\mu = 2\eta^{\mu\nu} \mathbb{1}_4. \quad (1.4)$$

It is worth noting that the free Dirac Lagrangian is invariant under a global $U(1)$ transformation

$$\psi \rightarrow e^{i\theta} \psi, \quad (1.5)$$

where the phase θ is spacetime independent and real-valued. In order to produce the physics of electromagnetism, the free Dirac Lagrangian, has to be invariant under *local* $U(1)$ phase transformations with a spacetime dependent phase $\theta(x)$. This is, however, not the case, as the transformed Lagrangian picks up an additional term from the spacetime derivative of the phase,

$$\mathcal{L}_{\text{Dirac}} \rightarrow \mathcal{L}_{\text{Dirac}} - (\partial_\mu \theta(x)) \bar{\psi} \gamma^\mu \psi. \quad (1.6)$$

For the Dirac Lagrangian to become invariant under a local gauge transformation, a new vector field $A_\mu(x)$ has to be introduced and the partial derivative has to be replaced with the covariant derivative

$$\partial_\mu \rightarrow D_\mu \equiv \partial_\mu + ieA_\mu, \quad (1.7)$$

where e can be identified with the elementary charge and represents the coupling of the fermion field to the gauge field A_μ . The prescription of achieving local gauge invariance by replacing ∂_μ with D_μ is called *minimal coupling* and leads to a Lagrangian that is invariant under the transformations

$$\psi \rightarrow e^{i\theta(x)} \psi, \quad A_\mu \rightarrow A_\mu - \frac{1}{e} \partial_\mu \theta(x). \quad (1.8)$$

The modified Lagrangian now includes a term for interactions between the gauge field and the fermion field,

$$\begin{aligned} \mathcal{L} &= \mathcal{L}_{\text{Dirac}} + \mathcal{L}_{\text{int}} \\ &= \bar{\psi} (i\gamma^\mu \partial_\mu - m) \psi - (e\bar{\psi} \gamma^\mu \psi) A_\mu, \end{aligned} \quad (1.9)$$

and is indeed invariant under a local phase transformation. Yet, it cannot be complete, as it is still missing a term describing the kinematics of the free gauge field A_μ . For a vector field, the

kinetic term is described by the Proca Lagrangian

$$\mathcal{L}_{\text{Proca}} = -\frac{1}{4}F_{\mu\nu}F^{\mu\nu} + \frac{1}{2}m_A^2 A^\nu A_\nu, \quad (1.10)$$

where $F^{\mu\nu} \equiv (\partial^\mu A^\nu - \partial^\nu A^\mu)$ is the field strength tensor that is invariant under the transformation in eq. (1.8). Since $A^\nu A_\nu$ is not invariant under the local transformation of above, the only way to keep the full Lagrangian invariant under a local phase transformation is by requiring $m_A = 0$, i.e. the gauge field A_μ introduced has to be massless, resulting in the Maxwell Lagrangian (ultimately generating the Maxwell equations),

$$\mathcal{L}_{\text{Maxwell}} = -\frac{1}{4}F_{\mu\nu}F^{\mu\nu}. \quad (1.11)$$

This finally yields the full Lagrangian

$$\begin{aligned} \mathcal{L}_{\text{QED}} &= \mathcal{L}_{\text{Dirac}} + \mathcal{L}_{\text{Maxwell}} + \mathcal{L}_{\text{int}} \\ &= \bar{\psi}(i\gamma^\mu\partial_\mu)\psi - m\bar{\psi}\psi - \frac{1}{4}F^{\mu\nu}F_{\mu\nu} - (e\bar{\psi}\gamma^\mu\psi)A_\mu, \end{aligned} \quad (1.12)$$

which can be identified to be the full Lagrangian of QED. The gauge field A_μ introduced is therefore nothing else than the electromagnetic potential with its associated massless particle, the photon. Thus, by applying the gauge principle on the free Dirac Lagrangian, i.e. forcing a global phase invariance to hold locally, a new massless gauge field has to be introduced, including interaction terms with the existing fields in the Lagrangian. In the case of the free Dirac Lagrangian, local gauge invariance produces all of QED.

As Yang and Mills have shown in 1954 [20], requiring a global phase invariance to hold locally is perfectly possible in the case of any continuous symmetry group. Considering a general non-Abelian symmetry group G , represented by a set of $n \times n$ unitary matrices $U(\alpha^1, \dots, \alpha^N)$, parametrised by N real parameters $\alpha^1, \dots, \alpha^N$, then a gauge-invariant Lagrangian can be constructed with a similar prescription [3] as previously in the case of $U(1)$.

A total of n fermion fields with mass m are needed, arranged in an n -dimensional multiplet $\Psi = (\psi_1, \dots, \psi_n)^T$. The free Lagrangian,

$$\mathcal{L}_{\text{free}} = \bar{\Psi}(i\gamma^\mu\partial_\mu - m)\Psi, \quad (1.13)$$

is invariant under a global phase transformation of the form

$$\Psi(x) \rightarrow U(\alpha^1, \dots, \alpha^N)\Psi(x). \quad (1.14)$$

Each element in the set of transformations U can be written in terms of the group generators T^a as

$$U(\alpha^1, \dots, \alpha^N) = e^{i\alpha^a T^a}, \quad (1.15)$$

where the group indices $a = 1, \dots, N$ are to be summed over. The group generators T^a satisfy the commutation relations

$$[T^a, T^b] = if^{abc}T^c, \quad (1.16)$$

where f^{abc} are the so-called structure constants quantifying the lack of commutativity between the generators. By convention, the basis for the generators T^a is typically chosen such that f^{abc} is completely anti-symmetric [3]. In order to make the Lagrangian invariant under local phase transformations, i.e. under transformations with a set of spacetime-dependent real parameters $\alpha^a(x)$, a vector field \mathbf{W}_μ together with a coupling constant g have to be introduced through the covariant derivative

$$\partial_\mu \rightarrow D_\mu = \partial_\mu - ig\mathbf{W}_\mu. \quad (1.17)$$

As D_μ acts on the n -dimensional multiplet Ψ , the introduced gauge field \mathbf{W}_μ has to be a $n \times n$ matrix and can thus be expanded in terms of the generators

$$\mathbf{W}_\mu(x) = T^a W_\mu^a(x), \quad (1.18)$$

thereby explicitly illustrating, that a total of N gauge fields W_μ^a are introduced through the covariant derivative. Similar to QED above, the covariant derivative also introduces an interaction term of the form

$$\mathcal{L}_{\text{int}} = g\bar{\Psi}\gamma^\mu\mathbf{W}_\mu\Psi, \quad (1.19)$$

into the Lagrangian in eq. (1.13), coupling the gauge fields W_μ^a to the fermion multiplet. For infinitesimal $\alpha^a(x)$, the gauge fields gauge transform according to

$$W_\mu^a \rightarrow W_\mu^a + \frac{1}{g}\partial_\mu\alpha^a + f^{abc}W_\mu^b\alpha^c, \quad (1.20)$$

where the term with α^a looks familiar to the $U(1)$ example and corresponds to the Abelian case, while the term with f^{abc} introduces the non-Abelian structure into the theory [3]. The same non-Abelian structure is again clearly visible when introducing a kinetic term for the gauge fields into the Lagrangian

$$\mathcal{L}_W = -\frac{1}{4}F_{\mu\nu}^a F^{\mu\nu,a}, \quad (1.21)$$

with the field-strength tensor now $F_{\mu\nu}^a = \partial_\mu W_\nu^a - \partial_\nu W_\mu^a + gf^{abc}W_\mu^bW_\nu^c$. As was already the case for QED, the above Lagrangian contains Abelian terms quadratic in W , describing the propagation of the free gauge fields. This time, the Lagrangian additionally includes non-Abelian terms cubic and quartic in W , leading to self-interaction of the gauge fields.

Quantum chromodynamics

QCD, the gauge theory describing the strong interaction between quarks and gluons in the SM, is an example for a non-Abelian Yang-Mills theory [20]. QCD is based on the gauge group $SU(3)_C$, with the subscript C indicating that the quantum number associated with the symmetry group is the *colour*. Each quark is described by a triplet of fermion fields $q = (q_r, q_g, q_b)^T$, where the subscripts refer to the three different colours. The symmetry group $SU(3)$ has a total of $n^2 - 1 = 8$ generators, usually expressed in terms of the Gell-Mann matrices λ^a [4]. The covariant derivative introducing the gauge fields G_μ^a acting on the quark triplets is then

$$D_\mu = \partial_\mu - ig_s \frac{\lambda^a}{2} G_\mu^a, \quad (1.22)$$

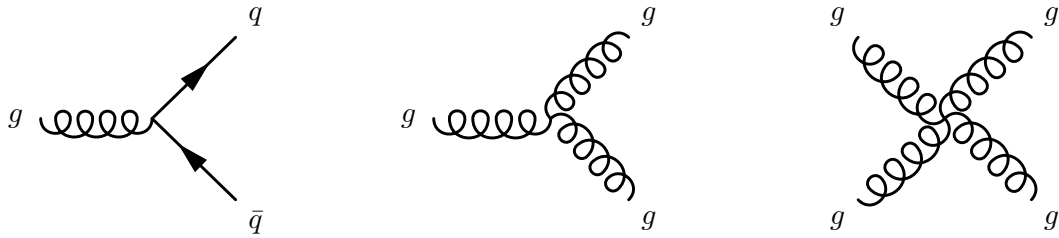


Figure 1.1: Possible vertices in QCD.

with g_s the coupling constant of the strong interaction, typically written as $\alpha_s = g_s^2/(4\pi)$ in analogy to the fine-structure constant in QED. Gauge invariance thus introduces a total of $N = 8$ gauge fields that can be identified with the eight gluons, leading to the full Lagrangian of QCD

$$\mathcal{L}_{\text{QCD}} = \sum_q \bar{q}(i\gamma^\mu D_\mu - m_q)q - \frac{1}{4}G_{\mu\nu}^a G^{\mu\nu,a}, \quad (1.23)$$

where $q = u, d, s, c, b, t$ and $G_{\mu\nu}^a$ are the gluon field strengths given by

$$G_{\mu\nu}^a = \partial_\mu G_\nu^a - \partial_\nu G_\mu^a + g_s f^{abc} G_\mu^b G_\nu^c. \quad (1.24)$$

As expected from the previous section, \mathcal{L}_{QCD} contains terms that are cubic and quartic in the gluon fields, resulting in gluon self-interaction in the theory. All possible QCD interaction vertices involving gluons and quarks are shown in fig. 1.1. The gluon self-interaction leads to a number of phenomena unknown to Abelian theories, rendering the kinematics of QCD highly non-trivial.

In QCD, an effect similar to the electric charge screening in QED happens through quark-antiquark pairs, resulting in a screening of the colour charge. However, the existence of gluon loops in the gluon propagator due to gluon self-interaction creates an opposing *antiscreening* effect of colour charges. At short distances or large momentum scales, colour-charged particles essentially become free particles, a phenomenon called *asymptotic freedom*. In this regime, where α_s is sufficiently small, QCD processes can be calculated using perturbation theory. At large distances or small moment scales, however, α_s becomes large, and gluons interact very strongly with colour-charged particles, meaning that no free gluons or quarks can exist. This phenomenon is called *confinement* and implies that free quarks and gluons will be subject to *hadronisation*, i.e. form colourless bound states by combining with other quarks or gluons (that can be created from the vacuum). In a particle detector, hadronisation manifests itself as collimated showers of particles, called *jets*. At momentum scales where the strong coupling constant α_s becomes large ($\alpha_s \approx \mathcal{O}(1)$), QCD processes can no longer be calculated using perturbation theory and instead lattice QCD [21, 22] is used.

Electroweak interaction

During the 1960s, Glashow, Weinberg and Salam [23–25] developed a unified theory of the electromagnetic and weak interactions, based on the $SU(2)_L \otimes U(1)_Y$ symmetry group. Known already experimentally from the Wu experiment [26] in 1956, weak interaction violates parity,

i.e. the symmetry transformations have to act differently on the left-handed and right-handed fermion fields. The left- and right-handed components of a fermion field can be projected out using

$$\psi_L = \frac{1 - \gamma^5}{2} \psi, \quad \psi_R = \frac{1 + \gamma^5}{2} \psi, \quad (1.25)$$

with $\gamma^5 = i\gamma^0\gamma^1\gamma^2\gamma^3$. As the weak interaction only acts on left-handed fermions, they can be ordered as $SU(2)$ doublets

$$\begin{pmatrix} \nu_e \\ e \end{pmatrix}_L, \quad \begin{pmatrix} u \\ d \end{pmatrix}_L, \quad \begin{pmatrix} \nu_\mu \\ \mu \end{pmatrix}_L, \quad \begin{pmatrix} c \\ s \end{pmatrix}_L, \quad \begin{pmatrix} \nu_\tau \\ \tau \end{pmatrix}_L, \quad \begin{pmatrix} t \\ b \end{pmatrix}_L. \quad (1.26)$$

The quantum number associated with $SU(2)$ symmetry transformations is called weak isospin I with the third component I_3 . Fermion doublets have $I = 1/2$, with the upper component having $I_3 = 1/2$ and the lower component $I_3 = -1/2$. Right-handed fermion fields have $I = 0$, i.e. are singlet states in weak isospin space

$$e_R, u_R, d_R, \quad \mu_R, c_R, s_R, \quad \tau_R, t_R, b_R, \quad (1.27)$$

and thus do not couple to the weak interaction. In the electroweak theory, neutrinos are assumed to be strictly massless, therefore no right-handed neutrino singlets exist.

The fermion doublets can be written in a free Lagrangian similar to eqs. (1.3) and (1.13),

$$\mathcal{L} = \bar{\psi}_L i\gamma^\mu \partial_\mu \psi_L, \quad (1.28)$$

with one crucial difference—the omission of the fermion masses. As $\bar{\psi}\psi = \bar{\psi}_L\psi_R + \bar{\psi}_R\psi_L$, mass terms would mix left- and right-handed terms and break gauge invariance. Section 1.1.2 will illustrate how fermion masses will instead be generated in the electroweak theory. For left-handed fermion fields, local $SU(2)_L$ transformations can be written as

$$\psi_L \rightarrow \exp\left(ig_2\alpha^a \frac{\sigma^a}{2}\right) \psi_L, \quad (1.29)$$

where g_2 is the coupling constant, α^a (with $a = 1, 2, 3$) are real parameters and the Pauli matrices σ^a are the generators of $SU(2)_L$. By introducing the covariant derivative $D_\mu = \partial_\mu + ig_2 \frac{\sigma^a}{2} W_\mu^a$ and including the usual kinetic term for the gauge fields, the Lagrangian becomes invariant under $SU(2)_L$ transformations and reads

$$\mathcal{L} = \bar{\psi}_L i\gamma^\mu D_\mu \psi_L - \frac{1}{4} W_{\mu\nu}^a W^{\mu\nu,a}, \quad (1.30)$$

with the gauge field strength tensors $W_{\mu\nu}^a = \partial_\mu W_\nu^a - \partial_\nu W_\mu^a + g_2 \epsilon^{abc} W_\mu^b W_\nu^c$, where ϵ^{abc} are the structure constants. As previously in the case of QCD, the non-Abelian structure of the symmetry group causes self-interactions of the gauge fields.

In order to include electromagnetic interactions, the weak isospin group is extended with the $U(1)_Y$, corresponding to the multiplication of a phase factor $e^{i\alpha \frac{Y}{2}}$ to each of the preceding doublets and singlets. Here, Y is the weak hypercharge as given by the Gell-Mann–Nishijima

relation [27–29],

$$Q = I_3 + \frac{Y}{2}, \quad (1.31)$$

with Q the electric charge. As will be discussed in section 1.1.2, the spontaneous breaking of the $SU(2)_L \otimes U(1)_Y$ gauge symmetry will recover the electromagnetic gauge group $U(1)_{\text{em}}$ [4].

By modifying the covariant derivative to include a $U(1)_Y$ gauge field and ensuring that $U(1)_Y$ acts the same on left-handed and right-handed fermions, it becomes $D_\mu = \partial_\mu + ig_2 \frac{\sigma^a}{2} W_\mu^a + ig_1 \frac{Y}{2} B_\mu$ for left-handed fermions and $D_\mu = \partial_\mu + ig_1 \frac{Y}{2} B_\mu$ for right-handed fermions. The full electroweak Lagrangian then is

$$\begin{aligned} \mathcal{L}_{\text{electroweak}} = & \sum_j \bar{\psi}_L^j i\gamma^\mu \left(\partial_\mu - ig_2 \frac{\sigma^a}{2} W_\mu^a + ig_1 \frac{Y}{2} B_\mu \right) \psi_L^j \\ & + \sum_j \bar{\psi}_R^j i\gamma^\mu \left(\partial_\mu + ig_1 \frac{Y}{2} B_\mu \right) \psi_R^j, \end{aligned} \quad (1.32)$$

where $B_{\mu\nu} = \partial_\mu B_\nu - \partial_\nu B_\mu$, and the two sums run over the left- and right-handed fermions, respectively.

Spontaneous symmetry breaking

In the electroweak theory a total of three vector fields W_μ^a and one vector field B_μ are associated with the gauge groups $SU(2)_L$ and $U(1)_Y$, respectively. As has been shown explicitly through the example of QED in section 1.1.2, the gauge fields need to be massless for the resulting Lagrangian to be gauge invariant under the respective symmetry group. In addition, the electroweak symmetry group does not allow for fermion masses. Both gauge bosons of the weak interaction and the fermions are, however, manifestly massive, hence the electroweak symmetry has to be broken in the SM.

The spontaneous symmetry breaking of the $SU(2)_L \otimes U(1)_Y$ gauge group to $U(1)_{\text{em}}$ is achieved through the Brout–Englert–Higgs mechanism [30–32]. In the SM, an isospin doublet of complex scalar fields, called Higgs doublet, is introduced

$$\Phi(x) = \begin{pmatrix} \phi^+(x) \\ \phi^0(x) \end{pmatrix}. \quad (1.33)$$

The Higgs doublet has hypercharge $Y = 1$, hence according to eq. (1.31), ϕ^+ has electric charge $+1$ while ϕ^0 is electrically neutral. With the covariant derivative introduced in section 1.1.2, the Higgs doublet gets an associated part in the SM Lagrangian,

$$\mathcal{L}_h = (D_\mu \Phi)^\dagger (D^\mu \Phi) - V(\Phi), \quad (1.34)$$

where $V(\Phi)$ is a gauge invariant potential

$$V(\Phi) = -\mu^2 \Phi^\dagger \Phi + \frac{\lambda}{4} (\Phi^\dagger \Phi)^2. \quad (1.35)$$

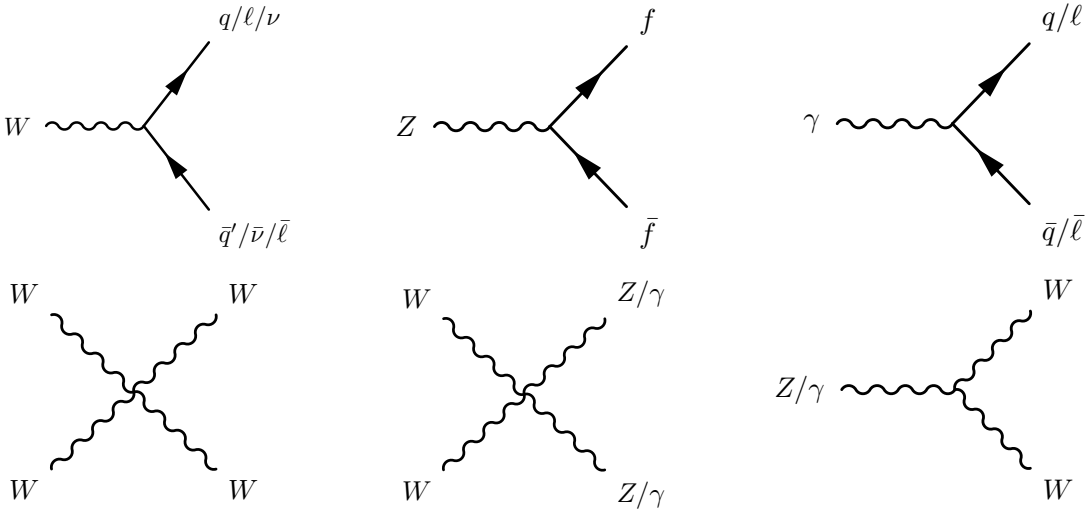


Figure 1.2: Possible vertices in the electroweak interaction.

For positive and real parameters μ^2 and λ , this potential has the form of a *Mexican hat* and an infinite number of minima for field configurations with $\Phi^\dagger\Phi = 2\mu^2/\lambda$. In the vacuum, i.e. in the ground state of the theory with minimal potential energy of the field, one of these minima is chosen such that the Higgs receives a vacuum expectation value (VEV),

$$\langle \Phi \rangle = \frac{1}{\sqrt{2}} \begin{pmatrix} 0 \\ v \end{pmatrix} \quad \text{with} \quad v = \frac{2\mu}{\sqrt{\lambda}} \approx 246 \text{ GeV.} \quad (1.36)$$

This is neither invariant under a $SU(2)_L$ transformation of the form $U = \exp(i\alpha^a \frac{\sigma^a}{2})$, nor under a $U(1)_Y$ transformation of the form $\exp(i\alpha \frac{Y}{2})$. Thus, the Lagrangian has a symmetry that the vacuum state does not have. As the VEV of ϕ^+ vanishes and ϕ^0 is invariant under $U(1)_{\text{em}}$, the symmetry group $SU(2)_L \otimes U(1)_Y$ is therefore spontaneously broken down to $U(1)_{\text{em}}$ [3].

The Higgs doublet can be expressed as excitations around the ground state

$$\Phi(x) = \frac{1}{\sqrt{2}} \begin{pmatrix} \phi_1(x) + i\phi_2(x) \\ v + h(x) + i\chi(x) \end{pmatrix}, \quad (1.37)$$

where h , χ , ϕ_1 and ϕ_2 are real-valued scalar fields with vanishing VEVs. Inserting eq. (1.37) back into the potential $V(\Phi)$ in eq. (1.35) yields

$$V = \mu^2 h^2 + \frac{\mu^2}{v} h(h^2 + \chi^2 + \phi_1^2 + \phi_2^2) + \frac{\mu^2}{4v^2} (h^2 + \chi^2 + \phi_1^2 + \phi_2^2), \quad (1.38)$$

where only h gets a mass term, thus describing an electrically neutral scalar particle with mass $m_h = \sqrt{2}\mu$. The remaining scalar fields remain massless, which is in accordance with the Nambu-Goldstone theorem [33, 34], stating that every spontaneously broken continuous symmetry generates a massless Goldstone boson. These bosons are unphysical and can be gauged away through a $SU(2)_L$ transformation, such that the expansion around the vacuum from eq. (1.37), involves only the physical scalar $h(x)$ in the so-called *unitary gauge*.

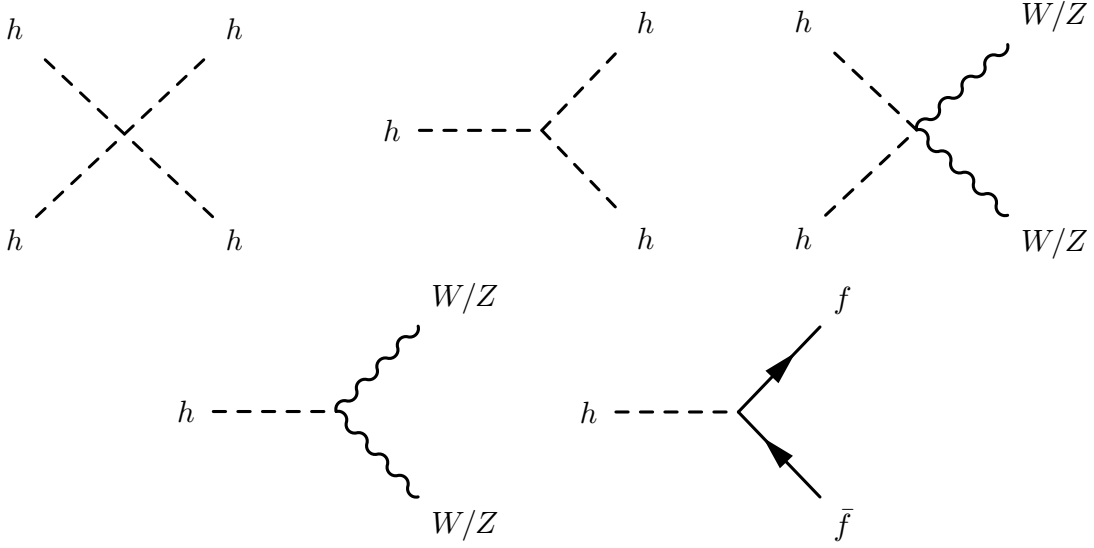


Figure 1.3: Possible vertices involving the Higgs boson.

Inserting eq. (1.37) and the potential V from eq. (1.38) back into the Lagrangian \mathcal{L}_h in eq. (1.34) leads to mass terms for the gauge fields through their couplings to the h field. The *physical* fields corresponding to the physically observable W^\pm , Z and γ bosons in the electroweak theory are then given by the linear combinations

$$\begin{aligned} W_\mu^\pm &= \frac{1}{\sqrt{2}}(W_\mu^1 \mp iW_\mu^2) & \text{with } m_W &= \frac{g_2}{2}v, \\ Z_\mu &= \cos\theta_W W_\mu^3 - \sin\theta_W B_\mu & \text{with } m_Z &= \frac{1}{2}\sqrt{g_1^2 + g_2^2}v, \\ A_\mu &= \sin\theta_W W_\mu^3 + \cos\theta_W B_\mu & \text{with } m_A &= 0, \end{aligned}$$

where θ_W is the weak mixing angle. It is related to the masses of the W and Z bosons, and the electroweak coupling constants by

$$\cos\theta_W = \frac{g_2}{\sqrt{g_1^2 + g_2^2}} = \frac{m_W}{m_Z}. \quad (1.39)$$

In the SM the W^\pm and Z bosons thus acquire masses through spontaneous breaking of the electroweak gauge symmetry $SU(2)_L \otimes U(1)_Y$ through the Higgs mechanism. The massless photon field A_μ associated with the electromagnetic $U(1)_{\text{em}}$ gauge symmetry is automatically recovered. All possible vertices between fermions and the physical electroweak gauge bosons are shown in fig. 1.2.

Furthermore, the masses of fermion fields are related to gauge-invariant Yukawa interactions with the Higgs field. For one fermion generation, the respective Yukawa terms in the Lagrangian are

$$\mathcal{L}_{\text{Yukawa,gen}} = -\lambda_\ell \bar{L}_L \Phi \ell_R - \lambda_d \bar{Q}_L \Phi d_R - \lambda_u \bar{Q}_L \Phi^\dagger u_R + \text{h.c.}, \quad (1.40)$$

where λ_f with $f = \ell, d, u$ are the dimensionless Yukawa couplings and $L_L = (\nu_L, \ell_L)^T$ and $Q_L = (u_L, d_L)^T$ are the left-handed lepton and quark doublets, respectively. The non-vanishing

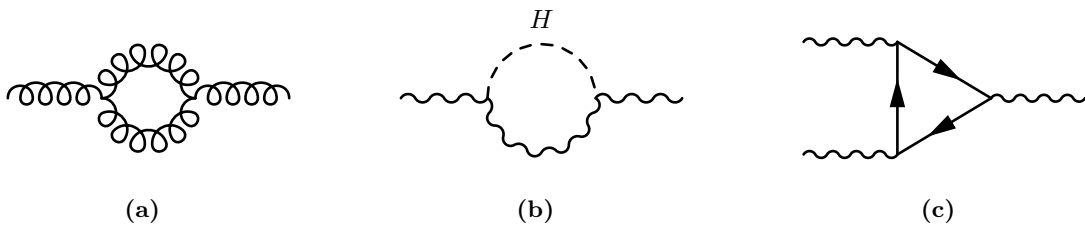


Figure 1.4: Examples of loop corrections to (a) the gluon propagator, (b) the W or Z propagator and (c) the cubic gauge boson vertex.

VEV of the Higgs field then gives rise to fermion mass terms of the form

$$m_f = \lambda_f \frac{v}{\sqrt{2}}, \quad (1.41)$$

yielding fermion couplings to the Higgs field proportional to the fermion masses m_f . All SM interaction vertices involving the Higgs boson are shown in fig. 1.3.

When introducing all three fermion generations, additional Yukawa terms mixing fermions of different generations appear in the Lagrangian [3]. The terms involving quark fields can be parametrised using the CKM matrix V_{CKM} [12, 13], quantifying the transition probability between quark generations. Since no right-handed neutrinos exist in the SM, no generation mixing in the lepton sector occurs and hence no neutrino mass terms are allowed in the SM. Neutrino oscillations have, however, been observed experimentally, thus at least two massive neutrino generations need to exist. Their mixing can then be described with the PMNS matrix [11], allowing neutrinos to acquire mass e.g. through the see-saw mechanism [35].

1.1.3 Renormalisation and divergencies

At lowest order in the perturbative expansion, the momenta of the internal lines in the Feynman diagrams are fixed by the external particles. For higher orders where the diagrams involve loops, the momenta of the internal lines need to be integrated over as they are not fixed by energy-momentum conservation. Some examples of loop corrections to propagators and vertices are shown in fig. 1.4. As each vertex in the Feynman diagrams is associated with a coupling constant that is usually much smaller than 1 (apart from the non-perturbative regime of QCD), higher orders in the perturbative expansion contribute less and less to the total amplitude of the full expansion.

The momentum integrals in loop corrections, however, lead to *ultraviolet divergencies* for large momenta. In order to eliminate the divergencies, the integrals have to be *regularised*, e.g. by applying a cut-off scale Λ or calculating the integrals in a number $D = 4 - \epsilon$ of dimensions where they converge. The potential divergencies are then absorbed in parameters of the Lagrangian, such as coupling constants and masses, after which the regulator is removed (e.g. $\epsilon \rightarrow 0$) again and a *renormalisation* procedure is applied, replacing the bare parameter values with the physical, measured values [3]. Renormalisation effectively absorbs the effects of quantum fluctuations acting on much smaller scales than the scale of the given problem in the parameters of the theory. As Veltmann and t'Hooft [36, 17] have shown, all Yang-Mills theories with massive gauge fields are renormalisable, making the SM as a whole a renormalisable theory.

1.2 Supersymmetry

Originally developed in the late 1960s and early 1970s as an attempt to combine the Poincaré group with internal symmetries into a single symmetry group [37], Supersymmetry (SUSY) is a class of theories transforming fermionic states into bosonic ones, and vice-versa. Since its theoretical discovery, driven purely by theoretical developments rather than by pressure of existing data [37], SUSY was found to have far-reaching phenomenological consequences that could solve some of the shortcomings of the SM.

This section starts with an overview of these shortcomings and illustrates how they could be solved by supersymmetric theories. This is followed by an introduction to the mathematical description and phenomenological consequences of SUSY. While the following sections are intended to highlight the most important concepts and relations, a much more complete and detailed introduction to SUSY can be found in Refs. [5, 6].

1.2.1 Shortcomings of the Standard Model

Although the SM is a remarkably successful theory able to predict and describe the interactions between elementary particles with unprecedented precision, there are still phenomena in nature that cannot be suitable understood within the theoretical framework of the SM.

Those limitations and open questions are the reason for numerous searches looking for new physics BSM, such as the one presented in this thesis. Some of these open questions are described in the following.

Dark Matter

The existence of DM, i.e. non-luminous and non-absorbing matter is nowadays well established [9]. Some of the earliest hints for the existence of DM came from the observation that the rotation curves of luminous objects are not consistent with the expected velocities based on the gravitational attraction of the visible objects around them. Zwicky already postulated in 1933 the existence of DM [38] based on rotation curves of galaxies in the Coma cluster. In 1970, Rubin measured rotation curves of spiral galaxies [39], revealing again a significant disagreement with the theoretically expected curves given the visible matter in the galaxies. Based on Newtonian dynamics, the circular velocity of stars outside the bulge of galaxies is expected to fall off with increasing radius as $v(r) \propto 1/\sqrt{r}$ [40]. Rubin's observations, however, revealed that the velocities of stars outside the bulge stay approximately constant, strongly suggesting the existence of a non-luminous (or *dark*) matter halo around the galaxies. Surveys of galaxy clusters and observations of gravitational lensing effects e.g. in the bullet cluster [41] or the Abell 1689 cluster [42] have since then further consolidated the existence of large accumulations of non-luminous mass in the universe.

The anisotropies in cosmic microwave background (CMB), studied by the COBE [43, 44], WMAP [45, 46] and Planck missions [47] are well described by the Lambda Cold Dark Matter (Λ CDM) model [48], which includes a density for cold dark matter. Planck's latest results [49]

for the cold DM relic density and baryonic density of

$$\begin{aligned}\Omega_c h^2 &= 0.1200 \pm 0.0012, \\ \Omega_b h^2 &= 0.02237 \pm 0.00015,\end{aligned}\tag{1.42}$$

respectively, suggest that ordinary baryonic matter only makes up $\sim 4.9\%$ of the universe's matter content, while DM accounts for $\sim 26.1\%^{\dagger}$.

Candidates for cold DM need to satisfy certain conditions: they have to be stable on cosmological timescales (otherwise they would have decayed by now), they have to couple only very weakly to the electromagnet interaction (if at all, otherwise they would be luminous matter) and they need to have the right relic density. Analyses of structure formations in the Universe have furthermore shown that most DM should have been *cold*, i.e. non-relativistic at the beginning of galaxy formation [40]. Candidates for DM particles are e.g. sterile neutrinos, axions, primordial black holes, or weakly interacting massive particles (WIMPs).

In the SM, the only DM candidate particle is the neutrino. Given the upper limits on the neutrino masses, an upper bound on their relic density can be computed, revealing that neutrinos are not abundant enough to be a dominant component of DM [40]. Furthermore, due to their low masses, neutrinos would still have been relativistic particles at the beginning of galaxy formation, preventing the *bottom-up*[§] structure formation favoured by a cold DM dominated universe.

Many BSM theories naturally predict new WIMPs with masses in the GeV to TeV range. In many SUSY models with exact R-parity conservation (a quantity introduced in section 1.2.5), the lightest supersymmetric particle is neutral and stable and could be a good candidate for DM.

Unification of forces

Although the SM provides a good description of nature up to the energy scale probed with today's accelerators, some of its peculiar aspects hint to a more fundamental theory. A prominent example is the question why the electric charges of the electrons and the charges of the quarks of the protons and neutrons in the nuclei exactly cancel, making for electrically neutral atoms [3]. Or in other words: why are the charges of all observed particles simple multiples of the fundamental charge? And why are they quantised in the first place?

An explanation to many of these peculiarities comes naturally when describing the SM as a unified theory with a single non-Abelian gauge group, e.g. $SU(5)$ [50]. The larger symmetry group with a single coupling constant is then thought to be spontaneously broken at very high energy, such that the known SM interactions are recovered at the lower energies probed in today's experiments. In such a grand unified theory (GUT), the particles in the SM are arranged in anomaly-free[‡] irreducible representations of the gauge group, thereby e.g. naturally ensuring the fractional charges of quarks [4].

[†] The remaining $\sim 69\%$ are taken up by *dark energy*, the nature of which is still an open question.

[§] The *bottom-up* structure formation begins with small objects that subsequently merge into ever larger structures and is the structure formation process favoured in a universe dominated by cold DM.

[‡] In the sense that loop corrections do not break symmetries the Lagrangian has.

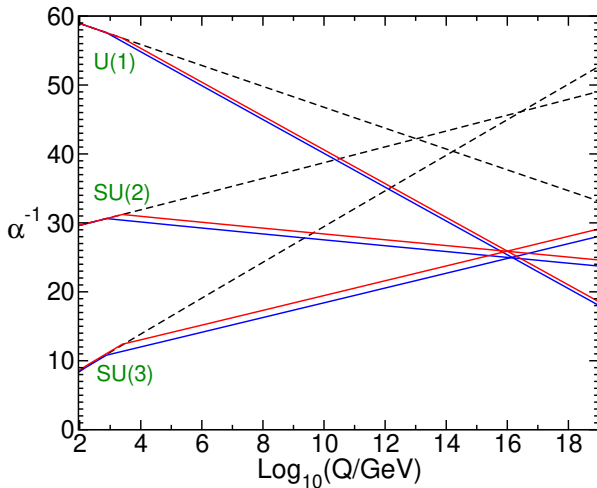


Figure 1.5: Evolution of the inverse coupling constants in the SM (dashed lines) and the MSSM (solid lines) in function of the energy scale Q . In the MSSM, the masses of the supersymmetric particles are treated as common threshold varied between 750 GeV and 2.5 TeV. Figure taken from Ref. [5].

In the SM, the coupling constants run towards each other with increasing energy scale, but never exactly meet. In the Minimal Supersymmetric Standard Model (MSSM), introduced in section 1.2.5, the running couplings meet within their current uncertainties if the supersymmetric particles are at the TeV scale, hinting that a supersymmetric GUT could be a good candidate for describing physics at the unification scale. Figure 1.5 shows that the running coupling constants in the MSSM are modified such that they meet at 10^{16} GeV .

The Hierarchy Problem

As the SM is a renormalisable gauge theory, finite results are obtained for all higher-order loop corrections, making the SM a theory that is in principle well-defined up to infinite energies. In renormalisation terms, this means that the cut-off scale Λ is theoretically allowed to go to arbitrarily high values. It is clear though, that the SM cannot be a complete theory of nature and that at some unknown high-energy scale Λ , *new physics* has to appear. At the very least, a new theoretical framework becomes necessary at the Planck scale $M_P \approx 10^{19} \text{ GeV}$ [6], where quantum gravitational effects can no longer be ignored.

The mass parameters of fermions and massive vector bosons are protected from large quantum corrections by chiral symmetry and gauge symmetry, respectively [51]. The mass parameter of the scalar Higgs field, on the other hand, receives loop corrections proportional at least to the scale at which new physics sets in. The Yukawa coupling of the Higgs field to a fermion f with mass m_f , depicted in fig. 1.6(a), yields a one-loop correction term to the Higgs square mass [6] given by

$$\Delta m_h^2 = -\frac{\lambda_f^2}{8\pi^2} \Lambda^2 + \dots \quad (1.43)$$

The Higgs mass thus quadratically diverges with the scale Λ . If the SM is to be valid up to the Planck scale, then $\Lambda = M_P$, and the correction to the Higgs squared mass becomes more than 10^{30} times larger than the expected value in the order of $(10^2 \text{ GeV})^2$ [5]. Similar quantum corrections arise from the Higgs quartic coupling to a heavy scalar boson S with mass m_S ,

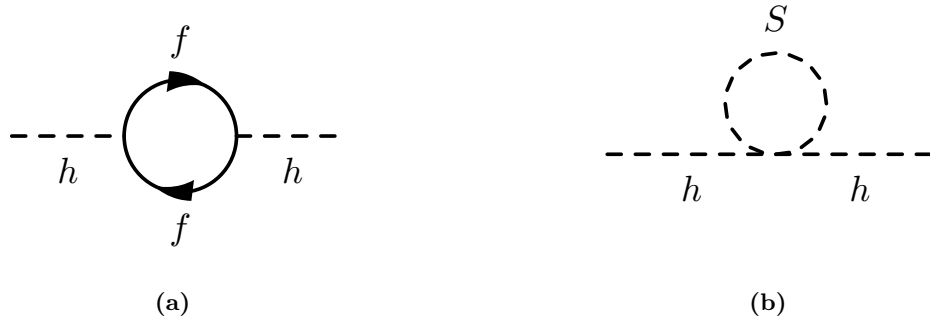


Figure 1.6: A massive fermion (a) and a hypothetical massive scalar particle (b) coupling to the Higgs boson.

shown in fig. 1.6(b), yielding a one-loop correction [6] given by

$$\Delta m_h^2 = \frac{\lambda_S}{16\pi^2} \Lambda^2 + \dots \quad (1.44)$$

In order to obtain the experimentally measured value of the Higgs mass, the quantum corrections to the bare Higgs parameter have to be tuned in such a way that they almost cancel, leading to a *fine-tuning* problem that is considered to be unnatural.

Interestingly, the terms quadratically divergent in Λ in eq. (1.43) and eq. (1.44) enter with opposite signs. If, for every fermionic loop, there are two bosonic loops with $\lambda_S = \lambda_f^2$, the quadratically diverging terms neatly cancel. As will be discussed, this is exactly the case in supersymmetric theories. Additional correction terms omitted above are at most logarithmic in Λ , and cancel if the scalar bosons and the fermion have the same masses (this is further discussed in section 1.2.5).

Anomalous magnetic moment of the muon

One of the longest standing disagreements between experiment and theory in the SM is the anomalous magnetic moment of the muon [9]. The magnetic moment of the muon $\vec{\mu}_\mu$ is related to its intrinsic spin \vec{S} through the gyromagnetic ratio g_μ by

$$\vec{\mu}_\mu = g_\mu \frac{q}{2m} \vec{S}. \quad (1.45)$$

For a structureless spin-1/2 particle with mass m and charge $q = \pm e$, the gyromagnetic ratio is $g_\mu = 2$ [52]. Loop corrections coupling the muon spin to virtual fields cause small deviations, parameterised by the anomalous magnetic moment

$$a_\mu = \frac{1}{2}(g_\mu - 2). \quad (1.46)$$

The anomalous magnetic moment can be precisely measured as well as predicted within the SM. A comparison between experimental data and theoretical prediction thus directly tests the SM at quantum loop level and may hint to effects from new physics in case of discrepancies [53]. In the SM, the most dominant contribution to a_μ comes from QED corrections involving

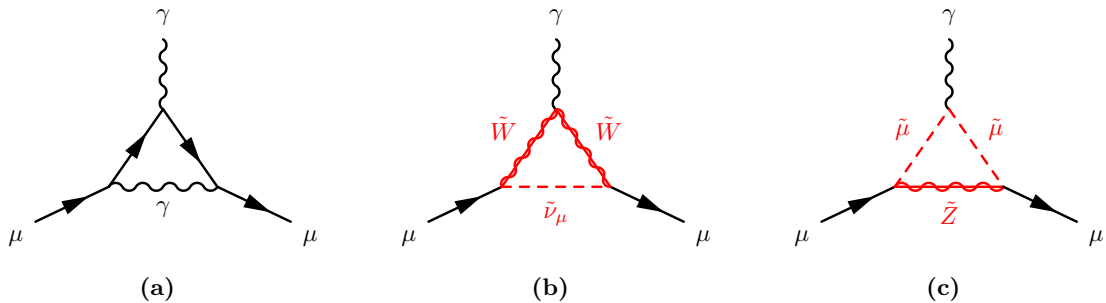


Figure 1.7: Electromagnetic (a) and supersymmetric (b), (c) contributions to a_μ . Supersymmetric particles are drawn in red. Adapted from Ref. [53].

photon and fermion loops. An exemplary diagram is shown in fig. 1.7(a). Weak contributions involving the heavy W^\pm , Z and Higgs particles are suppressed by their masses [54]. Although the contributions from QCD are relatively small, they give rise to the main theoretical uncertainties as they cannot be calculated from first principles but rely either on data-driven calculations, or lattice QCD evaluations [54].

The muon $g-2$ experiment at the Fermi National Accelerator Laboratory (FNAL) [55] has recently measured the anomalous magnetic moment of the muon, updating the results from the E821 experiment at Brookhaven National Laboratory (BNL) [52] obtained in 2004. The combined experimental average of both experiments finds a deviation from the SM expectation[†] of

$$\Delta a_\mu = a_\mu^{\text{exp}} - a_\mu^{\text{SM}} = (251 \pm 59) \times 10^{-11}, \quad (1.47)$$

which is quantified to have a significance of 4.2σ [55]. These results strongly hint at the existence of new physics beyond the SM.

In SUSY, additional Feynman diagrams exist, involving the supersymmetric partners of the muon, the muon neutrino and the electroweak gauge bosons, and thus the measured deviation in a_μ can easily be accommodated in many supersymmetric models [56, 57]. Two exemplary lowest-order diagrams involving supersymmetric particles (introduced in section 1.2.5) are shown in figs. 1.7(b) and 1.7(c).

1.2.2 Supersymmetric Algebra

The Coleman–Mandula no-go theorem [58] dictates that the symmetry group generating a consistent spacetime QFT must be the direct product of the internal symmetry group with the Poincaré group, which in principle rules out the possibility for SUSY. The Coleman–Mandula proof, however, assumes the new symmetry to be generated by bosonic integer spin generators. The Haag–Lopuszanski–Sohnius extension [59] showed that the only possible way of non-trivially combining internal and spacetime symmetry groups is to use a Lie superalgebra and fermionic spin-1/2 generators.

[†] The SM value of a_μ adopted in Ref. [55] relies on the data-driven evaluation of the hadronic contributions using e^+e^- collider data, recommended by the muon $g-2$ theory initiative [54].

A generator of supersymmetric transformations is thus an anti-commuting spinor Q that turns fermionic states $|f\rangle$ into bosonic states $|b\rangle$ and vice-versa.

$$Q|f\rangle = |b\rangle, \quad Q|b\rangle = |f\rangle. \quad (1.48)$$

As spinors are complex objects, Q^\dagger is also a symmetry operator. Both Q and Q^\dagger are necessarily fermionic and thus must carry half-integer spin, in the simplest case spin-1/2, meaning that SUSY must be a spacetime symmetry, i.e. a Poincaré symmetry. Thus, in order to obey the Haag–Lopuszanski–Sohnius loophole of the Coleman–Mandula theorem, and simultaneously allow for parity-violating interactions, the SUSY generators have to satisfy the following algebra of commutation and anti-commutation relations [6],

$$\begin{aligned} \{Q, Q^\dagger\} &= 2\sigma_\mu P^\mu, \\ \{Q, Q\} &= \{Q^\dagger, Q^\dagger\} = 0, \\ [P^\mu, Q] &= [P^\mu, Q^\dagger] = 0, \\ \{M^{\mu\nu}, Q\} &= \sigma^{\mu\nu} Q, \\ \{M^{\mu\nu}, Q^\dagger\} &= \bar{\sigma}^{\mu\nu} Q^\dagger, \end{aligned} \quad (1.49)$$

where P^μ is the four-momentum generator of spacetime translations, $\sigma_\mu = (\mathbb{1}_2, \sigma_i)$, $\bar{\sigma}_\mu = (\mathbb{1}_2, -\sigma_i)$ with $i = 1, 2, 3$ and the Pauli matrices σ_i , and $\sigma^{\mu\nu} = \frac{i}{4}(\sigma^\mu \bar{\sigma}^\nu - \sigma^\nu \bar{\sigma}^\mu)$ as well as $\bar{\sigma}^{\mu\nu} = \frac{i}{4}(\bar{\sigma}^\mu \sigma^\nu - \bar{\sigma}^\nu \sigma^\mu)$. This is the simplest version of SUSY, called $N = 1$ symmetry, as it introduces only one pair of generators. Supersymmetric theories with $N \geq 2$ pairs of generators also exist and generally have some theoretical advantages as e.g. fewer divergencies in the case of $N = 2$ or even no divergencies at all in the case of $N = 4$ [6]. SUSY models with $N \geq 2$, however, do not allow for parity violation and thus fail to describe the physics of the SM, disqualifying them from a phenomenological point of view [6].

As both SUSY generators commute with spacetime translations (see eq. (1.49)), they also both commute with the squared mass operator $-P^2$. Consequently, particles related by the generators, called *superpartners*, must have equal eigenvalues under $-P^2$, i.e. they must have equal masses. Furthermore, the SUSY generators also commute with the gauge transformation generators, hence superpartners must have same electric charge, weak isospin and degrees of freedom in colour space [5].

1.2.3 Supermultiplets

The SM and SUSY particles are arranged in irreducible representations of the SUSY algebra, called *supermultiplets*, each containing both fermionic and bosonic states that are superpartners of each other. It can be shown that each supermultiplet has an equal number of fermion and boson degrees of freedom, $n_f = n_b$ [5].

The simplest supermultiplet Ψ that can be constructed contains a single Weyl fermion ψ and two real scalars, described by a single complex field ϕ , called the *sfermion*. The Weyl fermion has two spin helicity states, hence $n_f = 2$, and the complex scalar field has two components with $n_b = 1$ each. An additional complex scalar field F , called *auxiliary field* and not corresponding to a physical particle, has to be introduced in order to allow the SUSY algebra to close off-shell

(where the energy-momentum relation does not hold) [5]. The supermultiplet Ψ thus reads

$$\Psi = (\phi, \psi, F). \quad (1.50)$$

Being a pure bookkeeping device, the auxiliary field does not propagate and can be eliminated on-shell with the equations of motion $F = F^* = 0$. This supermultiplet is called a *chiral* or *scalar* supermultiplet [5].

The next-simplest supermultiplet for which $n_f = n_b$ holds, is the *vector* or *gauge* supermultiplet Φ containing a spin-1 gauge boson A_a^μ , where a is the index of the gauge group. In order for the theory to be renormalisable, this gauge boson must be massless before spontaneous breaking of the symmetry. As a massless spin-1 boson has two helicity states, $n_b = 2$, the superpartner, called *gaugino*, must be a massless spin-1/2 Weyl fermion λ_a with two helicity states such that $n_f = 2$ [5]. An auxiliary real bosonic field D_a is needed in order to balance the degrees of freedom off-shell [6], completing the supermultiplet to be

$$\Phi = (\lambda_a, A_a^\mu, D_a). \quad (1.51)$$

Like the chiral auxiliary field, the gauge auxiliary field does not correspond to a physical particle and can be eliminated on-shell through its equations of motion [5].

1.2.4 Supersymmetric Lagrangian

The simplest supersymmetric model that can be shown to realise the superalgebra is the massless, non-interacting Wess–Zumino model [60] with the action [6, 5]

$$\begin{aligned} S &= \int d^4x (\mathcal{L}_{\text{scalar}} + \mathcal{L}_{\text{fermion}}), \\ \mathcal{L}_{\text{scalar}} &= -\partial^\mu \phi^* \partial_\mu \phi, \\ \mathcal{L}_{\text{fermion}} &= -i\psi^\dagger \bar{\sigma}^\mu \partial_\mu \psi, \end{aligned} \quad (1.52)$$

with a massless complex scalar ϕ and a spin-1/2 fermion ψ , corresponding to a single chiral supermultiplet. As discussed in section 1.2.3, in order for this Lagrangian to satisfy the supersymmetry off-shell where the equations of motion cannot be used, an auxiliary complex scalar field F has to be added. The free Lagrangian [6] in the action thus reads

$$\mathcal{L}_{\text{free}} = \mathcal{L}_{\text{scalar}} + \mathcal{L}_{\text{fermion}} + \mathcal{L}_{\text{aux}}, \quad \text{with } \mathcal{L}_{\text{aux}} = F^{*i} F_i. \quad (1.53)$$

The auxiliary term \mathcal{L}_{aux} implies the trivial equations of motion $F = F^* = 0$ which are needed to remove the auxiliary field in the on-shell case. The next step involves adding terms for non-gauge interactions for the chiral supermultiplets. Non-gauge interactions for chiral supermultiplets at most quadratic in the fermion fields can be achieved by introducing the term [6],

$$\mathcal{L}_{\text{int}} = -\frac{1}{2} W^{ij}(\phi, \phi^*) \psi_i \psi_j + V(\phi, \phi^*) + c.c., \quad (1.54)$$

where W^{ij} is a holomorphic[†] function of the complex scalar fields ϕ_i of the form [6]

$$W^{ij} = \frac{\partial^2 W}{\partial \phi_i \partial \phi_j}. \quad (1.55)$$

Here, W is called the *superpotential*. For the final Lagrangian to be renormalisable, the superpotential can at most be cubic [6], and thus can be written as

$$W = \frac{1}{2} m^{ij} \phi_i \phi_j + \frac{1}{6} y^{ijk} \phi_i \phi_j \phi_k, \quad (1.56)$$

where y^{ij} are the Yukawa couplings between the scalar and the two fermions, thus containing all non-gauge interactions. The term quadratic in the fields contains the fermion mass matrix m^{ij} , which is equal to the mass matrix of the scalar bosons due to supersymmetry, as will be shown below. Requiring \mathcal{L}_{int} to be invariant under supersymmetry transformations further defines the potential V . The equations of motion of the auxiliary fields F can be written as

$$F_i = -\frac{\partial W(\phi)}{\partial \phi^i} = -W_i^*, \quad F^{*i} = -\frac{\partial W(\phi)}{\partial \phi_i} = -W^i, \quad (1.57)$$

which thus yields for the potential $V = W_i^* W^i = F_i F^{*i}$, allowing to write the Lagrangian without explicitly introducing the auxiliary fields. The full Lagrangian of the Wess-Zumino model with general chiral interactions between the scalar and fermion fields in the chiral supermultiplets [6] is then given by

$$\mathcal{L} = -\partial^\mu \phi^{*i} \partial_\mu \phi_i - i \psi^{\dagger i} \bar{\sigma}^\mu \partial_\mu \psi_i - \frac{1}{2} m^{ij} \psi_i \psi_j - \frac{1}{2} m_{ij}^* \psi^{\dagger i} \psi^{\dagger j} - \frac{1}{2} y^{ijk} \phi_i \psi_j \psi_k - \frac{1}{2} y_{ijk}^* \phi^{*i} \psi^{\dagger j} \psi^{\dagger k} - V(\phi, \phi^*), \quad (1.58)$$

obtained by adding the interaction term \mathcal{L}_{int} from eq. (1.54) to the free Lagrangian in eq. (1.52) and inserting the expression for the superpotential from eq. (1.56) and the auxiliary fields from eq. (1.57).

The Lagrangian in eq. (1.58) immediately reveals that, as expected by supersymmetry, the masses of the fermions and bosons in the same supermultiplet are identical. In order to incorporate gauge supermultiplets and consider the interactions between fermions and gauge bosons observed in the SM, the usual minimal coupling rule has to be applied, replacing ∂_μ with D_μ . This leads to equation of motions for the auxiliary fields D^a

$$D^a = -g(\phi^* T^a \phi), \quad (1.59)$$

where T^a are the generators of the gauge group and g is the coupling constant [6]. The potential then becomes

$$V(\phi, \phi^*) = F^{*i} F_i + \frac{1}{2} \sum_a D^a D^a = W_i^* W^i + \frac{1}{2} \sum_a g_a^2 (\phi^* T^a \phi)^2, \quad (1.60)$$

where a runs over the gauge groups that generally have differing gauge couplings [6].

[†] A holomorphic function is a complex-valued function in one or more complex variables that is complex differentiable in a neighbourhood for every point of its domain.

Table 1.3: Particle content of the MSSM. The spin refers to the spin of the spartner. Adapted from [6].

Particle	Spartner 0	Spin
quarks q	squarks \tilde{q}	0
→ top t	stop \tilde{t}	
→ bottom b	sbottom \tilde{b}	
...		
leptons ℓ	sleptons $\tilde{\ell}$	0
→ electron e	selectron \tilde{e}	
→ muon μ	smuon $\tilde{\mu}$	
→ tau τ	stau $\tilde{\tau}$	
→ neutrinos ν_ℓ	stop $\tilde{\nu}_\ell$	
gauge bosons	gauginos	1/2
→ photon γ	photino $\tilde{\gamma}$	
→ boson Z	Zino \tilde{Z}	
→ boson B	Bino \tilde{B}	
→ boson W	Wino \tilde{W}	
→ gluon g	gluino \tilde{g}	
Higgs bosons $H_i^{\pm,0}$	higgsinos $\tilde{H}_i^{\pm,0}$	1/2

1.2.5 The Minimal Supersymmetric Standard Model

The MSSM is the simplest $N = 1$ supersymmetric extension of the SM in the sense that it introduces a minimal set of additional particles.

Particle content and interactions

The MSSM arranges all SM particles in chiral (all the fermions and quarks) and gauge (all spin-1 bosons) supermultiplets. As supersymmetric partners (*spartners*) have the same quantum numbers apart from spin, none of the SM particles can be spartners of each other. Thus, all spartners have to be new, unseen particles. Table 1.3 summaries the names, notations and spins of all spartners introduced in the MSSM. The naming convention is to prepend the names of the spartners of fermions with an 's' (e.g. *selectron*, *stop*, ...) and append '-ino' to the names of the spartners of the bosons (e.g. *Wino*, *Photino*, ...). Supersymmetric particles (*sparticles*) are generally denoted by adding a tilde to the symbol of SM particles (e.g. \tilde{e} , \tilde{u} , \tilde{g}).

An important detail to note is that right-handed and left-handed fermions get their own chiral supermultiplets and thus have distinct spartners, as otherwise the preference of the weak interaction for left-handed particles would be violated. For example, left-handed and right-handed quarks (q_L , q_R) get two different spartners (\tilde{q}_L , \tilde{q}_R), denoted with an index L and R. The index here refers to the handiness of the SM particle as scalar particles have only one helicity state. Additionally, the spartners of the left-handed and right-handed will mix to form physical mass eigenstates.

It is also worth asking why the spartners of SM particles are of lower spin in the first place, as e.g. spin-1 spartners of the SM fermions could also have been considered. The introduction of spin-1 bosons would entail the introduction of new gauge interactions, rendering the MSSM

non-minimal [6]. Furthermore, introducing sparticles with spin greater than 1 would make the resulting theory non-renormalisable [6].

In the MSSM, two Higgs doublets are needed in order to give masses to the up-type and down-type quarks via Yukawa couplings. A single Higgs field h cannot be used for this as it would require Yukawa terms including the complex conjugate h^* , which is forbidden as the superpotential, being a holomorphic function of the fields, cannot depend on the complex conjugates of the same fields [6]. Additionally, the use of a single Higgs doublet would lead to gauge anomalies in the electroweak gauge symmetry [61]. Instead two complex Higgs doublets with hypercharge $Y = \pm 1/2$ are used in the MSSM. The two Higgs doublets can be written as

$$H_u = \begin{pmatrix} H_u^0 \\ H_u^- \end{pmatrix}, \quad H_d = \begin{pmatrix} H_d^+ \\ H_d^0 \end{pmatrix}, \quad (1.61)$$

As illustrated in section 1.2.4 using the Wess–Zumino model, interactions are introduced using the superpotential. In the MSSM, the superpotential reads

$$W_{\text{MSSM}} = \bar{u} \mathbf{y}_u Q H_u - \bar{d} \mathbf{y}_d Q H_d - \bar{e} \mathbf{y}_e L H_d + \mu H_u H_d, \quad (1.62)$$

where Q and L correspond to the supermultiplets containing the left-handed quarks and leptons as well as their sparticles, respectively. Likewise, \bar{u} , \bar{d} , \bar{e} correspond to the supermultiplets containing the right-handed up-type quarks, down-type quarks and leptons as well as their sparticles, respectively. The parameters \mathbf{y}_u , \mathbf{y}_d and \mathbf{y}_e are the 3×3 Yukawa coupling matrices. Except for the third generation, the Yukawa couplings are known to be relatively small [5] and are thus not of direct interest for the phenomenology of the theory. Phenomenologically more interesting are the supersymmetric gauge interactions that dominate the production and decay process of sparticles in the MSSM [5]. The superpotential in eq. (1.62) illustrates again why two Higgs doublets are needed in the MSSM, since terms like $\bar{u} Q H_d^*$ or $\bar{e} L H_u^*$ are not allowed due to the holomorphism of the superpotential. The term $\mu H_u H_d$ contains the *higgsino mass parameter* μ and is the supersymmetric version of the Higgs mass term in the SM Lagrangian.

Soft supersymmetry breaking

As stated in section 1.2.2, all superpartners must have the same quantum numbers apart from their spin. They especially also should have the same masses. As such particles would have been discovered a long time ago, SUSY must be a broken symmetry. If broken SUSY is, however, still to provide a solution to the Hierarchy problem, i.e. cancel the quadratic divergencies in the loop corrections to the Higgs mass parameter, then the relations between the dimensionless couplings of the SM particles and their superpartners have to be maintained [5]. Hence, only symmetry breaking terms with positive mass dimension are allowed in the Lagrangian, especially also forbidding the presence of dimensionless SUSY-breaking couplings [5]. Such a breaking of SUSY is called *soft* breaking and can be written as

$$\mathcal{L} = \mathcal{L}_{\text{SUSY}} + \mathcal{L}_{\text{soft}}, \quad (1.63)$$

where $\mathcal{L}_{\text{soft}}$ contains all the symmetry breaking terms, whilst $\mathcal{L}_{\text{SUSY}}$ is the SUSY invariant Lagrangian with all the gauge and Yukawa interactions. In a softly broken SUSY, the loop

corrections to the Higgs mass parameter depend quadratically on the largest mass scale associated with the soft terms (m_{soft}). As the fine-tuning problem reappears if m_{soft} becomes too large, superpartners with masses not too far above the TeV scale are generally assumed [5].

A total of 105 new parameters with no counterpart in the SM are introduced through $\mathcal{L}_{\text{soft}}$ [5, 62]:

- Gaugino mass parameters M_1 , M_2 and M_3 .
- Trilinear scalar couplings, parametrised by 3×3 matrices in generation space \mathbf{a}_u , \mathbf{a}_d , \mathbf{a}_e , representing Higgs-squark-squark and Higgs-slepton-slepton interactions.
- Hermitian 3×3 matrices in generation space \mathbf{m}_Q^2 , $\mathbf{m}_{\tilde{u}}^2$, $\mathbf{m}_{\tilde{d}}^2$, \mathbf{m}_L^2 , $\mathbf{m}_{\tilde{e}}^2$ that represent the sfermion masses.
- SUSY breaking parameters $m_{H_u}^2$, $m_{H_d}^2$ and b .

The sfermion mass matrices and the trilinear scalar couplings may introduce additional flavour mixing and CP violation, both of which are heavily constrained by experimental results. Flavour mixing in the lepton sector is for example constrained by an upper limit on $\text{BR}(\mu \rightarrow e\gamma) < 4.2 \times 10^{-12}$ [63]. Bounds on additional CP violation as well as squark mixing terms come from measurements of the electron and neutron electric moments and neutral meson systems[†] [9]. Formally, in order to avoid these terms, SUSY breaking can be assumed to be *flavour-blind*, meaning that the mass matrices are approximately diagonal. The large Yukawa couplings for the third generation squarks and sfermions can then be achieved by assuming that the trilinear scalar couplings are proportional to the corresponding Yukawa coupling matrix [5].

As most of the parameters in the MSSM are related to soft SUSY breaking, it is not surprising that the phenomenology of the MSSM strongly depends on the exact breaking mechanism. The breaking is usually assumed to happen in a *hidden sector* and the effects of the breaking are then typically mediated by messenger fields from the hidden sector to the *visible sector* containing all the particles of the MSSM. Since the hidden sector is assumed to be only weakly or indirectly coupled to the visible sector, the phenomenology mostly depends on the mechanism mediating the breaking. The two most popular mechanisms are *gravity-mediated* and *gauge-mediated* SUSY breaking.

Mediating SUSY breaking through gravity is an attractive approach, since all particles share gravitational interactions. This makes it easy to imagine gravitational effects to be the only connection between the hidden and the visible sectors. In such models SUSY breaking is mediated through effects of gravitational strength, suppressed by inverse powers of the Planck mass [9]. The mass of the gravitino—the spartner of the hypothetical mediator particle of gravity, called *graviton*—is typically of electroweak scale [64, 65]. Due to its couplings of gravitational strengths, it usually does not play a role in collider physics [9].

In gauge-mediated SUSY breaking (GMSB), additional messenger fields sharing gauge interactions with the MSSM fields are transmitting the breaking from the hidden to the visible sector. In such models, the gravitino is typically the LSP, as its mass ranges from a few eV to a few GeV, making it a candidate for DM [66].

[†] While it is theoretically possible to fine-tune the numerous phases in the MSSM such that cancelling contributions are generated, such possibilities will not be discussed in the following.

Mass spectrum

In the MSSM electroweak symmetry breaking is generalised to the two Higgs doublets introduced in eq. (1.61). In total, the two doublets have eight degrees of freedom, three of which are used to give masses to the W^\pm and Z bosons during the breaking of $SU(2)_L \otimes U(1)_Y$ to $U(1)_{\text{em}}$ (see section 1.1.2). Thus, five physical Higgs bosons appear in the MSSM; two neutral Higgs bosons even under CP transformation, called h^0 and H^0 , one neutral Higgs boson odd under CP transformation, called A^0 , and finally two charged Higgs bosons, called H^\pm . The two Higgs doublets H_u and H_d each get a VEV (v_u and v_d , respectively) that are connected to the VEV v of the SM Higgs field by

$$v_u^2 + v_d^2 = v^2. \quad (1.64)$$

Phenomenologically, the ratio of the two VEVs is usually considered, conventionally called $\tan \beta$,

$$\tan \beta = \frac{v_u}{v_d}. \quad (1.65)$$

Due to electroweak symmetry breaking, the gauginos and higgsinos are not mass eigenstates but mix to form *electroweakinos*:

- The two charged higgsinos mix with the two charged winos to form two charged mass eigenstates $\tilde{\chi}_1^\pm, \tilde{\chi}_2^\pm$, called *charginos*.
- The remaining neutral higgsinos mix with the bino and neutral wino to form four neutral mass eigenstates $\tilde{\chi}_1^0, \tilde{\chi}_2^0, \tilde{\chi}_3^0, \tilde{\chi}_4^0$, called *neutralinos*.

Both charginos and neutralinos are by convention labeled in ascending mass order. As the exact diagonalised forms of their mass mixing matrices are, in general, relatively complicated [67], they are typically evaluated in limits where one component dominates. Neutralinos with a dominant wino, bino or higgsino component will be called wino-, bino- or higgsino-like, respectively, in the following. Likewise, charginos will be called wino- or higgsino-like, if the respective component dominates.

Squarks and sleptons also mix, respectively. As in principle any scalars with the same electric charge, colour charge and R-parity (see section 1.2.5) can mix with each other, the mass eigenstates of the sleptons and squarks should a priori be obtained through diagonalisation of three 6×6 mixing matrices (one for up-type squarks, one for down-type squarks and one for charged sleptons) and one 3×3 matrix (for sneutrinos). The assumption of flavour-blind soft SUSY breaking terms leads to most of the mixing angles being very small. As opposed to the first and second generation, the third generation sfermions have relatively large Yukawa couplings, therefore the superpartners of the left- and right-handed fermions mix to mass eigenstates $(\tilde{t}_1, \tilde{t}_2), (\tilde{b}_1, \tilde{b}_2), (\tilde{\tau}_1, \tilde{\tau}_2)$, again labeled in ascending mass order. The first and second generation sfermions, on the other hand, having very small Yukawa couplings, end up in nearly mass-degenerate, unmixed pairs.

The gluino, being the only colour octet fermion of the unbroken $SU(3)_C$ gauge group, cannot mix with another fermion and is thus a mass eigenstate with mass $m_{\tilde{g}} = |M_3|$ at tree level [5, 53].

R-parity

The superpotential of the MSSM in principle allows additional gauge-invariant terms that are holomorphic in the chiral superfields but violate either lepton number (L) or baryon number (B). However, L- or B-violating processes have not been observed. Also, the L- and B-violating terms would cause a finite lifetime of the proton by allowing for it to decay e.g. via $p \rightarrow e^+ \pi^0$, a process that is heavily constrained to have a lifetime longer than 1.6×10^{34} years [68], as found by the Super-Kamiokande experiment.

In order to avoid these terms, a new symmetry, called *R-parity*, is introduced. R-parity is a multiplicatively conserved quantum number defined to be

$$P_R = (-1)^{3(B-L)+2s}, \quad (1.66)$$

where s is the spin of the particle. Given this definition, all SM particles and the Higgs bosons have even R-parity ($P_R = +1$) while all sparticles have odd R-parity ($P_R = -1$). Assuming R-parity to be exactly conserved at each vertex in the MSSM, this leads to a number of interesting phenomenological consequences:

- Sparticles are always produced in pairs.
- Heavier sparticles decay into lighter ones.
- The number of sparticles at each vertex must be even.
- The lightest supersymmetric particle (LSP) must be stable as it cannot decay any further without violating R-parity.

The nature of the LSP can be further constrained by cosmological observations [69]. If it were electrically charged or coupled to the strong interaction, it would have dissipated its energy and mixed with ordinary matter in the galactic disks, where it would have formed anomalous heavy isotopes. Upper limits on such supersymmetric relics [70] heavily favour an electrically neutral and at most weakly interacting LSP. This excludes in particular the gluino as an LSP. Another possible LSP, the sneutrino, is ruled out by Large Electron Positron (LEP) and direct searches [71–73]. A gravitino LSP is especially attractive in gauge mediated theories. Another promising option is a neutralino LSP. In large portions of the MSSM parameter space, a neutralino LSP produces a DM relic density that is compatible with the DM relic density measured by Planck [49, 70].

Although both R-parity conserving and R-parity violating models exist and are searched for in ATLAS, for the phenomenological reasons explained above, only R-parity conserving SUSY models with neutralino LSPs are considered in the following.

1.2.6 The phenomenological MSSM

In addition to the 19 parameters of the SM, the MSSM adds a total of 105 additional parameters, too much to allow for a full exploration of the MSSM in experimental analyses. However, as discussed in section 1.2.5, not all values of the 105 additional parameters lead to phenomenologically viable models. By requiring a set of phenomenological constraints, the 105 free parameters

Table 1.4: Parameters of the phenomenological Minimal Supersymmetric Standard Model (pMSSM).

Parameter	Meaning
$\tan \beta$	ratio of the Higgs doublet VEVs
M_A	mass of the CP-odd Higgs boson
μ	Higgs-higgsino mass parameters
M_1, M_2, M_3	wino, bino and gluino mass parameters
$m_{\tilde{q}}, m_{\tilde{u}_R}, m_{\tilde{d}_R}, m_{\tilde{\ell}}, m_{\tilde{e}_R}$	first and second generation sfermion masses
$m_{\tilde{Q}}, m_{\tilde{t}_R}, m_{\tilde{b}_R}, m_{\tilde{L}}, m_{\tilde{\tau}_R}$	third generation sfermion masses
A_t, A_b, A_τ	third generation trilinear couplings

can be reduced to only 19 free parameters, spanning a model space called the pMSSM [74, 75]. The free parameters in the pMSSM are listed in table 1.4.

The reduction of free parameters is obtained by applying the following constraints on the MSSM:

- No new source of CP violation, as discussed in section 1.2.5, achieved by assuming all soft breaking parameters to be real.
- Minimal flavour violation, meaning that flavour-changing neutral currents (FCNCs), heavily constrained by experiment, are not allowed and the flavour physics is governed by the CKM matrix.
- First and second sfermion generations are mass-degenerate
- The trilinear couplings and Yukawa couplings are negligible for the first and second sfermion generations.

The pMSSM does not make any assumptions on the physics above the TeV scale, and therefore does not assume a specific SUSY breaking mechanism. With its 19 free parameters, and the typical complexity of a search for SUSY, the pMSSM is still computationally extremely challenging to probe. Using appropriate approximations, the computational complexity can be simplified enough for exhaustive scans and comparisons to experimental data to become possible. Two such approximations are discussed in chapters 9 and 10, respectively.

1.2.7 Simplified models

In searches for BSM physics at the Large Hadron Collider, it is common to use simplified models [76–78] as a way of reducing the available parameter space to a manageable level. Simplified models do not aim to represent complete supersymmetric models but are mostly defined by a single (or a few selected) decay chain(s) allowing only a small number of sparticles, usually only two or three. Other sparticles are decoupled by setting their masses to be kinematically inaccessible at current collider experiments. The decay chains of the participating sparticles are determined by fixed branching ratios, often set to be 100%. Experimental bounds from non-observation of a given model are then usually presented in function of the physical masses of the sparticles involved in the decay chain. The model space spanned by the free parameters

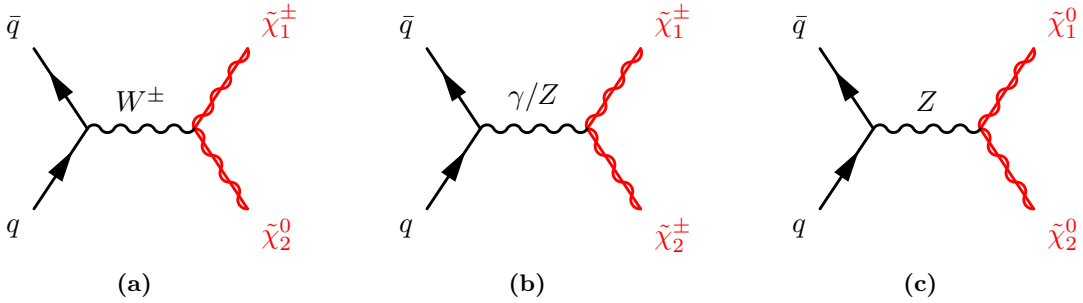


Figure 1.8: Dominant diagrams for production of electroweakino pairs at the Large Hadron Collider. Adapted from Ref. [5]

of the simplified model is typically called a *signal grid*, as each set of distinct mass parameter values, called *signal point*, occupies a single discrete point in this space. Figure 1.10(b) illustrates the signal grid used in part II of this thesis. The exact details of the signal grid are further discussed in section 1.3.2.

Simplified models have the inherent advantage that they circumvent the issue of having to search for SUSY in a vast parameter space where many of the parameters may only have small effects on observables. Their interpretation in terms of limits on individual SUSY production and decay topologies in function of sparticle masses is straightforward and very convenient. The hope is, that simplified models are a reasonable approximation of sizeable regions of parameter space of the more complete model they are embedded in [9]. The obvious downside is however, that the limits obtained in simplified models are not automatically a good approximation of the true underlying constraint on the respective model parameter when interpreted in more complete SUSY models. Often, the constraints set on sparticle masses in simplified models, significantly overestimate the true constraints obtained in more complex SUSY spectra, especially when the usual 100% branching fractions are assumed in the simplified models (see e.g. [79, 80]).

One way of circumventing these issues, while sticking to the simplified model approach, is to ensure that the limits obtained in different simplified models involving different production and decay mechanisms are combined into limits representing more complex SUSY spectra. In such an approach, the simplified model limits can be seen as building blocks for more realistic SUSY models that include many different production processes and decay modes. Another possibility is to perform reinterpretations of SUSY searches—optimised for one or more such simplified models—in more complete (and high-dimensional) SUSY model spaces, like e.g., in the pMSSM. This cannot only demonstrate the sensitivity of existing SUSY searches beyond simplified models, but also potentially identify blind spots and model regions not covered by current searches. In addition, connections to (in)direct DM searches and various SM measurements can be explored this way. Recent efforts in this direction include, e.g., Refs. [79, 81, 82]. As will be discussed in part III of this thesis, efforts reinterpreting ATLAS searches for SUSY In chapter 11, a reinterpretation of the search for electroweakinos presented herein using a set of pMSSM models, is discussed.

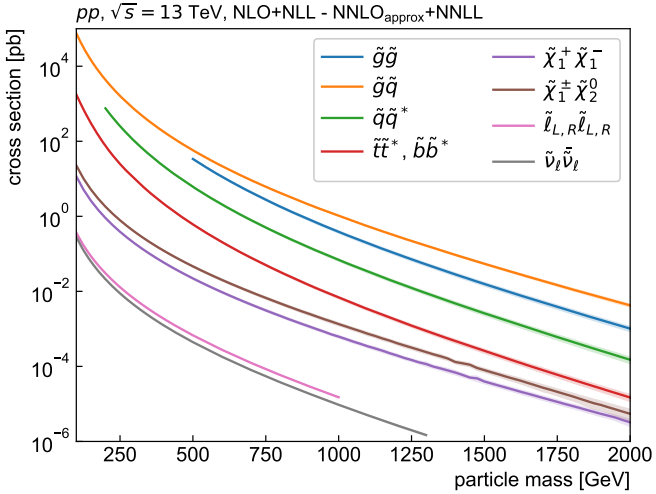


Figure 1.9: Cross sections of different SUSY production processes at $\sqrt{s} = 13 \text{ TeV}$ in pp collisions. Cross sections for pair-production of electroweakinos are significantly smaller than, e.g., those for pair-production of gluinos. The shaded bands correspond to the theory uncertainty of each cross section. Cross sections taken for coloured and electroweak sector taken from Refs. [87, 88] and Refs. [89–91], respectively.

1.3 Search for electroweakinos

While both the ATLAS experiment [83] and CMS experiment [84] at the Large Hadron Collider at CERN set strong limits on the presence of gluinos and squarks at the TeV scale, the limits on electroweakinos are mostly still below 1 TeV. The reason for the relatively low limits on electroweakinos are the low cross-sections of electroweakino production, compared to those of squark and gluino production. As can be seen in fig. 1.9, the cross sections for $\tilde{\chi}_1^\pm\tilde{\chi}_2^0$ pair-production (the production process considered in the following, as discussed below) is more than two orders of magnitude smaller than that for gluino pair-production.

Apart from the electroweakino mass limits set by the current collider experiments, some additional limits from the LEP experiments are still relevant in some corners of the phase space. Combining the results from all four LEP experiments leads to a general lower chargino mass limits of 103.5 GeV, except for scenarios with a low sneutrino mass [85]. For small mass splittings between the $\tilde{\chi}_1^\pm$ and the $\tilde{\chi}_1^0$, the lower limit is a little weaker, with dedicated searches excluding charginos with $m(\tilde{\chi}_1^\pm) < 91.9 \text{ GeV}$ [85]. For mass splittings larger than 1.5 GeV and up to 50 GeV, the LEP chargino limits have recently been superseded by a dedicated ATLAS search for compressed SUSY scenarios [86]. For the neutralino, a general lower limit on the lightest neutralino mass comes from limits on the invisible width of the Z boson, excluding $m(\tilde{\chi}_1^0) < 45.5 \text{ GeV}^\dagger$ [9].

1.3.1 Production of electroweakinos at the Large Hadron Collider

If gluinos and squarks are heavier than a few TeV, i.e. too heavy to be within reach of the Large Hadron Collider, the direct production of electroweakinos might be the dominant production mode of SUSY. At hadron colliders, electroweakinos can be pair-produced directly via electroweak processes. The direct production of electroweakino pairs dominantly happens through electroweak gauge bosons from s -channel $q\bar{q}$ annihilation, as shown in fig. 1.8. Contributions from t -channels via squark exchange are typically of less importance [5].

[†] Depending on the coupling between the Z boson and the lightest neutralino.

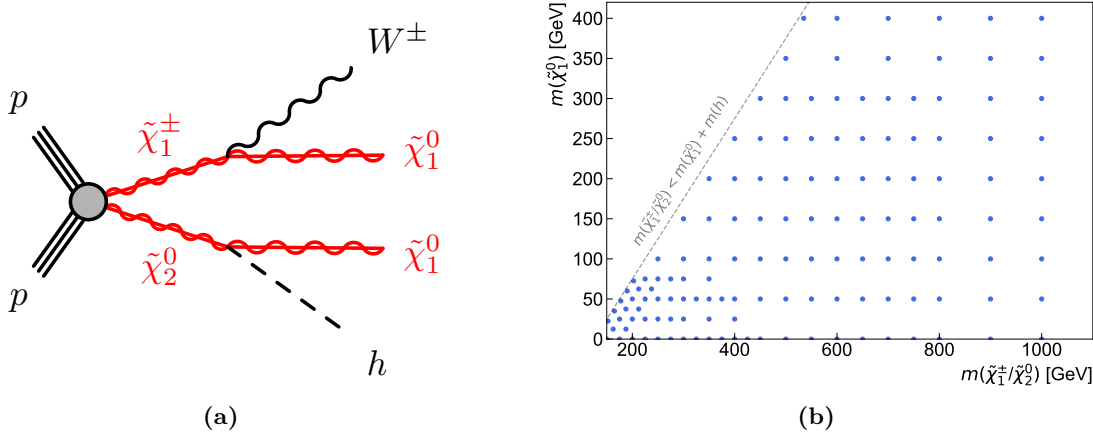


Figure 1.10: Simplified model used in this thesis. Fig. (a) shows a diagram for $\tilde{\chi}_1^\pm \tilde{\chi}_2^0$ pair-production with subsequent decays into $\tilde{\chi}_1^\pm \rightarrow W^\pm \tilde{\chi}_1^0$ and $\tilde{\chi}_2^0 \rightarrow h \tilde{\chi}_1^0$. Fig. (b) shows the signal grid used. Each discrete point represents a different signal model with a unique set of $\tilde{\chi}_1^\pm/\tilde{\chi}_2^0$ and $\tilde{\chi}_1^0$ masses.

1.3.2 Models used within this work

In SUSY scenarios where the sleptons and charged and pseudoscalar Higgs bosons are heavier than the charginos and neutralinos, a relatively pure wino lightest chargino decays predominantly through $\tilde{\chi}_1^\pm \rightarrow W^\pm \tilde{\chi}_1^0$, while the next-to-lightest neutralino decays via $\tilde{\chi}_2^0 \rightarrow Z/h \tilde{\chi}_1^0$. If, in addition, the higgsinos are much heavier than the wino, and the mass splitting between the two lightest neutralinos is larger than the Higgs boson mass, the decay $\tilde{\chi}_2^0 \rightarrow h \tilde{\chi}_1^0$ is the dominant decay mode of the $\tilde{\chi}_2^0$. In this case, both the $\tilde{\chi}_1^\pm$ and $\tilde{\chi}_2^0$ are wino-like and nearly mass-degenerate.

The main model used in the following is a simplified model considering direct production of a $\tilde{\chi}_1^\pm \tilde{\chi}_2^0$ pair, where the lightest chargino decays via $\tilde{\chi}_1^\pm \rightarrow W^\pm \tilde{\chi}_1^0$ and the next-to-lightest neutralino decays via $\tilde{\chi}_2^0 \rightarrow h \tilde{\chi}_1^0$, each with 100% branching ratio. The lightest chargino $\tilde{\chi}_1^\pm$ and the next-to-lightest neutralino $\tilde{\chi}_2^0$ are assumed to be degenerate in mass and pure wino states, while the lightest neutralino $\tilde{\chi}_1^0$ is considered to be a pure bino lightest supersymmetric particle (LSP). The mass parameter hierarchy for this model is thus $|M_1| < |M_2| \ll |\mu|$.

The masses of $\tilde{\chi}_1^\pm/\tilde{\chi}_2^0$ and $\tilde{\chi}_1^0$ are free parameters and are systematically varied, creating a two-dimensional signal grid to be scanned and compared to data. Figure 1.10(b) shows the two-dimensional signal grid used in part II of this thesis. In the simplified model, the Higgs boson mass is set to 125 GeV in accordance with the measured value [92, 93] and its branching ratios are the ones from the SM. An exemplary diagram for the simplified model considered is shown in fig. 1.10(a).

In addition to the simplified model targeted by the SUSY search presented in the following, an additional class of models is considered in the second part of this work. These models are sampled directly from the pMSSM parameter space and are used to reinterpret the aforementioned search for direct pair-production of electroweakinos. The mass spectrum of an exemplary pMSSM model point used is shown in fig. 11.4. Additional details on the sampling of the pMSSM models are given in section 11.2.

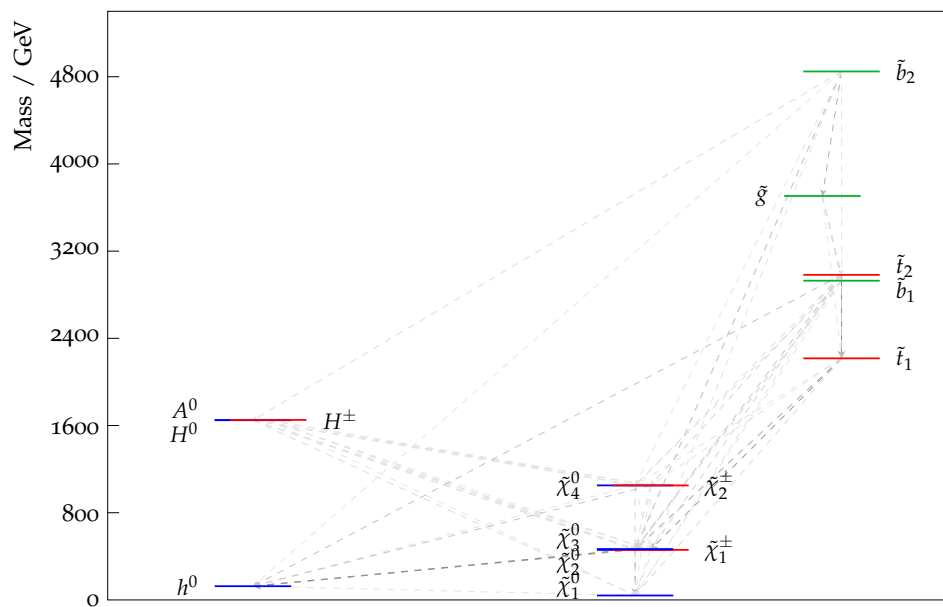


Figure 1.11: Mass spectrum of an example pMSSM model point considered in part III of this thesis. The kinematically allowed decays and their branching ratios are indicated through dashed lines. Figure generated using `pyslha` [94].

Chapter 2

Experiment

The European Laboratory for Particle Physics, CERN, is one of Europe's first joint ventures in science and one of the largest physics research facilities in the world [95]. It brings together more than 12,400 scientists of over 110 nationalities [96] with a common goal of pushing the frontiers of science and technology. Located at the Franco–Swiss border near Geneva, CERN was founded in 1954 and nowadays counts 23 member states [96]. CERN's main research area is particle physics, hence why the organisation operates a large complex of particle accelerators and detectors.

This chapter introduces the Large Hadron Collider (LHC), CERN's main particle accelerator, as well as the ATLAS experiment, in which the search for SUSY presented in this work is embedded in.

2.1 The Large Hadron Collider

The LHC [97] is the largest particle accelerator situated at CERN. It is installed in a tunnel with 26.7 km circumference, that was originally constructed from 1984 to 1989 for the LEP accelerator. The tunnel is situated on the Franco–Swiss border and wedged between the Jura mountains and lake Léman. It lies between 45 m (in the limestone of the Jura) and 170 m (in the molasse rock) below the surface, resulting in a tilt of 1.4% towards the lake. While proton–proton (pp) collisions are the main operating mode of the LHC, its design also allows it to accelerate and collide heavy ions like lead and xenon. Since data from pp collisions is used in this work, the following sections will mainly focus on this operating mode. As opposed to particle–antiparticle colliders that only need a single ring, the LHC, being a particle–particle collider, consists of two rings with counter-rotating beams. With an inner diameter of only 3.7 m, the tunnel is too narrow to fit two separate proton rings. Instead, the LHC is built in a twin bore design[†], housing two sets of coils and beam channels in a single magnetic and mechanical structure and cryostat [97]. While saving costs, this design has the disadvantage of both beams being magnetically coupled, consequently reducing the flexibility of the machine.

[†] Originally proposed by John Blewett at BNL for cost-saving measures of the Colliding Beam Accelerator [98, 99].

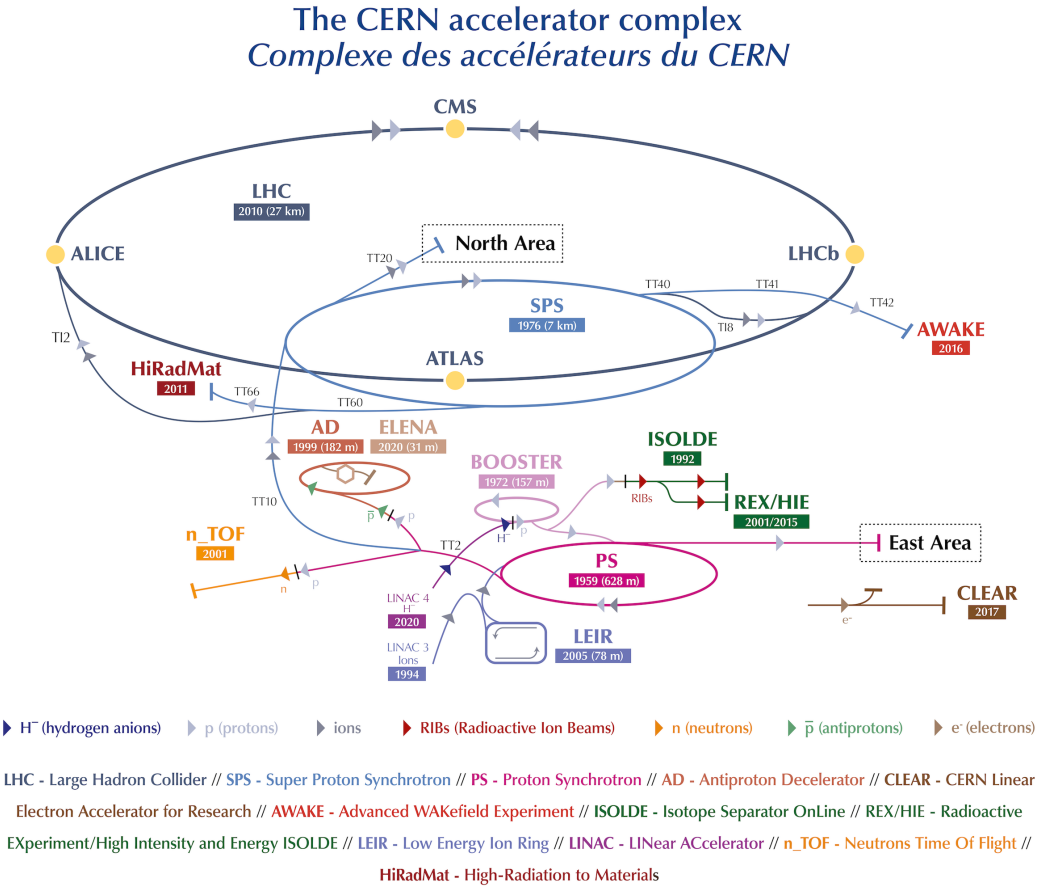


Figure 2.1: CERN accelerator complex as of 2021 [102].

Before being injected into the LHC, protons are pre-accelerated in an injection chain consisting of multiple existing machines in CERN's accelerator complex, pictured in fig. 2.1. The injection chain uses predecessor accelerators that have been upgraded in order to be able to handle the high luminosity and high energy requirements of the LHC. The protons for the LHC originally stem from a duoplasmatron source [100], stripping electrons from hydrogen atoms through electric discharges between a hot anode and cathode. The 90 keV protons are then accelerated by a radio frequency quadrupole to 750 keV before being injected into Linac 2[†], a linear accelerator producing a beam of 50 MeV protons through the use of radio frequency cavities. The protons then enter a set of circular accelerators, the Proton Synchrotron Booster, the Proton Synchrotron and the Super Proton Synchrotron, creating a stepwise acceleration up to an energy of 450 GeV, which is the injection energy to the LHC. The LHC finally accelerates the protons up to nominal beam energy before colliding them.

The LHC is composed of eight straight sections and eight arcs. The eight straight sections each serve as interaction points (referred to as *Point* in the following), either for particle detectors,

[†] Originally built to replace Linac 1 in order to produce higher energetic proton beams, Linac 2 has been replaced by Linac 4 in 2020 [101]. Linac 3 was built in 1994 and is still used for acceleration of heavy ions.

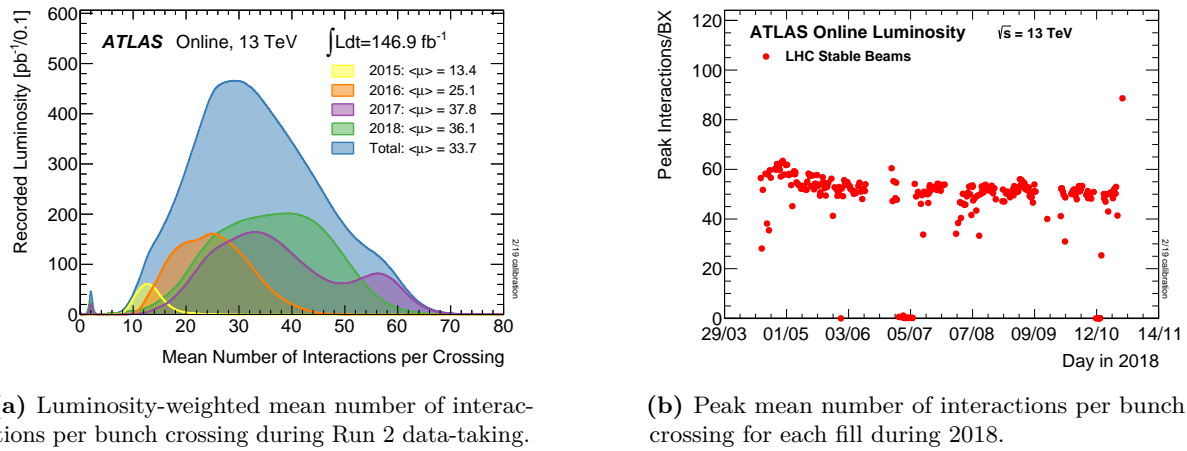
or for machine hardware of the collider itself. The Points are labelled clockwise, with Point 1 being closest to the CERN Meyrin site. Four of the eight Points house the main particle physics experiments at the LHC, called ATLAS, CMS, ALICE and LHCb, covering a wide range of fundamental research. The two general purpose particle detectors ATLAS [103] and CMS [104] are installed at Point 1 and Point 5, respectively. Both ATLAS and CMS are designed to perform high precision SM measurements including Higgs measurements as well as searches for BSM physics. Being very similar in terms of targeted phase space, ATLAS and CMS can be used to cross-check results of each other. ALICE [105] is situated at Point 2 and specializes on heavy ion physics, studying the physics of quark-gluon plasma at high energy densities. Assembled in Point 8, LHCb [106] targets B -physics and performs measurements of CP-violation. Apart from the four main experiments, three smaller experiments exist at the LHC: TOTEM, MoEDAL and LHCf. While TOTEM [107] and LHCf [108] study forwards physics close to CMS and ATLAS, respectively, MoEDAL [109] searches for magnetic monopoles.

The remaining four Points house accelerator equipment needed for operation of the LHC. Most of the collimation system is placed at Point 3 and Point 7, performing beam cleaning and machine protection through a series of beam intercepting devices, ensuring that no stray particles from experimental debris or beam halo can reach and damage other machine components [97]. The acceleration of the beam itself is performed at Point 4 with two radio frequency (RF) systems, one for each LHC beam. The RF cavities operate at 400 MHz and provide 8 MV during injection and 16 MV during coast [97]. Due to the RF acceleration, the accelerated protons are necessarily grouped in packages called *bunches*, each containing roughly 10^{11} protons, with a bunch spacing of 25 ns [97]. Although roughly 35,500 RF buckets are available, a design-value of only 2808 bunches are filled in each beam for data-handling reasons [97]. The remaining Point 6 houses the beam dumping system, allowing to horizontally deflect and fan out both beams into dump absorbers using fast-paced *kicker* magnets. The two nitrogen-cooled dump absorbers each consist of a graphite core contained in a steel cylinder, surrounded by 750 t [97] of concrete and iron shielding. Insertion of the beams from the Super Proton Synchrotron into the LHC happens at Points 2 and 8, close to the ALICE and LHCb experiments.

The eight arcs of the LHC are filled with dipole magnets built from superconducting NbTi Rutherford cables. The electromagnets are responsible for keeping the accelerated particles on their circular trajectory and are the limiting factor of the maximal centre-of-mass energy, \sqrt{s} , of the LHC. In order to achieve the design energy of $\sqrt{s} = 14$ TeV [97], the magnets have to create a field strength of 8.3 T [97]. In order to sustain the electric currents needed for such high field strengths, the magnets need to be cooled down to 1.9 K [97] using superfluid helium and operated in superconducting state. In addition to the dipole magnets, the arcs contain quadrupole magnets used to shape and focus the beams, as well as multipole magnets correcting and optimising the beam trajectory. Quadrupole magnets are also used to reduce the beam size before and after the interaction points.

2.1.1 Pile-up

Due to the high number of protons in each bunch, several pp collisions occur at each bunch crossing. This leads to a phenomenon called *pile-up*, where the recorded events not only contain information from the hard-scattering process of interest, but also remnants from additional, often low-energetic, pp collisions. During the Run 2 data-taking period, i.e. the period from



(a) Luminosity-weighted mean number of interactions per bunch crossing during Run 2 data-taking.

(b) Peak mean number of interactions per bunch crossing for each fill during 2018.

Figure 2.2: Number of interactions per bunch crossing recorded by the ATLAS experiment [110].

2015 throughout 2018, the mean number of inelastic pp collisions per bunch crossing, μ , has varied roughly from 10 to 70, with the majority of bunch crossings having a value of μ around 30. Figure 2.2(a) shows the mean number of interactions per bunch crossing during the Run 2 data-taking period, weighted by luminosity (a quantity introduced in section 2.1.2). The peak number of interactions per bunch crossing, μ_{peak} , has been consistently around 50 during the 2018 data-taking for each fill (cf. fig. 2.2(b)).

Experimentally, pile-up can be divided into five major components [111]:

- *In-time* pile-up: multiple interactions during a single bunch crossing, of which not all will be interesting, as often with relatively low energy. If they can be resolved, the main hard-scattering event can still be isolated and studied.
- *Out-of-time* pile-up: additional collisions occurring in bunch crossings before or after the main event of interest. This happens either due to read-out electronics integrating over longer time frames than the 25 ns bunch spacing, or detector components being sensitive to several bunch crossings.
- *Cavern background*: gas of thermal neutrons and photons that fill the experimental caverns during a run of the LHC and tend to cause random hits in detector components.
- *Beam halo events*: protons scraping an up-stream collimator, typically resulting in muons travelling parallel to the beam pipe.
- *Beam gas events*: interactions between proton bunches and residual gas in the beam pipe.

While the effects of cavern background can be mitigated through special pieces of shielding, beam halo and beam gas events leave signatures that can be recognised and removed. Signals from in-time and out-of-time pile-up create irreducible overlap with the events of interest, significantly impacting analyses, and thus need to be simulated [111].

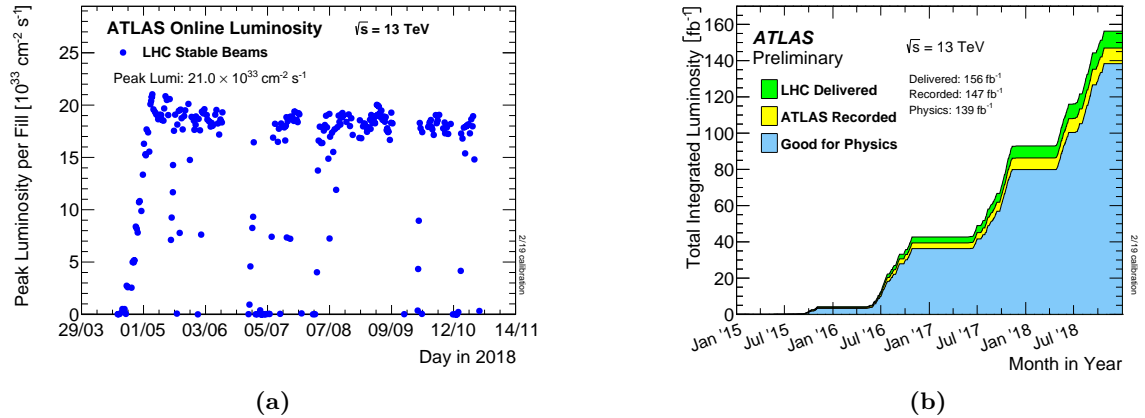


Figure 2.3: Instantaneous and cumulative luminosities in Run 2. Figure (a) shows the peak instantaneous luminosity delivered to ATLAS during pp collision data taking in 2018 as a function of time. Figure (b) shows the cumulative luminosity delivered to ATLAS (green), recorded by ATLAS (yellow) and deemed good for physics analysis (blue) during the entirety of Run 2 [110].

2.1.2 Luminosity and data-taking

Apart from the beam energy, the most important quantity for a collider is the instantaneous luminosity L_{inst} . For a synchrotron with Gaussian beam distribution, the instantaneous luminosity is given by

$$L_{\text{inst}} = \frac{N_b^2 n_b f_{\text{rev}}}{4\pi\sigma_x\sigma_y} F, \quad (2.1)$$

where n_b is the number of bunches, N_b the number of protons per bunch, f_{rev} the revolution frequency and σ_x and σ_y the transverse beam sizes. The parameter F is a geometrical correction factor accounting for the reduction in instantaneous luminosity due to the beams crossing at a certain crossing angle. While the design instantaneous luminosity of the LHC at the high-luminosity experiments ATLAS and CMS is $L_{\text{inst}} = 10^{34} \text{ cm}^{-2} \text{ s}^{-1}$ [97], the 2017 and 2018 data-taking periods saw a peak luminosity twice as high [112].

The instantaneous luminosity is related to the total number of events N through the cross section σ of the events in question

$$N = \sigma L = \sigma \int L_{\text{inst}} dt, \quad (2.2)$$

with L the total integrated luminosity, a measure for the total amount of collision data produced.

A precise knowledge of the integrated luminosity corresponding to a given dataset is crucial for both SM measurements as well as for searches for BSM physics. Searches for SUSY like the one presented in this work rely on precise measurements of the integrated luminosity in order to estimate the contribution from SM background processes. The luminosity measurement for the Run 2 dataset used within this work is described in detail in Refs. [113, 114] and relies on a measurement of the bunch luminosity L_b , i.e. the luminosity produced by a single pair of colliding bunches,

$$L_b = \frac{\mu f_{\text{rev}}}{\sigma_{\text{inel}}} = \frac{\mu_{\text{vis}} f_{\text{rev}}}{\sigma_{\text{vis}}}, \quad (2.3)$$

with μ the pile-up parameter, σ_{inel} the cross section of inelastic pp collisions, $\mu_{\text{vis}} = \epsilon\mu$ is the fraction ϵ of the pile-up parameter μ visible to the detector and $\sigma_{\text{vis}} = \epsilon\sigma_{\text{inel}}$ the visible inelastic cross section. If σ_{vis} is known, the currently recorded luminosity can be determined by measuring μ_{vis} . At the ATLAS experiment, the observed number of inelastic interactions per bunch crossing μ_{vis} is measured using dedicated detectors, as for example LUCID-2 [115], a forward Cherenkov-detector using the quartz windows from photomultipliers as Cherenkov medium. In order to use μ_{vis} as luminosity monitor, the respective detectors need to be calibrated through a measurement of the visible inelastic cross section σ_{vis} . This can be done using so-called van der Meer (vdM) scans [116, 117], in which the transverse distribution of protons in the bunches is inferred by measuring the relative interaction rates as a function of the transverse beam separation[†]. The algorithms used to determine the σ_{vis} calibration are described in Refs. [113, 114]. The luminosity during the vdM runs can then be determined using eq. (2.1). At the LHC, vdM scans are typically performed in special low- μ runs with well-known machine parameters in order to minimise uncertainties [113]. During high- μ physics runs, a luminosity measurement is obtained through an extrapolation from the vdM runs.

The LHC entered operation in 2008, with first beams in September and first collisions[§] in December 2009 [119]. Its operation is in general structured into so-called *Runs*, that are spanned by multiple years of data-taking. Run 1 spanned from 2009 to 2013 and delivered roughly 28.5 fb^{-1} of pp collision data to ATLAS, taken at centre-of-mass energies of 7 TeV and 8 TeV [120, 121, 114]. Run 2 lasted from 2015 to 2018 and saw a centre-of-mass energy increase to 13 TeV, delivering approximately 156 fb^{-1} of pp collision data to ATLAS [113]. Run 3 of pp collision data taking with two times design peak luminosity is currently planned to start its physics program in 2022 and last until the end of 2024 [122]. Current plans foresee Run 3 to deliver about 150 fb^{-1} of pp collision data with centre-of-mass energies of 13 TeV and 14 TeV. After Run 3, the LHC will be upgraded to the High Luminosity LHC (HL-LHC), significantly increasing the peak instantaneous luminosity and delivering up to 3000 fb^{-1} of pp collision data from 2027 until 2040 [122, 123].

This work uses pp collision data taken by ATLAS during Run 2 of the LHC. Of the 156 fb^{-1} delivered to ATLAS, 147 fb^{-1} were recorded, and 139 fb^{-1} were deemed to be good for physics analysis. Figure 2.3 shows the cumulative luminosity delivered to ATLAS during Run 2. Uncertainties on the measured total recorded luminosity stem from the measurements of μ_{vis} and σ_{vis} , but are dominated by the uncertainties on σ_{vis} as vdM scans can only be done during special runs with more or less fixed machine parameters, while the general conditions during high- μ conditions change continuously. For the full Run 2 dataset, the uncertainties accumulate to $\pm 1.7\%$ [113].

2.2 ATLAS Experiment

The ATLAS experiment is one of two general-purpose detectors at the LHC. Located at Point 1 in a cavern 100 m below the surface, it is approximately 44 m long and 25 m high [103]. The design of the ATLAS experiment is driven by the aim to allow for a diverse research program,

[†] This procedure is often referred to as *beam sweeping*.

[§] A delay was caused by an incident in September 2008. During powering tests of the main dipole circuit in one of the sectors of the LHC, an electrical bus connection between two magnets failed, causing mechanical damage and the release of helium into the tunnel [118].

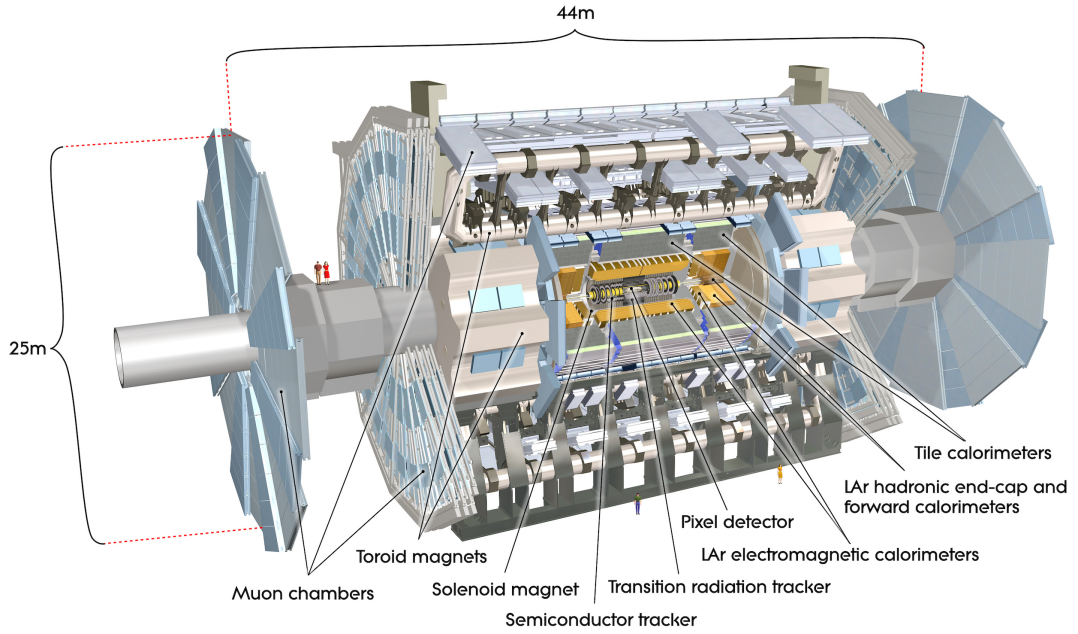


Figure 2.4: Computer generated picture of the ATLAS detector, giving an overview of the various subsystems [124].

including SM precision measurements, Higgs physics and searches for BSM physics, whilst at the same time taking into account the unique and challenging conditions set by the LHC. The various detector technologies used are designed to withstand the high-radiation environment of the LHC, while allowing particle measurements with high spatial and temporal granularity. The general structure of ATLAS is depicted in fig. 2.4, and consists of a central part, called *barrel*, that has a cylindrical shape around the beam pipe, and two discs, called *end-caps*, that close off the barrel on each side. This makes the ATLAS detector forward-backward symmetric with a coverage of nearly full solid angle of 4π , which is needed in order to measure momentum imbalances caused by particles that only interact weakly with the detector material.

The interface between the ATLAS experiment and the LHC is the beam pipe. In order to be maximally transparent to the particles created in the collisions, but be also able to withstand the forces from the vacuum, the beam pipe is made out of Beryllium close to the interaction point (IP), and stainless-steel further away from the IP [3].

The following sections introduce the working principles of the different detector components used in ATLAS, starting with the innermost component closest to the IP, the inner detector, followed by the calorimeters in the middle and finally the muon spectrometers on the outside. If not otherwise indicated, details on the detector components including the design parameter values are extracted from Ref. [103].

2.2.1 Coordinate system

In order to properly describe collision events in the ATLAS detector, a suitable detector system is needed. The right-handed coordinate system [125] used in ATLAS has its origin at the nominal IP in the centre of the detector. The positive x -axis points towards the centre of the LHC ring, the positive y -axis points upwards to the surface, and the beam pipe is used to define the z -axis. In the x - y plane, called the transverse plane, the azimuthal angle ϕ is the angle around the beam axis. The polar angle θ is measured from the beam axis. The rapidity v [9] is defined as

$$v = \frac{1}{2} \ln \left(\frac{E + p_z}{E - p_z} \right) = \tanh^{-1} \frac{p_z}{E}, \quad (2.4)$$

with E the energy of an object and p_z its momentum in z -direction. As opposed to the polar angle θ , differences in the rapidity are invariant under Lorentz boosts in z -direction.

The pseudorapidity η [9] is the high-energy limit ($p \gg m$) of the rapidity, and defined as

$$\eta = -\ln \tan \frac{\theta}{2}, \quad (2.5)$$

with $\cos \theta = p_z/p$. Pseudorapidity and rapidity are approximately equal in the limit where $p \gg m$ and $\theta \gg \frac{1}{\gamma}$. Compared to the rapidity, the pseudorapidity has the advantage of not depending on the energy and momentum calibration of the detected objects. Additionally, it gives a direct correspondence to the polar angle θ through the relation $\tanh \eta = \cos \theta$. Objects travelling along the beam axis have a pseudorapidity of $\eta = \infty$ and objects travelling in the x - y plane have $\eta = 0$.

The distance ΔR between two objects in the detector is given by

$$\Delta R = \sqrt{(\Delta\eta)^2 + (\Delta\phi)^2}. \quad (2.6)$$

The longitudinal momentum of the partons composing the colliding hadrons is only known by means of the parton distribution functions (PDFs), giving the probabilities of the partons to have a certain energy in the direction of the beam. Thus, the total longitudinal energy in each collision is not exactly known, impeding the use of physics quantities in the z -direction. In the x - y plane, however, momentum conservation can be applied, which is why mainly transverse physics quantities are used, indicated by a subscript ‘T’, e.g., E_T or p_T .

2.2.2 Magnet system

In order to perform precise momentum measurements of particles, ATLAS uses a system of magnets [103], whose magnetic fields force charged particles on curved tracks due to the Lorentz force. Using precise measurements of the tracks taken in the inner detector and in the muon spectrometers, the curvature of the tracks can be determined, allowing an inference of the charge-to-momentum ratio q/p of charged particles. ATLAS employs a set of four superconducting magnets, one central solenoid, and three toroids, all operating at a nominal temperature of 4.5 K, achieved through a cryogenic system using liquid helium.

The solenoid is aligned on the beam axis and provides a 2 T magnetic field for the inner detector. As it is located in front of the calorimeters (as seen from the IP), it is specially designed to have

minimal material thickness in order to avoid influencing the subsequent energy measurements. The solenoid consists of single-layer coils made of a Nb/Ti conductor and additional aluminium for stability. It operates at a nominal current of 7.73 kA and uses the hadronic calorimeter as return yoke.

The toroid magnets consist of a barrel toroid and two end-cap toroids, producing a magnetic field of 0.5 T and 1 T for the muon spectrometers in the barrel and end-caps, respectively[†]. Both barrel and end-cap toroids consist of Nb/Ti/Cu conductors with aluminium stabilisation, wound into double pancake-shaped coils. The barrel toroid coils are enclosed in eight stainless-steel vacuum vessels in a racetrack-shaped configuration and arranged around the barrel calorimeters with an azimuthal symmetry. Aluminium-alloy struts provide the support structure necessary for the vessels to withstand the inward-directed Lorentz force of 1400 t in addition to their own weight. For the same reasons, the end-cap toroid coils are assembled in eight square units, and bolted and glued together with eight wedges, forming rigid structures. Both end-cap and barrel toroids operate at a nominal current of 20.5 kA.

2.2.3 Inner detector

Embedded in the magnetic field of the solenoid, the inner detector (ID) [103] measures tracks of charged particles, allowing a determination of their momentum, while also providing crucial information for vertex reconstruction. As the ID is the detector closest to the beam pipe, its components need to be able to withstand the extreme high-radiation environment close to the IP. The ID consists of three subdetectors and uses two different working principles: semiconductor and gaseous detectors. In semiconductor-based tracking detectors, charged particles passing through the detector create a trail of electron-hole pairs that subsequently drift through the semiconductor material and cause electric signals. In gaseous detectors, traversing particles create electron-ion pairs that drift towards metal electrodes and induce electric signals.

Closest to the ID lies the pixel detector, followed by the silicon microstrip tracker (SCT), both of which are made of semiconductors. The SCT is surrounded by the transition radiation tracker (TRT), a gaseous detector. In total, the ID provides tracking and momentum information up to $|\eta| < 2.5$ and down to transverse momenta of nominally 0.5 GeV. A schematic illustration of the ID and its subdetectors is shown in fig. 2.5.

Pixel detector

In the high-rate environment directly adjacent to the beam pipe, the only detector technology able to operate and deliver high-precision tracking information over extended periods of time are semiconductor detectors segmented into pixels. As opposed to strip detectors, the reduced size of silicon pixel detectors and thus the significantly reduced hit rate per readout channel allows pixel detectors to be operational in the harsh environment close to the IP. In ATLAS, pixels [103] are hybrids of silicon sensors and readout electronics bonded together, and were originally arranged in three layers in the barrel and the end-caps with a typical pixel of 50 $\mu\text{m} \times 400 \mu\text{m}$, covering pseudorapidities up to $|\eta| < 2.5$. In order to increase robustness and performance in the

[†] The magnetic field in of the toroid magnets is designed to be higher in the end-caps in order to ensure sufficient bending power for precise momentum measurements.

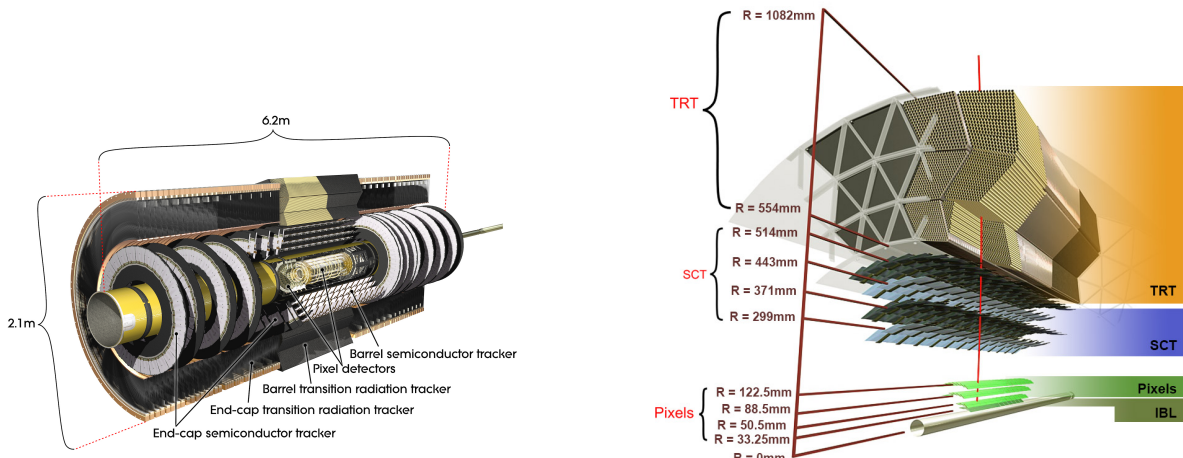


Figure 2.5: Schematic drawing of the ID and its subdetectors. Images adapted from [126, 127].

high-luminosity environment, a new innermost layer, called the insertable B-layer (IBL), was installed together with a new, smaller radius beam pipe between Run 1 and Run 2 [128, 129]. The IBL uses smaller pixels with a size of $50\text{ }\mu\text{m} \times 250\text{ }\mu\text{m}$ and improves the tracking precision as well as vertex identification performance [129]. It also improves the performance of identifying jets originating from b -quarks (through a procedure called b -tagging, see section 4.4.5) [130]. The tracking precision obtained by the pixel detector is $10\text{ }\mu\text{m}$ in $R-\phi$ and $115\text{ }\mu\text{m}$ in z for the barrel and R for the end-caps.

Silicon microstrip detector

The pixel detector is surrounded by the SCT [103], consisting of four layers in the barrel and nine disks in each of the end-caps. In order to provide two-dimensional tracking information, strips are arranged in double-layers with a small crossing angle of 40 mrad and a mean pitch of $80\text{ }\mu\text{m}$. A charged particle traversing the SCT through the barrel thus creates four space point measurements. In the barrel, one set of strips in each of the four double-layers is oriented in beam direction, thereby measuring the $R-\phi$ plane, and in the end-caps, one set of strips in each layer is oriented in radial direction. The SCT has roughly 6.3 million readout channels and provides tracking information up to $|\eta| < 2.5$. It achieves a precision of $17\text{ }\mu\text{m}$ in $R-\phi$ and $580\text{ }\mu\text{m}$ in z for the barrel and R for the end-caps.

Transition radiation tracker

The last and also largest of the three subdetectors of the ID is the TRT [103], a gaseous detector made of multiple layers of 4 mm diameter drift tubes, surrounding the pixel detector and the SCT. The drift tubes consist of an aluminium cathode coated on a polyimide layer reinforced by carbon fibres and use a gold-plated tungsten wire as anode. The tubes are filled with a Xe-based gas mixture, providing an electric permittivity different from the surrounding material, causing transition radiation when traversed by ultra-relativistic particles. While the 73 layers of 144 cm long tubes in the barrel region are aligned parallel to the beam pipe, the 160 layers of 37 cm long tubes in the end-caps are aligned in radial direction, providing coverage up to

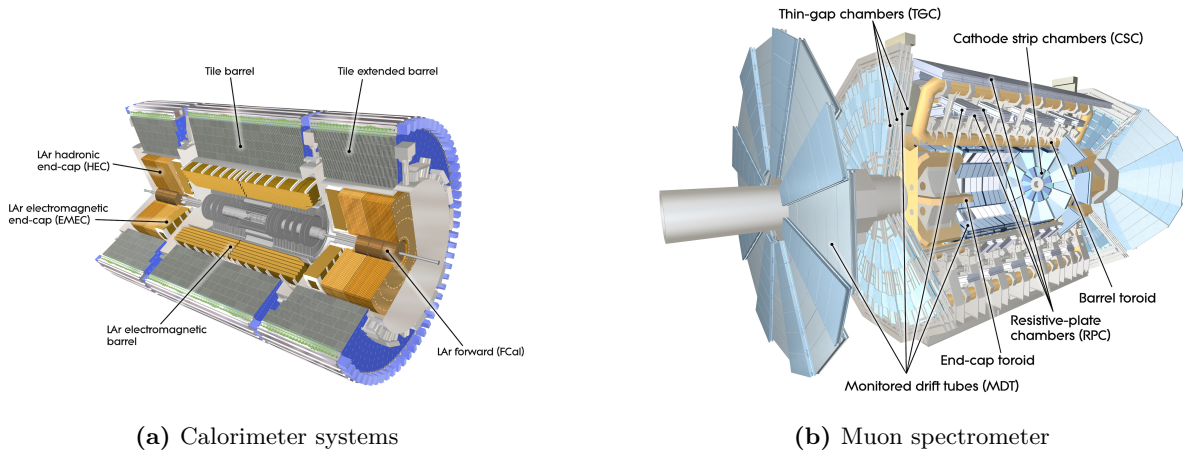


Figure 2.6: Schematic drawing of the (a) calorimeter systems and (b) the muon spectrometer in ATLAS. Images adapted from Refs. [132, 133].

$|\eta| < 2.0$ and an intrinsic accuracy of $130\text{ }\mu\text{m}$ in $R - \phi$. The low accuracy compared to the pixel detector and the SCT is compensated by the large amount of hits (typically 36 per track) and the longer measured track length. As the amount of transition radiation given off by a particle, is proportional to its Lorentz factor γ [9], the TRT is also used to improve electron identification [131]. For the same momentum, electrons will have a higher Lorentz factor than the heavier, charged pions, and consequently give off more transition radiation.

2.2.4 Calorimeters

The primary goal of calorimeters is to measure the energies of incoming particles by completely absorbing them. As the energies of neutral particles cannot be measured by other means, calorimeters are especially important for jet energy measurements (which contain neutral hadrons) [3]. Since particles like photons and electrons interact mostly electromagnetically, while hadrons predominantly interact through the strong interaction, two different calorimeter types are adopted in ATLAS. For values in η matching the coverage of the ID, the electromagnetic calorimeter uses a finer granularity designed for precision measurements of electrons and photons. The subsequent hadronic calorimeter has a coarser granularity sufficient for the requirements of jet reconstruction and missing transverse momentum measurements. With a coverage up to $|\eta| < 4.9$, the calorimeter system in ATLAS provides the near hermetic energy measurements needed for the inference of missing transverse momentum created by neutrinos and other weakly interacting neutral particles.

Both calorimeters are sampling calorimeters, consisting of alternating layers of active and absorbing material. The absorbing material interacts with the incoming particles, causing them to deposit their energy by creating cascades (often called *showers*) of secondary particles. The active layers are then used to record the shape and intensity of the showers produced. This alternating structure results in reduced material costs but also reduced energy resolution as only part of the particle's energy is sampled. Due to the typically longer cascades in hadronic interactions compared to electromagnetic ones, and in order to minimise punch-through into the muon system, the hadronic calorimeter requires a greater material depth than

the electromagnetic one. The calorimeter systems in ATLAS are schematically illustrated in fig. 2.6(a).

Electromagnetic calorimeter

The Electromagnetic (EM) calorimeter [103] uses liquid argon (LAr) as active material and lead as absorber. Due to its accordion-shaped geometry, it provides full ϕ symmetry without azimuthal cracks. It is divided into a barrel part and two end-caps, covering $|\eta| < 1.475$ and $1.375 < |\eta| < 3.2$, respectively, and arranged in a way to provide uniform performance and resolution as a function of ϕ . The barrel EM calorimeter consists of two identical half-barrels with a small gap of 4 cm at $z = 0$. In the end-caps, the electromagnetic end-cap calorimeter (EMEC) consists of two coaxial wheels, covering the region $1.375 < |\eta| < 2.5$ and $2.5 < |\eta| < 3.2$, respectively. Calorimeter cells in the EM calorimeter are segmented into multiple layers with fine granularity in the first layers in the η region matching the ID, and coarser granularity in the outer layers and for $2.5 < |\eta| < 3.2$. In order to offer good containment of electromagnetic showers, the EM calorimeter has a depth of at least 22 (24) radiation lengths in the barrel (end-caps). A single instrumented LAr layer serves as presampler in the region with $|\eta| < 1.8$, allowing measurements of the energy losses upstream of the EM calorimeter, as for example in the cryostats. The design energy resolution of the EM calorimeter is $\sigma_E/E = 10\%/\sqrt{E} \oplus 0.7\%$.

Hadronic calorimeter

Placed directly outside the envelope of the EM calorimeter is the hadronic tile calorimeter [103]. It uses steel plates as absorber and polystyrene-based scintillating tiles as active material, and is subdivided into one central and two extended barrels. Each barrel is segmented in three layers in depth, with a total thickness of 7.4 interaction lengths. The tiles are oriented radially and perpendicular to the beam pipe and grouped in 64 tile modules per barrel, resulting in a near hermetic azimuthal coverage. Wavelength shifting fibres are used to shift the ultraviolet light produced in the scintillator to visible light and guide it into photomultipliers located at the radially far end of each module. The tile calorimeter covers a region with $|\eta| < 1.7$ and has a granularity of $\Delta\eta \times \Delta\phi = 0.1 \times 0.1$ except for the outermost layer which has a slightly coarser granularity in η . The design energy resolution of the tile calorimeter is $\sigma_E/E = 56.4\%/\sqrt{E} \oplus 5.5\%$.

Hadronic calorimetry in the end-caps is provided by two independent calorimeter wheels per end-cap, situated directly behind the EMEC. Similar to the EMEC, the hadronic end-cap calorimeter (HEC) also uses LAr as active material, allowing both calorimeter systems to share a single cryostat per end-cap. Instead of lead, the HEC uses copper as absorber, which not only drastically reduces the mass of a calorimeter at a given interaction length, but also improves the linearity of low-energy hadronic signals [134]. Each of the four wheels of the HEC is comprised of 32 wedge-shaped modules, divided into two layers in depth. The HEC provides coverage in the region with $1.5 < |\eta| < 3.2$, slightly overlapping with the tile calorimeter and thus reducing the drop in material density in the transition region. While the granularity in the precision region with $1.5 < |\eta| < 2.5$ is the same as for the tile calorimeter, more forward regions with large $|\eta|$ have a granularity of $\Delta\eta \times \Delta\phi = 0.2 \times 0.2$. The design resolution of the HEC is $\sigma_E/E = 70.6\%/\sqrt{E} \oplus 5.8\%$.

Forward Calorimeter

The forward region with $3.1 < |\eta| < 4.9$ is covered by the LAr forward calorimeter (FCal) [103], which is integrated into the end-cap cryostats. This hermetic design not only minimises energy losses in cracks between the calorimeter systems, but also reduces the amount of background reaching the muon system in the outer shell of the ATLAS experiment. In order to limit the amount of neutrons reflected into the ID, the FCal is recessed by about 1.2 m with respect to the EM calorimeter, motivating a high-density design due to space constraints. The FCal in each end-cap consists of three layers with a total depth of 10 interaction lengths. While the first layer uses copper as absorber and is optimised for electromagnetic measurements, the remaining two layers are made of tungsten and cover hadronic interactions. The metals comprising each layer are arranged in a matrix structure with electrodes consisting of rods and tubes parallel to the beam pipe filling out regular channels. The small gaps (0.25 mm in the first layer) between the rods and tubes of the electrodes are filled with LAr as active material.

2.2.5 Muon spectrometer

Muons, being minimum ionising particles, are the only charged particles that consistently pass through the entire detector including the calorimeter system. Providing one of the cleanest signatures for BSM physics [3], muonic final states are measured with a dedicated detector system on the outermost layer of the ATLAS experiment. Embedded in the magnetic field of the toroid magnets, the muon spectrometer (MS) [103] consists of three concentric cylindrical layers in the barrel region, and three wheels in each end-cap, providing momentum measurements up to $|\eta| < 2.7$. It is designed to deliver a transverse momentum resolution of 10% for 1 TeV tracks and be able to measure muon momenta down to roughly 3 GeV.

The MS uses two high-precision gaseous detector chamber types, Monitored Drift Tube (MDT) chambers and Cathode Strip Chambers (CSCs). As both the MDTs and CSCs are drift chambers relying on charges drifting to an anode or cathode, the maximum response times of 700 ns and 50 ns, respectively, are slow compared to the bunch-spacing of 25 ns. ATLAS therefore uses Resistive Plate Chambers (RPCs) in the barrel and Thin Gap Chambers (TGCs) in the end-caps as triggers in order to associate measurements to the right bunch-crossing.

Monitored drift tubes

The MDT chambers [103] are the main subcomponent providing precision measurements of the muon tracks up to $|\eta| < 2.7$, except in the innermost end-cap layer where their coverage only extends to $|\eta| < 2.0$. The MDT are made of 3–4 layers of ~ 30 mm diameter drift tubes operated with Ar/CO₂ gas[†] pressurised to 3 bar. Charged particles traversing the drift tubes ionise the gas, creating electrons that drift towards a central tungsten-rhenium anode wire with a diameter of 50 μm . Following the symmetry of the barrel toroid magnet, the MDT chambers are arranged as octets around the calorimeters with the drift tubes in ϕ direction, i.e. tangential to circles around the beam pipe. In order to be able to correct for potential chamber deformations due to varying thermal gradients, each MDT chamber is equipped with an internal optical alignment system. Apart from the regular chambers in the barrel and the

[†] With a small admixture of 300 ppm of water to improve high voltage stability.

end-cap wheels, special modules are installed in order to minimise the acceptance losses due to the ATLAS support structure (the *feet* of the experiment). With a single-tube accuracy of 80 μm , two combined 3 (4)-tube multi-layers yield a resolution of 35 (30) μm . As MDT chambers only provide precision measurement in η , information in ϕ is taken from the RPCs and TGCs.

Cathode strip chambers

In the region with $|\eta| > 2.0$ in the first layer of the end-caps, the particle flux is too high to allow for safe operation of MDT chambers. Instead, CSCs [103], multiwire proportional chambers, are used for precision measurements in this region. The gold-plated tungsten-rhenium anode wires in the CSCs have a diameter of 30 μm and are oriented in radial direction. The wires are enclosed on both sides by cathode planes, one segmented perpendicular to the wires (thus providing the precision coordinate), the other parallel to the wires. Each chamber is filled with an Ar/CO₂ gas mixture and consists of four wire planes, resulting in four measurements of η and ϕ for each track. In addition to the chamber-internal alignment sensors, ATLAS also employs an optical alignment system in order to align the precision chambers to each other. The CSCs provide a resolution of about 45 μm in R and 5 mm in ϕ .

Resistive plate chambers

RPCs [103] are gaseous parallel electrode-plate chambers filled with a non-flammable low cost tetrafluorethane-based gas mixture. They use two resistive plastic laminate plates kept 2 mm apart by insulating spacers. Due to an electric field of roughly 4.9 kV mm⁻¹ between the plates, charged particles traversing the chamber cause avalanches of charges that can be read out through capacitive coupling to metallic strips mounted on the outside of the resistive plates. In order to provide tracking information in both coordinates, each RPC consists of two rectangular units each containing two gas volumes with a total of four pairwise orthogonal sets of readout strips. The three concentric cylindrical layers of RPCs in the barrel region cover $|\eta| < 1.05$ and provide six measurements of η and ϕ .

Thin gap chambers

The TGCs [103] are not only necessary for triggering in the end-cap MS but also provide measurements of a second coordinate orthogonal to the measurements of the MDTs. TGCs are multi-wire proportional chambers enclosed by two cathode planes and a wire-to-wire gap of 1.8 mm. The gas mixture of CO₂ and n-pentane allows for a quasi-saturated operation mode resulting in a relatively low gas gain. Each TGC unit is built from a doublet or triplet of such chambers, separated by a supporting honeycomb structure. In each unit, the azimuthal coordinate is measured by radial copper readout strips, while the bending coordinate is provided by the wire groups. The TGCs are mounted in two concentric disks in each end-cap, one covering the rapidity range $1.05 < |\eta| < 1.92$ and one covering the more forward region $1.92 < |\eta| < 2.4$.

2.2.6 Forward detectors

Apart from the relative luminosity monitor LUCID-2 [115] (introduced in section 2.1.2) located at $\pm 17\text{ m}$ from the IP, ATLAS uses three additional small detectors in the forward region. At $\pm 140\text{ m}$ from the IP, immediately behind the location where the straight beam pipe splits back into two separate beam pipes, lies the Zero-Degree Calorimeter (ZDC) [135]. The ZDC is embedded in a neutral particle absorber and mainly measures forward neutrons with $|\eta| > 8.3$ in heavy-ion collisions. Even further out from the IP at $\pm 240\text{ m}$, lies the Absolute Luminosity for ATLAS (ALFA) detector [136], consisting of scintillating fibre trackers placed in Roman pots [137] measuring the absolute luminosity through small scattering angles of $3\text{ }\mu\text{rad}$ (necessitating the special beam conditions also used for the LUCID-2 calibrations). The last of the forward detectors is the ATLAS Forward Proton (AFP) [138] detector, installed at the end of 2016 and operational since early 2017, situated $\pm 205\text{ m}$ and $\pm 217\text{ m}$ from the IP. It consists of Roman pots containing silicon trackers and time-of-flight detectors and allows to study very forward protons from elastic and diffractive scattering processes.

2.2.7 Trigger and data acquisition system

With a nominal bunch spacing of 25 ns, the bunch crossing rate within ATLAS is 40 MHz. Even with only a single pp collision event per bunch crossing, a mean event size of $\sim 1.6\text{ MB}$ would result in a data volume of more than 60 TB per second. Building and maintaining computing and storage facilities able to handle this bandwidth would significantly exceed the available resources. Luckily, interesting[†] physics events will often only occur at relatively low rates, and generally be hidden in vast amounts of QCD processes that have much higher cross-sections. In order to reduce the event rate written to disk and focus on interesting signatures worth studying, ATLAS used a two-level *trigger* system during the Run 2 data-taking period [139]. The general approach is to buffer events into temporary memory until the trigger system has decided to keep or discard them. The size of the temporary memory directly dictates the latency available to the trigger system for making a decision.

The Level 1 (L1) trigger [140] is the first stage of the trigger system. It is hardware-based and uses only coarse granularity calorimeter and muon detector information. With the inclusion of the Level-1 Topological Processor (L1Topo) [141] in Run 2, the L1 trigger is able to exploit topological features based on angular and kinematic selections and defines regions of interest (ROIs), i.e. regions in η and ϕ with interesting properties, that will be further analysed by the subsequent trigger step. Memory constraints allow for a decision time of 2.5 μs per event, thus the L1 trigger reduces the event rate from the bunch-crossing rate of 40 MHz to 100 kHz.

The ROIs generated by the L1 trigger are subsequently processed by the High Level Trigger (HLT) [142], a software-based trigger running on a dedicated computing farm. The HLT has access to the full detector granularity in the ROIs as well as the entire event and runs reconstruction algorithms similar to those used in offline analysis, allowing to significantly refine the decisions from the L1 trigger. The HLT reduces the event rate from 100 kHz to 1 kHz. Events that pass one of the HLT chains are written to permanent storage at CERN. Data flow

[†] The definition of what is deemed to be interesting is to some extent subjective and is at the origin of the diverse *trigger menu* [139] used in ATLAS.

from the detectors to the storage elements and between the L1 and HLT trigger elements is handled by the Data Acquisition System (DAQ) [142].

2.2.8 Monte Carlo simulation

Monte Carlo (MC) methods play a crucial role for simulating physics events in ATLAS. MC simulations are computational algorithms using repeated random sampling to solve complex problems, often the estimation of multi-dimensional integrals for which analytical solutions are not known. According to the law of large numbers, the numerical approximations obtained by such a stochastic method become more accurate, the larger the sample size is. In addition, the central limit theorem also allows to state an uncertainty on the estimation of an expected value. This method can in principle be used for any problem with a probabilistic interpretation and is therefore well suited for particle physics where many aspects are inherently connected to probability density functions (pdfs).

In the ATLAS experiment, MC methods are not only used in physics analysis to estimate contributions from various physics processes in different phase space regions, but also to simulate particle interactions with the detector material. This method even finds ample applications in detector design and optimisation as well as physics objects reconstruction techniques. All of these applications rely on the MC simulations being as precise as possible, i.e. correctly describing the physics processes and detector responses underlying the data recorded by the ATLAS experiment. For reasons of efficient computing resource utilisation and easier software validation, the ATLAS simulation infrastructure [143] can be divided into three main steps:

- (i) Event generation,
- (ii) Detector simulation,
- (iii) Digitisation,

producing an output format identical to that of the DAQ for recorded pp collision events, such that the same trigger and reconstruction algorithms can be run on simulated data.

Event generation

Only a fraction of all pp events actually involve a *hard-scattering* event with high-momentum transfer, rendering them interesting for particle physicists to study. Generating and understanding the final states of these pp collision events is an enormously challenging problem as it typically involves hundreds of particles with energies spanning many orders of magnitude [145]. This makes the matrix elements connected to these processes too complicated to be computed beyond the first few orders of perturbation theory. The treatment of divergences and the integration over large phase spaces further complicates the calculation of experimental observables.

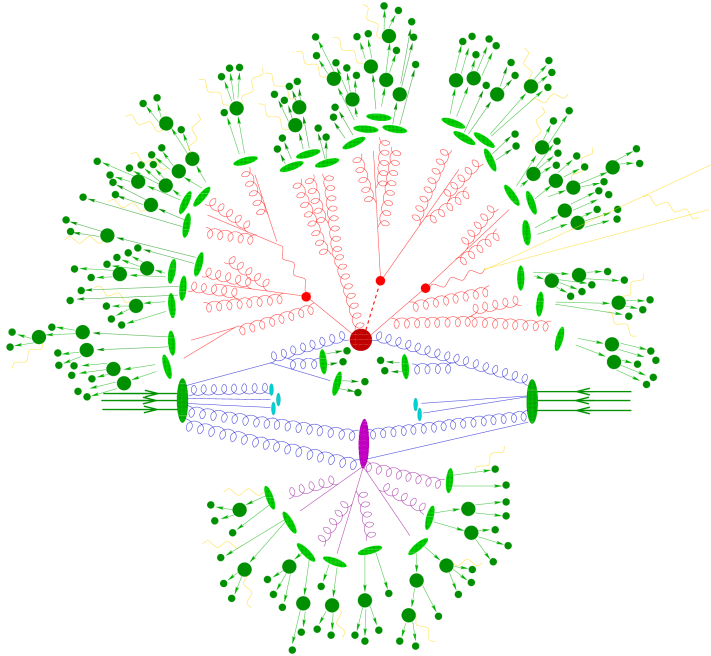


Figure 2.7: Pictorial representation of a $t\bar{t} + H$ event simulated by a MC event generator. The hard interaction (big red blob) is followed by the decay of the two top quarks and the Higgs boson (small red blobs). ISR and FSR are shown as curly blue and red lines, respectively. A second interaction is simulated (purple blob) and contributions from the underlying event are modelled (purple lines). The hadronisation of final-state partons (light green blobs) is followed by the decays of unstable hadrons (dark green blobs). QED radiation (yellow lines) is added at each stage of the event simulation. Figure adapted from [144].

Due to the high-momentum transfer scale, the cross section of the hard-scatter interaction can be calculated perturbatively using collinear factorisation [145],

$$\sigma = \sum_{a,b} \int_0^1 dx_a dx_b \int d\Phi_n f_a^{h_1}(x_a, \mu_F) f_b^{h_2}(x_b, \mu_F) \times \frac{1}{2x_a x_b s} |\mathcal{M}_{ab \rightarrow n}|^2(\Phi_n; \mu_F, \mu_R), \quad (2.7)$$

where x_a and x_b the momentum fractions of the partons a and b with respect to their parent hadrons h_1 and h_2 , μ_F and μ_R are the unphysical factorisation and the renormalisation scales, respectively, and $d\Phi_n$ is the differential final state phase space element. The phase space integration is typically done using MC sampling methods. The choices for μ_R and μ_F are to some extent arbitrary, but are typically chosen to be in accordance with the logarithmic structure of QCD, such that the matrix elements can be combined with the subsequent parton showers [145]. The matrix element (ME) $|\mathcal{M}_{ab \rightarrow n}|^2$ can be calculated using different methods [145], with most MC generators employing LO computations. As LO matrix elements are only reliable for the shapes of the distributions, an additional *K-factor* correcting the normalisation of the cross section to NLO is typically used [145]. The probability of finding a parton with momentum fractions x in a hadron h , is given by the PDF $f_a^h(x, \mu_F)$ and depends on the probed factorisation scale μ_F . The PDFs depend on non-perturbative aspects of the proton wave function and can thus not be calculated from first principles. Instead, they are extracted from measurements in deep inelastic scattering experiments (see e.g. [146, 147]). The variety of PDFs provided by different groups, is accessible in a common format through a unified interface implemented by the LHAPDF library [148]. In MC generators, the choice of PDFs not only play a crucial role for the simulation of the hard process, but also in the subsequent parton showers and multiple parton interactions, thus influencing both cross sections and event shapes.

Fixed-order matrix elements work well for describing separated, hard partons but are not sufficient to describe soft and collinear partons. Higher order effects from gluon radiation can be simulated using a parton shower (PS) algorithm. The emitted gluons will radiate additional

gluons or split into quark–antiquark pairs which can in turn undergo additional gluon radiation. The PS thus describes an evolutionary process in momentum transfer scales from the scale of the hard scatter interaction down to the infrared scale $\mathcal{O}(1\text{ GeV})$ where QCD becomes non-perturbative and partons are confined into hadrons. Both ISR and FSR are simulated through the PS. As opposed to ME calculations, PSs offer poor modelling of few hard partons, but excel in the simulation of collinear and soft multi-parton states.

In order to avoid double counting, the hard partons described by the calculation of the ME and the soft collinear emissions of the PS have to be connected to each other. This is done either through *matching* or *merging*. ME matching approaches [149] integrate higher-order corrections to an inclusive process with the PS [145]. Merging techniques like the CKKW [150] or CKKW-L [151] methods define an unphysical merging scale which can be understood as a jet resolution scale such that higher order ME corrections are only calculated for jets above that scale (while jets below that scale are modelled with the PS). Additional activity in the event not directly associated to the hard process is simulated. The underlying event is typically defined to be all additional activity after ISR and FSR off the hard process has been taken into account [145]. Furthermore, *multiple interactions* can occur in a single pp collision. The modelling of multiple interactions involves multiple hard scatter processes per pp collision as well as multiple soft interactions in addition to the hard scatter process.

Once the PS reaches energies of $\mathcal{O}(1\text{ GeV})$, entering the non-perturbative regime of QCD, the coloured objects need to be transformed into colourless states. This so-called *hadronisation* step cannot be calculated from first principles but has to be modelled, typically with either a *string* or a *cluster* model. The most advanced of the string models is the *Lund* model [152, 153]. It starts from linear confinement and considers a linear potential between a $q\bar{q}$ pair, that can be thought of as a uniform colour flux tube stretching between the q and \bar{q} , with a transverse dimension of the order of typical hadronic size (i.e. around 1 fm). As the $q\bar{q}$ pair moves apart, the flux tube stretches in length, leading to an increase in potential energy, finally breaking apart once enough energy is available to create a new $q'\bar{q}'$ pair, resulting in two colourless quark pairs $q\bar{q}'$ and $q'\bar{q}$. The new quark pairs can again move apart and break up further, leading to quark anti-quark pairs with low relative momentum, forming the final hadrons. The cluster model is based on the preconfinement property of PSs [154], stating that the colourless clusters of partons can be formed at any evolution scale Q_0 of the PS, and result in universal invariant mass distributions that depend only on Q_0 and the QCD scale Λ , but not on the energy scale Q or nature of the hard process at the origin of the PS [145]. The universal invariant mass distribution holds in the asymptotic limit where $Q_0 \ll Q$. If further $Q_0 \gg \Lambda$, then the mass, momentum and multiplicity distributions of the colourless clusters can even be calculated perturbatively [145]. Cluster models start with non-perturbative splitting of gluons and $q\bar{q}$ pairs, followed by the formation of clusters from colour-connected pairs. Clusters further split up until the Q_0 scale is reached, at which point they form the final mesons.

As not all hadrons formed in the hadronisation process are stable, the affected hadrons need to be decayed until they form resonances stable enough to reach the detector material. In addition QED radiation, that can happen at any time during the event, needs to be simulated. This is typically either done with algorithms similar to the ones used for the PS, or using the Yennie–Frautschi–Suura formalism proposed in Ref. [155].

The simulation steps that cannot be performed from first principles but rely on phenomenological models (underlying event, PS, hadronisation) introduce free parameters that need to be derived

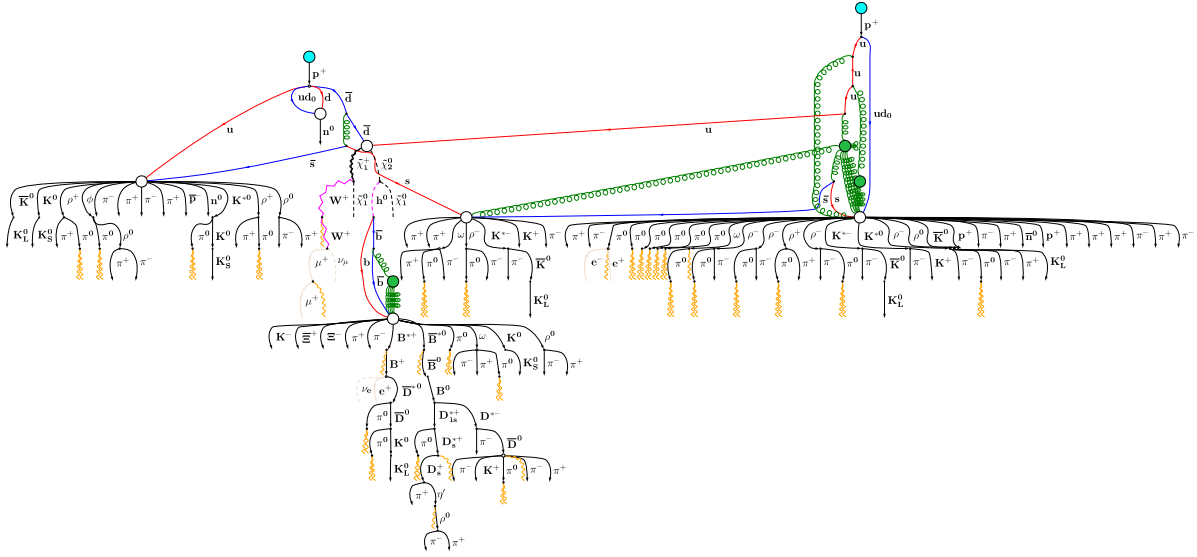


Figure 2.8: Pictorial representation of a (relatively simple) fully showered electroweakino pair production event with a final state including an electron and two b -jets. Most of the additional activity in the event stems from QCD interactions and results in a large amount of hadrons in the final state. The two incoming protons are marked as blue blobs. Gluons are represented as green curly green lines, and gluon self interaction is shown as green blobs (indicating only initial and final particles). Gauge and Higgs bosons are shown as pink lines. Photon radiation is shown as curly yellow lines.

or *tuned* from parameter optimisations against experimental data. In ATLAS, the output of MC event generators is stored in so-called EVNT data format containing HepMC-like [156] event records. Although only the stable final-state particles are propagated to the detector simulation, the original event record contains the connected tree (either the entirety or only part of it, depending on the MC generator used) as so-called *Monte Carlo truth*. A representation of a full simulated SUSY signal event considering the simplified model for electroweakino pair-production from fig. 1.10(a) is shown in fig. 2.8.

Detector simulation

Only the final-state particles generated by the MC event generator are read into the detector simulation. In ATLAS, the full detector simulation is handled by GEANT4 [157], a toolkit providing detailed models for physics processes as well as an infrastructure for particle transportation through a given geometry. GEANT4 has knowledge about the full detector geometry as well as the materials used in the subdetectors and is able to compute the energy deposits (so-called *hits*) from single particles in the different sensitive portions of the detector components. The GEANT4 simulation adds information to the Monte Carlo truth content created during the event generation, including however only the most relevant tracks (mostly from the ID) due to size constraints [143].

The complicated detector geometry and the detailed description of physics processes requires large computing resources for the full detector simulation using GEANT4, rendering it inaccessible for many physics studies requiring large statistics. Several varieties of fast simulations are available as an alternative. One of the most-used ones is ATLFAST-II [143], a fast sim-

ulation that uses the GEANT4 full simulation only for the ID and MS. The slow simulation in the calorimeters—taking about 80% of the full simulation time—is replaced with FASTCALOSIM [158], using parameterised electromagnetic and hadronic showers. Compared to the $\mathcal{O}(10^3)$ s simulation time per event in the full simulation, the ATLASFAST-II detector simulation only takes $\mathcal{O}(10^2)$ s [143].

For the large-scale reinterpretation discussed in part III of this thesis, even the ATLASFAST-II detector simulation is still too computationally expensive, and instead the truth-level MC events have to be used. In order to approximate the detector response, dedicated *four-vector smearing techniques*, introduced in chapter 9, are employed.

Digitisation

During the digitisation step, the hits from the detector simulation are converted into detector responses, so-called *digits* that are typically produced when currents or voltages in the respective readout channels rise above a certain threshold in a given time window. The digitisation considers a modelling of the peculiarities of each detector component, including electronic noise and cross-talk [143]. The effects from out-of-time and in-time pile-up are also considered by reading in multiple events and overlaying their hits. In order to match the true pile-up distribution in data, the number of events to overlay per bunch crossing can be set at run time. As described in section 2.1.1, effects from cavern background, beam halo and beam gas can either be mitigated or removed at analysis level and are therefore typically not simulated.

Chapter 3

Statistical data analysis

In high energy physics (HEP), statistical models are used in order to quantify the correspondence between theoretical predictions and the experimental observations. This chapter introduces the statistical concepts, methods and formulae used for statistical inference in this thesis. A frequentist approach is employed, interpreting probabilities as the frequencies of the outcomes of repeatable experiments that may either be real, based on computer simulations, or mathematical abstraction [9]. The following description largely adheres to Refs. [159, 160].

3.1 The likelihood function

In measurements in HEP, a *statistical model* $f(\mathbf{x}|\boldsymbol{\phi})$ is a parametric family of pdfs describing the probability of observing data \mathbf{x} given a set[†] of model parameters $\boldsymbol{\phi}$. The latter typically describe parameters of the physical theory or unknown detector effects. The *likelihood function* $L(\boldsymbol{\phi})$ is then numerically equivalent to $f(\mathbf{x}|\boldsymbol{\phi})$ with \mathbf{x} fixed. As opposed to the probability density function (pdf) $f(\mathbf{x})$ describing the value of f as a function of \mathbf{x} given a set of fixed parameters $\boldsymbol{\phi}$, the likelihood refers to the value of f as a function of $\boldsymbol{\phi}$ given a fixed[‡] value of \mathbf{x} .

Searches for BSM physics are often[‡] centred around the measurement of several disjoint binned distributions, called *channels* c , each associated with different event selection criteria yielding observed event counts \mathbf{n} . In such counting experiments where each event is independently drawn from the same underlying distribution, each bin is described by a Poisson term. The Poisson probability to observe n events with an expectation of ν events, $\text{Pois}(n|\nu)$, is given by

$$\text{Pois}(n|\nu) = \frac{\nu^n}{n!} e^{-\nu}. \quad (3.1)$$

[†] Sets of parameters (as opposed to single parameters) will henceforth be written using bold face.

[‡] This important difference is why the likelihood is written here as $L(\boldsymbol{\phi})$ instead of the equally common $L(\mathbf{x}|\boldsymbol{\phi})$.

[‡] While searches for BSM physics using unbinned distributions also exist, only binned searches are considered in the following.

The expectation ν_{cb} in each channel c and bin b is a sum over the set of physics processes considered, called *samples* in the following,

$$\nu_{cb} = \sum_{s \in \text{samples}} \nu_{csb}(\boldsymbol{\eta}, \boldsymbol{\chi}), \quad (3.2)$$

where ν_{csb} is the expected sample rate in a given bin of a given channel. The sample-wise rates are in general a function of the model parameters $\boldsymbol{\phi}$ that can either be *free parameters* $\boldsymbol{\eta}$ or *constrained parameters* $\boldsymbol{\chi}$. Possible modifications of the expected sample rates due to model parameters are considered to be either multiplicative or additive changes to the nominal estimate ν_{csb}^0 of the form

$$\nu_{csb}(\boldsymbol{\eta}, \boldsymbol{\chi}) = \left(\prod_i f_{csb}^i(\boldsymbol{\eta}, \boldsymbol{\chi}) \right) \left(\nu_{csb}^0 + \sum_j \Delta_{csb}^j(\boldsymbol{\eta}, \boldsymbol{\chi}) \right). \quad (3.3)$$

Here, $f(\boldsymbol{\phi})$ and $\Delta(\boldsymbol{\phi})$ are the multiplicative and additive *rate modifiers*, respectively, modifying the nominal estimates. Although in practice often only a function of a single model parameter, the rate modifiers can in general be a function of a set of model parameters.

Free parameters directly determined by the data observations are called *normalisation factors*. The constrained parameters represent the systematic uncertainties considered in the model, which—in frequentist statistics—have fixed but unknown true values. The degree to which they cause a deviation of the expected event rates from the nominal event rates is limited through *constraint terms* $c_\chi(a_\chi|\boldsymbol{\chi})$ that can be viewed as *auxiliary measurements* with global observed data \mathbf{a} .

For a given observation $\mathbf{x} = (\mathbf{n}, \mathbf{a})$ of observed events \mathbf{n} and auxiliary data \mathbf{a} , the likelihood then reads

$$L(\boldsymbol{\eta}, \boldsymbol{\chi}) = \prod_{c \in \text{channels}} \prod_{b \in \text{bins}_c} \text{Pois}(n_{cb} | \nu_{cb}(\boldsymbol{\eta}, \boldsymbol{\chi})) \prod_{\chi \in \boldsymbol{\chi}} c_\chi(a_\chi|\boldsymbol{\chi}), \quad (3.4)$$

where, given a certain integrated luminosity, n_{cb} and ν_{cb} refer to the corresponding observed and expected rate of events, respectively [161]. Most of the systematic uncertainties are so-called *interpolation parameters* $\boldsymbol{\alpha}$ representing either normalisation uncertainties or correlated shape uncertainties. Their constraint terms $c_\alpha(a_\alpha|\boldsymbol{\alpha})$ are parametrised by a Gaussian[†] with mean $a = 0$ and variance $\sigma = 1$, with $\alpha = 0$ representing the nominal value. The *up* and *down* variations are then given by $\alpha = \pm 1$, thereby representing $\pm 1\sigma$ variations. The impact of any given value of the parameter on the event rates is subsequently evaluated through polynomial interpolation and exponential extrapolation[§], a method that avoids discontinuous first and second derivatives at $\alpha = 0$ and ensures positive values for the predicted event rates [162].

Sample rates derived directly from theory calculations (i.e. MC simulation), are scaled to the integrated luminosity corresponding to the observed data. As discussed in section 2.1.2, the integrated luminosity is itself a measurement that is subject to uncertainties, requiring an additional constraint term in the likelihood. It is parametrised by a Gaussian with mean corresponding to the nominal integrated luminosity measurement and standard deviation equal

[†] Other parameterisations are also possible and discussed in Ref. [162], but not used in the following.

[§] Different interpolation and extrapolation strategies are discussed in Ref. [162] but not mentioned herein as they will not be used in the following.

to the integrated luminosity measurement uncertainty. Uncertainties arising from the finite size of the MC datasets used to derive estimated event rates are modelled by bin-wise scale factors γ_b . The constraint terms are Gaussian distributions with central value equal to unity and standard deviations calculated from the individual uncertainties of the samples defined in the respective channel.

As the event rate in a given bin can depend on multiple parameters, and likewise, a single parameter can affect the expected event rate in multiple bins across various channels, correlations between the model parameters ϕ can occur.

The above prescription for building binned likelihoods is called the HISTFACTORY template [162]. In this work, two independent implementations of the HISTFACTORY template are used. The first implementation, predominantly used in part II, relies on RooFit [163] (using the Minuit [164] package) and RooStats [165] for model parameter estimation and hypothesis tests, and is fully integrated into the ROOT data analysis framework [166, 167]. The user interface and the steering of statistical fits, as well as the bookkeeping of their results, is provided by HISTFITTER [168]. The second implementation, used in part III, makes use of pyhf [169, 170], a recent pure-python implementation of HISTFACTORY that is independent of the ROOT environment. The pyhf implementation of HISTFACTORY relies on NUMPY [171] and uses computational graph libraries like PYTORCH [172], TENSORFLOW [173] and JAX [174] to significantly speed up the parameter estimation process by leveraging the computational advantages of tensor algebra and automatic differentiation.

Apart from separating the model parameter set into free and constrained parameters $\phi = (\eta, \chi)$, a separate partition $\phi = (\psi, \theta)$ is frequently used in the context of hypothesis testing. Here, ψ are so-called *parameters of interests* of the model for which hypothesis tests are performed, and θ are *nuisance parameters* that are not of immediate interest but need to be accounted for to correctly model the data. In the search presented in this work, the only Parameter of Interest (POI) is the *signal strength* parameter μ , representing the ratio of the signal process cross section to its reference cross section as expected from theory. The expected event rate ν_i in each bin i can then be parametrised through

$$\nu_b = \mu S_b + B_b, \quad (3.5)$$

where S_b and B_b are the bin-wise expected signal and background rates, respectively. Fixing $\mu = 0$ thus yields an expected event rate containing only SM processes, which is why this is also called a *background-only* configuration. Setting $\mu = 1$ represents a *signal-plus-background* description at nominal signal cross section. Scanning multiple values of μ allows to set limits on the visible cross sections of the signal models considered in the search.

3.2 Parameter estimation

Given a likelihood $L(\phi)$ for a fixed set of observations \mathbf{x} , a measurement can be understood as a parameter estimation. In general, an estimator $\hat{\phi}$ is a function of the observed data used to estimate the true value of the model parameter ϕ .

In particle physics, the most commonly used estimator is the maximum likelihood estimator (MLE). The MLEs for the model parameters $\hat{\phi}$ are defined to be the parameter values that

maximise $L(\phi)$, or equivalently, maximise $\ln L(\phi)$ and minimise $-\ln L(\phi)$. The logarithm of the likelihood is used for computational reasons, as it not only reduces the computational complexity by avoiding exponentials and products, but also avoids potential problems arising from finite floating point precision. As the logarithm is a monotonically increasing function, $\ln L(\phi)$ has maxima at the same parameter values as $L(\phi)$. The negative logarithm of the likelihood is chosen in order to stick to the convention of optimisers in statistical packages typically minimising the result of a *loss function*.

The MLEs $\hat{\phi}$ can thus be found by solving the system of equations

$$\frac{\partial \ln L}{\partial \phi_i} = 0, \quad (3.6)$$

where the index i runs over all parameters. Due to the complexity of the likelihood, a solution typically needs to be found numerically using minimisation algorithms. In the following, the parameter estimation is referred to as a *fit* of the model to data, and the maximum likelihood estimates of the parameters are consequently called *best-fit values*.

3.3 Statistical tests

In addition to estimating the values of model parameters, searches for SUSY are naturally interested in claiming discovery (or alternatively exclusion) of hypothesised signal models. In the frequentist approach, this can be formulated in terms of hypothesis tests, evaluating a *null hypothesis* H_0 against an *alternative hypothesis* H_1 , with the goal of rejecting the null hypothesis. For discovering a new signal process, H_0 is defined to describe only known SM processes and thus called *background-only* hypothesis. The alternative hypothesis H_1 is then the *signal-plus-background* hypothesis describing both SM background processes as well as the signal process considered. When excluding a signal model the signal-plus-background hypothesis takes over the role of H_0 and is tested against the background-only hypothesis.

The degree of agreement of observed data with a certain hypothesis H is quantified by calculating a *p-value*, representing the probability of finding data of greater or more extreme incompatibility under assumption of H . The hypothesis can then be considered as excluded if its observed *p-value* is below a specified threshold. It is common to convert the *p-value* into a *significance* Z , defined in such a way that a Gaussian distributed observable with measured value Z standard deviations above its mean gives a one-sided upper tail probability equal to p . This yields the expression

$$Z = \Phi^{-1}(1 - p), \quad (3.7)$$

where Φ^{-1} is the quantile of the standard Gaussian. In HEP, claiming discovery of a signal conventionally requires a significance of at least $Z = 5$. If the significance is lower but still $Z > 3$, it is classified as a hint or evidence. For exclusion of a signal hypothesis at 95% confidence level, a *p-value* of 0.05, i.e. $Z = 1.64$, is required [160].

The *p-values* are calculated using a *test statistic* that parameterises the compatibility between the hypothesis and data in a single value. At the LHC experiments, the test statistics used for

hypothesis testing are based on the *profile likelihood ratio* $\lambda(\mu)$, defined to be

$$\lambda(\mu) = \frac{L(\mu, \hat{\theta}(\mu))}{L(\hat{\mu}, \hat{\theta})}, \quad (3.8)$$

where the conditional maximum likelihood estimators (CMLEs) $\hat{\theta}$ are the values of θ that maximise the likelihood with μ fixed. The distribution of the profile likelihood ratio depends explicitly on μ , and implicitly on $\mathbf{x} = (\mathbf{n}, \mathbf{a})$, but is asymptotically (i.e. in the limit of a large number of events) independent of the nuisance parameters θ^\dagger in the case where the tested value of μ is the true value μ' [159]. The asymptotic independence from θ follows from Wilks' theorem [175] and is one of the main motivations for using the profile likelihood ratio, as it avoids the problem of having to compute p -values for all possible values of θ . A generalisation to tested values of μ not corresponding to the true value μ' can be derived using Wald's theorem [176], allowing to obtain the distribution $f(\lambda(\mu)|\mu', \theta)$. The profile likelihood ratio takes values between 0 and 1, with $\lambda(\mu) = 1$ corresponding to cases where the tested value of μ is in good agreement with the observed data. In eq. (3.8), the nuisance parameters result in a broadening of the profile likelihood distribution, reflecting the loss of information about μ due to systematic uncertainties [160].

As the rate of signal processes considered in the following is in general non-negative, an estimator for μ should satisfy $\hat{\mu} \geq 0$. In order to avoid the formal complications of having a boundary at $\mu = 0$, it is convenient to consider an effective estimator $\hat{\mu}$ that is allowed to become negative, provided that the respective Poisson terms for $\mu S_b + B_b$ remain positive. Imposing a constraint equivalent to requiring $\mu \geq 0$ on the test statistic itself, leads to the alternative definition of the profile likelihood as

$$\tilde{\lambda}(\mu) = \begin{cases} \frac{L(\mu, \hat{\theta}(\mu))}{L(\hat{\mu}, \hat{\theta})}, & \hat{\mu} \geq 0, \\ \frac{L(\mu, \hat{\theta}(\mu))}{L(0, \hat{\theta}(0))}, & \hat{\mu} < 0, \end{cases} \quad (3.9)$$

where $\hat{\theta}(0)$ and $\hat{\theta}(\mu)$ are the CMLEs of θ given a signal strength parameter of 0 and μ , respectively.

Discovery

For the important special case where $\mu = 0$ is tested in a model with $\mu \geq 0$, i.e. discovery of a non-negative signal (rejection of the background-only hypothesis), the profile likelihood $\tilde{\lambda}(\mu)$ is used to build the test statistic

$$q_0 = -2 \ln \tilde{\lambda}(0) = \begin{cases} -2 \ln \lambda(0), & \hat{\mu} \geq 0, \\ 0, & \hat{\mu} < 0. \end{cases} \quad (3.10)$$

This definition ensures that the background-only hypothesis is not rejected due to a downward fluctuation in data, causing $\hat{\mu} < 0$. In case more events are seen in data than expected based on the background-only hypothesis, eq. (3.10) produces increasingly large values of q_0 , corresponding

[†] Eliminated by choosing specific values of the nuisance parameters for a given \mathbf{x} and μ , often referred to as *profiling*.

to an increasing incompatibility between data and the background-only hypothesis. The p -value quantifying the disagreement between the $\mu = 0$ hypothesis and data can then be computed using

$$p_0 = \int_{q_{0,\text{obs}}}^{\infty} f(q_0|0) dq_0, \quad (3.11)$$

with $q_{0,\text{obs}}$ the observed value of the test statistic q_0 in data and $f(q_0|0)$ the pdf of q_0 under assumption of the background-only hypothesis. In the asymptotic limit [160] with a single POI, the test statistic q_0 can be written as

$$q_0 = \begin{cases} \hat{\mu}^2/\sigma^2, & \hat{\mu} \geq 0, \\ 0, & \hat{\mu} < 0, \end{cases} \quad (3.12)$$

where $\hat{\mu}$ has a Gaussian distribution with mean μ' and variance σ^2 . In the case of $\mu' = 0$, the pdf of q_0 has the form of a half χ^2 distribution with one degree of freedom, and its cumulative distribution is $F(q_0|0) = \Phi(\sqrt{q_0})$ [159]. Using eq. (3.7), the p -value obtained with eq. (3.11) can be expressed with the significance Z_0 as

$$Z_0 = \sqrt{q_0}. \quad (3.13)$$

Exclusion and upper limits

If the background-only ($\mu = 0$) hypothesis cannot be rejected, the hypotheses can be switched around and instead the signal-plus-background ($\mu = 1$) hypothesis can be tested against a hypothesis where signal events are produced at a rate smaller than μ . For excluding the signal-plus-background hypothesis and setting upper limits on the signal strength μ , the test statistic is defined as

$$\tilde{q}_\mu = \begin{cases} -2 \ln \tilde{\lambda}(\mu), & \hat{\mu} \leq \mu \\ 0, & \hat{\mu} > \mu \end{cases} = \begin{cases} -2 \ln \frac{L(\mu, \hat{\theta}(\mu))}{L(\hat{\mu}, \hat{\theta})}, & \hat{\mu} < 0, \\ -2 \ln \frac{L(\mu, \hat{\theta}(\mu))}{L(0, \hat{\theta}(0))}, & 0 \leq \hat{\mu} \leq \mu, \\ 0 & \hat{\mu} > \mu. \end{cases} \quad (3.14)$$

Setting $\tilde{q}_\mu = 0$ in the case where $\hat{\mu} > \mu$ ensures that an overfluctuation of data is not considered as evidence against the signal hypothesis. This is opposed to the definition of q_0 , where an underfluctuation of data ($\hat{\mu} < \mu$) is not regarded to be evidence against the background-only hypothesis. It is worth highlighting that the discovery test statistic q_0 in eq. (3.11) is not just the special case of \tilde{q}_μ with $\mu = 0$, but hinges on a different definition.

The p -value, quantifying the level of agreement between data and the tested value of μ is then given by

$$p_\mu = \int_{\tilde{q}_{\mu,\text{obs}}}^{\infty} f(\tilde{q}_\mu|\mu) d\tilde{q}_\mu, \quad (3.15)$$

where, as before, $\tilde{q}_{\mu,\text{obs}}$ is the observed value of the test statistic in data and $f(\tilde{q}_\mu|\mu)$ is the pdf of \tilde{q}_μ given the hypothesis μ . In the asymptotic limit [160], the test statistic \tilde{q}_μ can be written

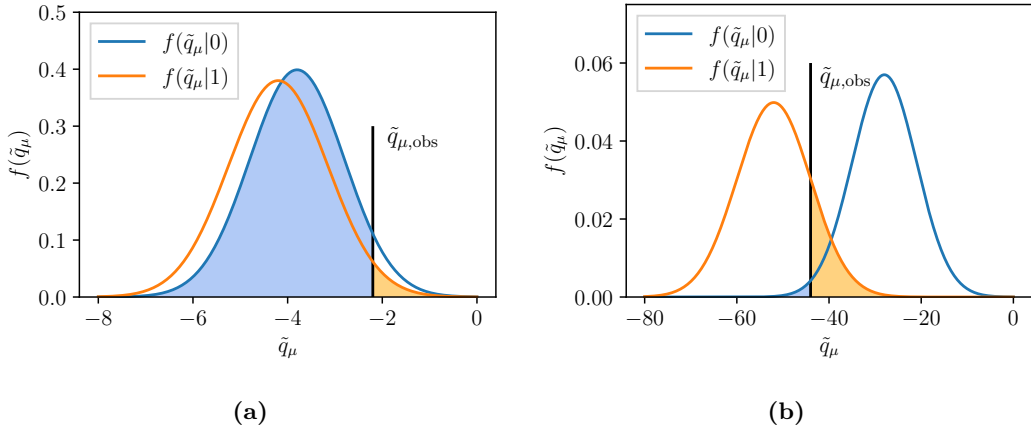


Figure 3.1: Distribution of the pdfs of the signal plus background (in orange) and background-only (in blue) models. The orange and blue coloured areas represent the p_{s+b} and p_b values, respectively. Figure (a) shows a case where both pdfs are close together, while figure (a) shows a case where they are well separated. Figures created by the author but based on Ref. [177].

as

$$\tilde{q}_\mu = \begin{cases} \mu^2/\sigma^2 - 2\mu\hat{\mu}/\sigma^2, & \hat{\mu} < 0, \\ (\mu - \hat{\mu})^2/\sigma^2, & 0 \leq \hat{\mu} \leq \mu, \\ 0 & \hat{\mu} > \mu, \end{cases} \quad (3.16)$$

which yields for the significance Z_μ the expression

$$Z_\mu = \begin{cases} \sqrt{\tilde{q}_\mu}, & 0 < \tilde{q}_\mu \leq \mu^2/\sigma^2 \\ \frac{\tilde{q}_\mu + \mu^2/\sigma^2}{2\mu/\sigma}, & \tilde{q}_\mu > \mu^2/\sigma^2. \end{cases} \quad (3.17)$$

3.4 CL_s approach

In the CL_{s+b} method, a signal-plus-background model is excluded if $p_{s+b} < \alpha$, where α is defined by the desired confidence level, typically $\text{CL} = 1 - \alpha = 95\%$, and p_{s+b} can be calculated using the test statistic \tilde{q}_μ (with $\mu = 1$) introduced in eq. (3.14). If the experiment has very low sensitivity to a specific signal-plus-background model, e.g. because the production cross section is too low, the distribution of the test statistic of the signal-plus-background model will be very close to that of the background-only model. In case of an underfluctuation in data, the $\mu = 1$ model can then be falsely excluded, even though no sensitivity is expected. Figure 3.1 illustrates this with a simple example. In fact, the exclusion of models to which the experiment has no sensitivity has a probability of at least α [177].

This problem can be remedied by adopting the CL_s method [178], altering the threshold for excluding a model in a way to avoid exclusion of models to which the experiment has very low sensitivity. The CL_s value is defined as

$$\text{CL}_s = \frac{p_{s+b}}{1 - p_b}, \quad (3.18)$$

where p_b is the p -value of the background-only hypothesis[†]. If the distributions of the test statistics for the signal-plus-background and the background-only models are close to each other (as seen in fig. 3.1(a)) a small value of p_{s+b} due to an underfluctuation in data will entail a large value of p_b . Consequently, in the calculation of the CL_s value, p_{s+b} will be penalised by $1 - p_b$ (that will be close to 0), resulting in $\text{CL}_s > p_{s+b}$, preventing the exclusion of the signal-plus-background model. Conversely, in the case where the two test statistics are well-separated (see fig. 3.1(b)) and $p_{s+b} < \alpha$, then p_b will also be small and thus CL_s will be close to p_{s+b} obtained by the frequentist approach.

3.5 Asimov dataset

Searches for BSM physics are not only interested in the significance obtained using the dataset measured by the experiment, but also in the expected (or median) significance obtained for rejecting different values of μ . For example, for rejecting the $\mu = 1$ hypothesis, searches are interested in the expected significance obtained assuming data generated according to the $\mu = 0$ hypothesis.

The expected experimental sensitivity can be determined using an artificial dataset called the *Asimov dataset*, defined such that MLEs of all parameters determined using Asimov data correspond to the true parameter values. This is achieved by constructing a dataset where the number of events in each bin is exactly equal to the expected event rate in that bin. Using Asimov data, the Asimov likelihood L_A as well as the profile likelihood λ_A can be evaluated and thus a median significance can be determined. Non-integer values for data are not an issue as factorial terms from the Poisson probabilities are canceled in the profile likelihood and can thus be dropped altogether.

3.6 Sensitivity estimation

When designing search regions for an analysis, it is necessary to achieve an optimal signal-to-background separation power. A significance metric is needed in order to quantify the separation power and to have a metric to optimise for. In the following, the expected discovery significance introduced in Ref. [179] is used. As the full statistical model is in general not yet known when designing the search regions, appropriate assumptions have to be made. In a *cut-and-count* selection where only the total number of events after a selection are relevant (and not e.g. their distribution), the significance is determined by the total number of signal events S , the total number of background events B and the uncertainty on the expected number of background events ΔB . This can be modelled as a so-called *on/off problem*[§] [179, 180], where the cut-and-count experiment uses two bins, a signal region (SR) enriched in signal events, and

[†] It is worth highlighting that p_b is equal to p_μ from eq. (3.15) with $\mu = 0$. This is strictly different from p_0 in eq. (3.11) as it relies a different test statistic.

[§] The *on/off* nomenclature originates from gamma ray astronomy where *on* refers to the telescope pointing on-source (measuring signal and background photons), while *off* refers to it pointing off-source (measuring only background photons). This problem is an exact analog to the HEP problem herein, where the off-source measurement typically corresponds to some *sideband* measurement, i.e. a measurement of events in a region of a parameter disjoint from the parameter range where the signal might exist.

a control region (CR) containing only background events. In the background-only hypothesis, the parameter $\tau = n_{\text{CR}}/n_{\text{SR}}$ then denotes the ratio between the event rate in the CR, n_{CR} , and the event rate in the SR, n_{SR} .

If τ is known, then the likelihood of this simple configuration can be written in terms of the expected background event rate

$$L(\mu, B) = \text{Pois}(n_{\text{SR}}|\mu S + B) \cdot \text{Pois}(n_{\text{CR}}|\tau B), \quad (3.19)$$

where μ is again the signal strength parameter. The relative background uncertainty can thus be treated as coming from a Poisson-distributed auxiliary measurement containing only background (i.e. in the CR) with corresponding uncertainty $\sqrt{\tau B}$, leading to the approximation

$$\tau = \frac{B}{\Delta B^2}. \quad (3.20)$$

As n_{SR} and n_{CR} are each drawn from a Poisson probability with unknown means ν_{SR} and ν_{CR} , the background-only hypothesis corresponds exactly to the case where the ratio of Poisson means $\lambda = \nu_{\text{CR}}/\nu_{\text{SR}}$ is equal to τ [179]. The two Poisson terms can then be written as the product of a single Poisson term with mean $n_{\text{tot}} = n_{\text{SR}} + n_{\text{CR}}$ and the binomial probability of picking n_{SR} events out of n_{tot} with probability $\rho = \nu_{\text{SR}}/\nu_{\text{tot}} = 1/(1 + \lambda)$. The likelihood can thus be written as

$$\begin{aligned} L(\mu, B) &= \text{Pois}(n_{\text{tot}}|\lambda_{\text{tot}}) \cdot B(n_{\text{SR}}|\rho, n_{\text{tot}}) \\ &= \frac{e^{-\lambda_{\text{tot}}} \lambda_{\text{tot}}^{n_{\text{tot}}}}{n_{\text{tot}}!} \cdot \binom{n_{\text{tot}}}{n_{\text{SR}}} \rho_{\text{tot}}^\lambda (1 - \rho)^{n_{\text{tot}} - n_{\text{SR}}}. \end{aligned} \quad (3.21)$$

Since the background-only hypothesis cannot only be expressed as $\mu = 0$ but also as $\nu_{\text{SR}} = \nu_B$, $\lambda = \tau$, and especially also as $\rho = 1/(1 + \tau)$ [179], its p -value can be calculated using the well-known frequentist binomial test,

$$p_B = \sum_{j=n_{\text{SR}}}^{n_{\text{tot}}} B(j|n_{\text{tot}}, \rho). \quad (3.22)$$

The significance corresponding to p_B can be derived using eq. (3.7) and is computable in a numerically fast way using the incomplete beta function. The algorithm used for calculating Z_B in this work is implemented in the `RooStats::NumberCountingUtils` methods in ROOT [166, 167].

Part II

The 1-lepton analysis

Chapter 4

Analysis overview

This chapter aims to give an introduction to the search for electroweakinos presented in this work. First, the targeted final state is introduced and motivated, followed by the SM background processes that need to be considered when performing searches for SUSY in this final state. Next, the reconstruction and identification of physics objects as well as the event selection requirements are described.

4.1 Search for electroweakinos in the 1ℓ final state

In the search for electroweakinos presented herein, the simplified model introduced in section 1.3.2 is interpreted in a final state with one lepton, two b -jets and high missing transverse momentum. This final state can occur when the W boson decays through $W^\pm \rightarrow \ell^\pm \nu_\ell$, while the Higgs boson decays into $h \rightarrow bb$. Although a final state without leptons would benefit from the higher branching fraction of the decay $W^\pm \rightarrow q'\bar{q}$, due to the large QCD couplings these final states are largely dominated by QCD multi-jet background processes that are omnipresent at hadron colliders like the LHC. Final states with exactly one lepton have lower cross sections but allow to reject a majority of the QCD background, as pure QCD multi-jet events can only enter the 1ℓ final state through false reconstruction of a jet as a lepton (so-called *fake* leptons).

Targeting the decay of the Higgs boson into a pair of b quarks allows to search to benefit from the high branching ratio of 58.3% of this decay mode and permits a full reconstruction of Higgs candidates, a procedure that will be used in the following to achieve a high signal-to-background ratio. Figure 4.1 shows the full signal model targeted in this search, including the considered decays of the W and Higgs bosons.

Previous searches for electroweakinos in this final state have been performed by the ATLAS [181, 182] and CMS [183] collaborations, and have excluded $\tilde{\chi}_1^\pm/\tilde{\chi}_2^0$ masses up to 540 GeV and 490 GeV, respectively, for massless $\tilde{\chi}_1^0$. The two previous ATLAS searches used 20.3 fb^{-1} of $\sqrt{s} = 8\text{ TeV}$ and 36.1 fb^{-1} of $\sqrt{s} = 13\text{ TeV}$ pp collision data, respectively. As opposed to this, the search presented in the following uses the full dataset available from the Run 2 data taking period, amounting to an unprecedented 139 fb^{-1} of pp collision data at $\sqrt{s} = 13\text{ TeV}$ [184]. As this search analysis events in final states with exactly one lepton, it will often be referred to as the *1 ℓ search* in the following.

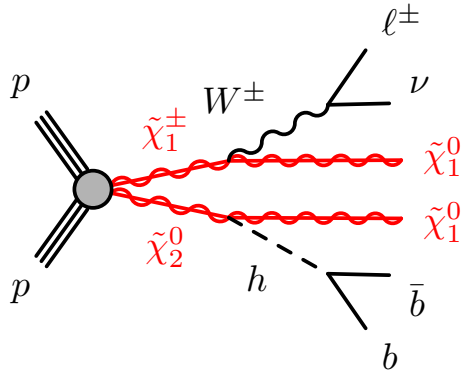


Figure 4.1: Diagram for the simplified model used in this work including the decays $W^\pm \rightarrow \ell^\pm \nu_\ell$ and $h \rightarrow b\bar{b}$.

4.2 Standard Model backgrounds

Although the requirement of exactly one lepton isolated from surrounding hadronic activity significantly reduces the contribution from QCD multi-jet background, numerous other SM processes can still result in final states with exactly one isolated lepton, multiple jets and missing transverse momentum. Background sources are generally classified into *reducible* and *irreducible* backgrounds. Irreducible backgrounds, on the one hand, are processes with a physical phase space indistinguishable from the final state of the signal process in question. Reducible backgrounds, on the other hand, result from partially misreconstructed processes as well as mismeasurements. Examples of reducible processes are events where a lepton originates from a heavy flavour (HF) decay, photon conversions or misreconstructed jets. SM processes that result in final states with an isolated lepton, multiple jets and missing transverse momentum typically involve a W boson decaying into a lepton–neutrino pair (a so-called *leptonic decay*). The neutrino will contribute to the total missing transverse momentum in the event, while additional jets can appear in the final state through QCD radiation or other branches of the decay chain.

By far the largest SM background contribution relevant for this search, stems from the production of top quarks, predominantly occurring as top quark pair production ($t\bar{t}$), where both top quarks decay into a W boson and a b quark. Final states with one isolated lepton can occur through leptonic decay of one of the W bosons. Figure 4.2(a) shows a diagram of an exemplary decay of a $t\bar{t}$ system into a final state with one lepton, multiple jets (two of which originate from b quarks) and missing transverse momentum. In addition to $t\bar{t}$, single top production (through s -channel, t -channel or tW -channel processes) can also result in similar final states as the SUSY signal and thus constitutes a significant SM background process. An exemplary decay into a final state relevant for this search is shown in fig. 4.2(b).

Apart from processes involving top quarks, the production of a W boson in association with multiple jets ($W + \text{jets}$) is the third major background considered in the 1ℓ search. If the W boson undergoes a leptonic decay and two of the produced jets are tagged as originating from b quarks, the signature of this process can be similar to that of signal events. An exemplary diagram for a $W + \text{jets}$ event is shown in fig. 4.2(c).

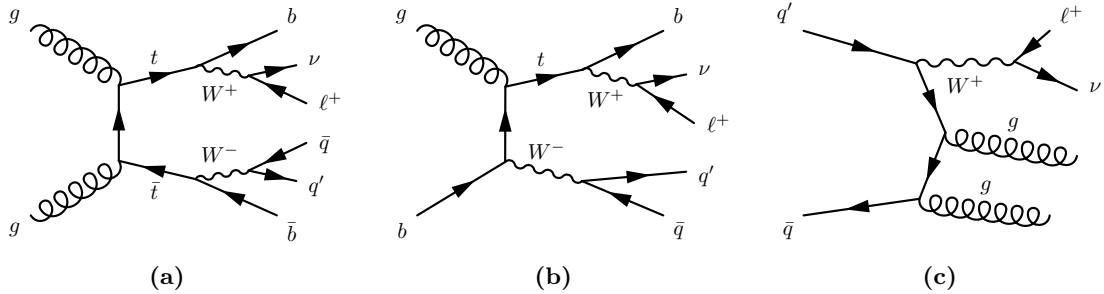


Figure 4.2: Exemplary Feynman diagrams showing the dominant processes (a) $t\bar{t}$, (b) single top and (c) $W + \text{jets}$ production with subsequent decays.

Production of multiple vector bosons V ($= W, Z$)—although not a dominant background due to low cross sections—can still result in the same final state as the signal process. In the following, diboson VV and multiboson VVV processes are considered.

Other SM backgrounds with small contributions in the phases spaces targeted by the search include $Z + \text{jets}$ production, $t\bar{t} + V$ production, as well as various processes involving Higgs bosons. $Z + \text{jets}$ plays only a minor role, as the only irreducible component originates from $Z(\rightarrow \tau\tau) + \text{jets}$ processes, where one τ -lepton undergoes a leptonic decay while the other one decays hadronically. Production of $t\bar{t} + V$ has a similar topology as ordinary $t\bar{t}$ processes, but with lower cross section and additional objects in the final state. This background therefore only plays a minor role in the analysis. Higgs processes considered in the following include single Higgs production through vector boson fusion (VBF) or gluon–gluon fusion (ggF) as well as $h + V$ and $h + t\bar{t}$ processes. In the following, all minor backgrounds are grouped together and collectively labelled as *other* backgrounds.

Pure QCD multi-jet events can only appear in the 1-lepton final state through false reconstruction of a jet as a lepton (so-called *fake* leptons) and mismeasurement of E_T^{miss} . It has been shown that this background is negligible in all selections relevant to this search, hence no estimation for QCD contribution is considered in the following [184].

4.3 Monte Carlo samples

Table 4.1 summarises all MC generators and software versions executed during generation of the simulated events used in the following. Further details are given in the relevant ATLAS simulation notes [185–188].

4.3.1 Signal samples

The $\tilde{\chi}_1^\pm/\tilde{\chi}_2^0$ pair production signal samples were generated at LO using MADGRAPH5_AMC@NLO 2.6.2 [189, 190] with up to two additional partons in the ME. MADGRAPH5_AMC@NLO is interfaced with PYTHIA8 [191] for the PS, hadronisation and underlying event, using the CKKW-L [192] scheme for matching the PS to the MEs. The NNPDF 2.3 LO [193] PDF set and the A14 set of tuned parameters [194] are used. For modelling the decay of HF quarks, EVTGEN v1.6 [195] is used.

As the $\tilde{\chi}_1^\pm/\tilde{\chi}_2^0$ and $\tilde{\chi}_1^0$ masses are free parameters of the signal model, they are systematically varied, resulting in a set of 164 distinct signal models, evenly distributed in the two-dimensional grid spanned by the two mass parameters. In the following, this two-dimensional grid will be referred to as *signal grid*, while the distinct signal scenarios (each with a unique set of mass parameter values) will be referred to as *signal points*. The generated signal grid covers $\tilde{\chi}_1^\pm/\tilde{\chi}_2^0$ masses from 150 GeV to 1.1 TeV and $\tilde{\chi}_1^0$ masses from 0 GeV to 550 GeV, avoiding the kinematically forbidden region with $m(\tilde{\chi}_1^\pm/\tilde{\chi}_2^0) < m(\tilde{\chi}_1^0) + m(h)$ that does not allow for production of on-shell Higgs bosons.

MC datasets of signal models well within the expected sensitivity range of the analysis, i.e. with relatively low $\tilde{\chi}_1^\pm/\tilde{\chi}_2^0$ and $\tilde{\chi}_1^0$ masses, are generated using the ATLFAST-II detector simulation. The full detector simulation using GEANT4 is used for the remaining model points for maximum accuracy in the parameter space relevant to the expected sensitivity. In order to account for pileup effects, all signal samples are overlaid with simulated minimum bias events generated using PYTHIA8 and the A3 tune [196], and reweighted to match the pileup distribution measured in data.

The cross sections for electroweakino pair production have been calculated using RESUMMINO [197] at NLO in the strong coupling constant and including next-to-leading logarithm (NLL) terms in the soft gluon resummation [89, 90].

4.3.2 Background samples

Top quark pair production and single top processes were generated using POWHEG-Box v2 [198], implementing the POWHEG method [199, 200] for merging NLO MEs with the PSs. The PS, hadronisation and underlying event were simulated using PYTHIA8 with the A14 tune. Production of $t\bar{t}$ in association with a vector boson ($t\bar{t} + V$) is generated using MADGRAPH5_AMC@NLO 2.3.3, interfaced with PYTHIA8 for the PS. The set of PDFs used for simulation of $t\bar{t}$, single top, and $t\bar{t} + V$ is the NNPDF2.3LO set.

Production of a vector boson V with additional jets ($W/Z + \text{jets}$) is simulated using SHERPA 2.2.1 [144, 201], allowing up to two (four) additional parton emissions at NLO (LO) accuracy. The CKKW ME+PS matching and merging scheme [202, 150] is used, extended to NLO accuracy [203]. Diboson (VV) and multiboson (VVV) processes are simulated using SHERPA 2.2.1 and 2.2.2 with the default SHERPA generator tune. The PDFs used are provided by the NNPDF3.0NNLO set [204].

All Higgs processes are simulated using POWHEG-Box v2 for the ME calculations and PYTHIA8 for the PS, underlying event and hadronisation. While the generation of $h + t\bar{t}$ uses the A14 tune and the NNPDF2.3LO set, $h + V$ and single Higgs production are simulated using the NNPDF 3.0 NNLO set and the AZNLO [205] set of tuned generator parameters.

The detector simulation for all MC background samples was performed using the full detector simulation based on GEANT4. Except for the MC samples generated using SHERPA, all background samples use EVTGEN v1.2 or v1.6 to model the decay of HF quarks. Similar to the signal models, all background samples are overlaid with simulated minimum bias events generated with PYTHIA8 and the A3 tune.

Table 4.1: Overview of the configuration of MC generators used for simulating the various SUSY signal and SM background processes.

Process	Matrix element	Parton shower	PDF set	Cross section	Tune
Signal	MADGRAPH5_AMC@NLO 2.6.2	PYTHIA 8.230	NNPDF 2.3 LO	NLO+NLL [197, 89, 90]	A14
$t\bar{t}$	POWHEG-BOX	PYTHIA 8.230	NNPDF2.3LO	NNLO+NNLL [206, 207]	A14
t (s-channel)	POWHEG-BOX	PYTHIA 8.230	NNPDF2.3LO	NLO [208]	A14
t (t-channel)	POWHEG-BOX	PYTHIA 8.230	NNPDF2.3LO	NLO [208]	A14
$t + W$	POWHEG-BOX	PYTHIA 8.230	NNPDF2.3LO	NNLO [208, 209]	A14
$t\bar{t} + V$	MADGRAPH5_AMC@NLO 2.3.3	PYTHIA 8.210	NNPDF2.3LO	NLO [210, 211]	A14
$V + \text{jets}$	SHERPA 2.2.1		NNPDF3.0NNLO	NNLO [212]	SHERPA default
VV	SHERPA 2.2.1/2.2.2		NNPDF3.0NNLO	NLO [188]	SHERPA default
VVV	SHERPA 2.2.1/2.2.2		NNPDF3.0NNLO	NLO [188]	SHERPA default
$h + t\bar{t}$	POWHEG-BOX	PYTHIA 8.230	NNPDF2.3LO	NLO [213]	A14
$h + V$	POWHEG-BOX	PYTHIA 8.212	NNPDF3.0NNLO	NNLO [213]	AZNLO
h (ggF)	POWHEG-BOX	PYTHIA 8.212	NNPDF3.0NNLO	N^3LO+N^3LL [213]	AZNLO
h (VBF)	POWHEG-BOX	PYTHIA 8.212	NNPDF3.0NNLO	NNLO [213]	AZNLO

4.4 Object definitions

The reconstruction of physics objects requires the combination of data from multiple detector components. Due to finite detector resolutions, and the considerable amount of particles produced in each collision, this process does not always work without flaws. Sometimes, objects are falsely reconstructed or not reconstructed at all. In order to minimise reconstruction errors, different identification and reconstruction criteria are introduced for each physics object category. Electrons and muons are categorised into *baseline* and *signal* objects. Baseline objects have a smaller purity but a higher acceptance which is e.g. useful for the reconstruction of the missing transverse momentum. Stricter identification and isolation criteria are required for signal objects, resulting in lower acceptances but also lower probability of reconstruction errors. In the following, signal-type objects are used as the physical objects. Table 4.2 provides a comprehensive summary of the object definitions introduced in the ensuing sections.

4.4.1 Tracks and vertices

The reconstruction of tracks of charged particles starts with the formation of clusters from raw data recorded in the Pixel and SCT detectors. Clusters are formed by grouping together adjacent pixels and strips with energy deposits above a certain threshold and are subsequently used to create three-dimensional space-points, representing the points where charged particles traversed the active ID material [214]. Sets of three space-points form track seeds that serve as inputs for a combinatorial Kalman filtering technique [215] that includes additional space-points from the remaining pixel and SCT layers to extend the preliminary trajectory. A χ^2 track fit is performed at each step of the extension. Where seeds can be extended by more than one compatible space-point in a given layer, multiple track candidates are formed. Ambiguities between candidates are resolved by assigning them a score, taking into account basic track properties like the χ^2 of the track fit and its associated p_T [214]. The ambiguity solver requires track candidates to contain a minimum of 7 pixel and SCT clusters, have a maximum of one shared pixel cluster and two shared SCT clusters on the same layer and have no more than two

holes[†] of which only one is allowed to be in the pixel detector. Track candidates also need to have $p_T > 400 \text{ MeV}$, $|\eta| < 2.5$ and have longitudinal (z_0) and transversal (d_0) impact parameters with respect to their associated vertex satisfying $|z_0 \sin \theta| < 3.0 \text{ mm}$ and $|d_0| < 2.0 \text{ mm}$, where θ is the polar angle of the track [214]. Track candidates surviving the ambiguity solver are extended by compatible hits in the TRT [216] and subject to a global high-resolution track fit before being added to the final track collection [214].

Vertex reconstruction uses a selection of tracks satisfying a set of quality requirements [217] in order to fit the best vertex position through a procedure iteratively down-weighting less compatible tracks [218]. Once the vertex position has been determined, incompatible tracks with small weights are removed and can be reused for the reconstruction of additional vertices [218]. All reconstructed vertices with at least two associated tracks are kept as valid primary vertex candidates. In events with multiple candidates, the primary vertex is defined to be the one with the highest $\sum p_T^2$ of its associated tracks.

4.4.2 Electrons and Photons

Electron and photon candidates are reconstructed from energy deposits in topologically connected cells in the electromagnetic and hadronic calorimeters. The reconstruction algorithm starts with the preparation of energy deposits into so-called *topo-clusters* [219]. These are formed by calorimeter cells containing energy deposits above a certain noise threshold, so-called *seed* cells, including their neighbouring cells which, in turn, can also act as seed cells. All cell signals are measured at the electromagnetic scale, assuming that energy deposits stem only from electromagnetic interactions. Although the topo-clustering algorithm starts with cells from both calorimeters, only energies from cells in the EM calorimeter are used in the subsequent electron and photon reconstruction steps [220]. Using only EM topo-clusters with a certain threshold ratio of the EM energy to the total cluster energy significantly reduces contamination from pileup clusters [220]. Next, the EM topo-clusters are loosely matched to ID tracks which are subsequently re-fitted in order to account for energy losses through bremsstrahlung [220]. Vertices from photon conversions are reconstructed from tracks matched to fixed-size clusters [221] and also matched to the EM topo-clusters. In the final step of the reconstruction algorithm, EM topo-clusters are sorted according to descending E_T and tested as seed clusters for dynamic, variable-size *superclusters*, with different seed requirements for electrons and photons [220]. Clusters near seed candidates can be added as satellite cluster candidates, originating e.g. from bremsstrahlung. The supercluster technique allows to dynamically change the cluster size as needed in order to recover energy losses from bremsstrahlung or photon conversions [220]. Electrons are finally built from superclusters with matched tracks. While converted photons are built from supercluster and matched conversion vertices, unconverted photons are constructed using superclusters not matched to any electron tracks or conversion vertices. The energies of both electrons and photons are calibrated using $Z \rightarrow ee$ decays [220].

The identification of prompt electrons relies on a likelihood discriminant built from quantities measured in the ID and calorimeters. The quantities are chosen according to their ability to discriminate prompt isolated electrons from non-prompt leptons originating in e.g. HF decays, from photon conversions or from jets. They include the properties of the electron track, the shape of the EM shower and the quality of the match between the electron track and

[†] Holes are intersections of the track trajectory with sensitive detector material not containing a cluster.

the calorimeter clusters [222]. Photon identification, on the other hand, relies on a cut-based selection exploiting the shape of the EM shower [220].

In the 1ℓ search, electrons are required to satisfy $p_T > 7 \text{ GeV}$ and $|\eta| < 2.47$. Baseline electrons are identified using the *LooseAndBLayer* requirement on the identification likelihood, requiring a hit in the innermost layer of the pixel detector, at least two additional hits in the remaining pixel layers and seven hits in the pixel and SCT detectors combined [222]. In addition, the longitudinal impact parameter z_0 of baseline electrons needs to satisfy $\Delta z_0 \sin \theta < 0.5 \text{ mm}$ with respect to the primary vertex. The *LooseAndBLayer* identification yields an average efficiency of about 93%, increasing from low to high electron E_T [222]. Signal electrons are a subset of baseline electrons and need to satisfy the *Tight* likelihood identification, yielding an efficiency of 80% for prompt electrons with $E_T = 40 \text{ GeV}$ [222]. In addition to the longitudinal impact parameter, signal leptons also need to satisfy $d_0/\sigma_{d_0} < 5$, where the transverse impact parameter d_0 and its uncertainty σ_{d_0} are measured with respect to the beam line.

Finally, electrons need to be *isolated*, meaning that their vicinity must be clear of additional significant detector activity. Requiring electrons to be isolated prevents the selection of non-prompt electrons originating from e.g. HF decays or misidentifications of light hadrons. Isolation is quantified using two observables, one using tracking information and the other one using calorimeter data. The tracking based isolation variable, $p_T^{\text{varcone}20}$, is the sum of all track momenta above 1 GeV (excluding the electrons track itself) in a cone around the electron. The size of the cone is chosen to be $\Delta R = \min(10 \text{ GeV}/p_T, 0.2)$, i.e. is shrinking with increasing transverse momentum of the electron. The calorimeter based variable $E_T^{\text{cone}20}$ corresponds to the sum of the transverse energies in topo-clusters (excluding the electrons itself and after correcting for pileup effects) in a cone with $\Delta R = 0.2$ around the electrons. Both baseline and signal electrons are required to satisfy the *Loose* working point [220], corresponding to the requirements $p_T^{\text{varcone}20}/p_T < 0.2$ and $E_T^{\text{cone}20} < 0.15$. In order to improve the rejection of non-prompt electrons at high transverse momenta, electrons with $p_T > 200 \text{ GeV}$ need to satisfy the *HighPtCaloOnly* working point, applying the tighter requirement $E_T^{\text{cone}20} < \max(0.015 \cdot p_T, 3.5 \text{ GeV})$.

Photons are required to have $p_T > 13 \text{ GeV}$ and $|\eta| < 2.37$ and need to satisfy the *Tight* identification and *FixedCutTight* isolation requirements introduced in Ref. [220]. In this analysis, photons are only used in the calculation of the missing transverse momentum.

4.4.3 Muons

The reconstruction of muons uses primarily data from the ID and MS and is based on the minimum ionising nature of muons. Muon candidates are independently reconstructed in the ID and the MS as muon tracks and only then combined to a muon candidate that can be used by physics analysis [223, 224]. The track reconstruction in the ID follows the same procedure used for other charged-particle tracks, described in section 4.4.1. In the MS, the muon track reconstruction starts with the identification of short, straight-line track segments. Segments from different MS layers are combined into preliminary muon track candidates if they are loosely compatible with the IP and match a first-order approximation of the parabolic trajectory describing the muon track in the magnetic field [224]. Track candidates are then passed through a global χ^2 fit, taking into account possible MS chamber misalignments as well as interactions with the detector material [224]. In order to increase the reconstruction performance, MS muon tracks are subsequently combined with the ID tracks using five different reconstruction

strategies, described in detail in Ref. [224]. Only two of these strategies are relevant for this analysis:

- *combined muons*, formed by combining the ID and MS tracks through a global fit, taking into account the energy loss in the calorimeters. An *outside-in* approach is employed, reconstructing muons first in the MS before performing an inward extrapolation and match to an ID track.
- *MS extrapolated muons*, built using MS muon tracks only, but extrapolating the tracks back to the IP and requiring them to be loosely compatible with the IP. Extrapolated muons are mainly used for providing acceptance in the region $2.5 < |\eta| < 2.7$, which is beyond the coverage provided by the ID.

After resolving the overlaps between the different muon types, the muon objects used for physics analysis are subject to a momentum calibration using data from $J/\Psi \rightarrow \mu\mu$ and $Z \rightarrow \mu\mu$ decays [224].

Identification of muons is performed using quality requirements designed to suppress non-prompt muons originating from pion and kaon decays while allowing a robust momentum measurement. Muons in this analysis are built using combined and extrapolated muons that satisfy the *Medium* identification requirements [223]. This requires combined muons to have at least three hits in at least two MDT layers—except for the region with $|\eta| < 0.1$, where a single MDT layer is enough, as long as there is no more than one MDT hole layer [224]. Extrapolated muons need to have at least three hits in at least three MDT and CSC layers [224]. In addition, all muons need to have a significance of the ratio of the measured charge and momentum satisfying $\sigma(q/p) < 7$. The identification of muons with the *Medium* identification working point is evaluated in $J/\Psi \rightarrow \mu\mu$ and $Z \rightarrow \mu\mu$ events and yields an efficiency of more than 98% for muons with $p_T > 6$ GeV and $|\eta| < 2.5$ [224]. The light-hadron rejection rate, measured in simulated $t\bar{t}$ events, is roughly 98 for low- p_T muons with $p_T < 20$ GeV, and increases to 830 for muons with $p_T > 100$ GeV [224].

Baseline muons in this analysis need to satisfy $p_T > 6$ GeV and $|\eta| < 2.7$. Furthermore, the longitudinal impact parameter of baseline muons with respect to the primary vertex is required to be $\Delta z_0 \sin \theta < 0.5$ mm. Signal muons additionally need to be within $|\eta| < 2.5$ and have a transverse impact parameter satisfying $d_0/\sigma_{d_0} < 3$. Similar to electrons, muons also need to be isolated, using the same variables used for electron isolation. Both signal and baseline muons need to conform to the *Loose* working point, requiring $p_T^{\text{varcone}20}/p_T < 0.3$ and $E_T^{\text{cone}20} < 0.15$ [224]. The *Loose* isolation working point yields an efficiency quickly increasing from 86% for muons with $5 \text{ GeV} < p_T < 20 \text{ GeV}$ to 97% for muons with $20 \text{ GeV} < p_T < 100 \text{ GeV}$. Muons with $p_T > 100$ GeV have an isolation efficiency of more than 99% [224]. The rejection rate for muons from HF decays ranges from 14 to 8 with increasing p_T in the range relevant for the 1ℓ search [224].

4.4.4 Jets

Jets are reconstructed using the anti- k_t algorithm [225] implemented in the FASTJET [226, 227] package. A radius parameter of $R = 0.4$ is used for all jets considered in the following. The inputs to the anti- k_t algorithm are topo-clusters [228], built at the EM scale using the procedure introduced in section 4.4.2. Tracks with $p_T > 500$ MeV and an association to the primary vertex

are assigned to jets using *ghost association* [229], a method treating them as particles with infinitesimal momentum such that the properties of the calorimeter-based jets are not changed.

Reconstructed jets undergo a jet energy scale (JES) calibration, correcting the four-momentum and scaling the energy and mass [228]. In a first step, energy contributions from in-time and out-of-time pileup are removed using a data-driven jet-by-jet approach based on jet areas and pileup p_T density. Additionally, a residual correction derived from MC simulation is applied, parameterised in the number of mean interactions per bunch crossing and the number of reconstructed primary vertices [228, 229]. The reconstructed jet four-momentum is corrected to the particle-level energy scale through an absolute JES and η calibration. In order to reduce the dependence of the jet response (i.e. the ratio between the measured jet energy and the true jet energy) on the flavour and energy distribution of its constituents, a series of multiplicative corrections is applied [230]. These corrections improve the jet energy resolution (JER) and are based on data from the calorimeters, jet-related tracking information as well as MS information. Differences between the jet response in data and MC simulation, caused by imperfect detector and physics simulations, are corrected using so-called *in situ* calibrations [228]. The jet response in data and MC simulations is measured separately, allowing to derive a correction factor that is applied on data. Similar to the JES, the JER is also calibrated. Its calibration is performed using p_T asymmetry measurements in dijet events [231].

Even after the subtraction of pileup effects, some pileup jets still remain. The jet vertex tagger (JVT) [232], a multivariate discriminant, is used to suppress pileup jets. It is based on variables that describe the fraction of the total jet momentum corresponding to tracks associated to the primary vertex. In the 1ℓ search, jets with $p_T < 120 \text{ GeV}$ and $|\eta| < 2.5$ need to be associated to the primary vertex using the *medium* working point, achieving an average 92% efficiency for jets originating from the hard scatter interaction [228].

Baseline jets in this analysis are required to have $p_T > 20 \text{ GeV}$ and $|\eta| < 4.5$. Analysis variables built using jets use signal-level jets with $p_T > 30 \text{ GeV}$ and $|\eta| < 2.8$.

4.4.5 Flavour tagging

As can be seen through the CKM matrix, b -quarks primarily decay through $b \rightarrow Wc$. However, due to the small coupling constant proportional to the corresponding CKM matrix element V_{cb} (corresponding to the $b \leftrightarrow c$ transition), b -hadrons have relatively long lifetimes of the order of 1.5 ps ($\langle c\tau \rangle \approx 450 \mu\text{m}$) [9]. In the typical momentum ranges, b -hadrons can thus have a measurable flight length before decaying, leading to secondary vertices that are displaced from the hard-scatter vertex. ATLAS uses a collection of algorithms designed to discern HF jets containing b -hadrons from light-flavour jets by exploiting the impact parameters or reconstructing the displaced vertices. A multivariate classifier, called MV2 [233], combines the outputs of the different taggers using a boosted decision tree (BDT) algorithm that is trained on simulated $t\bar{t} + Z'$ events.

Due to the Higgs decay $h \rightarrow b\bar{b}$ in the signal model targeted, b -jets play a crucial role in the analysis. Baseline jets with $|\eta| < 2.5$ are used as input to the MV2c10 b -tagging algorithm, an implementation of the MV2 discriminant using a c -jet fraction of 7% during the BDT training [234, 235]. The working point chosen for the MV2c10 tagger achieves a b -tagging

efficiency of 77% with a rejection rates of 4.9, 15, and 110 for c -jets, τ -jets and light-flavour jets, respectively, measured in simulated $t\bar{t}$ events [234].

4.4.6 Missing transverse momentum

Momentum conservation in the transverse plane implies that the sum of the transverse momenta of all objects in a pp collision should vanish. Particles escaping the detector without being measured thus lead to a momentum imbalance, in the following referred to as missing transverse momentum $\mathbf{p}_T^{\text{miss}}$ with magnitude E_T^{miss} . The missing transverse momentum in each event is computed using all reconstructed objects and takes into account tracks associated to the primary vertex but not used for any reconstructed objects [236], yielding

$$\mathbf{p}_T^{\text{miss}} = - \sum \mathbf{p}_T^e - \sum \mathbf{p}_T^\gamma - \sum \mathbf{p}_T^\mu - \sum \mathbf{p}_T^{\text{jet}} - \sum \mathbf{p}_T^{\text{track}}. \quad (4.1)$$

While terms originating from the reconstructed, calibrated objects are collectively referred to as the *hard term*, the remaining track term is referred to as *soft term*. As τ -leptons are not explicitly reconstructed in this analysis, no corresponding term is included in eq. (4.1). Hadronic decays of τ -leptons are, however, included in the jet term as they are generally reconstructed as jets. The computation of E_T^{miss} uses all baseline objects introduced in the previous sections. Ambiguities between objects are resolved using an overlap removal procedure [236] that is separate and independent from the procedure described in section 4.5. In order to reduce effects from pileup, the E_T^{miss} is computed using the *Tight* working point described in Ref. [237], excluding forward jets with $|\eta| > 2.4$ and $p_T < 30 \text{ GeV}$.

Events without any true E_T^{miss} can have non-zero reconstructed E_T^{miss} due to residual pileup effects, object mismeasurements or particles escaping through uninstrumentalised regions of the detector. Such *fake* E_T^{miss} allows events without any real E_T^{miss} (e.g. $Z(\rightarrow ee) + \text{jets}$) to pass the event selection criteria and end up in the kinematic regions of interest, even after requiring a certain threshold value of E_T^{miss} .

4.5 Overlap removal

As the reconstruction procedure runs independently for each object type, it may happen that the same tracks or energy deposits in the calorimeters are used for the reconstruction of two different objects. For example, electrons tend to cluster as well as jets and are therefore often also reconstructed as electron-seeded jets [238]. In order to resolve ambiguities and prevent double-counting, an overlap removal procedure using the distance parameter $\Delta R_y = \sqrt{(\Delta y)^2 + (\Delta \phi)^2}$ is performed. The procedure sequentially runs the following steps on baseline objects, with only surviving objects participating in subsequent steps:

1. Electrons sharing an ID track with a muon are removed, preventing duplication of muons as electrons via bremsstrahlung with subsequent photon conversion [238].
2. Jets within $\Delta R_y < 0.2$ of an electron are rejected, preventing the pure duplication of electrons as electron-seeded jets [238].

Table 4.2: Overview of the object definitions used in the analysis.

Property	Baseline type	Signal type
Electrons		
Kinematic	$p_T > 7 \text{ GeV}, \eta < 2.47$	$p_T > 7 \text{ GeV}, \eta < 2.47$
Identification	<i>LooseAndBLayer</i> [222]	<i>Tight</i> [222]
Impact parameters	$\Delta z_0 \sin \theta < 0.5 \text{ mm}$	$\Delta z_0 \sin \theta < 0.5 \text{ mm}, d_0/\sigma_{d_0} < 5$
Isolation	–	<i>Loose</i> [220] ($p_T \leq 200 \text{ GeV}$) <i>HighPtCaloOnly</i> [220] ($p_T > 200 \text{ GeV}$)
Muons		
Kinematic	$p_T > 6 \text{ GeV}, \eta < 2.7$	$p_T > 6 \text{ GeV}, \eta < 2.5$
Identification	<i>Medium</i> [223]	<i>Medium</i> [223]
Impact parameters	$\Delta z_0 \sin \theta < 0.5 \text{ mm}$	$\Delta z_0 \sin \theta < 0.5 \text{ mm}, d_0/\sigma_{d_0} < 3$
Isolation	–	<i>Loose</i> [224]
Jets		
Kinematic	$p_T > 20 \text{ GeV}, \eta < 4.5$	$p_T > 30 \text{ GeV}, \eta < 2.8$
JVT	–	<i>Medium</i> [228], $p_T < 120 \text{ GeV}, \eta < 2.5$
<i>b</i> -jets		
Kinematic	$p_T > 20 \text{ GeV}, \eta < 4.5$	$p_T > 30 \text{ GeV}, \eta < 2.5$
JVT	–	<i>Medium</i> [228], $p_T < 120 \text{ GeV}, \eta < 2.5$
<i>b</i> -tagging	–	<i>MV2c10</i> [234] with 77% efficiency

3. Electrons overlapping with remaining jets within $\Delta R_y = \min(0.4, 0.04 + 10 \text{ GeV}/p_T)$ are removed, resolving the regime where hadronic jets lose a fraction of their energy to electron-seeded jets [238]. The shrinking cone size avoids unnecessary rejection of electrons originating from decays of boosted particles together with jets.
4. Jets with less than three associated tracks, within $\Delta R_y < 0.2$ of a muon or where the muon has been matched to the jet through ghost association [239] are removed. This resolves for example scenarios where a muon is reconstructed as a jet due to bremsstrahlung or FSR with subsequent photon conversion reconstructed both as electron and jet [238].
5. Muons overlapping with a remaining jet are removed. The same shrinking cone size as for electrons is used. This predominantly removes non-prompt muons produced in light meson or HF decays together with jets [238].

4.6 Analysis variables

In order to separate supersymmetric signal events from SM processes, it is necessary to apply requirements on different discriminating observables, creating so-called *signal regions* enriched in signal events. In addition, these variables are also used to construct regions enriched in SM background events, in the following used to derive a reliable background estimate for the signal regions. The distributions of all discriminating variables obtained from MC simulation are illustrated in fig. 4.3, comparing signal and SM background distributions. Both are normalised

to unity in order to highlight their differences in shape. Most observables show a dependence on the absolute mass scale of the supersymmetric particles, as well as the mass difference between $\tilde{\chi}_1^\pm/\tilde{\chi}_2^0$ and $\tilde{\chi}_1^0$, resulting in different shapes for different signal points.

Number of jets

The simplified model depicted in fig. 4.1 features two b -jets in the final state, originating from the decay of the Higgs boson. In the following, all events are thus required to have exactly two b -jets in the final state, significantly reducing contributions from e.g. $W + \text{jets}$ processes that have a relatively low probability of producing two b -jets. In order to avoid rejecting signal events with ISR or FSR (as e.g. in fig. 2.8), a third, light-flavour jet is allowed in the final state.

Invariant mass of the b -tagged jets

The invariant mass of the two b -jets $m_{b\bar{b}}$ can be defined using the well-known energy-momentum relation,

$$m_{b\bar{b}}^2 = (\mathbf{P}_{b_1} + \mathbf{P}_{b_2})^2 = m_{b_1}^2 + m_{b_2}^2 + 2(E_{b_1}E_{b_2} - \mathbf{p}_{b_1}\cdot\mathbf{p}_{b_2}) \quad (4.2)$$

where \mathbf{P}_{b_1} and \mathbf{P}_{b_2} are the four-vector momenta of the leading and subleading b -jets, respectively. The term *leading* henceforth refers to the object with the largest p_T in its object category. In the high-relativistic limit $E \gg m$, the invariant mass of the two b -jets can be written as

$$m_{b\bar{b}} = \sqrt{2p_T^{b_1}p_T^{b_2}(\cosh \Delta\eta_{bb} - \cos \Delta\phi_{bb})}, \quad (4.3)$$

where $\Delta\eta_{bb}$ and $\Delta\phi_{bb}$ are the differences in pseudorapidity and azimuthal angle between the two b -jets, respectively.

As the two b -jets originate from the Higgs decay $h \rightarrow b\bar{b}$, their measured invariant mass will in general be close to the measured Higgs boson mass of around 125 GeV [9], leading to a peak in the $m_{b\bar{b}}$ distribution. This behaviour is clearly visible in fig. 4.3(d). In most SM background processes relevant to the search, the b -jets do not originate from a Higgs decay, and thus their $m_{b\bar{b}}$ distribution does not exhibit the same peak-like structure. In order to enrich signal events in a selection, all signal regions defined in the following will require events to have a value in $m_{b\bar{b}}$ close to the Higgs boson mass.

Missing transverse energy

The missing transverse energy E_T^{miss} is an observable finding widespread usage in searches for SUSY at the LHC. In SM processes, E_T^{miss} only stems from neutrinos and fake E_T^{miss} arising e.g. from mismeasurements or imperfect detector hermeticity. In the case of the SUSY scenario considered in the following, two LSPs escape the detector, leaving a considerable amount of missing transverse momentum, such that a lower requirement on E_T^{miss} allows to separate signal and background processes. Figure 4.3(c) shows the E_T^{miss} distribution, and illustrates the fact that signal models with high electroweakino masses as well as high sparticle mass differences tend to have the largest E_T^{miss} .

Transverse mass

The transverse mass m_T [240, 241] is one of the most important observables considered in 1ℓ search. It aims to reconstruct the mass of a heavy particle decaying into two daughter particles subject to a co-linear boost in the laboratory transverse plane. In SUSY searches targeting the 1ℓ final state, m_T is commonly used to reconstruct the transverse mass of the W boson decaying into a lepton–neutrino pair, and is therefore defined as

$$m_T = \sqrt{2p_T^\ell E_T^{\text{miss}}(1 - \cos[\Delta\phi(p_T^\ell, p_T^{\text{miss}})]}, \quad (4.4)$$

where p_T^ℓ is the momentum three-vector of the lepton in the event. As events with additional leptons are vetoed, the vast majority of the leptons in background processes stem from leptonic decays of W bosons. In background events where the neutrino from $W \rightarrow \ell\nu$ is the only source of E_T^{miss} , the transverse mass has a theoretical kinematic endpoint at the W boson mass,

$$m_T^{\text{max}} = m_W \approx 80 \text{ GeV}. \quad (4.5)$$

Due to finite detector resolution, mismeasurements or additional E_T^{miss} in the event, background events can sometimes have $m_T > m_W$, leading to a kinematic endpoint at m_W that is not infinitely sharp.

In the signal scenarios considered in the analysis, the LSPs constitute a majority of the E_T^{miss} in an event, which typically leads to a transverse mass distribution that is significantly broader than that of background processes and does not present the same kinematic endpoint. A lower requirement on the transverse mass slightly above the W boson mass thus allows to reject a majority of the SM background events while largely unaffected the signal distribution. As can be seen in fig. 4.3(c), the range of the m_T distribution depends on the scale of the signal mass parameters, with increasing mass differences leading to increasingly broad distributions. For this reason, different signal regions with varying requirements on m_T can be constructed, targeting different kinematic regimes in the signal grid. The optimisation of multiple signal regions will be discussed in chapter 5.

Contransverse mass

The contransverse mass m_{CT} [242] is designed to have a kinematic endpoint for events with pair-produced heavy particles decaying into invisible and visible particles subject to a contra-linear boost. In the following, m_{CT} is defined as

$$m_{\text{CT}} = \sqrt{2p_T^{b_1} p_T^{b_2}(1 + \cos \Delta\phi_{bb})}, \quad (4.6)$$

where $p_T^{b_1}$ and $p_T^{b_2}$ are the transverse momenta of the two b -jets in the final state. Although m_{CT} is invariant under co-linear boosts in the beam direction[†], it is not invariant under transverse boosts, e.g. due to ISR jets, such that m_{CT} as well as its kinematic endpoint depend on both the size and direction of the transverse boost. For this reason, a boost-corrected version of the contransverse mass is used in the following. The correction algorithm is described in detail in Ref. [243] and uses an estimate of the energy of the upstream pair-produced heavy particles to

[†] This is by construction the case, as only transverse quantities are used to compute m_{CT} .

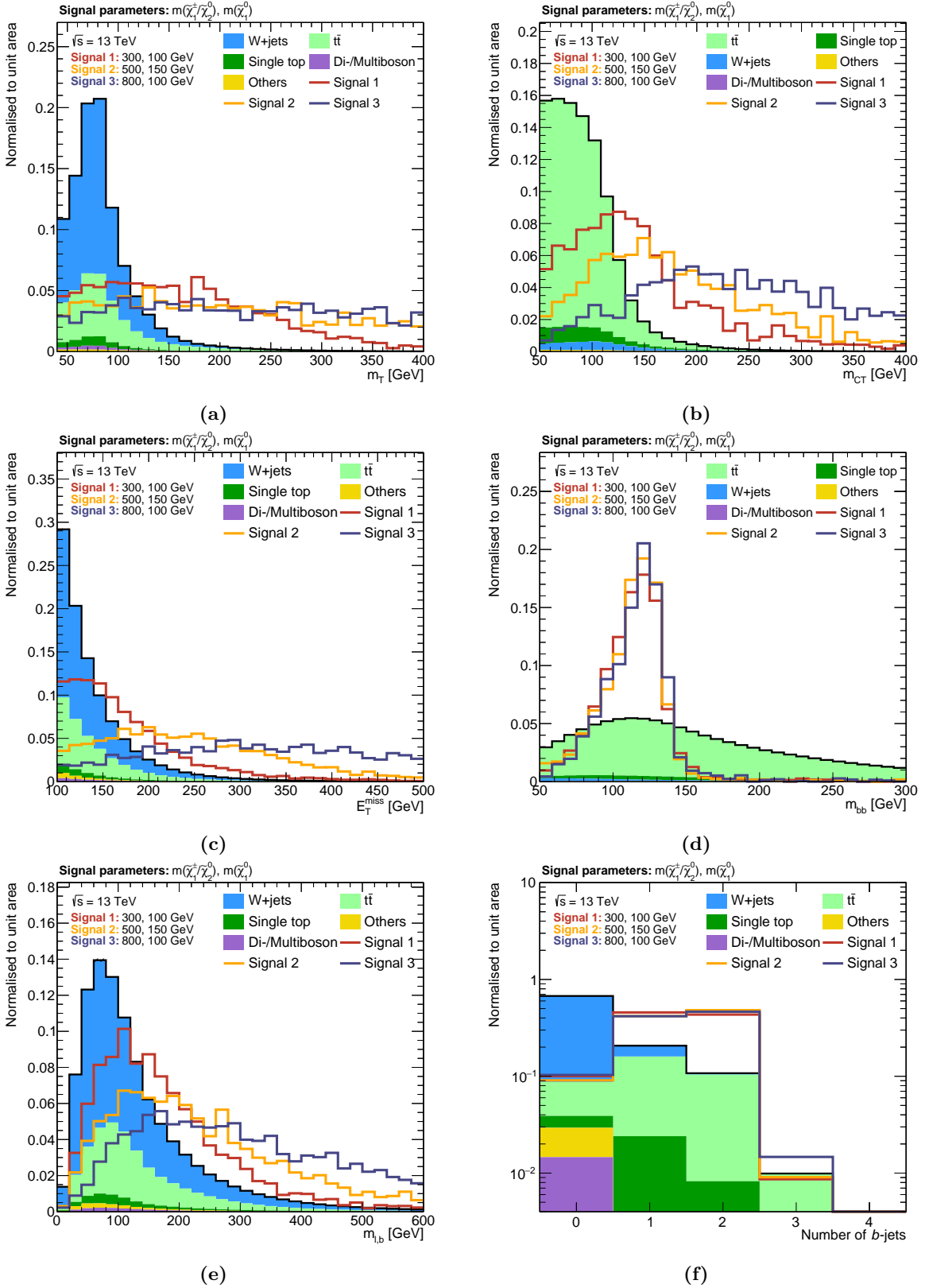


Figure 4.3: Distributions of the most important observables used in the analysis. The simulated SM backgrounds are stacked on top of each other, and distributions from exemplary signal models with the quoted mass parameters are overlaid. In order to emphasise the shape differences, both background and signal distributions are normalised to unity. A preselection of exactly one lepton (signal and baseline), at least two jets and $E_T^{\text{miss}} > 100$ GeV is applied.

boost the four-momenta of the visible decay products back into the centre-of-mass frame of the pair-produced particles. The approach provides a conservative value of m_{CT} that is always smaller than the true m_{CT} value measured in the centre-of-mass frame of the pair-produced particles.

For $t\bar{t}$ events where each top quark decays via $t \rightarrow bW$, the two b -jets used for calculating m_{CT} stem from each of the two decay branches of the $t\bar{t}$ system. It can be shown [243] that, in this case, the boost-corrected contransverse mass has a kinematic endpoint at

$$m_{\text{CT}}^{\max} = \frac{m^2(t) - m^2(W)}{m(t)} \approx 135 \text{ GeV}. \quad (4.7)$$

In signal events, the two input b -jets originate from the same Higgs boson, and thus m_{CT} does not exhibit a kinematic endpoint, but tends to yield higher values. Figure 4.3(b) clearly illustrates the kinematic endpoint for $t\bar{t}$ backgrounds and further shows that signal distributions result in higher values depending on their mass parameter scales. Similar as for the transverse mass, varying lower bounds on m_{CT} will be used in chapter 5 to define signal regions optimised to different kinematic regimes.

Invariant mass of the lepton and leading b -jet

The invariant mass of the lepton and the leading b -jet, $m_{\ell b_1}$, is designed to offer high rejection power towards $t\bar{t}$ and single top processes. In events where the lepton and leading b -jet originate from the same top quark decay $t \rightarrow bW \rightarrow b\ell\nu$, the $m_{\ell b_1}$ distribution has a kinematic endpoint at

$$m_{\ell b_1}^{\max} = \sqrt{m^2(t) - m^2(W)} \approx 153 \text{ GeV} \quad (4.8)$$

In signal events, the lepton and leading b -jet originate from the decay chains of the $\tilde{\chi}_1^\pm$ and $\tilde{\chi}_2^0$, respectively and thus the $m_{\ell b_1}$ distribution depends on the mass scale of the SUSY particles, yielding especially good discriminative power for signal scenarios with high $\tilde{\chi}_1^\pm/\tilde{\chi}_2^0$ masses.

4.7 Trigger strategy

The trigger strategy of an analysis is crucial to select pp events worth investigating, and typically relies on triggers sensitive to physics objects that are important to the signal scenarios considered. The data used in this analysis have been recorded with $E_{\text{T}}^{\text{miss}}$ triggers. Selecting events with invisible particles is inherently difficult precisely because these particles do not leave a trace in the detector. Like offline analysis, the trigger algorithms thus need to infer the $E_{\text{T}}^{\text{miss}}$ from the momenta of the visible particles, all the while having to satisfy the stringent event rate constraints set by the high-luminosity environment of the LHC.

As described in section 2.2.7, the L1 trigger uses only parts of the instrumented regions, a technique that is not well suited for momentum imbalance triggers that rely on a sum of momenta over the full solid angle [244]. In the L1 trigger, dedicated hardware sums the signals from calorimeter cells into *towers* with a granularity matching that of the calorimeter. Towers of calorimeter cells exceeding a certain threshold are used to generate larger towers with coarser granularity, the x and y projections of which are subsequently summed to get an estimate of

E_T^{miss} in the event. The tower thresholds are varied such that stable trigger rates are provided during the different data-taking periods. The L1 triggers used in this analysis employed a threshold of $E_T^{\text{miss}} > 50 \text{ GeV}$, before feeding passing events to the HLT for further analysis.

Two different types of E_T^{miss} triggers are used by the HLT, one based on jets (**mht** algorithm), and one implementing local pile-up suppression (**pufit** algorithm). As hadronic jets dominate the visible momentum in most interesting events, using them for E_T^{miss} computation and triggering is well-motivated [244]. The **mht** algorithm was used during the 2015–2016 data taking period and computes the E_T^{miss} from the negative vectorial sum of the transverse momenta of all jets with a transverse momentum $p_T > 7 \text{ GeV}$ before calibration [244]. The HLT jets are reconstructed and calibrated using a similar procedure as for offline analysis, and are thus corrected for pile-up effects [245]. The **pufit** algorithm was used during the 2017–2018 data taking period and takes as input topo clusters formed using the method described in section 4.4.2. The clusters are subsequently combined into η - ϕ patches of approximately jet size and corrected for pile-up effects based on the distribution of the energy deposits in the calorimeter. The **pufit** algorithm assumes that high E_T deposits stem from the hard-scatter events, while low E_T deposits originate mostly from pile-up effects [244]. The online E_T^{miss} threshold used increased from 70 GeV to 110 GeV in order to keep the trigger rate more or less stable under the rising instant luminosities during the different data-taking periods.

Since the online reconstruction techniques used by the triggers are slightly different to those used in offline physics analysis, the performance of triggers is in general not a simple step function but consists a so-called *turn-on curve* with rising efficiency, followed by a *plateau region* with constant efficiency. In order to achieve the same trigger selection in MC as in data, the MC events are each assigned a random run number that are distributed according to the respective integrated luminosities of each data taking period. Using the run numbers, the same triggers used for data-taking during each run can be applied for MC events.

Figure 4.4 shows the combined E_T^{miss} trigger efficiencies for the electron and muon channels separately. In the following, an offline requirement of $E_T^{\text{miss}} > 240 \text{ GeV}$ is applied for all analysis regions, selecting events where the E_T^{miss} triggers are fully efficient and no significant difference between MC and data is observed. Thus, no trigger efficiency correction is considered in the following. A statistical uncertainty of 2% is used to account for the difference between data and MC in the trigger plateaus.

4.8 Event cleaning

Before being considered for analysis, events need to pass a series of quality requirements. Data events need to be certified to be good for physics analysis by the ATLAS data quality system [246], requiring that no transient detector issues have compromised the quality of the data events recorded. Losses in data quality could happen due to e.g. high-voltage trips in detector components or noise bursts in the detector electronics [246]. Only data events are considered where all detector components were flagged as being operational, a process that is performed at the granularity of a *luminosity block*—a time period of roughly 60 s of data-taking where the instantaneous luminosity, detector and trigger configuration are considered to be constant.

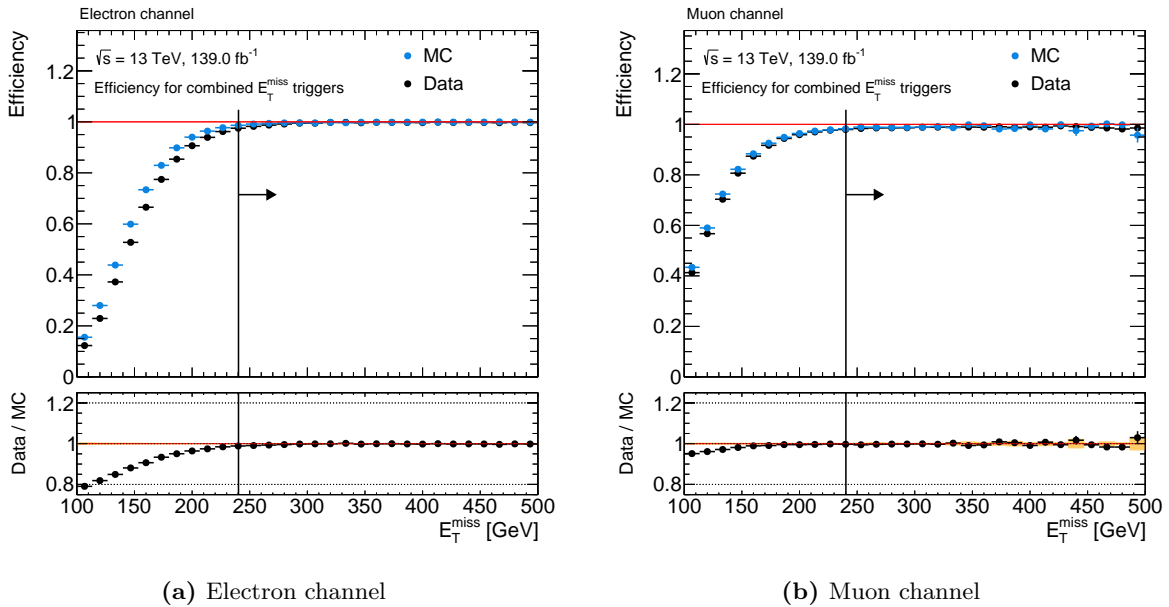


Figure 4.4: Efficiencies of the combined E_T^{miss} triggers in data and MC events, triggered by single lepton triggers in the (a) electron and (b) muon channels. A preselection requiring exactly one lepton (baseline and signal), at least two jets, and $E_T^{\text{miss}} > 100$ GeV is applied on all events. The arrow indicates the offline E_T^{miss} requirement applied on all selections in the analysis.

A second series of quality requirements is applied on both data and MC events. To be considered in any subsequent analysis step, events need to have at least one reconstructed primary vertex with a minimum of two tracks with $p_T > 500$ MeV associated to it. Events are discarded where a jet is tagged as originating from a non-collision background process. The `Loose` working point described in Ref. [247] is used to tag such jets, yielding an efficiency of 99.5% for jets from pp collision events with $p_T > 20$ GeV. Similarly, events are rejected if they contain a *bad* muon with a significantly worse than usual momentum resolution that can affect many variables in the entire event and therefore may have sizeable effects on the analysis. In the following, muons are flagged as *bad* if the relative error on the combined q/p measurement is either larger than 0.2 or worse than the one from the individual ID and MS track fits. Events are also rejected if a reconstructed muon is flagged to originate from cosmic radiation, using thresholds on the transverse and longitudinal impact parameters of $d_0 > 0.2$ mm and $z_0 > 1$ mm with respect to the primary vertex.

Chapter 5

Signal region optimisation

In order to discover the rare SUSY signals considered in the following, dedicated kinematic regions enriched in signal events, so called signal regions (SRs) are constructed. They are optimised such as to be sensitive to a maximum number of signal models considered in the analysis. In this chapter, the optimisation procedures leading to the final signal regions are introduced and discussed.

5.1 Optimisation methods

All optimisation methods used in the following require a figure of merit that is maximised in order to find configurations yielding best performance. While the multidimensional cut scan and the $N - 1$ plots approach introduced in sections 5.1.1 and 5.1.2, respectively, use the binomial discovery significance Z_B , the fit scan procedure discussed in section 5.1.3 aims to maximise the area of the expected exclusion contour.

5.1.1 Multidimensional cut scan

The first optimisation method used for designing the SRs is an N -dimensional cut[†] scan using N observables. For each unique combination of requirements on the set of observables considered, the expected signal and background rate as well as the statistical uncertainty on the background rate is determined from the MC simulated events. As this takes a considerable computational effort, it is crucial to restrict the amount of cut combinations to be tested. By comparing with distributions at preselection level, as for example those shown in fig. 4.3, a set of discrete cuts can be defined for each observable. In practice, a total number of $\mathcal{O}(10^7\text{--}10^8)$ cut combinations can still be tested on a single machine with a reasonable turnaround time.

After determining the expected event rates and statistical uncertainties, the different cut combinations are binned into a predefined number of signal efficiency bins. For each bin, the background rejection is subsequently maximised, i.e. the cut combination with the highest background rejection is chosen as a candidate combination for the respective signal efficiency bin.

[†] In the following, the term *cut* refers to a simple upper or lower requirement on kinematic observables like e.g. requiring $m_T > 100 \text{ GeV}$.

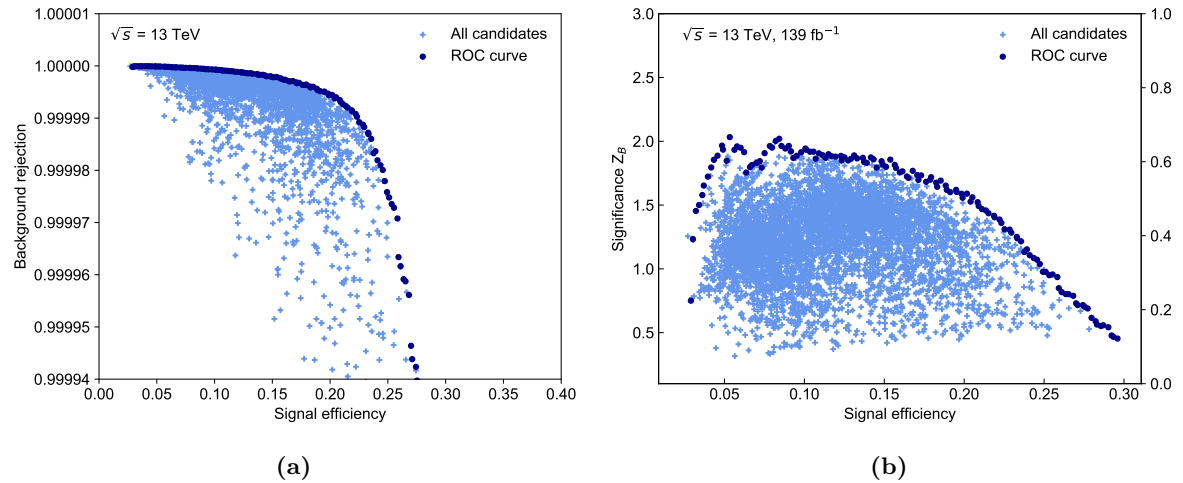


Figure 5.1: Small N -dimensional cut scan using 10^4 unique cut combinations, illustrating the approach of (a) generating a receiver operating characteristic (ROC) curve from the scanned cut combinations in order to (b) reduce the number of candidates used in computationally expensive significance calculations. The cut combination candidates forming the ROC curve (dark blue) also maximise the discovery significance. In (b), the significance Z_B includes the MC statistical uncertainty on the expected background rate as well as 30% flat systematic uncertainty.

The assumption is that, for a fixed signal efficiency, the cut combination candidate maximising the background rejection also maximises the discovery significance Z_B . With the significance definition used herein, this is in general a valid assumption, as the significance tends to monotonically increase with decreasing background rate, even while the statistical uncertainty on the background estimation increases due to tighter requirements and less available MC statistics (cf. fig. 5.1). This procedure effectively generates a ROC curve, that can be used to perform more computationally intensive calculations, as e.g. calculating different variations of the discovery significance. The approach is illustrated in a small scan using 10^4 cut combinations in fig. 5.1. The cut combination candidates maximising the background rejection and thus lying on the ROC curve in fig. 5.1(a) are the same candidates that maximise the discovery significance in fig. 5.1(b).

A common problem of N -dimensional scans is the concept of *overtightening* the selections given the available MC statistics. Since the cross sections of the SUSY process considered are many orders of magnitude smaller than those of the dominant SM processes, it is often necessary to apply tight requirements on the kinematic observables in order to achieve a significant signal-to-background separation. However, due to the finite amount of MC statistics available, many of the more extreme cut combinations select kinematic regions where not enough MC statistics are available for a reasonable estimation of the background rates. Thus, by maximising the background rejection, it may occur that cut combinations are selected where the mere lack of MC statistics, needed to properly estimate the background rates, causes a high significance value. As the significance values obtained for such configurations are obviously not trustworthy, they need to be avoided.

In the N -dimensional cut scan implementation used herein, the available MC datasets are split in two statistically independent, equally sized subsets. Although resulting in an additional dilution

of the available MC statistics, this approach allows to generate two independent ROC curves and to compute two independent values for the discovery significance for each cut combination candidate. A large difference in either the ROC curves or the significance values is an indication for statistical fluctuations as a result of overtightened cuts. In addition, requirements on the minimum number of unweighted MC events for different background processes, as well as the maximum allowed statistical uncertainty on a given process, can be applied. In combination, these precautions offer a good handle against statistical fluctuations. In the following, the N -dimensional cut scan implementation provided by AHOI [248] is used.

5.1.2 $N - 1$ plots

Instead of performing a brute-force scan of a large set of cut combinations, a more manual approach, using iterative one-dimensional scans can be employed. In so-called ‘ $N - 1$ plots’, the kinematic distributions of the background components as well as exemplary signal processes are plotted in conjunction with the significance achieved by applying a cut on each value on the x -axis of the one-dimensional distribution plotted. All other selection requirements, except the one on the observable plotted, are applied. This method allows to investigate the impact of a single kinematic requirement on the overall significance value. By repeatedly executing this process for each observable considered, it is possible to iteratively approach a cut combination yielding results comparable to that of a brute-force cut scan. Especially when considering a sizeable set of observables, this manual approach however quickly becomes very cumbersome and inefficient, and risks missing optimal cut combinations that would have been found by a brute-force approach.

For this reason, the following optimisation uses an N -dimensional cut scan to cover the full space spanned by the observables and scan ranges considered, while $N - 1$ plots are used to verify and fine-tune results obtained by the brute-force approach.

5.1.3 Scans using asymptotic formulae

The last of the optimisation methods used in the following relies on scans over sets of simplified fit setups in order to run a simplified version of the full statistical inference machinery on a large number of signal region candidates. While the preceding optimisation methods rely on the binomial significance computed in independent cut-and-count signal regions, the simplified fit scans statistically combine disjunct signal regions by building a single likelihood, and compute the p -values using the asymptotic formulae introduced in chapter 3. In addition, the simplified fits use all available signal points instead of relying on a limited set of benchmark points, and can thus derive an estimate of the expected exclusion contour for a large number of signal region candidates. The estimation of the background event rates in the signal regions is taken from MC simulation only and considers a flat systematic uncertainty of 30% on the estimated event rate, correlated over all signal region bins. Statistical uncertainties on the background estimate from limited MC statistics are also taken into account.

As building the likelihood and executing the statistical inference takes a considerable computational effort, this method benefits from the previous optimisation steps defining promising signal region candidates worth scanning over. In order to keep the number of configurations to be tested at a manageable level, the signal region candidates obtained from the previous

Table 5.1: List of observables and cut ranges used in the N -dimensional cut scan. All cuts are optional and allowed not to be applied at all.

Observable	Cut values
E_T^{miss} [GeV]	$>$ $\in \{200, 220, 240, 260, 280, 300, 320, 340\}$
E_T^{miss} significance \mathcal{S}	$>$ $\in \{5, 10, 15\}$
m_T [GeV]	$>$ $\in \{100, 120, 140, 160, 180, 200, 220, 240, 260, 280, 300\}$
m_{CT} [GeV]	$>$ $\in \{100, 120, 140, 160, 180, 200, 220, 240, 260, 280, 300\}$
$m_{b\bar{b}}$ lower [GeV]	$>$ $\in \{85, 90, 95, 100, 105, 110, 115\}$
$m_{b\bar{b}}$ upper [GeV]	$<$ $\in \{130, 135, 140, 145, 150\}$
p_T^ℓ [GeV]	$>$ $\in \{20, 40, 60, 80\}$
$p_T^{\text{jet}1}$ [GeV]	$>$ $\in \{50, 100, 150\}$
$p_T^{\text{jet}2}$ [GeV]	$>$ $\in \{50, 75, 100\}$
ΔR_{jj}	$<$ $\in \{0.8, 1.0, 1.2, 2.0\}$
$\Delta R_{b\bar{b}}$	$<$ $\in \{0.8, 1.0, 1.2, 2.0\}$
N_{jet}	\leq $\in \{2, 3, 4\}$
$\Delta\phi(E_T^{\text{miss}}, p_T^\ell)$ [rad]	$>$ $\in \{0.5, 1.0, 2.0, 2.5\}$

methods are only varied to a limited degree, assuming that they were already close to optimal to begin with.

5.2 Optimisation for the 1ℓ search

The optimisation of the signal regions for the 1ℓ search presented herein benefits from experience past analyses investigating the same simplified model in the same final state [181, 182], and explores new observables and signal region configurations optimised for the integrated luminosity of the full Run 2 dataset.

5.2.1 Starting from benchmark signal points

A total of six so-called *benchmark* signal points, each representative for a different part of the model parameter space, are chosen for the first step of the optimisation procedure involving N -dimensional cut scans and $N - 1$ plots. Apart from the variables introduced in section 4.6, a set of additional, potentially discriminative observables are considered in the N -dimensional cut scan[†]:

- Transverse momenta of the two leading jets as well as the lepton ($p_T^{\text{jet}1}, p_T^{\text{jet}2}, p_T^\ell$). Especially for signal models with high mass differences between the electroweakinos, the transverse momenta of the lepton and the jets tend to have higher values than in SM background processes.
- Object-based E_T^{miss} significance \mathcal{S} [249], a quantity designed to quantify how genuine the reconstructed E_T^{miss} in an event is. It is determined through a hypothesis test using a log-likelihood ratio that takes into account the resolution of all objects entering the

[†] These variables will turn out not to be used for the final signal regions and are only introduced here for completeness of the optimisation procedure description.

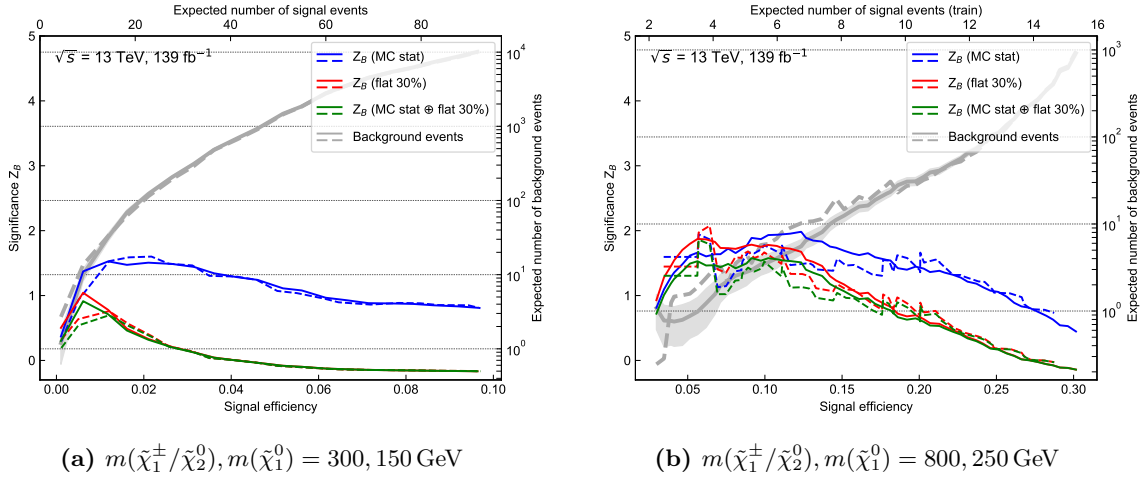


Figure 5.2: Results of the N -dimensional cut scan for two exemplary benchmark points. The binomial discovery significance Z_B is plotted against the signal efficiency for different uncertainty configurations. Additionally, the expected SM background event rates are shown (grey), including their statistical uncertainty for one of the two statistically independent samples (grey shaded area). The solid and dashed lines represent the two statistically independent subsets that the MC samples are split into.

computation of E_T^{miss} . As such, \mathcal{S} offers good discrimination against events with a sizeable fraction of fake E_T^{miss} in the event originating e.g. from jet mismeasurements or the non-hermeticity of the detector. Events with a large share of fake E_T^{miss} accumulate at low values of \mathcal{S} , while events with mostly real E_T^{miss} tend to have large values of \mathcal{S} .

- The distance between the two leading jets ΔR_{jj} as well as the two b -jets ΔR_{bb} . Especially in events with a large mass difference between the electroweakinos, the Higgs can get a significant boost, such that the two b -jets from the Higgs decay tend to be close together in the laboratory frame (and are also the highest- p_T jets in an event), resulting in small values of both ΔR_{jj} and ΔR_{bb} . In SM background processes, however, the two leading (b -)jets often do not originate from the same object and thus tend to be further apart.
- The azimuthal distance between the lepton p_T and the missing transverse momentum, $\Delta\phi(\mathbf{p}_T^\ell, \mathbf{p}_T^{\text{miss}})$. This observable exploits the fact that the lepton and the E_T^{miss} tend to have a more back-to-back configuration in signal events than in many SM processes where the lepton and the neutrino (the latter often responsible for a large part of the E_T^{miss} in an event) often originate from the same W boson decay.

In order to avoid selecting cut combination candidates with overtightened selection criteria compared to the available MC statistics, constraints on the relative statistical uncertainty on the background and on the number of unweighted MC events passing the cut combination candidates are applied. Cut combinations are only considered if they result in less than 50% relative statistical uncertainty on the total background. In addition, all cut combinations need to result in at least five unweighted MC events for each of the three major backgrounds, $t\bar{t}$, single top and $W + \text{jets}$.

The discrete selection possibilities for each of the observables are shown in table 5.1. A preselection of one lepton and exactly two b -jets (and thus at least two jets overall in the event)

Table 5.2: Optimal cut combination for each benchmark signal point obtained with a brute force cut scan and a round of $N - 1$ plots. The parameters of the benchmark points $m(\tilde{\chi}_1^\pm/\tilde{\chi}_2^0)$ and $m(\tilde{\chi}_1^0)$, both given in GeV. The significance is computed for 139 fb^{-1} with the binomial discovery significance Z_B and includes MC statistical uncertainty as well as a flat 30% systematic uncertainty. A dash ‘-’ is used where no requirement on the respective observable is applied.

Observable	(300, 150)	(400, 200)	(600, 300)	(800, 250)	(800, 150)	(800, 0)
$N_{b\text{-jet}}$	2	2	2	2	2	2
N_{jet}	2	2	2 – 3	2 – 3	2 – 3	2 – 3
$m_{b\bar{b}} \text{ [GeV]}$	[105 – 135]	[100 – 140]	[100 – 140]	[95 – 145]	[95 – 145]	[95 – 145]
$E_T^{\text{miss}} \text{ [GeV]}$	> 240	> 240	> 240	> 240	> 240	> 240
$m_{\text{CT}} \text{ [GeV]}$	> 200	> 240	> 260	> 260	> 260	> 280
$m_T \text{ [GeV]}$	> 100	> 120	> 140	> 200	> 240	> 240
$m_{\ell b_1} \text{ [GeV]}$	–	–	> 150	> 120	> 120	> 120
$Z_B [\sigma]$	0.8	1.9	2.1	1.8	2.2	2.3

is always applied. Requirements on the different observables in table 5.1 are optional and do not need to be applied by the optimisation algorithm. The results of the brute-force N -dimensional cut scans for each benchmark signal point can be visualised by plotting the expected discovery significance Z_B against the signal efficiency. Figure 5.2 shows the results of two such cut scans using two of the benchmark signal points. The corresponding plots for the remaining benchmark points are shown in fig. A.1. In these figures, the binomial significance is calculated for different uncertainty configurations for each of the two statistically independent subsets. In addition, the expected background rate is shown for each subset. A cut combination with high achieved significance can be chosen, while avoiding statistical fluctuations and overtightening. The cut combinations chosen for each benchmark point, after a round of $N - 1$ plots, are shown in table 5.2. The $N - 1$ plots, shown in figs. A.2 to A.7, are used to validate and fine-tune the cut values obtained through the cut scan and allow to identify and remove cuts on observables that do not contribute significantly to the achieved Z_B value. From the 12 observables initially considered, only six (excluding the b -jet multiplicity technically not part of the scan) are part of the optimised cut combination candidates. The remaining observables turned out not to significantly improve the sensitivity and are therefore dropped in the following.

5.2.2 Towards final signal regions

The optimal cut combinations obtained for the benchmark signal points, shown in table 5.2, need to be consolidated into a finite set of signal region. From table 5.2, it can be concluded, that all benchmark points favour a common baseline selection including exactly two b -jets, possibly one additional light jet, a Higgs mass window requirement of roughly $m_{b\bar{b}} \in [100, 140] \text{ GeV}$, and $E_T^{\text{miss}} > 240 \text{ GeV}$. The remaining requirements on m_T , m_{CT} and $m_{\ell b_1}$ are however not easily consolidated into a single signal region, as they vastly differ depending on the model parameter space and kinematic regime represented by each benchmark point.

From the normalised distributions in fig. 4.3, it can already be seen that signal points from different kinematic regimes in the parameter space would in principle prefer different requirements on all three of these observables. Designing a single signal region that achieves optimal

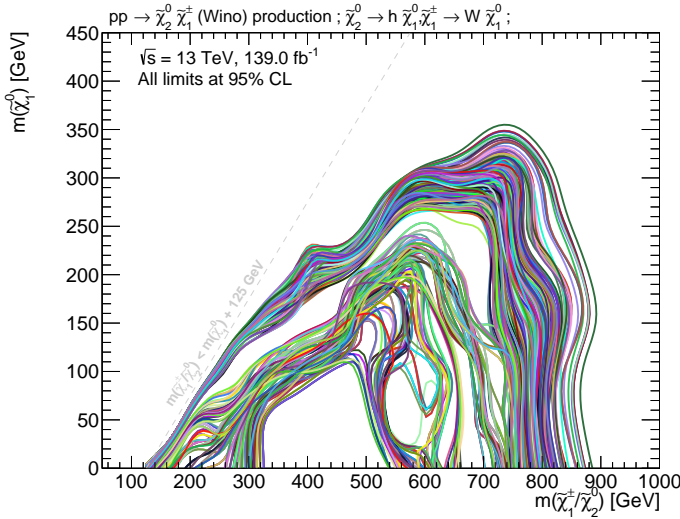


Figure 5.3: Expected exclusion contours obtained from a subset of the signal region candidates. The background estimation is taken directly from MC and includes MC statistical uncertainty as well as an uncorrelated shape uncertainty of 30%. For the sake of visibility, only the nominal contours are shown (without uncertainty bands). Configurations resulting in multiple, disjoint patches of excluded areas are rejected.

sensitivity to the entire parameter space studied, is thus not possible. Instead, a more generalised configuration is chosen, defining multiple signal region bins orthogonal to each other through their requirement on m_T and the m_{CT} . Being mutually exclusive, such signal region bins can be statistically combined in a single likelihood, effectively creating a two-dimensional shape-fit in these observables as the different signal region bins can be fit simultaneously. Such a shape-fit configuration allows to exploit the differences in shape between signal and background distributions, and is able to accommodate the varying shapes of signal points from different regions in the parameter space, making it an ideal statistical tool to cover a wide range of kinematic regimes.

The optimal number of bins as well as values of the individual bin edges in both distributions depends on the available MC statistics and is determined using the simplified fit scans introduced in section 5.1.3. The MC statistical uncertainty as well as a systematic uncertainty of 30%, correlated over all bins, is considered in each scanned configuration. The number of bins are varied in each direction (m_T and m_{CT}) between two and five and different bin edges, varying within ranges determined by the optimal cut values obtained for the benchmark points, are tested. As configurations with more bins could, in some circumstances, potentially benefit from the additional MC statistics resulting from looser selection criteria on the remaining variables, the previously consolidated baseline selection is also allowed to vary to some extent. Finally, although not expected to yield better performance, configurations with multiple orthogonal SR bins in the E_T^{miss} or $m_{b\bar{b}}$ are also included in the scan. A subset of the investigated candidates are shown in fig. 5.3, only showing the nominal expected exclusion limit at 95% without uncertainty bands. Configurations with multiple, disjoint patches of excluded areas in the parameter space are discarded, as they typically result from high statistical fluctuations.

As expected from table 5.2, the best performing configurations define multiple signal region bins in the m_T and m_{CT} distributions, while keeping a constant baseline selection on the remaining observables. Figure 5.4(a) shows a comparison of the expected exclusion contour for exemplary two-dimensional shape-fit configurations, using signal regions binned in (m_T, E_T^{miss}) , $(m_T, m_{b\bar{b}})$ or (m_T, m_{CT}) . The setup using a two-dimensional shape-fit in m_T and m_{CT} clearly maximises the expected excluded area. In addition, this configuration also leads to optimal sensitivity within the expected limit, as is illustrated in fig. A.8(a). Finally, applying a requirement on

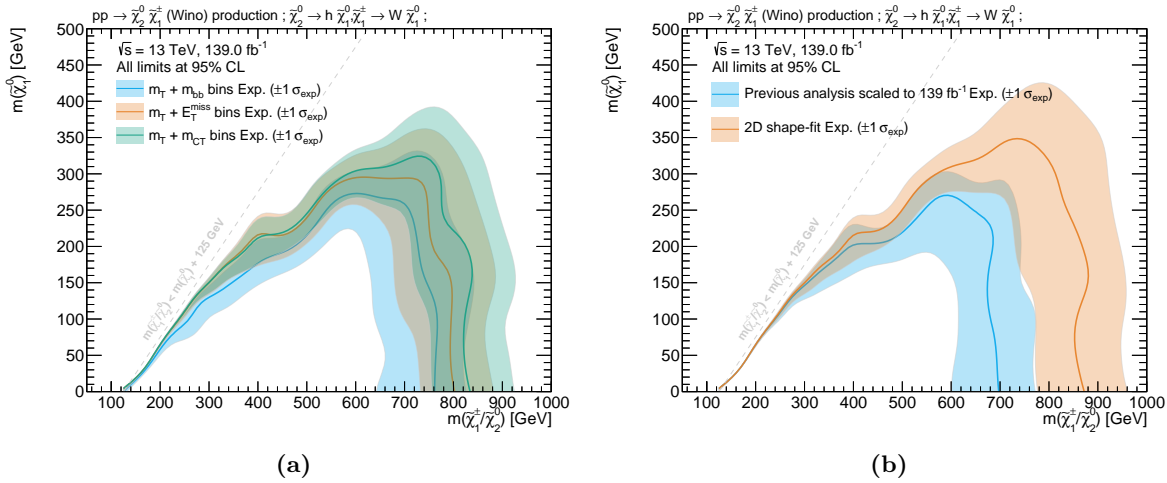


Figure 5.4: Comparison of different shape-fit configurations. Fig. (a) compares three different two-dimensional shape-fit configurations using 3×3 bins in (m_T, E_T^{miss}) , (m_T, m_{bb}) and (m_T, m_{CT}) . Fig. (b) compares the two-dimensional shape-fit in m_T and m_{CT} to the previous analysis iteration signal regions scaled to 139 fb^{-1} . All shown exclusion limits are expected limits at 95% CL, using MC statistical and 30% systematic uncertainty.

high values of $m_{\ell b_1}$ in the highest m_T bins has been shown (cf. fig. A.8(b)) to significantly improve sensitivity to signal models with high mass differences.

In fig. 5.4(b), the fully optimised two-dimensional shape-fit configuration is compared with the signal regions of the previous iteration of the search [182], scaled up to the integrated luminosity of the full Run 2 dataset. It can be seen that a significant improvement in sensitivity can be achieved through the introduction of the two-dimensional shape-fit strategy.

5.3 Signal region definitions

An overview of the final signal region definitions is provided in table 5.3. Based on the previously discussed results, three signal regions bins in m_T are defined, optimised for the low (SR-LM), medium (SR-MM), and high (SR-HM) mass difference regimes. While SR-LM targets the smallest values of m_T , SR-MM and SR-HM target progressively increasing values of m_T . All three signal regions are further divided into three m_{CT} bins each, resulting in a total of nine disjoint SR bins. The signal region with the highest requirement on m_T (SR-HM) also requires $m_{\ell b_1} > 120 \text{ GeV}$, for the reason explained previously. All three SRs otherwise share a common set of requirements on the number of jets, E_T^{miss} and m_{bb} . As shape-fits are by construction highly model-dependent[†], these SRs will be used for deriving model-dependent limits in the case where no significant excess compared to the expected SM background rate is seen in data. For this reason, the shape-fit regions will be referred to as *exclusion* regions in the following. A graphical representation of the nine exclusion signal region bins is shown in fig. 5.5. The kinematic distributions in each SR-LM, SR-MM and SR-HM are shown as $N - 1$ plots in figs. 5.6 to 5.8.

[†] The signal shapes need to be known in order to estimate the expected signal rates in multiple, disjoint signal region bins.

Table 5.3: Overview of the selection criteria for the signal regions. Exclusion SRs ('excl.') are defined for model-dependent limits, and discovery SRs ('disc.') are defined for model-independent upper limits. A dash '-' is used where no requirement on the respective observable is applied.

	SR-LM	SR-MM	SR-HM
N_{lepton}		$= 1$	
p_T^ℓ [GeV]		$> 7(6)$ for $e(\mu)$	
N_{jet}		$= 2$ or 3	
$N_{b\text{-jet}}$		$= 2$	
E_T^{miss} [GeV]		> 240	
$m_{b\bar{b}}$ [GeV]		$\in [100, 140]$	
$m(\ell, b_1)$ [GeV]	$-$	$-$	> 120
m_T [GeV] (excl.)	$\in [100, 160]$	$\in [160, 240]$	> 240
m_{CT} [GeV] (excl.)	$\{ \in [180, 230], \in [230, 280], > 280 \}$		
m_T [GeV] (disc.)	> 100	> 160	> 240
m_{CT} [GeV] (disc.)		> 180	

For evaluating a potential excess in data compared to the expected background rate, a second set of signal regions is derived from the optimised shape-fit setup. For each of the three bins in the transverse mass (SR-LM, SR-MM, and SR-HM), the three m_{CT} bins are summed up and the upper bound on m_T is removed (if present). This results in three cut-and-count signal regions that make minimal model assumptions and can be interpreted in any BSM model, as long as the expected signal rates are known. In case no significant excess over the SM expectation is seen in data, these so-called *discovery* SRs can be used to derive model-independent upper limits on the visible cross section of BSM processes.

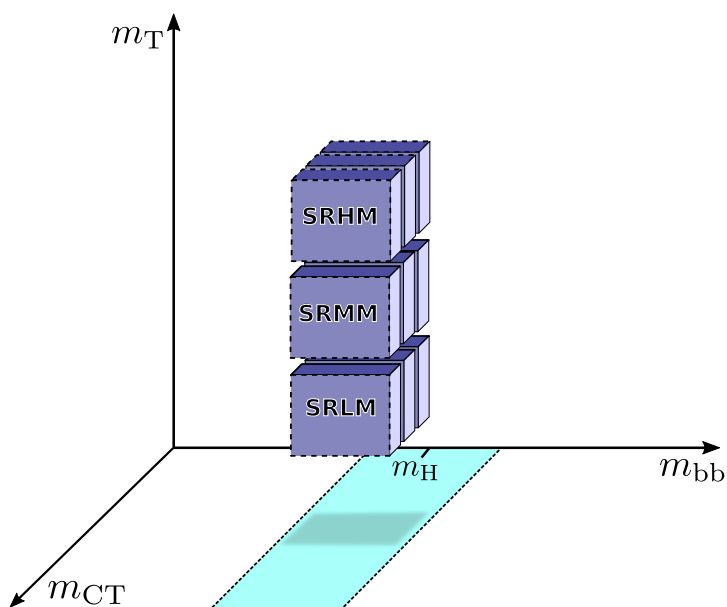


Figure 5.5: Configuration of the exclusion signal regions. Nine signal region bins are defined on m_T and m_{CT} within the Higgs mass window. All signal regions can be statistically combined using a single likelihood, effectively resulting in a two-dimensional shape-fit.

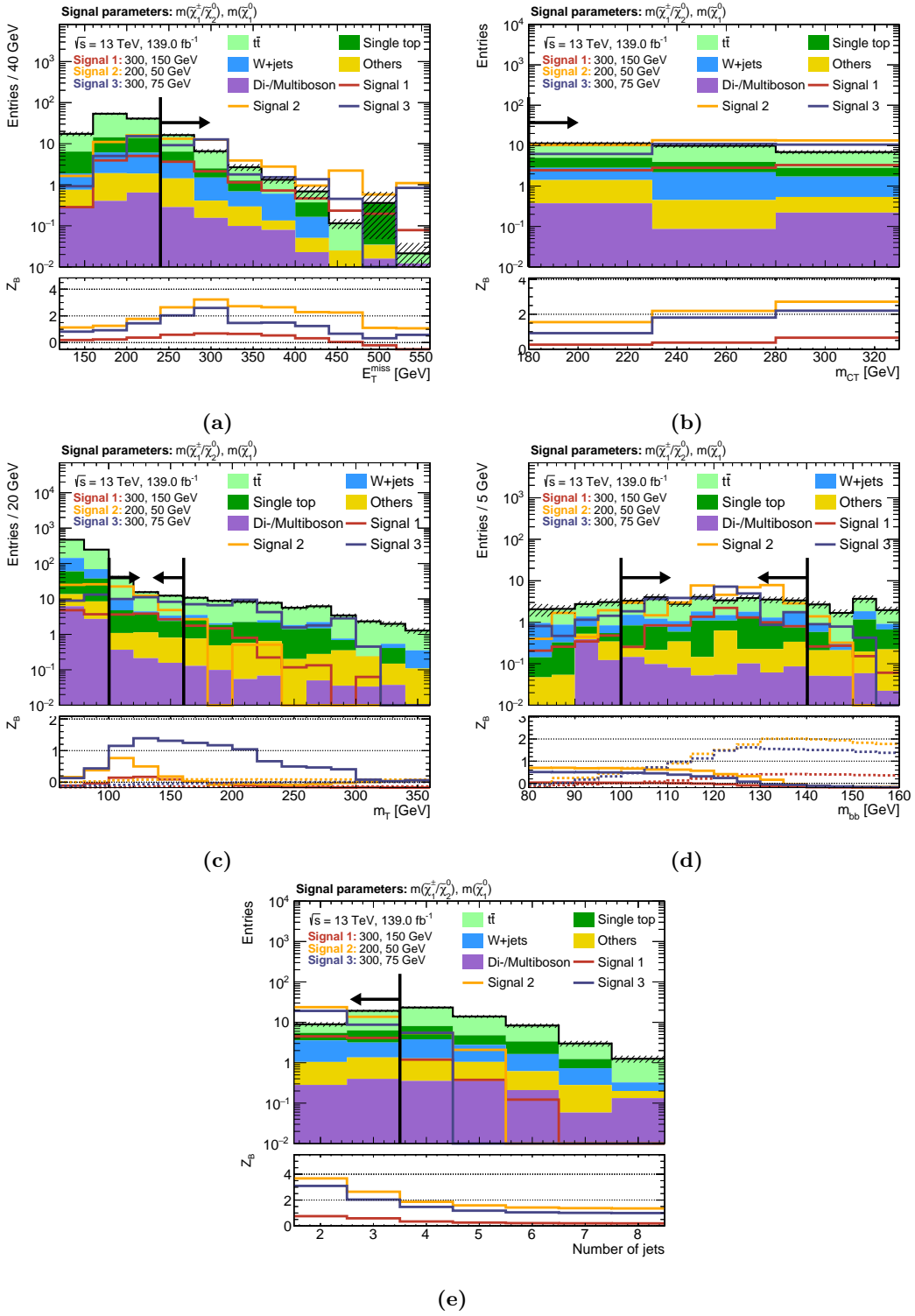


Figure 5.6: $N - 1$ plots for SR-LM, with exemplary signal points and all m_{CT} bins included. The dashed area represents MC statistical uncertainty on the background. In all figures except fig. (b), the significance in the lower pad is obtained by summing up all the events in the direction of the cut arrow and includes 30% uncertainty as well as MC statistical uncertainty. In fig. (b) the significance is only computed on a bin-by-bin basis, i.e. not summing up all events in the direction of the cut arrow.

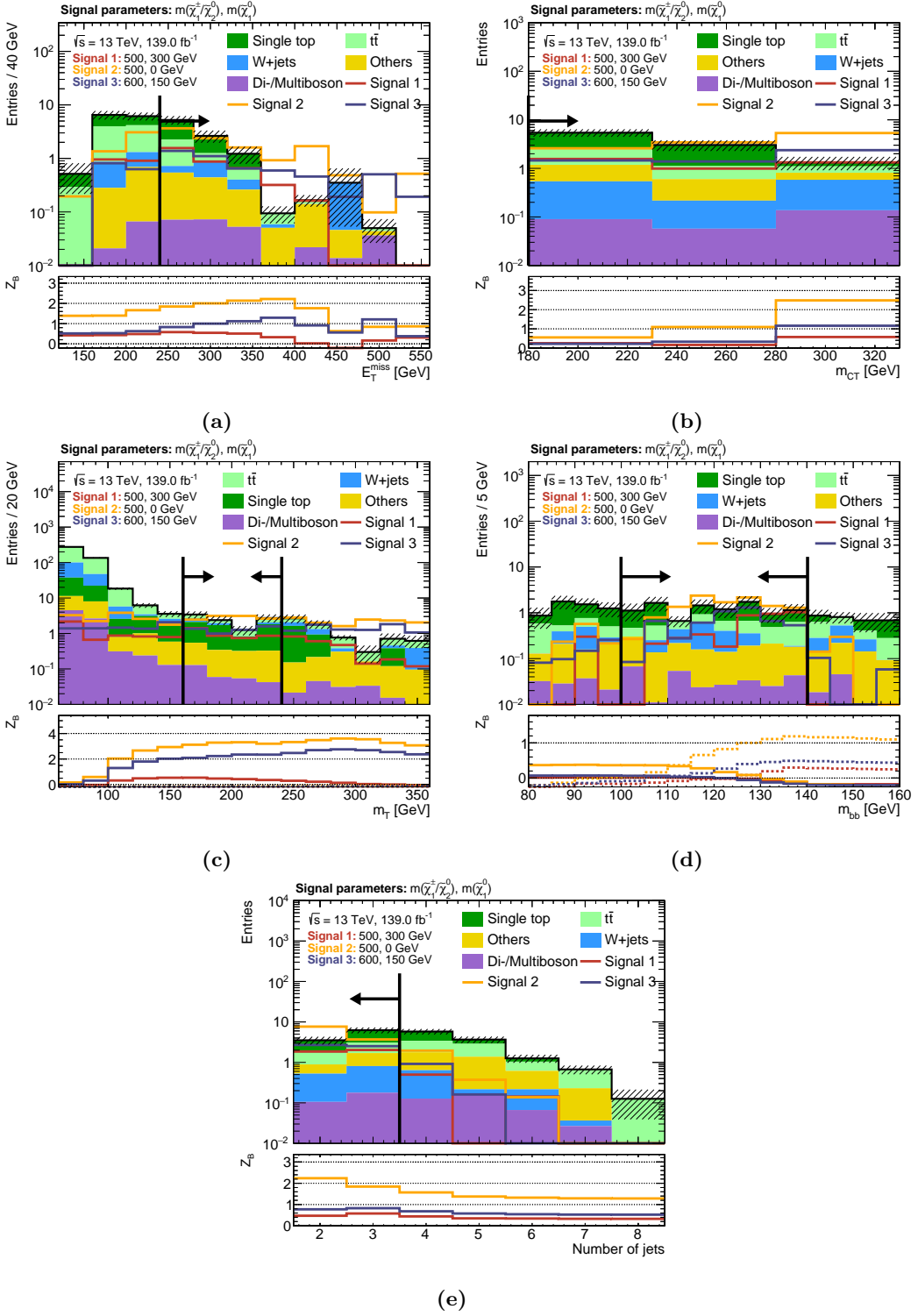


Figure 5.7: $N - 1$ plots for SR-MM, with exemplary signal points and all m_{CT} bins included. The dashed area represents MC statistical uncertainty on the background. In all figures except fig. (b), the significance in the lower pad is obtained by summing up all the events in the direction of the cut arrow and includes 30% uncertainty as well as MC statistical uncertainty. In fig. (b) the significance is only computed on a bin-by-bin basis, i.e. not summing up all events in the direction of the cut arrow.

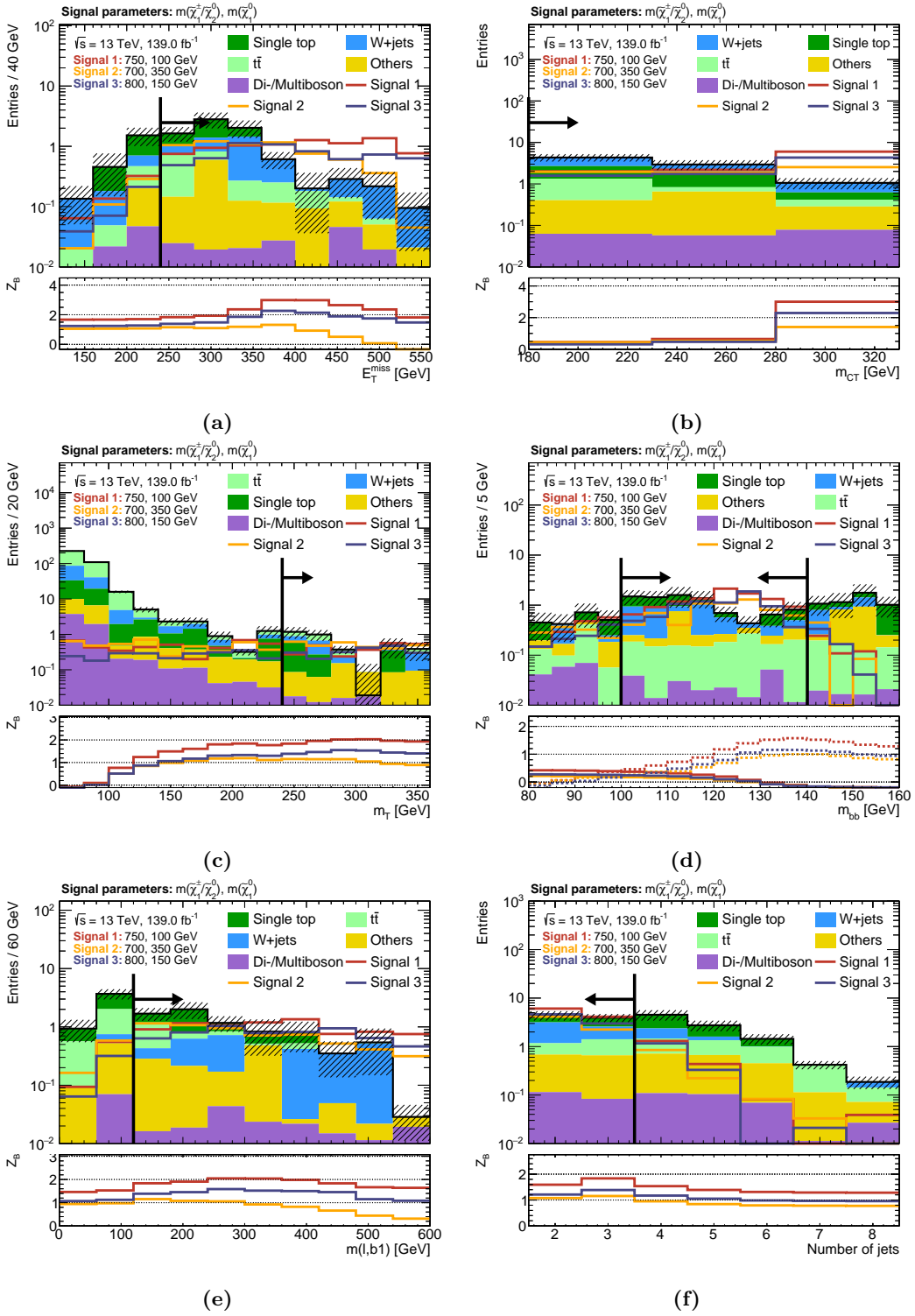


Figure 5.8: $N - 1$ plots for SR-HM, with exemplary signal points and all m_{CT} bins included. The dashed area represents MC statistical uncertainty on the background. In all figures except fig. (b), the significance in the lower pad is obtained by summing up all the events in the direction of the cut arrow and includes 30% uncertainty as well as MC statistical uncertainty. In fig. (b) the significance is only computed on a bin-by-bin basis, i.e. not summing up all events in the direction of the cut arrow.

Chapter 6

Background estimation

A reliable and trustworthy estimation of the expected SM background rates in the signal regions is crucial for exercising the statistical machinery laid out in chapter 3 and making conclusive statistical statements about the SUSY scenarios studied. The background estimation approaches used herein either rely on semi-data-driven techniques, or on MC-only estimations. As estimating backgrounds only from MC simulation is sometimes problematic due to e.g. mis-modelings in the phase space targeted not being appropriately covered by the uncertainties, a (semi-)data-driven approach is often favoured. In the following, the major backgrounds $t\bar{t}$, single top and $W + \text{jets}$ are estimated using a semi-data-driven approach, while the expected rates from the remaining, smaller backgrounds rely purely on MC simulations and are normalised to their theoretical cross section.

6.1 General strategy

6.1.1 Transfer factor approach

Estimating background contributions in SRs in a semi-data-driven approach usually involves the introduction of so-called control regions (CRs), used to control dominant background processes by comparing their expected event rates to data. The CRs are designed to be enriched in events of a given background process (or type) while being approximately free of signal contamination. If $N_p^{\text{MC}}(\text{SR})$ and $N_p^{\text{MC}}(\text{CR})$ are the expected rates for a given background process p obtained from MC simulation in a given SR and CR, respectively, then the transfer factor $N_p^{\text{MC}}(\text{SR})/N_p^{\text{MC}}(\text{CR})$ allows to convert the number of observed background events in the CRs, $N_p^{\text{obs.}}(\text{CR})$, into a background estimate in the SRs, $N_p^{\text{est.}}(\text{SR})$, through

$$N_p^{\text{est.}}(\text{SR}) = N_p^{\text{obs.}}(\text{CR}) \frac{N_p^{\text{MC}}(\text{SR})}{N_p^{\text{MC}}(\text{CR})} = \mu_p N_p^{\text{MC}}(\text{SR}). \quad (6.1)$$

Here, μ_p is the process-specific normalisation factor introduced in section 3.1. An important benefit of this approach is that the impact of systematic uncertainties on the estimated background rates can be evaluated on the transfer factors, that are ratios of MC estimates. As such, systematic uncertainties can cancel in the extrapolation to the SRs. The uncertainty on

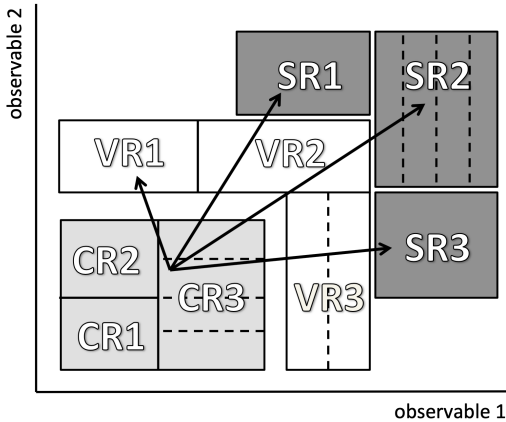


Figure 6.1: Schematic view of an analysis strategy including multiple control, validation and signal regions with one or multiple bins each. Extrapolations from the control regions into the signal regions can be verified in the validation regions lying in the phase space extrapolated over. All regions are designed to be statistically independent. Figure adapted from Ref. [168].

the background estimate in the SRs is then a combination of statistical uncertainties in the CRs and remaining uncertainties affecting the extrapolation [168]. For this reason, CRs are usually deliberately chosen to have large statistics, effectively reducing the uncertainties on the extrapolation to the SRs.

As indicated in eq. (6.1), the transfer factor approach is formally equivalent to using the process-specific normalisation factors from section 3.1, effectively *normalising* the number of total background events expected from MC simulation to the number of observed events in each control region. In the profile likelihood fits used in the following, implemented using HISTFITTER [168], the normalisation factors μ_p are fit to data instead of the background processes as expected from MC simulation. Multiple disjoint CRs are used to simultaneously normalise multiple background processes to data in a combined fit. In order not to have an underdetermined minimisation problem, at least the same number of CRs as normalisation factors need to be used. Two different profile likelihood fit configurations are used in the following; the first configuration being a so-called *background-only* fit configuration, assuming no signal contribution and typically only including the CRs. The second configuration is a so-called *model-dependent* fit configuration with nominal signal contribution using all CRs as well as SRs.

In order to verify the quality of the extrapolation from the CRs to the SRs, so-called validation regions (VRs) are defined. VRs do not participate in the actual fit of the model parameters to data, but serve as intermediate regions to verify the extrapolation. For this reason, VRs are typically placed in the region between the CRs and SRs that is extrapolated over. A schematic view of an analysis strategy using all three types of regions is shown in fig. 6.1. All three types of regions can have more than one bin and are separated using suitable observables that are extrapolated over. In order to be able to use information from all control and signal regions in a single profile likelihood fit, all regions necessarily need to be statistically independent.

6.1.2 Analysis blinding

An important concept in the design phase of searches for new physics is the idea of *blinding* regions of interest [250], meaning that measured data are not looked at in these regions. This avoids issues of *experimenter's bias*, i.e. unintended influences on the design of the analysis

based on the observed data. If data were already known when designing the signal regions (and therefore the outcome of the analysis would be known to some extent), experimenter's bias could for example occur during the selection of the final signal region definitions.

During the design of a search for SUSY, signal regions are generally kept blinded until the complete analysis strategy is fixed. Once the SRs have been designed, the next step is to develop a suitable background estimation strategy, often involving the introduction of CRs with negligible signal contamination. This is then often followed by the design of VRs that can be unblinded once the CRs are fixed. The SRs are only unblinded after the extrapolation of the background estimate (obtained using a background-only fit) from the CRs has been verified in the VRs, allowing to either quantify potential excesses in data or set limits on model parameters.

6.1.3 Data versus Monte Carlo plots

In this chapter, all plots comparing data versus MC are so-called *pre-fit* plots, meaning that no background-only fit has been run in order to determine the normalisation factors and total systematic uncertainties for the background estimate. Instead, the contributions from the dominant backgrounds $t\bar{t}$, $W + \text{jets}$ and single top are normalised simultaneously in the control regions by solving the system of i equations

$$n_{\text{data}}^{\text{CR}_i} = \mu_{t\bar{t}} B_{t\bar{t}}^{\text{CR}_i} + \mu_W B_W^{\text{CR}_i} + \mu_{\text{ST}} B_{\text{ST}}^{\text{CR}_i} + B_{\text{other}}^{\text{CR}_i}, \quad (6.2)$$

where i runs over the list of CRs introduced in section 6.2 and $\mu_{t\bar{t}}$, μ_W and μ_{ST} are the normalisation factors of the $t\bar{t}$, $W + \text{jets}$ and single top backgrounds, respectively, that are to be determined. $B_{t\bar{t}}^{\text{CR}_i}$, $B_W^{\text{CR}_i}$, $B_{\text{ST}}^{\text{CR}_i}$ and $B_{\text{other}}^{\text{CR}_i}$ are the background rates expected from MC simulation in the i -th CR. The normalisation factors obtained are 0.96 for $t\bar{t}$, 1.24 for $W + \text{jets}$ and 0.73 for single top. As will be shown in section 8.1, the normalisation factors obtained using the full statistical procedure will be close to these values.

Additionally, the uncertainty bands on the background estimate will include only MC statistical uncertainty as well as experimental uncertainties. The variations of the experimental uncertainties are normalised to the nominal background estimate in the case of $t\bar{t}$, $W + \text{jets}$ and single top, such that only the shapes of the dominant backgrounds are affected. For the remaining minor backgrounds, the experimental uncertainties can affect both normalisation and shape. All experimental uncertainties are assumed to be fully correlated over all processes and bins, allowing them to be summed in quadrature. Finally, the uncertainty bars on the data points are obtained by assuming data to be Poisson distributed and correspond to the 68% confidence interval.

6.2 Control regions

The contributions from $t\bar{t}$, $W + \text{jets}$ production and single top processes are normalised to data in dedicated control regions. Other processes like $Z + \text{jets}$, diboson and multiboson, $t\bar{t} + V$, $t\bar{t} + h$ and $V + h$ are estimated directly from MC simulation and normalised to their theoretical cross sections. All CRs are designed to be kinematically as close as possible to the respective

Table 6.1: Overview of the CR and VR definitions. With the exception of $m_{\ell b_1}$, which is not used in the definitions of the CRs and VRs, all regions share the same selection as the SRs on the remaining kinematic observables not listed here.

CR	TR-LM	TR-MM	TR-HM	WR	STR	
$m_{b\bar{b}}$ [GeV]		<100 or >140		$\in [50, 80]$	>195	
m_T [GeV]	$\in [100, 160]$	$\in [160, 240]$	>240	$\in [50, 100]$	>100	
m_{CT} [GeV]		<180		>180	>180	
VR	VR-onLM	VR-onMM	VR-onHM	VR-offLM	VR-offMM	VR-offHM
$m_{b\bar{b}}$ [GeV]		$\in [100, 140]$		$\in [50, 80] \cup [160, 195]$	$\in [50, 80] \cup [160, 195]$	$\in [50, 75] \cup [165, 195]$
m_T [GeV]	$\in [100, 160]$	$\in [160, 240]$	>240	$\in [100, 160]$	$\in [160, 240]$	>240
m_{CT} [GeV]		<180			>180	

SRs, such that the normalisation factors derived in the CRs are also valid in the SRs. The CRs are mutually exclusive and made orthogonal to the SRs through their requirements on m_T , m_{CT} and $m_{b\bar{b}}$. Apart from the requirements on these three observables, as well as the requirement on $m_{\ell b_1}$ (removed altogether in the CRs), the CRs share the same set of cuts as the SRs. Figure 6.4(a) illustrates the configuration of all CRs, especially highlighting the fact that all CRs are located in sideband regions off the $m_{b\bar{b}}$ window, significantly reducing signal contamination. Table 6.1 summarises the kinematic requirements separating the CRs from other regions of interest in the analysis. The pre-fit distributions of all CRs in representative observables are shown in fig. 6.2.

Control regions for $t\bar{t}$

As events from $t\bar{t}$ processes constitute the dominant SM background in the majority of the SRs, it is necessary to have a precise and reliable estimate of their contributions. Three CRs are defined for $t\bar{t}$, following the same binning in m_T , and thus called TR-LM, TR-MM and TR-HM in the following. A good purity of $t\bar{t}$ processes as well as the necessary high MC statistics are achieved by inverting the requirement on m_{CT} , selecting events below the kinematic endpoint for $t\bar{t}$ processes. The achieved pre-fit $t\bar{t}$ purities are 79.6% in TR-LM, 85.9% in TR-MM and 84.1% in TR-HM. The remaining contributions stem mostly from single top and $W + \text{jets}$ processes and vary between 8.6%–14.1% and 1.8%–4.3%, respectively, depending on the SR.

For a trustworthy estimate of the contributions from $t\bar{t}$ processes, it is important that the control regions associated to each signal region exhibit approximately the same composition of $t\bar{t}$ decay modes. The decay mode most relevant to the 1ℓ search at relatively low and moderate values of m_T is the semi-leptonic decay ($\ell\nu qq$), where one of the W bosons decays leptonically, while the other one undergoes a hadronic decay. The semi-leptonic decay mode exhibits the well-known kinematic endpoint in m_T and thus quickly loses importance at high transverse mass values. Events involving a hadronic decay of a τ -lepton originating from $W \rightarrow \tau_{\text{had}}\nu$ in one of the two branches and a leptonic W boson decay in the other branch ($\ell\nu\tau_{\text{had}}\nu$), are the dominant decay mode in selections with high values of m_T . Due to the additional neutrino in such events, the $\ell\nu\tau_{\text{had}}\nu$ decay mode does not exhibit the same kinematic endpoint as the semi-leptonic one. Finally, di-leptonic decays ($\ell\nu\ell\nu$) and events with a leptonically decaying τ -lepton ($\ell\nu\tau_\ell\nu$), where one of the two leptons is not reconstructed, play a sub-dominant but non-negligible role in all regions. Other $t\bar{t}$ decay modes are negligible in all analysis selections.

In the low-mass regions with moderate values in m_T not far above its kinematic endpoint, 80% (40%) of $t\bar{t}$ events involve the semi-leptonic decay mode in the control region (signal region). The sub-dominant decay mode in these regions involves the $\ell\nu\tau_{\text{had}}\nu$ decay mode, with a contribution of 25% and 10% in TR-LM and SR-LM, respectively. Di-leptonic and $\ell\nu\tau_\ell\nu$ decay modes each contribute about 15% of all events in TR-LM and about 3% in SR-LM. Overall, the composition in the low-mass regions is hence not exactly the same in the control and signal regions, but the agreement is still considered to be acceptable. With about 45% (36%) and 30% (35%), the largest contributions in TR-MM (SR-MM) originate from $\ell\nu\tau_{\text{had}}\nu$ decays and di-leptonic events, respectively. Events with a $\ell\nu\tau_\ell\nu$ decay contribute to about 10% (15%) in TR-MM (SR-MM). In the high-mass control and signal regions with a high requirement on m_T , the majority (about 50%) of events involve the $\ell\nu\tau_{\text{had}}\nu$ decay mode, while the di-leptonic and $\ell\nu\tau_\ell\nu$ decay modes contribute with about 30% and 20%, respectively. Overall, the compositions of the different $t\bar{t}$ decay modes in each control region are thus similar to the contributions in the respective signal region, meaning that the proportions of $t\bar{t}$ processes constrained through the log-likelihood fit in the CRs are the same as those to be estimated in the SRs.

Signal contamination in the $t\bar{t}$ CRs is avoided by inverting the requirement on $m_{b\bar{b}}$, i.e. placing the $t\bar{t}$ CRs in the $m_{b\bar{b}}$ sideband. The maximum signal contamination over the entire signal grid is 0.8%, 1.1% and 1.9% for TR-LM, TR-MM and TR-HM, respectively, and thus negligible. Figures 6.3(a) to 6.3(c) show the signal contamination in the $t\bar{t}$ CRs over the full signal grid.

Control region for $W + \text{jets}$

Events from $W + \text{jets}$ production represent the second largest contribution of SM background processes in most SRs. A single $W + \text{jets}$ control region, called WR in the following, is defined by replacing the signal region requirements on m_T and $m_{b\bar{b}}$ with $50 \text{ GeV} < m_T < 100 \text{ GeV}$ and $50 \text{ GeV} < m_{b\bar{b}} < 80 \text{ GeV}$, respectively. No bins in m_{CT} or m_T are defined for WR, as the composition of $W + \text{jets}$ is approximately constant in all regions.

Applying a low requirement on m_T allows to predominantly select events below the kinematic endpoint of the transverse mass of the W boson, resulting in a high statistics control region with a pre-fit $W + \text{jets}$ purity of roughly 52.5%. The sub-dominant background component of WR is $t\bar{t}$ with 35.2%. Minor contributions of 7.0% and 4.2% originate from single top and diboson processes, respectively. The composition of $W + \text{jets}$ events in WR and all signal regions is found to be dominated by W boson production in association with two real b -jets. Minor contributions originate from processes with mis-tagged c -jets or light-flavour jets.

As was the case for the $t\bar{t}$ control regions, placing WR off the Higgs mass peak allows to achieve a tolerable maximum signal contamination of only 2.4% without affecting the composition of processes in the $W + \text{jets}$ background too much. Most signal points have significantly less than 1% signal contamination in WR, as can be seen in fig. 6.3(d).

Control region for single top

Single top processes result in significant background contributions in some SRs, necessitating a proper semi-data-driven estimation. A single top CR (STR) is defined starting from the SRs by

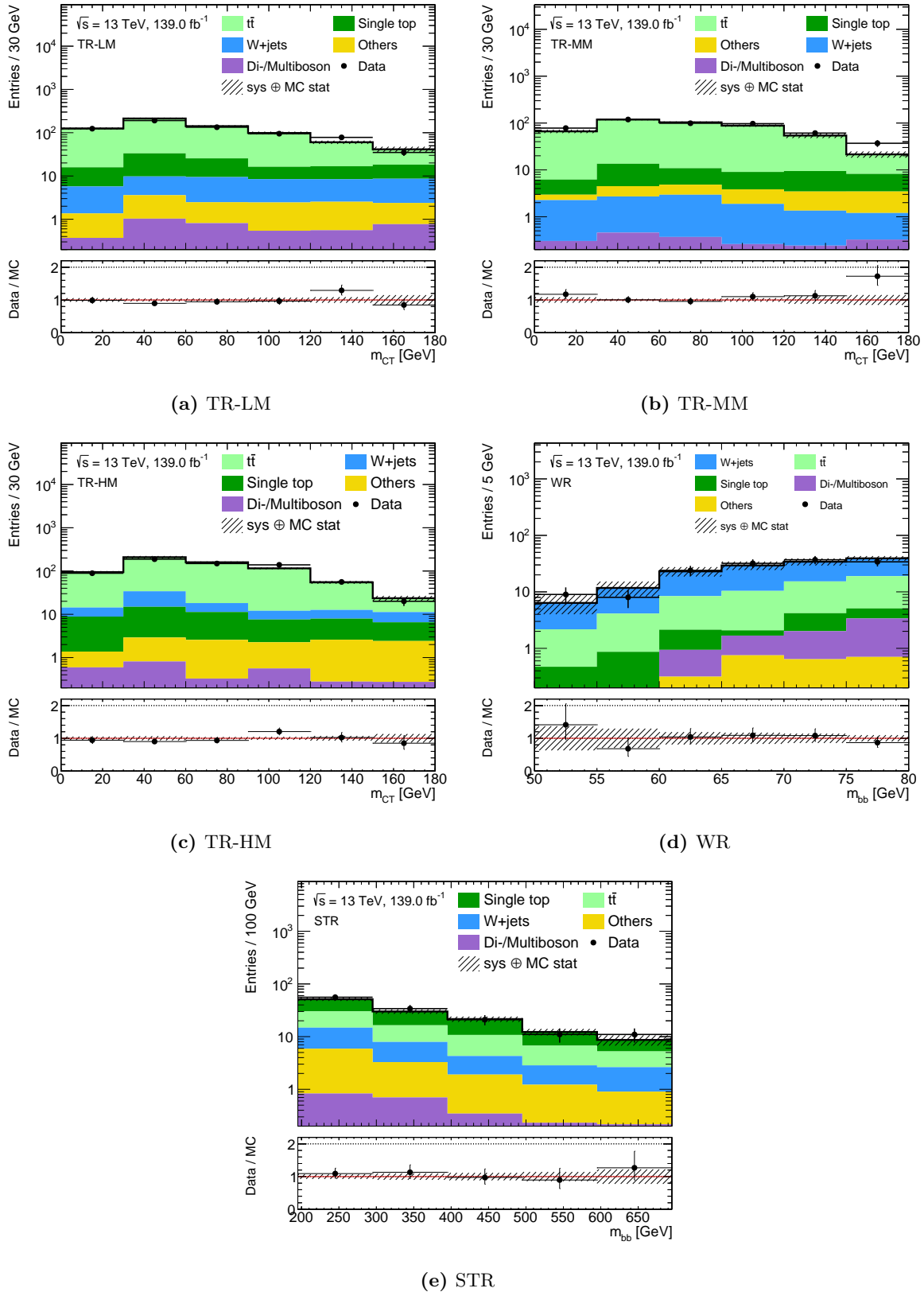


Figure 6.2: Exemplary pre-fit distributions for each control region. As laid out in the beginning of this chapter, the shaded region includes MC statistical uncertainty as well as experimental uncertainties, added in quadrature. A good agreement between MC expectation and data is observed in all CRs.

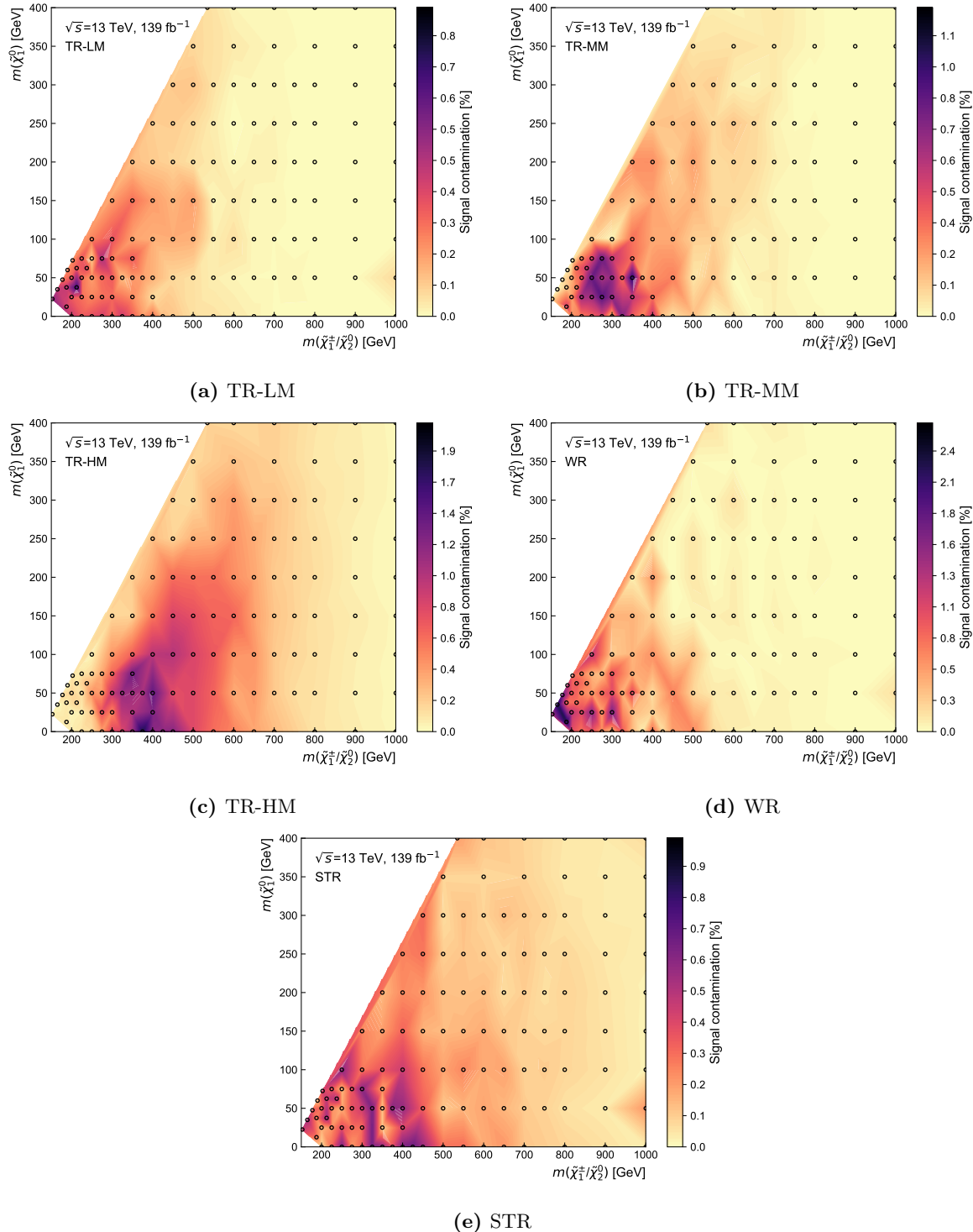


Figure 6.3: Signal contamination (shown on the z -axis) for all CRs throughout the signal grid. The space between the signal points (indicated by the black circles) is interpolated using Delaunay triangles.

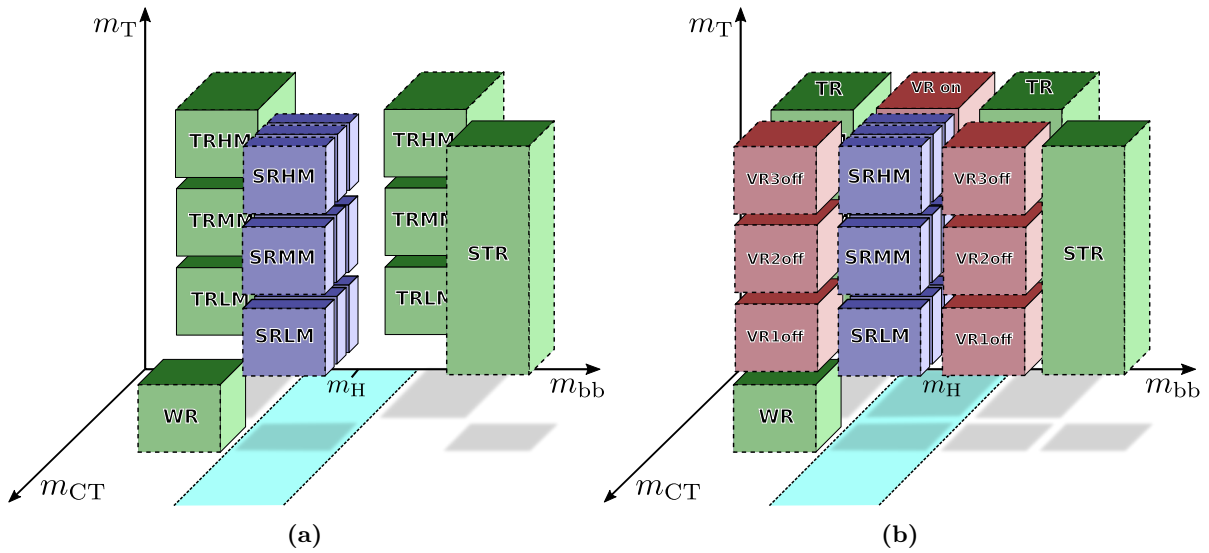


Figure 6.4: Configuration of (a) the CRs placed around the SRs off the m_{bb} window as well as (b) the validation regions in the phase space between the CRs and SRs. The VRs are arranged such that each of the extrapolations can be validated separately for SR-LM, SR-MM and SR-HM.

replacing the Higgs mass window cut on m_{bb} with $m_{bb} > 195$ GeV and removing the bins in m_{CT} .

The sideband approach achieves again a low maximum signal contamination of roughly 0.8%. The signal contamination across the entire signal grid is shown in fig. 6.3(e). The pre-fit purity of the single top processes in STR is 51.7% and sub-dominant contributions arise from $t\bar{t}$ processes (29%), $W + \text{jets}$ (10%) and $t\bar{t} + V$ (6%) production.

6.3 Validation regions

Two sets of VRs regions are introduced in order to verify the extrapolations over the different distributions. The selections defining all VRs are summarised in table 6.1. The first set, called VR-on is situated on the Higgs boson mass peak but with the m_{CT} requirement inverted to $m_{CT} < 180$ GeV. This allows the VR-on regions to validate the extrapolation over m_{bb} , performed when extrapolating the background estimate from the control regions into the signal regions. Three disjunct VR-on regions are introduced, with m_T requirements matching those of the SRs, such that the extrapolations can be validated separately for each signal region. The three VR-on regions are aptly named VR-onLM, VR-onMM and VR-onHM. A similar composition of $t\bar{t}$ decay modes as in the control and signal regions is observed in the VR-on regions, necessary for a trustworthy validation of the $t\bar{t}$ estimate. A maximum signal contamination of about 5%–14% is achieved, depending on the requirement in m_T . As can be seen from fig. A.9, most signal points have a signal contamination well below 5% for all VR-on regions.

The second set of VRs is located on both sides off the Higgs boson mass peak at same values in m_{CT} than the SRs. This set of *off-peak* VRs, called VR-off, is used to validate the extrapolation over the m_{bb} distribution performed in the case of STR. Additionally, the VR-off regions validate

the extrapolation over the m_{CT} performed in the $t\bar{t}$ control regions. Similar to the on-peak validation regions, the VR-off regions are split into m_{T} bins matching the signal regions, allowing a validation of the background estimate in their respective signal region. The bins in VR-off are called VR-offLM, VR-offMM and VR-offHM. The maximum signal contamination in the VR-off regions is found to be about 7%–13%, depending on the requirement on m_{T} . Most signal points, however, reveal a signal contamination in the VR-off regions of less than 3% (cf. fig. A.9).

Chapter 7

Systematic uncertainties

Several sources of systematic uncertainties need to be considered in the following. As laid out in chapter 3, they enter the likelihood as nuisance parameters and can be interpreted as a loss of information on the signal strength parameter. In the following, they are separated into experimental uncertainties, arising e.g. from finite detector resolution, and theoretical uncertainties due to modelling of the physics processes during simulation.

7.1 Experimental uncertainties

Experimental uncertainties arise from the methods used to reconstruct, identify and calibrate the physics objects used in the 1ℓ search. They are evaluated using up and down variations provided either as variational weights in the case of efficiency uncertainties, or as additional variational samples derived by re-executing the entire object reconstruction pipeline with varied parameters.

7.1.1 Pile-up reweighting and luminosity

The MC simulated events used in the 1ℓ search were largely already generated before the full Run 2 dataset was recorded, and therefore before the full pile-up profile in data was known. For this reason, the number of average interactions $\langle\mu\rangle$ per bunch crossing in MC is in general not identical to that in data, necessitating a reweighting procedure in MC. In order to account for differences in the measured inelastic pp cross section [251] and the one obtained from MC simulation, a scale factor of 1.03 is applied before the reweighting procedure. As MC samples are generated with integer values of $\langle\mu\rangle$ only, the scale factor is applied to data instead. The uncertainty on the pileup reweighting is evaluated by varying the data scale factor by ± 0.04 and deriving variational pileup weights.

As detailed in section 2.1.2, the total integrated luminosity relies on the measurement of the bunch luminosity which, in turn, needs precise measurements of the visible inelastic cross section σ_{vis} , as well as the visible pile-up parameter μ_{vis} . Uncertainties on the measurement of the total recorded cross section are dominated by the uncertainties on σ_{vis} that is measured during special vdM scans. For the full Run 2 dataset, an overall luminosity uncertainty of $\pm 1.7\%$, is

considered for all MC processes not normalised to data using a CR, derived using the methods described in Ref. [113].

7.1.2 Triggers

As all selections considered in the analysis apply a minimum requirement of $E_T^{\text{miss}} > 240 \text{ GeV}$, thus targeting a region where the E_T^{miss} triggers are fully efficient (see section 4.7). For this reason, no trigger scale factors and associated uncertainties are needed. Instead, only a 2% normalisation uncertainty correlated over all bins is considered in order to cover differences between the trigger plateaus due to MC statistical uncertainties.

7.1.3 Leptons

A large number of uncertainties on electrons arise from energy scale and resolution measurements [220, 222]. They are assumed to be fully correlated in η and are summed in quadrature, resulting in one nuisance parameter for the energy scale and one for the resolution. Uncertainties on muons arise from calibrations of the muon momentum scale and resolution, and are evaluated using variations in the smearing of the ID and MS tracks as well as the momentum scale, resulting in a total of five Gaussian-constrained nuisance parameters entering the likelihood [223]. Additional lepton-related uncertainties considered in the following originate from measurements of the reconstruction, identification and isolation efficiencies. Two more uncertainties arising from track-to-vertex association and bad muon identification efficiencies are considered in the case of muons.

7.1.4 Jets

The calibration of the jets to the absolute JES is subject to uncertainties arising e.g. from the *in situ* measurements, pile-up effects or flavour-dependence [228], encoded in a large set of 125 parameters. The full detail contained in the complete set of uncertainty components offers far greater statistical precision than needed for the 1ℓ search. As the majority of the parameters (a total of 98) stems from *in situ* measurements, an eigenvector decomposition is performed on the covariance matrix of these components [252], allowing to determine the 15 principal orthogonal components (including a residual term adding the remaining terms in quadrature), with minimal loss in bin-by-bin correlation information. Five additional parameters evaluating uncertainties arising from *in situ* η -intercalibrations of forward jets with respect to central jets are kept separate due to their two-dimensional dependence on p_T and η [228]. Effects from pile-up are described by four additional nuisance parameters. Uncertainties arising from differing detector responses to gluon- and quark-initiated jets as well as flavour-related differences are accounted for by two more nuisance parameters. Uncertainties from jets that are not contained in the calorimeters and *punch-through* into the MS are evaluated with an additional parameter. A last parameter encodes the uncertainty arising from the calibration of MC samples reconstructed using ATLFAST-II instead of the full detector simulation.

Systematic uncertainties on the JER arise from measured differences between data and MC simulation, noise from pile-up, and *in situ* measurements of the jet p_T imbalance. A similar eigenvector decomposition as for part of the JES uncertainties is used, reducing the set of

nuisance parameters considered in the following to 13 [228]. Finally, uncertainties related to the efficiency of jet vertex tagging are evaluated using a weight systematic.

7.1.5 Flavour tagging

Uncertainties on the flavour tagging efficiency originate from e.g. modelling uncertainties, as well as uncertainties on the reconstruction of physics objects. Similar to the JER and JES uncertainties, the full set of nuisance parameters that would in principle need to be included in order to consider the full bin-by-bin correlations and p_T and η dependence of the flavour-tagging uncertainties, is reduced to a more manageable size using an eigenvector decomposition. This leads to a total of five nuisance parameters encoding uncertainties on the b -tagging efficiency, c-jet and light-jet mis-tagging rate as well as the extrapolation to high- p_T jets [234, 235].

7.1.6 Missing transverse energy

The uncertainties on E_T^{miss} are evaluated using the systematic variations of all calibrated objects as inputs to the E_T^{miss} calculation. Additional uncertainties arise from the calculation of the track soft term. In the following, uncertainties on the soft term scale and resolution are considered, resulting in one nuisance parameter for the soft term scale and two nuisance parameters—corresponding to the perpendicular and parallel components—for the soft term resolution uncertainty. All track soft term uncertainties are derived by comparing MC simulation to $Z \rightarrow \mu\mu$ events [236].

7.2 Theoretical uncertainties

As discussed in section 2.2.8, due to finite order calculations, the different steps of the MC simulation generally introduces a certain number of unphysical scales and parameters. In order to quantify the uncertainties arising from the ad-hoc values of these, the MC simulation generally needs to be re-run with systematically varied parameter values. Since varied MC simulation parameters affect the event kinematics even before reconstruction and calibration, it is computationally very expensive to produce a full set of variations for each MC simulated dataset used in the nominal analysis.

In the following, different approaches are used to derive the theory uncertainties. For some of the variational MC datasets, the full MC simulation chain was run with reduced statistics. For others, different MC datasets produced with a different set of MC generators and tunes were available. For still others, variations were already processed during the initial MC simulation of the nominal sample and subsequently stored as variational weights. Finally, some of the variational MC datasets were simulated at MC truth-level, i.e. without detector simulation. The latter approach was used especially in the case of SUSY signal samples, where the impact of the full detector simulation compared to truth-level comparisons is expected to be small in the context of theory uncertainties. Additionally, a full simulation of MC datasets for all parameter variations and all signal points considered, would be computationally unfeasible.

For background processes that are normalised to data in a dedicated CR, the theory uncertainties are evaluated on the transfer factors. For a process p , a control region CR_i , and a destination

region R_j , the transfer factor reads

$$f_p(\text{CR}_i \rightarrow R_j) = \frac{N_p^{\text{MC}}(R_j)}{N_p^{\text{MC}}(\text{CR}_i)}, \quad (7.1)$$

where $N_p^{\text{MC}}(R_j)$ and $N_p^{\text{MC}}(\text{CR}_i)$ are the expected event rates for the process p in CR_i and R_j , respectively. The systematic uncertainty on the transfer factor is then given by

$$\Delta f_p^{\text{syst}} = \frac{f_p^{\text{variation}}}{f_p^{\text{nominal}}} - 1, \quad (7.2)$$

with $f_p^{\text{variation}}$ and f_p^{nominal} the transfer factors from the variational and nominal samples, respectively. If the MC datasets used for deriving the variational and nominal transfer factors are statistically independent, a statistical component of the uncertainty is derived using the individual statistical uncertainties on the background estimate,

$$\Delta f_p^{\text{stat}} = (\Delta f_p^{\text{syst}} + 1) \sqrt{\sum_{n \in N} \left(\frac{\sigma_n}{n} \right)^2}, \quad (7.3)$$

where n runs over the set of expected event rates and σ_n is the absolute MC statistical uncertainty associated to each expected event rate n . In the following, the control region used to evaluate the uncertainties on the transfer factors is taken to be the sum of all CRs introduced in section 6.2. This approach not only significantly improves the statistics in the region used for normalisation, but also results in a consistent treatment across all theoretical uncertainties on all relevant processes.

For backgrounds directly estimated from MC simulation, the systematic uncertainty on the expected event rate in each region R_i is given by

$$\Delta n_p^{\text{syst}}(R_i) = \frac{n_p^{\text{syst}}(R_i)n_p^{\text{nominal}}(P)}{n_p^{\text{nominal}}(R_i)n_p^{\text{syst}}(P)} - 1, \quad (7.4)$$

where the region P is a so-called *loose preselection* with minimal analysis selection criteria, used for normalisation of the event rates to be compared. If not otherwise indicated, the loose preselection used for normalisation requires exactly one isolated lepton, 2–3 jets of which at least one is b -tagged, $E_T^{\text{miss}} > 220 \text{ GeV}$ and $m_T > 50 \text{ GeV}$.

Apart from the hard scattering and parton showering uncertainties on top processes, all other theoretical uncertainties enter the likelihood as asymmetric correlated shape uncertainties. The hard scattering and parton showering uncertainties on top processes described below are estimated using MC generator comparisons and thus need to be symmetrised. The shape information is however still kept, i.e. the uncertainties are not one-sided.

7.2.1 Background

$t\bar{t}$ and single top

Theory uncertainties on the estimate of $t\bar{t}$ and single top processes arise for example from the simulation of the hard scattering between the interacting partons. These are evaluated by comparing the estimates from the nominal MC datasets generated using POWHEG and PYTHIA8 with those from alternative datasets generated using MADGRAPH_AMC@NLO and PYTHIA8. An uncertainty resulting from the hadronisation and fragmentation scheme chosen in PYTHIA8 is estimated by comparison to a MC dataset generated using POWHEG and HERWIG++ [253]. Uncertainties arising from ISR are evaluated at full reconstruction level by varying up and down by a factor of two the unphysical renormalisation μ_R and factorisation μ_F scales as well as the parameters controlling the showering and ME+PS matching [254]. Likewise, uncertainties arising from simulation of FSR are estimated by varying the effective coupling α_s^{FSR} [254].

Uncertainties also originate from the PDF set used during generation of the nominal MC dataset. As detailed in table 4.1, the NNPDF3.0NLO is used for the simulation of both $t\bar{t}$ and single top processes. An envelope around the variational expected event rates obtained from the NNPDF3.0NLO uncertainties are used to compute an uncertainty on the transfer factor.

Beyond LO single top production diagrams, interference appears between Wt and $t\bar{t}$ production. Two approaches are commonly used to try and isolate the Wt channel: diagram removal (DR) and diagram subtraction (DS) [255]. While the former removes all diagrams in the NLO Wt amplitude that are doubly resonant (meaning that they involve an intermediate top quark that can be on-shell), the latter introduces subtraction terms in the NLO Wt cross section cancelling the $t\bar{t}$ contribution [255]. As the DR scheme is used for estimating the event rate of the Wt channel in the analysis, a comparison with an estimation using the DS scheme allows to derive an uncertainty associated to the interference.

$W/Z + \text{jets}$

For $W/Z + \text{jets}$ processes, simulated using SHERPA 2.2.1, four different unphysical scales can be varied in order to evaluate uncertainties on the modelling. The renormalisation μ_R and factorisation μ_F scales are both independently and together varied up and down by a factor of two, resulting in a total of seven combined variations. Three envelopes are determined from varying only μ_R , only μ_F or μ_R and μ_F together, allowing to determine three separate uncertainties. The CKKW ME+PS matching scheme also uses an unphysical scale for determining the overlap between jets from the ME and the PS. The nominal value of 20 GeV for the merging scale is varied to 30 GeV and 15 GeV for the up and down systematic variations, respectively. Finally, the scale used for resummation of soft gluon emission, μ_{QSF} , is varied up and down by a factor of two, and the effect on the expected event rates are determined.

An additional uncertainty arises from the choice of PDF set used for simulating $W/Z + \text{jets}$. It is evaluated by propagating the PDF error set (containing slightly different parameterisations of the PDF) to the analysis observables. Uncertainties due to the choice of the strong coupling constant $\alpha_s(m_Z) = 0.118$ for fitting the PDFs are estimated by comparing with variations using $\alpha_s(m_Z) = 0.119$ and $\alpha_s(m_Z) = 0.117$, and added in quadrature to the PDF uncertainty.

As $Z + \text{jets}$ is not normalised to data in a dedicated CR but to its nominal SM cross section, an additional normalisation uncertainty corresponding to the theoretical uncertainty on the cross section is considered.

Other backgrounds

For diboson, multiboson and $t\bar{t} + V$ processes, uncertainties arising from the unphysical scales μ_F , μ_R as well as μ_{QSF} and the CKKW ME+PS matching scale are considered using the same prescription described above for $W/Z + \text{jets}$. For these three processes as well as for the other minor backgrounds $V + h$ and $t\bar{t} + h$, an additional uncertainty on the SM cross section used for normalisation is taken into account.

7.2.2 Signal

Theoretical uncertainties on the SUSY signal processes arise from the unphysical factorisation, renormalisation and CKKW-L ME+PS merging scales. These are evaluated using a similar procedure as for background processes, varying the different scales up and down by a factor of two and comparing the expected signal rates. An additional uncertainty on PS originating from the chosen PYTHIA8 tune is estimated by varying up and down the chosen value for α_s^{ISR} .

As detailed in section 4.3.1, the cross section of electroweakino pair production is calculated using RESUMMINO. A theoretical uncertainty on the cross section is considered in the following, but does not enter the statistical fit procedure as nuisance parameter. Instead, in addition to the set of observed CL_s values using the nominal cross section, two additional variational sets are derived using signal cross sections fixed at their $\pm 1\sigma$ variations. This allows to draw a cross section uncertainty band on the observed exclusion contour.

Due to the large number of MC samples, all theory uncertainties on SUSY signal processes are evaluated at MC truth-level only. As the VRs typically have relatively low signal contamination and thus low signal MC statistics available for evaluating theory uncertainties, requirements on observables with negligible impact on the shapes of the theoretical uncertainties are loosened. In the on-peak VRs, the requirements loosened are $m_T > 60 \text{ GeV}$ and $E_T^{\text{miss}} > 140 \text{ GeV}$. The same loosened selection is applied in SRs in cases where the MC statistical uncertainty is too high for a reliable estimation of the theoretical uncertainties. In the off-peak VRs, the requirements loosened are $m_T > 60 \text{ GeV}$ and $E_T^{\text{miss}} > 60 \text{ GeV}$ and $m_{\text{CT}} > 60 \text{ GeV}$. Overall, the theoretical uncertainties on the expected signal rate range from about 10% in phase space regions with large mass splitting between $\tilde{\chi}_1^\pm/\tilde{\chi}_2^0$ and $\tilde{\chi}_1^0$ to about 25% in regions with small mass splittings.

7.3 Impact on signal regions

Table 7.1 shows a breakdown of the dominant systematic uncertainties on the background prediction in the SRs, obtained after a background-only fit in the CRs with subsequent extrapolation to the SRs. The total uncertainty in the SRs amounts to 15% in SR-LM and increases to 25% in SR-MM and 34% in SR-HM. Theoretical uncertainties have the largest contribution to the total uncertainty. For SR-LM, the largest uncertainty, amounting to 10% of the total background estimate, originates from the $t\bar{t}$ parton shower uncertainty. For SR-MM

Table 7.1: Breakdown of the dominant systematic uncertainties on background estimates in the various exclusion signal regions (m_{CT} bins summed up). As the individual uncertainties can be correlated, they do not necessarily add up in quadrature to the total background uncertainty. The percentages show the size of the uncertainty relative to the total expected background. Table adapted from Ref. [184].

Signal Region	SR-LM	SR-MM	SR-HM
Total background expectation	27	8.6	8.1
Total uncertainty	± 4 [15%]	± 2.2 [25%]	± 2.7 [34%]
Theoretical systematic uncertainties			
$t\bar{t}$	± 2.6 [10%]	± 0.6 [7%]	± 0.33 [4%]
Single top	± 0.8 [2.7%]	± 1.1 [12%]	± 1.9 [23%]
$W + \text{jets}$	± 0.23 [0.9%]	± 0.07 [0.8%]	± 0.19 [2.3%]
Other backgrounds	± 0.13 [0.5%]	± 0.15 [1.7%]	± 0.08 [1.0%]
MC statistical uncertainties			
MC statistics	± 1.7 [6%]	± 1.1 [13%]	± 1.2 [14%]
Uncertainties in the background normalisation			
Normalisation of dominant backgrounds	± 1.3 [5%]	± 1.6 [18%]	± 1.3 [16%]
Experimental systematic uncertainties			
$E_{\text{T}}^{\text{miss}}/\text{JVT}/\text{pile-up}/\text{trigger}$	± 1.8 [7%]	± 0.4 [4%]	± 0.4 [5%]
Jet energy resolution	± 1.6 [6%]	± 0.5 [6%]	± 0.4 [5%]
b -tagging	± 1.1 [4%]	± 0.29 [3.4%]	± 0.13 [1.5%]
Jet energy scale	± 0.9 [3.2%]	± 0.9 [10%]	± 0.29 [4%]
Lepton uncertainties	± 0.32 [1.2%]	± 0.09 [1.0%]	± 0.19 [2.3%]

(SR-HM), the single top generator uncertainties are the largest ones with 10% (21%) of the total background estimate. Theoretical uncertainties on $W + \text{jets}$ and other minor backgrounds have only small to negligible effects. The experimental uncertainties in general have less impact on the total uncertainty than the theoretical ones, with the largest experimental uncertainties contributing only 5–10% depending on the SR. The dominant experimental uncertainties arise from the JES and JER as well as $E_{\text{T}}^{\text{miss}}$ modelling and pile-up effects. The MC statistical uncertainties contribute 5–18%, depending on the SR.

Chapter 8

Results

This chapter discusses the results of the different log-likelihood fits to data and hypothesis tests performed in the analysis. After the background estimation, obtained through a background-only fit in the control regions, is validated in the validation regions, the signal regions are unblinded and the observed data is compared to the SM background expectation.

8.1 Background-only fit results

8.1.1 Results in the control regions

As all CRs are mutually exclusive, a background-only fit simultaneously using information from all CRs can be run. Only the terms related to the CRs enter the likelihood and any signal contamination present in the CRs is suppressed. This allows to fit the dominant backgrounds to data, and thus, by construction, leads to a good agreement between observed data and the total fitted background estimate in all CRs. The best-fit values and uncertainties of the free normalisation parameters for $t\bar{t}$ (μ_T), single top (μ_{ST}) and $W + \text{jets}$ (μ_W) entering the likelihood are determined to be

$$\begin{aligned}\mu_T &= 1.02^{+0.07}_{-0.09}, \\ \mu_{ST} &= 0.6^{+0.5}_{-0.25}, \\ \mu_W &= 1.22^{+0.26}_{-0.24}.\end{aligned}\tag{8.1}$$

While the dominant $t\bar{t}$ background stays roughly at its nominal expectation with respect to MC simulation, $W + \text{jets}$ processes are slightly scaled up, and the single top expectation is scaled down. The high uncertainty on μ_{ST} can be attributed to the relatively low MC statistics and comparably low purity of single top events in STR.

Table 8.1 summarises the background estimate including all uncertainties for all control regions after the fit to data. As discussed in chapter 6, $t\bar{t}$ dominates in all control regions (except WR), followed by single top and $W + \text{jets}$ processes. In WR, $W + \text{jets}$ is the largest background, followed by $t\bar{t}$ processes. Due to the relatively small normalisation factor for single top processes, $t\bar{t}$ and single top contribute to roughly equal amounts to STR. Small contributions come from

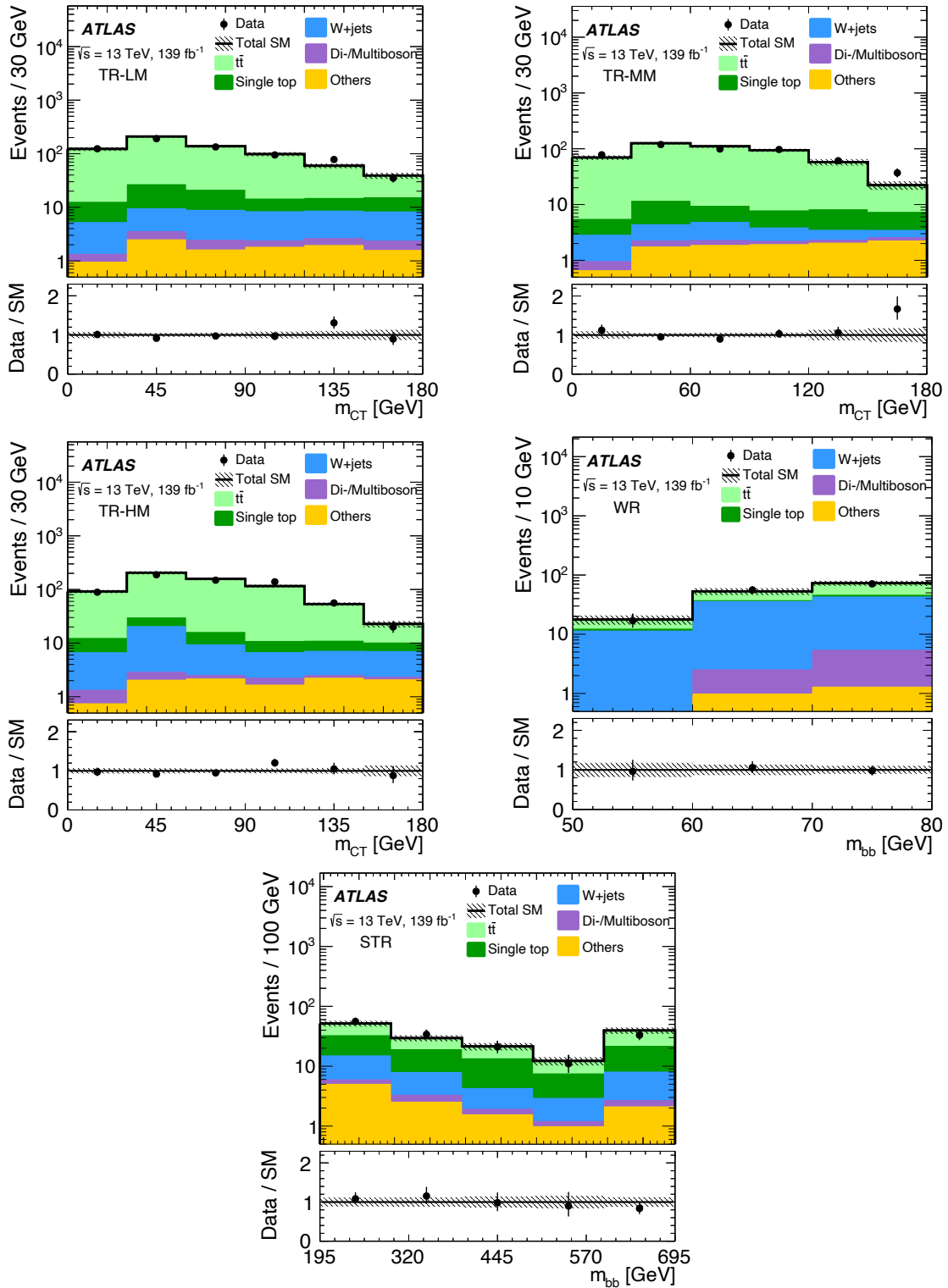


Figure 8.1: Exemplary distribution shown in each control region after the background-only fit. The shaded region includes all systematic uncertainties as well as MC statistical uncertainty. The $t\bar{t}$, single top and $W + \text{jets}$ are normalised simultaneously in all CRs. A good agreement between MC expectation and data is observed in all CRs. Adapted from Ref. [184].

Table 8.1: Background-only fit results for the CRs for an integrated luminosity of 139 fb^{-1} . Nominal MC expectations (normalised to MC cross-sections) are given for comparison. The errors shown include the MC statistical and systematic uncertainties. PDG rounding is applied to the event rates and uncertainties [9].

Region	TR-LM	TR-MM	TR-HM	WR	STCR
Observed events	657	491	641	144	155
Fitted SM events	666 ± 25	480 ± 21	645 ± 26	143 ± 12	154 ± 15
$t\bar{t}$	560 ± 40	430 ± 33	550 ± 40	47 ± 9	59 ± 12
Single top	60 ± 40	27 ± 23	33 ± 27	5 ± 4	57 ± 22
$W + \text{jets}$	34 ± 8	10.5 ± 2.8	44 ± 11	83 ± 16	23 ± 6
Di-/Multiboson	4.3 ± 1.2	2.0 ± 0.5	2.8 ± 0.5	5.7 ± 1.0	2.8 ± 0.9
Other	10.5 ± 1.3	10.6 ± 1.4	11.1 ± 1.4	2.4 ± 0.4	12.3 ± 1.5
MC exp. SM events	720 ± 80	474 ± 33	680 ± 50	130 ± 13	180 ± 50
$t\bar{t}$	570 ± 70	407 ± 30	570 ± 40	46 ± 10	52 ± 10
Single top	102 ± 18	46 ± 13	58 ± 16	9 ± 6	90 ± 40
$W + \text{jets}$	29 ± 4	8.4 ± 1.2	36.1 ± 3.1	67 ± 5	19.0 ± 2.0
Di-/Multiboson	4.1 ± 1.1	2.0 ± 0.5	2.8 ± 0.5	5.6 ± 1.0	2.8 ± 0.9
Other	10.6 ± 1.3	10.6 ± 1.4	11.2 ± 1.4	2.5 ± 0.4	12.4 ± 1.5

diboson, multiboson as well as other backgrounds like $t\bar{t} + V$, $t\bar{t} + h$ and $V + h$. All processes estimated directly from MC simulation cumulatively account for only 10%, 5.5% and a maximum of 2.6% in the single top, $W + \text{jets}$ and $t\bar{t}$ control regions, respectively. Exemplary distributions in the CRs after the background-only fit are shown in fig. 8.1, revealing a good agreement between observed data and the SM background estimate throughout the distributions shown.

8.1.2 Results in the validation regions

In order to validate the extrapolations from the CRs to the SRs, the results of the background-only fit in the CRs are first validated in the VRs. Table 8.2 summarises the observed data and SM background estimate in the different VR bins before and after the background-only fit in the CRs. Exemplary $N - 1$ distributions in m_{CT} in all VRs are shown in fig. 8.2.

In the on-peak VRs, designed to validate the extrapolation from the control regions over the $m_{b\bar{b}}$ distribution, $t\bar{t}$ is by far the most dominant background after the background-only fit. Contributions from single top and $W + \text{jets}$ each amount to only 1–5%, depending on the validation region bin. Diboson, multiboson and other SM processes result in minor contributions of the level of not more than 3% of the total background estimate. As the total uncertainties on the background estimate in the on-peak regions are dominated by the $t\bar{t}$ uncertainties, the sizeable uncertainties on the $W + \text{jets}$ and single top estimates due to relatively limited MC statistics do not have a significant impact.

In the off-peak VRs, after the background-only fit, $t\bar{t}$ is the dominant process in the low mass regime, where contributions from single top and $W + \text{jets}$ are subdominant. In the medium and high mass regimes, $t\bar{t}$, single top and $W + \text{jets}$ all result in similar contributions. Diboson, multiboson and other SM processes are only minor backgrounds in all off-peak regions,

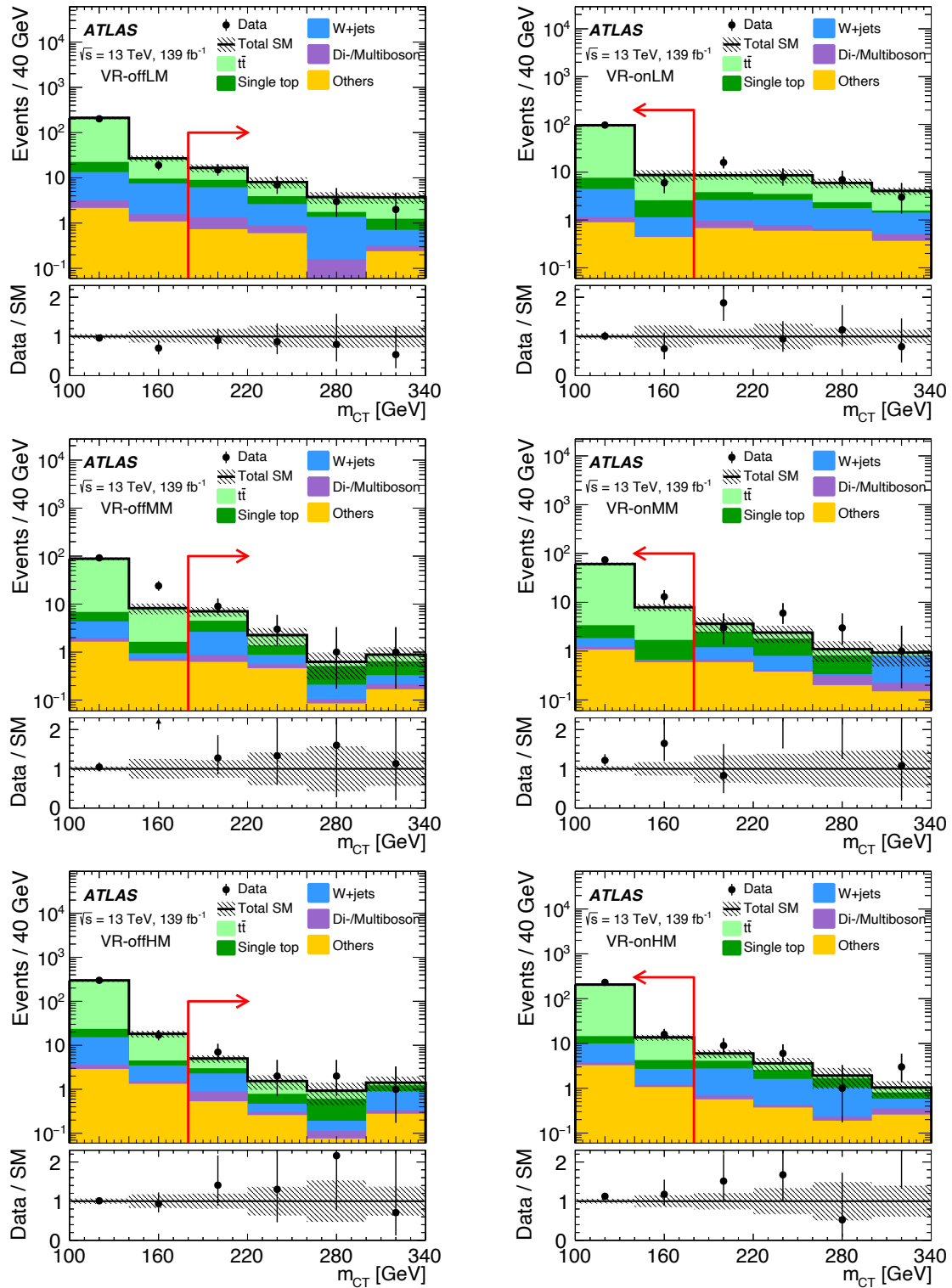


Figure 8.2: Exemplary $N - 1$ distributions shown in each validation region after the background-only fit with subsequent extrapolation to the VRs. All selection cuts except for the requirement on m_{CT} (indicated using the red arrow) are applied. The shaded region includes all systematic uncertainties as well as MC statistical uncertainty. Adapted from Ref. [184].

Table 8.2: Background-only fit results from the CRs extrapolated to the VRs for an integrated luminosity of 139 fb^{-1} . Nominal MC expectations (normalised to MC cross-sections) are given for comparison. The errors shown include the MC statistical and systematic uncertainties. Uncertainties in the fitted event rates are symmetric by construction, except where the negative error is truncated at an event rate of zero. PDG rounding is applied to the event rates and uncertainties [9].

Region	VR-onLM	VR-onMM	VR-onHM	VR-offLM	VR-offMM	VR-offHM
Observed events	103	87	247	27	14	12
Fitted SM events	100 ± 19	64 ± 9	215 ± 18	34 ± 6	9.5 ± 2.7	7.5 ± 2.6
$t\bar{t}$	90 ± 19	59 ± 9	196 ± 19	18 ± 4	2.4 ± 1.4	1.8 ± 1.8
Single top	5^{+5}_{-5}	$2.6^{+2.9}_{-2.6}$	6 ± 6	5 ± 4	3.0 ± 1.8	1.8 ± 1.5
$W + \text{jets}$	4 ± 4	0.6 ± 0.5	7.9 ± 2.1	8.2 ± 2.6	2.3 ± 0.8	2.2 ± 0.6
Di-/Multiboson	0.24 ± 0.08	0.19 ± 0.08	0.54 ± 0.19	1.07 ± 0.27	0.39 ± 0.11	0.51 ± 0.14
Other	1.34 ± 0.22	1.67 ± 0.28	4.4 ± 2.0	1.6 ± 0.5	1.34 ± 0.25	1.15 ± 0.24
MC exp. SM events	110 ± 40	69 ± 17	218 ± 22	34 ± 7	12.8 ± 3.4	9.7 ± 3.3
$t\bar{t}$	92 ± 35	62 ± 17	196 ± 21	16 ± 5	3.8 ± 2.2	3.1 ± 1.9
Single top	8 ± 5	4.5 ± 3.4	11 ± 6	9 ± 4	5.3 ± 2.2	3.1 ± 2.5
$W + \text{jets}$	2.8 ± 2.3	0.5 ± 0.5	6.5 ± 1.2	6.5 ± 1.6	2.0 ± 0.5	1.80 ± 0.34
Di-/Multiboson	0.24 ± 0.07	0.19 ± 0.08	0.50 ± 0.17	1.07 ± 0.28	0.37 ± 0.10	0.50 ± 0.15
Other	1.35 ± 0.23	1.70 ± 0.28	4.4 ± 0.9	1.6 ± 0.5	1.36 ± 0.25	1.16 ± 0.24

cumulatively amounting to only 10–14% of the total background estimate, depending on the mass regime.

The agreement between data and the background estimate is summarised in fig. 8.4. In VR-onMM and VR-onHM, light overfluctuations with a significance [179] of 1.3σ and 1.7σ , respectively, are observed in data. In the remaining VRs, the agreement between observed data and SM expectation is within 1σ . The overall agreement in the validation regions is thus considered to be acceptable, paving the way for further extrapolation of the background estimate into the SRs.

8.1.3 Results in the signal regions

By extrapolating the results from the background-only fit in the control regions, the background estimate in the signal regions can be obtained. In the following, the results in all discovery and exclusion signal regions are discussed.

Table 8.3 compares the background estimate with the observed data for all discovery signal regions. In the low-mass discovery signal region, $t\bar{t}$ is the dominant background, followed by $W + \text{jets}$ and single top. At higher values of m_T , i.e. in the medium-mass discovery signal region, all three main SM backgrounds contribute to roughly equal amounts. Finally, in the high-mass signal region, $W + \text{jets}$ is the largest SM background, followed by single top and $t\bar{t}$. In all discovery signal regions, diboson, multiboson and other SM backgrounds yield only minor contributions.

Table 8.3: Background-only fit results extrapolated to the discovery SRs for an integrated luminosity of 139 fb^{-1} . Nominal MC expectations (normalised to MC cross-sections) are given for comparison. The errors shown include the MC statistical and systematic uncertainties. Uncertainties in the fitted yields are symmetric by construction, except where the negative error is truncated at an event yield of zero. PDG rounding is applied to the event rates and uncertainties [9].

Region	SR-LM (disc.)	SR-MM (disc.)	SR-HM (disc.)
Observed events	66	32	14
Fitted SM events	47 ± 6	21 ± 5	8.6 ± 2.8
$t\bar{t}$	22 ± 4	5.9 ± 1.9	1.9 ± 0.7
Single top	9 ± 6	6 ± 5	$2.0^{+2.4}_{-2.0}$
$W + \text{jets}$	11.1 ± 2.9	5.6 ± 1.4	3.7 ± 1.0
Di-/Multiboson	1.23 ± 0.24	0.56 ± 0.11	0.21 ± 0.06
Other	4.8 ± 0.5	2.6 ± 0.4	0.74 ± 0.16
MC exp. SM events	50 ± 7	22 ± 5	8 ± 4
$t\bar{t}$	21 ± 5	4.9 ± 1.6	1.2 ± 0.6
Single top	14 ± 4	9 ± 5	$2.9^{+3.5}_{-2.9}$
$W + \text{jets}$	9.1 ± 1.3	4.5 ± 0.7	3.0 ± 0.6
Di-/Multiboson	1.20 ± 0.23	0.56 ± 0.11	0.21 ± 0.06
Other	4.8 ± 0.5	2.6 ± 0.4	0.74 ± 0.16

The results in the exclusion signal regions are shown in table 8.4. As for the discovery signal regions, $t\bar{t}$ is the dominant background in the low-mass exclusion signal region bins SR-LM, while $W + \text{jets}$ slightly dominates in the high-mass exclusion signal region bins SR-HM. The m_{CT} distributions of all three exclusion SRs are shown in fig. 8.3.

None of the exclusion or discovery signal regions reveal a significant deviation in data compared to the SM expectation, and all observations are in good agreement with the SM. A slight overfluctuation of data in the discovery SRs is quantified to have a significance of 1.8σ , 1.6σ and 1.2σ in the discovery signal regions SR-LM, SR-MM and SR-HM, respectively[†]. In the exclusion signal regions, the agreement between data and SM expectation is well within 1σ , except for the SR-LM low m_{CT} , SR-MM medium m_{CT} and SR-HM high m_{CT} bins, where a slight overfluctuation of 1.5σ , 1.6σ and 1.3σ , respectively, is observed in data. Figure 8.4 summarises, across all regions, the observed data, SM background expectation as well as the significances of any observed deviations from the SM expectation.

Since no significant excess is seen in data, the signal regions will be used in the following to derive model-dependent exclusion limits as well as model-independent upper limits on the visible cross section of BSM processes. As a consequence of the minor overfluctuations of data observed in some signal region bins, the observed model-dependent and model-independent limits will be slightly weaker than expected.

[†] The discovery signal regions are not mutually exclusive, thus the small overfluctuations observed in data are not statistically independent in these regions.

Table 8.4: Background-only fit results in the exclusion SRs for an integrated luminosity of 139 fb^{-1} . The first column shows the sum of all m_{CT} bins (including overflow). Subsequent columns indicate the different bins in m_{CT} , overflow is included in the last bin. The errors shown include the MC statistical and systematic uncertainties. Uncertainties in the fitted yields are symmetric by construction, except where the negative error is truncated at an event yield of zero. PDG rounding is applied to the event rates and uncertainties [9]. Table adapted from Ref. [184].

SR-LM	All m_{CT} bins	Low m_{CT}	Medium m_{CT}	High m_{CT}
Observed	34	16	11	7
Expected	27 ± 4	8.8 ± 2.8	11.3 ± 3.1	7.3 ± 1.5
$t\bar{t}$	16.2 ± 3.4	4.4 ± 2.2	7.3 ± 2.5	4.6 ± 1.2
Single top	2.7 ± 1.8	1.3 ± 1.1	$0.9^{+1.0}_{-0.9}$	0.6 ± 0.6
$W+\text{jets}$	5.5 ± 2.0	2.0 ± 0.9	2.4 ± 1.3	1.1 ± 0.5
Di-/Multiboson	0.67 ± 0.19	0.39 ± 0.13	$0.09^{+0.11}_{-0.09}$	0.18 ± 0.04
Others	2.23 ± 0.29	0.81 ± 0.25	0.64 ± 0.15	0.77 ± 0.12
SR-MM	All m_{CT} bins	Low m_{CT}	Medium m_{CT}	High m_{CT}
Observed	13	4	7	2
Expected	8.6 ± 2.2	4.6 ± 1.7	2.6 ± 1.3	1.4 ± 0.6
$t\bar{t}$	2.7 ± 1.4	1.6 ± 0.9	0.8 ± 0.7	0.30 ± 0.24
Single top	2.7 ± 1.9	1.6 ± 1.5	$1.0^{+1.1}_{-1.0}$	$0.15^{+0.19}_{-0.15}$
$W+\text{jets}$	1.5 ± 0.7	0.6 ± 0.4	$0.3^{+0.4}_{-0.3}$	0.57 ± 0.26
Di-/Multiboson	0.29 ± 0.08	0.09 ± 0.04	0.065 ± 0.028	0.14 ± 0.06
Others	1.33 ± 0.27	0.69 ± 0.20	0.40 ± 0.13	0.24 ± 0.09
SR-HM	All m_{CT} bins	Low m_{CT}	Medium m_{CT}	High m_{CT}
Observed	14	6	5	3
Expected	8.1 ± 2.7	4.1 ± 1.9	2.9 ± 1.3	1.1 ± 0.5
$t\bar{t}$	1.4 ± 0.5	0.8 ± 0.4	0.36 ± 0.25	0.22 ± 0.15
Single top	$2.0^{+2.4}_{-2.0}$	$0.9^{+1.5}_{-0.9}$	0.9 ± 0.9	$0.16^{+0.26}_{-0.16}$
$W+\text{jets}$	3.7 ± 1.0	1.9 ± 0.8	1.4 ± 0.8	0.45 ± 0.19
Di-/Multiboson	0.21 ± 0.06	0.057 ± 0.025	0.075 ± 0.027	0.08 ± 0.04
Others	0.74 ± 0.16	0.34 ± 0.09	0.19 ± 0.08	0.21 ± 0.08

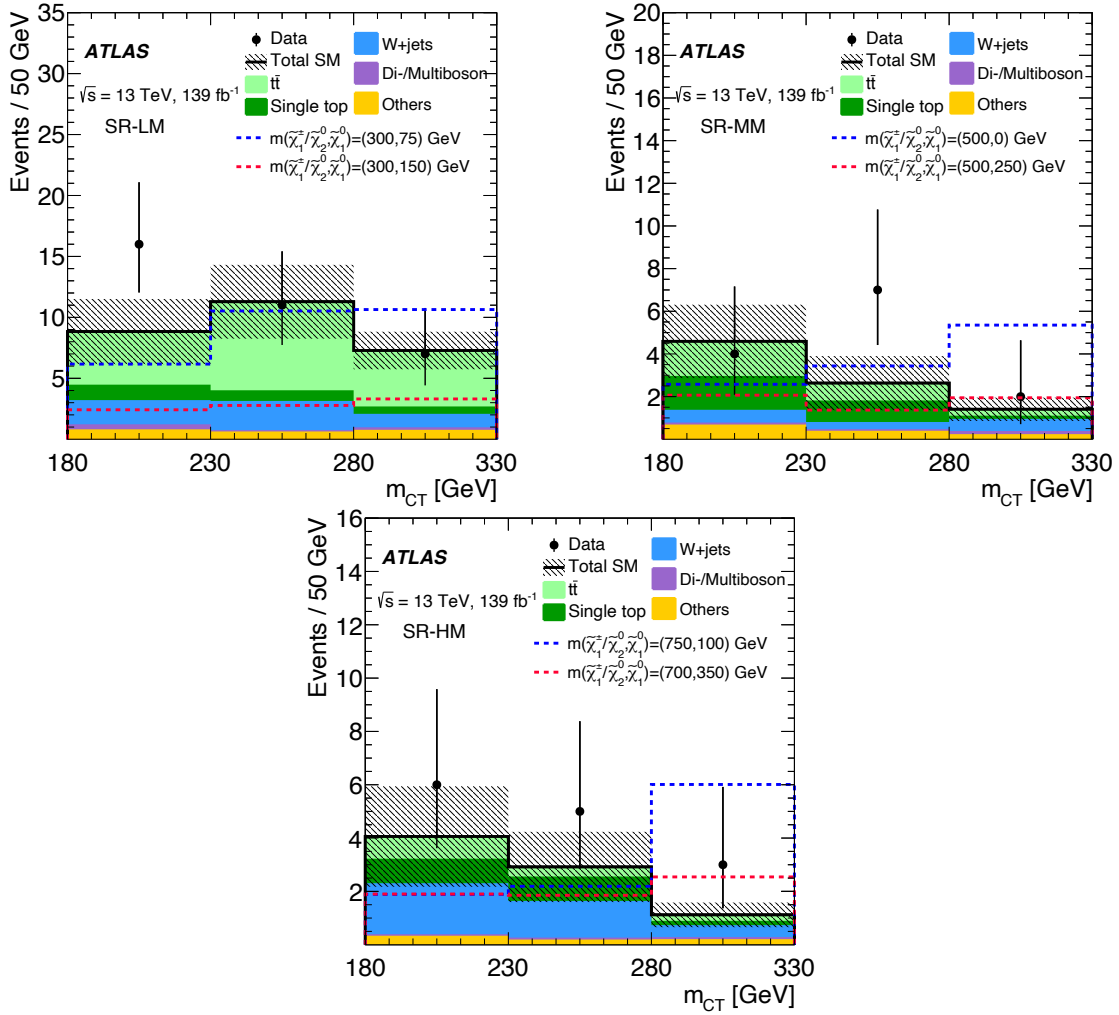


Figure 8.3: Exemplary distribution shown in each exclusion signal region after the background-only fit. The shaded region includes all systematic uncertainties (including correlations) as well as MC statistical uncertainty. Taken from Ref. [184].

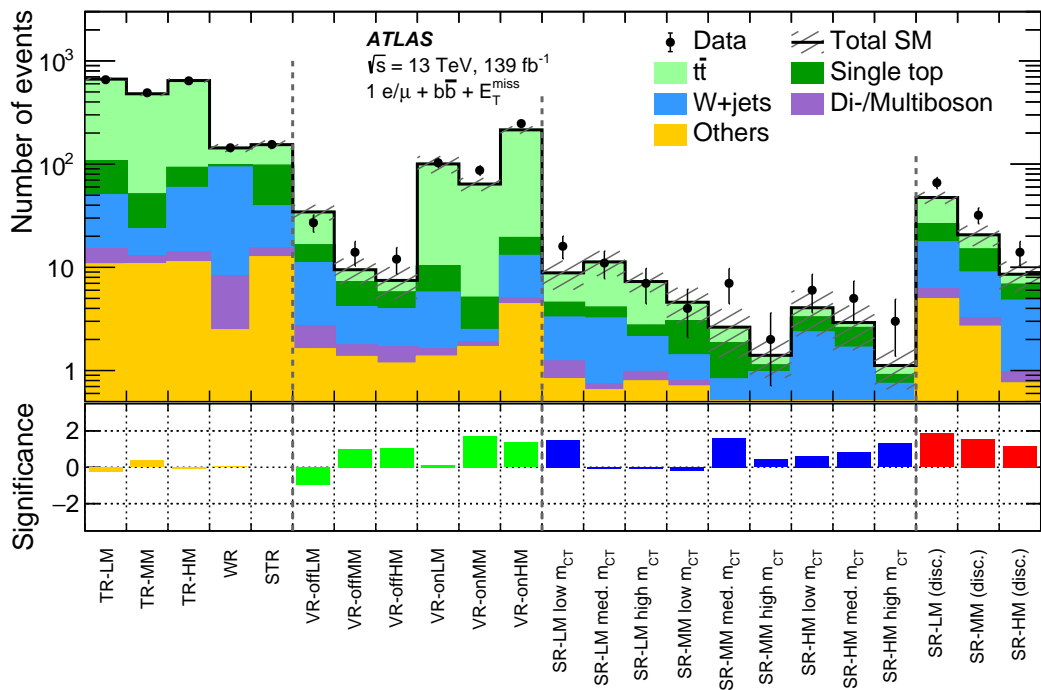


Figure 8.4: Comparison of the observed data and expected event rates in all regions considered in the analysis. The shaded uncertainty band includes both MC statistical and systematic uncertainties. The significances [179] of the differences between the observed data and expected event rates are shown in the bottom panel. The discovery signal regions are not statistically independent from each other, nor from the exclusion signal regions. Figure adapted from Ref. [184].

8.2 Interpretation

As no significant excess of data is observed in any of the signal regions, model-independent upper limits as well as model-dependent exclusion limits are computed.

8.2.1 Model-independent upper limits

Model-independent upper limits on the visible cross section of BSM processes are derived using the discovery signal regions. For this, a likelihood containing terms for the control regions and the discovery signal regions is used. Since the discovery signal regions are not statistically independent from each other, only one region enters the likelihood at a time. This results in three distinct fit configurations in which the signal strength μ is the POI and no signal contamination is assumed in the control regions. The POI is subsequently scanned in distinct steps from zero to high values[†], followed by a hypothesis test at each scan step. The upper limit on the number of observed signal events S_{obs}^{95} is then given by the value of μ for which the corresponding CL_s value drops below 0.05. An upper limit on the visible cross section $\langle \epsilon \sigma \rangle_{\text{obs}}^{95}$ is obtained by dividing S_{obs}^{95} by the integrated luminosity of 139 fb^{-1} . The visible cross section corresponds to the product of the cross section times the acceptance times the efficiency of the analysis selection. In addition to the upper limits on $\langle \epsilon \sigma \rangle_{\text{obs}}^{95}$ and S_{obs}^{95} , table 8.5 also gives the p -values (and corresponding significances) for rejecting the background-only hypothesis in favour of the signal-plus-background hypothesis. As all significances are well below 2σ for all SRs, the background-only hypothesis cannot be rejected.

8.2.2 Model-dependent exclusion limits

For each signal point in the signal grid considered, a separate *exclusion* fit is run using all control regions and exclusion signal regions. As all exclusion signal region bins are mutually exclusive, a likelihood containing terms for all nine signal region bins can be constructed, effectively creating a shape-fit in the binned variables m_T and m_{CT} (cf. chapter 5). As opposed to the background-only fit, the exclusion fits allow for signal contribution in all regions. For each point in the signal grid, the expected and observed CL_s value is calculated using the method discussed in section 3.4. Expected (observed) contour lines can then be drawn at expected (observed)

[†] The signal strength is in principle allowed to exceed unity in order for the scan to find a 95% CL upper limit

Table 8.5: The 95% CL upper limits on the visible cross-section ($\langle \epsilon \sigma \rangle_{\text{obs}}^{95}$) and on the number of signal events (S_{obs}^{95}) are given. Additionally, the expected 95% CL upper limits on the number of signal events if no BSM signal is present (S_{exp}^{95}) are given, including their $\pm 1\sigma$ excursions. The last three columns indicate the confidence level observed for the background-only hypothesis (CL_B), the discovery p -value (p_0) and the significance Z [179].

Signal Region	$\langle \epsilon \sigma \rangle_{\text{obs}}^{95} [\text{fb}]$	S_{obs}^{95}	S_{exp}^{95}	CL_B	p_0	Z
SR-LM (disc.)	0.26	36.8	$20.0^{+8.0}_{-5.4}$	0.97	0.03	1.88
SR-MM (disc.)	0.18	24.8	$15.3^{+6.2}_{-4.6}$	0.94	0.06	1.54
SR-HM (disc.)	0.11	14.7	$9.7^{+3.3}_{-2.7}$	0.89	0.10	1.30

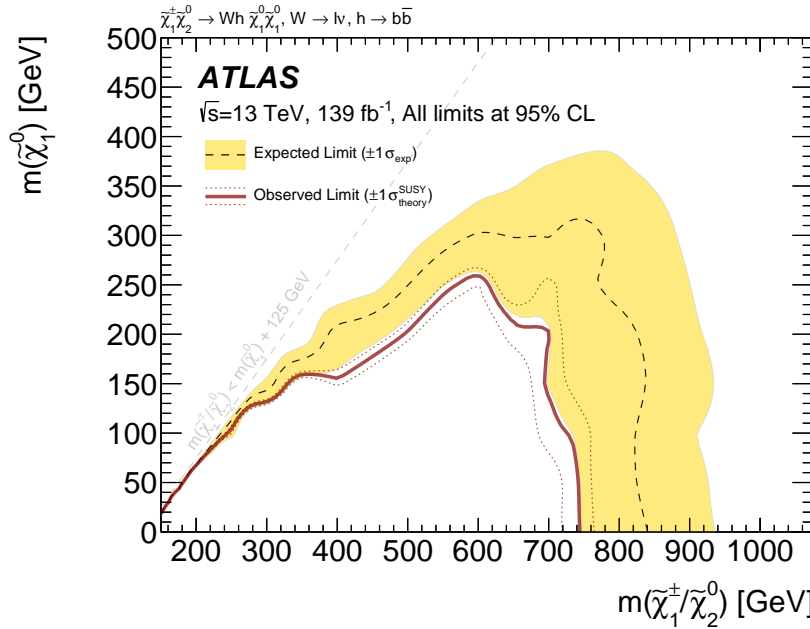


Figure 8.5: Model-dependent exclusion contour on $\tilde{\chi}_1^\pm/\tilde{\chi}_2^0$ pair production. The dashed black line represents the expected limit obtained using Asimov data. The uncertainties are given by the yellow band. The red solid line represents the observed limit obtained using 139 fb^{-1} of data taken by ATLAS. By varying the signal cross sections up and down by their uncertainty, the red dashed lines are obtained. All contours are given at 95% CL. Figure adapted from Ref. [184].

$\text{CL}_s = 0.05$ in the $m(\tilde{\chi}_1^\pm/\tilde{\chi}_2^0)$ - $m(\tilde{\chi}_1^0)$ plane spanned by the simplified model parameters. Signal points inside the contour are then excluded at 95% CL. Figure 8.5 shows the exclusion contours obtained in the signal grid considered for the $\tilde{\chi}_1^\pm \tilde{\chi}_2^0$ simplified model in the 1ℓ search. The dashed black line corresponds to the expected exclusion contour, obtained using the Asimov dataset. The yellow uncertainty band represents the interval containing 68% of all exclusion contours obtained for repeated observations distributed according to the background-only hypothesis. The solid red line represents the observed exclusion limit obtained using the data recorded by ATLAS. As discussed in section 7.2.2, the dashed red lines are obtained by varying the signal cross sections up and down by 1σ .

Due to the slight overfluctuations of data observed in some of the exclusion signal region bins, the observed limit is slightly weaker than the expected one. The observed exclusion limit extends to about 740 GeV in $m(\tilde{\chi}_1^\pm/\tilde{\chi}_2^0)$ for models with a massless $\tilde{\chi}_1^0$, and up to 600 GeV in $m(\tilde{\chi}_1^\pm/\tilde{\chi}_2^0)$ for models with $m(\tilde{\chi}_1^0) = 250$ GeV. This extends the previous limit set by ATLAS in this simplified model and decay channel by more than 200 GeV in $m(\tilde{\chi}_1^\pm/\tilde{\chi}_2^0)$ for a light $\tilde{\chi}_1^0$, an improvement made possible not only by the significant increase in integrated luminosity but also the introduction of a two-dimensional shape fit in the analysis strategy.

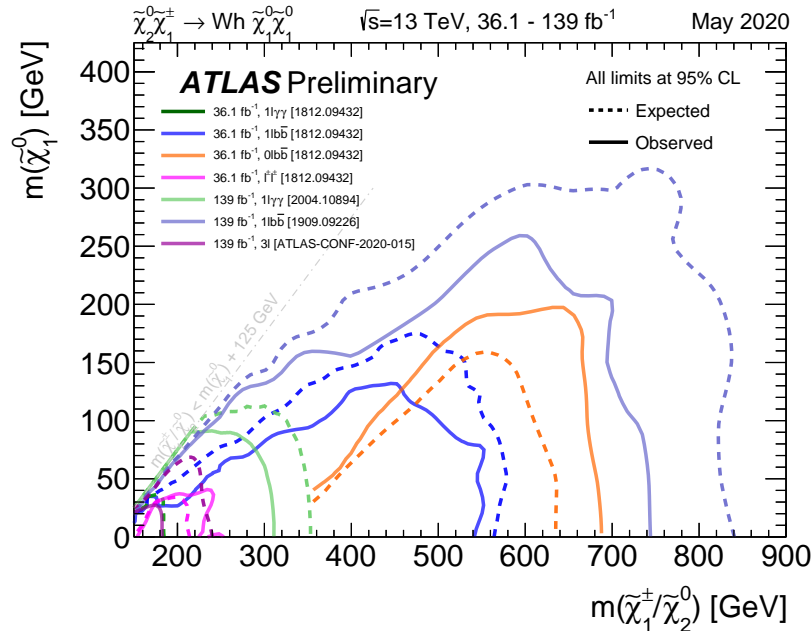


Figure 8.6: Summary of ATLAS limits on $\tilde{\chi}_1^\pm/\tilde{\chi}_2^0$ masses in the $\tilde{\chi}_1^\pm\tilde{\chi}_2^0 \rightarrow Wh\tilde{\chi}_1^0\tilde{\chi}_1^0$ simplified model. The exclusion limit obtained by the analysis presented in this work is referred to as *1Lbb* (the 139 fb^{-1} iteration) and is the most stringent limit in this simplified model set by an ATLAS search thus far. Figure adapted from Ref. [256].

8.3 Discussion

At the time of writing, the limits derived in this analysis are the most stringent limits on the $\tilde{\chi}_1^\pm\tilde{\chi}_2^0 \rightarrow Wh\tilde{\chi}_1^0\tilde{\chi}_1^0$ simplified model set by an ATLAS search, surpassing not only the previous iteration of the analysis [182], but also yielding more stringent limits than those published by ATLAS in other decay channels of the same simplified model [256]. Figure 8.6 shows a summary of results published by ATLAS searches in the $\tilde{\chi}_1^\pm\tilde{\chi}_2^0 \rightarrow Wh\tilde{\chi}_1^0\tilde{\chi}_1^0$ simplified model, the search presented in this thesis is referred therein as ‘*1Lbb*’. Additional ATLAS searches in the 0ℓ as well as 1ℓ final states are being worked on, and are expected to extend the limits[†] on $m(\tilde{\chi}_1^\pm/\tilde{\chi}_2^0)$ up to roughly 1 TeV for massless $\tilde{\chi}_1^0$ as well as slightly extend the excluded parameter space towards the diagonal with $m(\tilde{\chi}_1^\pm/\tilde{\chi}_2^0) = m(\tilde{\chi}_1^0) + m(h)$. Recently, a CMS search for SUSY, interpreted using the same simplified model and targeting the 1ℓ final state has excluded $\tilde{\chi}_1^\pm/\tilde{\chi}_2^0$ masses up to 820 GeV for a massless LSP [257].

Various other searches for SUSY at both ATLAS and CMS are constraining a multitude of supersymmetric particle production and decay processes. The limits on gluino and squark pair production at the LHC are particularly heavily constrained, reaching 2 TeV in many cases. With the large integrated luminosity available through the full Run 2 dataset and the improved analysis techniques and strategies developed over the last years, the typically weaker limits on electroweakinos and sleptons are also significantly increasing and, in some cases, approach the 1 TeV mark (cf. fig. A.10 and Refs. [256, 258]). The diverse SUSY search programs at ATLAS and CMS thus increasingly constrain the existence of SUSY at the TeV scale at the LHC.

[†] Assuming that no significant excess in data is seen in the search regions of these analyses.

Still, a number of arguments can be made that discarding the possibility for SUSY to exist at the energies available with the LHC is much too early. By the end of the lifetime of the LHC (including the high luminosity upgrade HL-LHC), a projected amount of 3000 fb^{-1} [259] will have been delivered to the particle physics experiments. Many supersymmetric models not accessible with the full Run 2 dataset using today’s analyses will hence only come into reach in the upcoming runs of the LHC.

More importantly however, most of the quoted limits assume simplified models and are thus only valid if the assumptions of the respective simplified model are satisfied. In any realistic supersymmetric scenario that might be realised in nature and is accessible to the LHC, assumptions like 100% branching fractions or a small set of supersymmetric particles participating in the decay chains are likely not exactly fulfilled. Thus, the quoted simplified model limits can in general not be trivially interpreted as the true underlying constraint on the respective parameter of a more realistic supersymmetric scenario. Due to the optimistic assumptions like 100% branching fractions, the true constraints will in general be weaker than the simplified model limits. Reinterpretations of Run 1 ATLAS searches for SUSY in the pMSSM [82] have indeed shown that, in more complex SUSY models, constraints on the supersymmetric masses are somewhat weaker than those quoted for the simplified models studied in the respective analyses.

Naturally, there is thus a large interest in the HEP community—both within ATLAS as well as outside of the collaboration—to perform reinterpretations of the existing searches for SUSY in new, promising signal models. Compelling reasons for performing reinterpretations include, amongst others, the possibility to state a combined sensitivity of the ATLAS SUSY search program to more realistic and complex SUSY scenarios (compared to the simplified model limits). Such models are, however, embedded in high-dimensional parameter spaces and depend on a large set of parameters. Reinterpretations in such high-dimensional parameter spaces, like e.g. the pMSSM, quickly become computationally expensive (or even unfeasible) and therefore require appropriate approximations. For this reason, the next part of this thesis will introduce and discuss some of these approximations and apply them in a reinterpretation of the 1ℓ search in the pMSSM.

Part III

Reinterpretation

Chapter 9

Preservation and reusability

The current particle physics experiments are designed to collect physics data over a span of several decades, and operate at scales and complexities that make it impossible for the experiments to be repeated in the foreseeable future. The data taken at these experiments and physics results derived are thus highly valuable and major problems arise from a scientific reproducibility point of view.

In the following, reusability problems directly related to an individual analysis are discussed, and approaches taken in view of analysis preservation and reinterpretation are presented. This chapter starts with a brief motivation for reinterpretations, followed by a description of the main ingredients required. The remaining sections discuss three separate efforts aiming to improve the reinterpretability of the 1ℓ search in light of new signal models. All three efforts are not only relevant in the scope of this thesis, but also for reinterpretation activities currently ongoing in ATLAS.

9.1 The case for reinterpretations

9.1.1 Motivation

Designing and executing searches for BSM physics requires a substantial amount of person-power and computing resources. As laid out in detail in part II of this thesis, an analysis generally aims to design signal regions in which a given BSM signal can be efficiently discriminated against SM background. Although the careful design of such regions already requires a significant amount of resources, it constitutes only a fraction of the work necessary for concluding the search. Contributions in the signal regions from SM processes need to be estimated, usually requiring expensive MC simulations and the development of background estimation strategies. Systematic uncertainties arising from numerous sources need to be considered and their impact estimated. For the BSM signal, a similar processing pipeline involving MC simulation, event reconstruction and event selection including uncertainties needs to be executed. Furthermore, recorded data also has to be reconstructed and processed through the analysis-specific event selection. Only after the expected and observed event rates in all regions are known, can the statistical evaluation be performed.

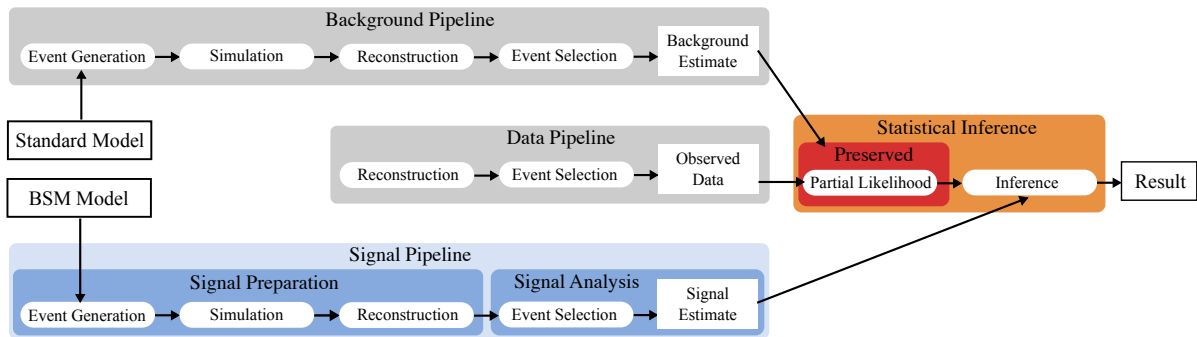


Figure 9.1: Full analysis workflow including the three main processing pipelines for deriving background and signal estimates as well as observed data rates. The outputs of the three processing pipelines are combined into a likelihood forming the basis for the statistical inference. In a RECAST setup (details in the text), the estimated background rates and observed data are archived, and the signal pipeline is fully preserved, such that it can be re-executed with different inputs at any time. Figure recreated from Ref. [261].

As shown in fig. 9.1, an analysis can thus be divided into three main processing pipelines; a *background pipeline*, a *signal pipeline* and a *data pipeline*. After all three processing pipelines are concluded, the next analysis step can be performed—the *statistical inference*, producing the final analysis results, like quantifying excesses in data or setting limits on model parameters.

Due to the substantial amount of resources necessary for developing and performing an analysis, it is not feasible to develop dedicated searches for every possible BSM scenario. Instead, analyses are typically only interpreted in a finite set of models with a small number of free parameters that need to be varied. Still, it is likely that a given analysis is sensitive to a variety of different BSM scenarios not considered in the original publication.

Consequently, it is not surprising that there is significant interest in the HEP community to reinterpret BSM searches in different signal models. Reinterpretations of ATLAS searches for SUSY are routinely performed by various reinterpretation efforts. In the context of direct constraints on BSM physics, the search results published by the experimental collaborations represent the only windows into the LHC data that are available to the wider HEP community. Reinterpretations of BSM searches are thus the only possibility to determine the implications of LHC data for a broad range of models [260].

As will be discussed in detail in chapter 11, reinterpretations are not only of interest for the wider HEP community, but also for the experimental collaborations themselves. Within ATLAS, reinterpretations of SUSY searches in complete SUSY models can, for example, serve as powerful tools to state a comprehensive summary of the overall sensitivity to realistic supersymmetric models. As such, the efforts discussed in the remainder of this chapter, as well as chapters 10 and 11, are not only relevant for the work presented in this thesis, but also reinterpretation efforts currently ongoing in ATLAS.

9.1.2 Approaches for reinterpretations

As the event selection of an analysis is fixed, the pre-fit background estimates and observed data in the regions of interest of the analysis do not change. Hence, the data and background pipelines

shown in fig. 9.1, entering the statistical inference of the analysis by means of event rates, can be archived in a format significantly smaller than the original input data. In consequence, reinterpreting a search in the light of a new signal model requires the re-execution of two main analysis ingredients with (partially) new inputs; the signal pipeline and the statistical inference.

Recently, it has become possible to preserve, in a pure-text format [161], the partial analysis likelihood[†] built from the background estimates and observed data, including all auxiliary data and details of the statistical model used for inference. In fig. 9.1, this is indicated through a red rectangle. Once the signal estimates are known, a new full analysis likelihood can be built, and the viability of the new signal model can be tested with respect to the analysis in question. The publication of the likelihood of the 1ℓ search will be discussed further in section 9.2.

Different approaches can be taken for rendering the signal pipeline reusable to the extent that signal estimates for a new BSM scenarios of interest can be derived. Manifestly the most precise approach involves executing the original analysis software, but using a different BSM model as input. As this requires the preservation of the entirety of the original software environment, including the workflows used in the analysis, this is arguably the most involved approach, especially since it involves executing the computationally expensive detector simulation. A framework designed to facilitate such an effort, called RECAST and originally proposed in Ref. [262], is under development and aims to provide the cyber-infrastructure needed for offering *reinterpretations as a service*. Through a web interface, physicists wishing to reinterpret a search with RECAST, would provide an alternative BSM model and trigger a computational workflow that would re-execute the original analysis using the new signal inputs and ultimately deliver the *recasted* results. An attempt to fully preserve the 1ℓ search using the RECAST paradigm is discussed in section 9.3.

As the details of the existing RECAST implementations of ATLAS searches for SUSY are not publicly available, but only meant to be interacted with through a RECAST request, the exact implementation of the analysis selection is in general not available outside the ATLAS collaboration. For this reason, a number of public tools aiming to reimplement an approximated version of the event selections of a number of BSM searches at the LHC are available. Prominent examples include CHECKMATE [263, 264] and MADANALYSIS5 [265]. ATLAS has internally maintained a similar catalogue of its SUSY analyses and is publishing event selection snippets in C++ for many SUSY searches on HEPDATA [266], a repository for high energy physics data. Recently, this package maintained by ATLAS, called SIMPLEANALYSIS [267], has been made publicly available, allowing the C++ snippets published to be executed outside the collaboration.

A crucial step, necessary for achieving a reliable reimplementation of the signal pipeline, is the detector simulation. Executing the full detector simulation requires access to the collaborations's detector description and is computationally expensive, disfavouring[§] its usage in the context of large-scale reinterpretations over a large set of models. For this reason, it is often approximated using simplified detector geometries and granularities. The most commonly used package for a fast detector simulation outside of the ATLAS collaboration is DELPHES [268], which is used in, e.g., CHECKMATE and MADANALYSIS5. Other packages like, e.g., RIVET [269, 270] approximate the detector response using dedicated four-vector smearing techniques, assuming that the detector response roughly factorises into the responses of single particles. Internally,

[†] As before, this only refers to likelihoods built using the HISTFACTORY template.

[§] This is especially true for reinterpretation efforts outside the ATLAS collaboration, which, for reasons not discussed herein, cannot make use of the collaboration's detector description.

ATLAS also maintains a dedicated framework for four-vector smearing, used in scenarios where other fast simulation techniques are still too expensive. Section 9.4.2 discusses these dedicated smearing functions further.

Finally, instead of trying to estimate the signal rates of a new model using MC simulation and (reimplemented) analysis event selections, some reinterpretation efforts like, e.g., SMODELS [271, 272], use *efficiency maps* encoding the selection and acceptance efficiencies of the analysis as a function of the model parameters (typically the sparticle masses in the case of SUSY searches) and analysis selections. Such efficiency maps are routinely published on HEPDATA by ATLAS SUSY searches, and allow for efficient reinterpretations, as long as the signal efficiencies mostly depend on the signal kinematics and are largely independent from the specific details of the signal model [271]. For the 1ℓ search presented herein, the efficiency maps, including additional analysis data products, are available at Ref. [273].

9.2 Public full likelihood

The likelihood is arguably one of the most information-dense and important data products of an analysis. If the exact likelihood function of the original analysis is not known in reinterpretation efforts[†], approximations need to be made for the statistical inference, e.g. in terms of the correlations between event rate estimates as well as the treatment of uncertainties. Recently, ATLAS has started to publish full analysis likelihoods built using the HISTFACTORY pdf template [161]. This effort has been facilitated by the development of `pyhf` (cf. section 3.1), in conjunction with the introduction of a JSON specification fully describing the HISTFACTORY template. As a pure-text format, the JSON likelihoods are human- and machine-readable, highly compressible and can easily be put under version control, all of which are properties that make them suitable for long-term preservation, which is a crucial condition for reinterpretations.

The full likelihood of the 1ℓ search is publicly available at Ref. [274] and is not only heavily used in the following chapters, but also in various analysis reinterpretation and combination efforts currently ongoing in ATLAS. Several efforts outside of the ATLAS collaboration have already included the analysis likelihood into their reinterpretations, and the SMODELS [275] and MADANALYSIS5 [276, 277] collaborations have both reported significant precision improvements through its use. Furthermore, the full likelihood of the search presented herein has recently been used to demonstrate the concept of scalable distributed statistical inference on high-performance computers (HPCs) [278]. Through the `funcX` package [279], `pyhf` is used as a highly scalable *function as a service* to fit the entire 1ℓ signal grid of 125 signal points with a wall time of 156 s using 85 available worker nodes[§].

[†] Up until recently, the exact likelihood function was not part of the data products published by ATLAS searches for SUSY, hence approximations of the statistical models were a crucial part of most reinterpretation efforts.

[§] These benchmarks use `pyhf`'s NUMPY backend and SCIPY optimiser, a combination that has a slower log-likelihood minimisation time than e.g. PYTORCH coupled with SCIPY, as will be shown in section 10.3.

9.3 Full analysis preservation using containerised workflows

For an analysis to be fully reusable under the RECAST paradigm, the signal pipeline of the original analysis (cf. fig. 9.1) needs to be preserved such that it can be re-executed on new inputs. As typically only the processing steps after the event reconstruction are analysis-specific, it is sufficient to preserve this part of the signal pipeline. Processing steps including and preceding the event reconstruction only involve the central ATLAS production system, introduced in section 2.2.8, and result in an ATLAS-internal data format serving as input for physics analyses. These processing steps are preserved using centrally provided ATLAS infrastructure and thus do not need to be within the scope of the preservation discussed in the following.

In the following, the term *signal analysis* (cf. fig. 9.1) will refer to the analysis-specific processing steps that are not handled by the central ATLAS production system, typically starting with the selection of events that have passed the reconstruction step in fig. 9.1, provided in the aforementioned internal data format. Preserving the signal analysis not only needs preservation of the full software environment required for the different processing steps, but also knowledge of the correct usage of the software through parameterised job templates together with a workflow graph connecting the different processing steps. A graph representation of the entire analysis, implemented in RECAST is shown in fig. 9.2.

9.3.1 Software preservation

As much of the software is only tested, validated and deployed on a narrow set of architectures and platforms, the full software environment defining an analysis pipeline not only includes the original analysis-specific code used for object definitions, calibrations, event selection and statistical inference, but also the operating system used, and a number of low-level system libraries that the applications depend upon. Preserving the full software environment can be achieved through the use of *Docker containers* [280, 281], a technology that—except for the operating system kernel—packages the full software environment in a portable data format, including a layered file system, the operating system as well as the actual application and all of its dependencies. As opposed to full virtualisation, Docker containers do not rely on actual hardware virtualisation but share the operating system kernel with the host. As such, they only interact with the host through system calls to the Linux kernel [281], offering a highly stable interface. This makes Docker containers a well-suited solution for deploying isolated applications on a heterogeneous computing infrastructure.

Due to the specific software structure of the 1ℓ search, a containerisation requires a total of three container images. Two images contain the software necessary for performing the physics object calibrations and event selection, as well as the conversion of the information in a format that can be used by the downstream steps. The third image contains the software necessary for the statistical inference, relying on the `pyhf`-implementation of the HISTFACTORY models in order to benefit from the possibility of using a partial JSON likelihood to preserve background and data rates.

The Docker images are built from suitable base images containing the software environment used for deriving the published 1ℓ search results, expanded with the relevant analysis software. All docker images are subject to version control and continuous integration, such that changes

to the underlying software environment can be tracked and tagged. This allows for a consistent preservation of multiple versions of the analysis pipeline.

9.3.2 Processing steps preservation

Preserving the software environment is not sufficient, as detailed instructions on how to use it have to be given. This is achieved through parameterised job templates that specify the precise commands and arguments required to re-execute the analysis code for specific processing steps. As re-executing the analysis pipeline using different signal models involves varying input parameters, all job template parameters are exposed to the user. In fig. 9.2, the parameterised job templates including their output are shown as blue rectangles, connected together through a workflow specification represented via black arrows.

User-specifiable arguments and inputs to the event selection and physics object calibration step include the actual reconstructed MC events in the aforementioned ATLAS-internal format, obtained through the central ATLAS production system, as well as corresponding files necessary for the pile-up correction in MC. In addition, the signal process cross section as well as MC generator-level efficiencies need to be given for the correct normalisation of the estimated signal rates to the integrated luminosity of the full Run 2 dataset. For each new signal model to be tested, three MC samples need to be provided, generated with specific pile-up profiles close to the pile-up profile in data during the 2015–2016, 2017 and 2018 data-taking periods, respectively[†]. In all three jobs, the events processed are weighted according to the integrated luminosity of the data-taking period they represent within the full Run 2 dataset. A subsequent *merging* step uses the same docker image as the previous processing step, and serves to merge the three produced outputs into a single ROOT file that can be read by the subsequent step.

In addition, a JSON file containing theory uncertainties on the expected signal rates can be provided. These are optional and do not have to be specified if deemed to be negligible for the signal model under consideration.

The statistical inference step requires, as external input, the archived partial likelihood containing observed data as well as expected background rates including systematic variations thereof. This step generates a new full analysis likelihood and performs the necessary hypothesis tests.

9.3.3 Workflow preservation

Finally, the preserved processing steps need to be linked together, creating a parameterised workflow completely defining the analysis pipeline, starting from centrally produced MC datasets up to the statistical inference results. Within RECAST, this is achieved using the workflow description language `yadage` [282], capturing the full workflow in YAML format. The workflow uses the job templates and defines their processing order and dependencies.

The RECAST implementation of the analysis presented in this work has been validated against original analysis inputs. The expected and observed CL_s values derived in the original analysis were successfully re-derived using the containerised workflow implementation. On a non-isolated CPU, the full preserved analysis pipeline for a single signal model can be executed with a wall

[†] This allows to have pile-up weights relatively close to unity, avoiding unnecessary statistical dilution.

time of about 50 min. Due to the highly portable nature of the containerised workflow, the pipeline can easily be run in a distributed setup, allowing scalable reinterpretations at full analysis precision. Although not explicitly used in the remainder of this thesis, the RECAST implementation of the 1ℓ search is crucial for the large-scale reinterpretation efforts in the pMSSM currently ongoing in ATLAS (and discussed to some extent in chapter 11). In these efforts, the RECAST implementation allows the systematic reinterpretation of the 1ℓ search in any pMSSM model of interest using the full analysis precision.

9.4 Truth-level analysis

A full preservation of the entire analysis pipeline, as presented in the previous section, is highly desirable as it allows for a maximum precision reinterpretation of the original analysis using a new BSM model. As the full detector simulation needs a significant amount of computing resources in addition to the non-negligible wall time of the actual preserved analysis pipeline, this approach can only be used on a limited set of models. In large-scale reinterpretations over high-dimensional parameter spaces, the amount of models that need to be sampled and investigated using the analysis is too high to employ the fully preserved analysis pipeline in every case. In order to significantly reduce the number of models that need to be passed through the full analysis pipeline, a pre-sorting of the models needs to be performed, filtering models for which (non-)exclusion based on a simplified analysis implementation is uncertain.

In the following, two major, complementary approaches to analysis simplifications are discussed, targeting both the *signal pipeline* as well as the *statistical inference* blocks in fig. 9.1. This section discusses the SIMPLEANALYSIS implementation of the analysis, an approach implementing the signal pipeline at *truth-level*, i.e. using the generator-level objects without running a dedicated detector simulation. An approximation of the detector response using four-vector smearing techniques is discussed.

The second simplification is discussed in chapter 10, introducing a procedure for building simplified likelihoods from the full likelihoods of ATLAS SUSY searches in order to significantly lower the wall time needed for the statistical inference. In chapter 11, both approximations are combined and applied on a set of SUSY models sampled from the pMSSM.

9.4.1 Truth-level selection

All signal and control regions considered in the original 1ℓ search are implemented at truth-level using the publicly available framework SIMPLEANALYSIS. The exact implementation has been published, together with the previously discussed efficiency maps and analysis likelihood, as part of the auxiliary analysis data at Ref. [273]. In fact the SIMPLEANALYSIS implementation of the search was already used in chapter 7 for the derivation of some of the theory uncertainties.

The truth-level implementation explicitly specifies all object definitions introduced in section 4.4, even though some of them, like the lepton isolation, are technically not well-defined at truth-level. The four-vector smearing subsequently described is, however, in many cases implemented as a function of said object definitions and hence still allows to consider them to some extent. Additionally, as discussed in section 9.1, the full specification of the original analysis event selection including all object definitions allows for more straightforward reinterpretations by

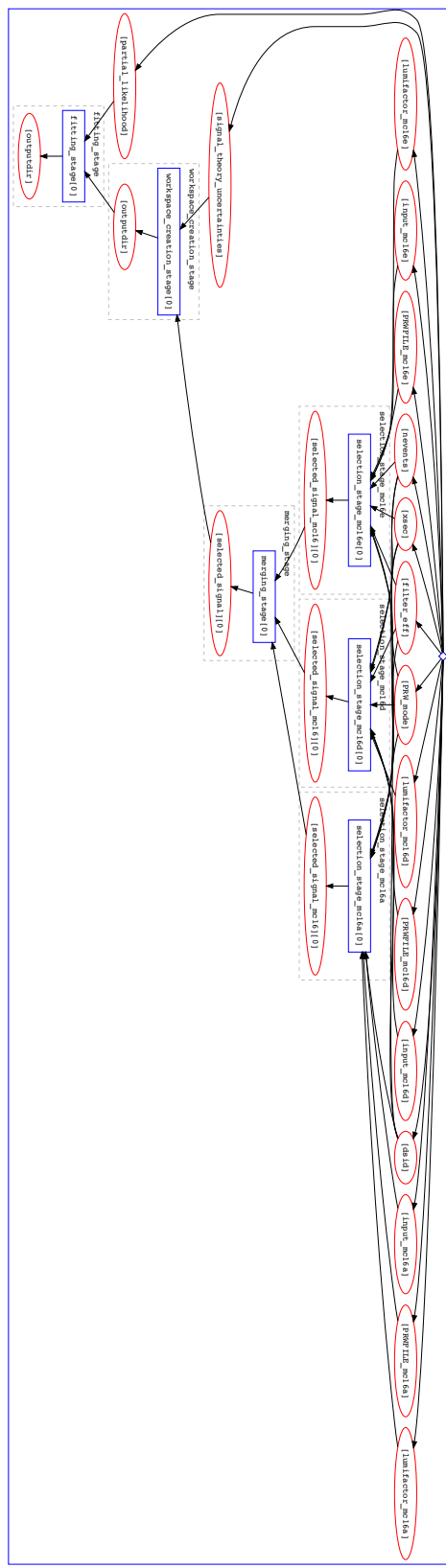


Figure 9.2: Graph of the workflow as specified for the analysis pipeline. The containerised processing steps are represented as blue rectangular nodes, while input parameters, input files and outputs are shown as red oval nodes. The workflow is comprised of four processing steps: `selection_stage_mc16(a,d,e)`, `merging_stage`, `workspace_creation_stage` and `fitting_stage`. The first two steps perform the object calibration, event selection and merging of the three MC datasets representing the three data-taking periods 2015–2016, 2017 and 2018. The latter two steps implement the generation of the signal JSON patch as well as the final statistical inference. Compared to fig. 9.1 the first two steps implement the *signal analysis* part, while the latter two steps implement the *statistical inference* deriving the final results.

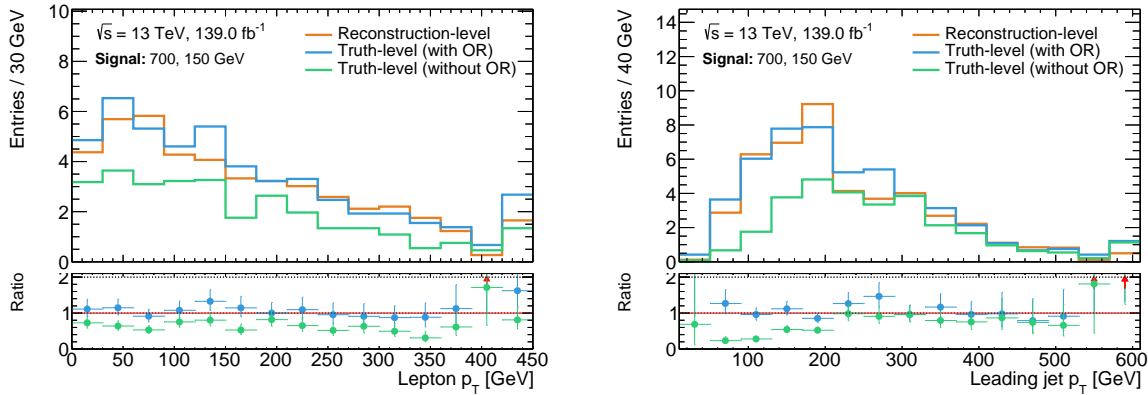


Figure 9.3: Impact of the overlap removal (OR) procedure at truth-level illustrated in the lepton and leading jet transverse momenta distributions. The truth-distributions with (blue) and without (green) overlap removal (green) are compared with a reconstruction-level (orange) distribution. The exemplary benchmark signal point with $m(\tilde{\chi}_1^\pm/\tilde{\chi}_2^0), m(\tilde{\chi}_1^0) = 700, 150 \text{ GeV}$ is shown in both plots. Both truth-level distributions are shown after smearing. All distributions are shown in a loose preselection requiring exactly one lepton, $E_T^{\text{miss}} > 50 \text{ GeV}$, $m_T > 50 \text{ GeV}$, and 2–3 jets, two of which need to be b -tagged.

efforts outside of the ATLAS collaboration that generally do not have access to the original analysis software.

Following the object definitions, an overlap removal procedure following the same prescription as described in section 4.5 for the reconstruction-level analysis is performed, i.e. especially also using the same shrinking cone definitions. Since tracking information is not available at truth-level, the overlap removal step removing electrons sharing a track with a muon is approximated by using a distance parameter of $\Delta R = 0.01$ between the objects. Although often neglected[†] in reinterpretation efforts outside of the collaboration, the correct implementation of the overlap removal procedure employed in the original analysis is crucial to reproduce the signal estimates of the original analysis. Figure 9.3 illustrates this by showing exemplary kinematic distributions of an exemplary signal point in configurations with and without overlap removal at truth-level, and comparing it with the distributions obtained at reconstruction-level[§]. Not implementing the overlap removal procedure of the original 1ℓ search, results in many truth-level events not passing the analysis selections because of additional objects in the final state that would otherwise have been removed through the overlap removal.

Finally, the exact implementation of all analysis observables is explicitly given, followed by the definition of all control and signal regions.

9.4.2 Truth smearing

The general assumption of the truth smearing applied in the following is that the detector response roughly factorises into the responses of single particles. This allows to use the ATLAS

[†] The overlap removal procedures in ATLAS SUSY searches tend to be quite intricate, making them non-trivial to re-implement without ATLAS and analysis-specific knowledge.

[§] The term *reconstruction-level* here refers to distributions obtained with MC simulated datasets for which the full detector simulation and reconstruction has been run.

detector performance results in order to construct detector response maps parameterised in different observables for each physics object. Detector response maps include object reconstruction and identification efficiencies as well as scale factors to correct for differences between MC and observed data. Likewise, effects from the finite resolution of energy measurements in the detector are modelled through energy resolution maps. In the following, the four-vector components of electrons, muons, jets and E_T^{miss} are smeared.

In the case of truth electrons, the identification efficiencies considered are parameterised in η and p_T as well as the identification working point used [222]. In η , nine fixed-width bins are used. In p_T , six bins are implemented and a linear interpolation between two adjacent p_T -bins is used to get the efficiency for the given p_T of each truth electron. The probability of finding a fake electron in a truth jet is estimated through a similar two-dimensional map depending on the truth jet η and p_T , again using fixed-width bins in η and a linear interpolation in p_T . The range of the p_T interpolation for identification efficiencies and fake rates extends from 7 GeV to 120 GeV, covering the majority of all electrons in the analysis. If the truth p_T of the electron is outside of that range, the identification efficiency and fake rate from the respective bound of the corresponding η -bin are used. The probability for misidentifying an electron as a photon is estimated using different fixed values for the barrel and end-cap regions [221]. Finally, the transverse energy of the electron is smeared using a random number drawn from a Gaussian distribution with standard deviation corresponding to the η - and p_T -dependent energy resolution, measured in $Z \rightarrow ee$ and $J/\Psi \rightarrow ee$ events [283].

For truth muons, the identification efficiencies are also parameterised in η and p_T as well as the identification working point used [224]. Similar to truth electrons, the p_T of the muon is smeared using a Gaussian distribution with standard deviation corresponding to the momentum resolution. The momentum resolution of combined truth muons, σ_{CB} , is computed from the resolutions in the ID, σ_{ID} , and MS, σ_{MS} , as

$$\sigma_{\text{CB}} = \frac{\sigma_{\text{ID}}\sigma_{\text{MS}}}{\sqrt{\sigma_{\text{ID}}^2 + \sigma_{\text{MS}}^2}}, \quad (9.1)$$

where σ_{ID} and σ_{MS} are parameterised in η and p_T and measured in $Z \rightarrow \mu\mu$ and $J/\Psi \rightarrow \mu\mu$ events [223].

The transverse momentum of truth jets is smeared using a Gaussian with standard deviation equal to the JER, provided in a map parameterised in five bins in $|\eta|$, ranging from $|\eta| = 0$ to $|\eta| = 4.5$. The jet energy resolutions are measured in dijet events [228] and provided as parameterisations of a noise N , stochastic S and constant C term for each of the seven bins in $|\eta|$, such that the resolution can be computed as

$$\frac{\sigma(p_T)}{p_T} = \frac{N}{p_T} \oplus \frac{S}{\sqrt{p_T}} \oplus C. \quad (9.2)$$

Only truth jets with $10 \text{ GeV} < p_T < 1.5 \text{ TeV}$ are smeared. For truth jets with $p_T > 20 \text{ GeV}$, the flavour tagging efficiency is considered using efficiencies parameterised in η , p_T and the MV2c10 efficiency working point (introduced in section 4.4) used, measured in fully reconstructed simulated $t\bar{t}$ events [234].

Finally, the smeared missing transverse energy is computed using the transverse momenta of all smeared truth objects in the event, including an approximation for the track soft term. The

latter is approximated using resolution measurements from $Z \rightarrow \ell\ell$ events [237], allowing to infer a distribution of the mean soft term projected in the direction longitudinal to the total transverse momentum of all hard objects in an event, $\mathbf{p}_T^{\text{hard}}$. The measured resolution parallel and perpendicular to $\mathbf{p}_T^{\text{hard}}$ is then used to smear the nominal soft track value.

9.5 Validation of the truth-level analysis

9.5.1 Validation in loose preselection

The performance of the truth smearing is illustrated in fig. 9.4 in a loose preselection for an exemplary benchmark signal point. The loose preselection applied requires a final state with exactly one lepton, $E_T^{\text{miss}} > 50 \text{ GeV}$, $m_T > 50 \text{ GeV}$, and 2–3 jets, two of which need to be b -tagged. The reconstruction-level distributions are compared with the truth-level distributions before and after truth smearing. It can be observed that the truth smearing noticeably improves the agreement between the truth- and reconstruction-level distributions. While the lepton and jet reconstruction and identification efficiencies are—due to their dependence on η , p_T and individual working points—crucial for the overall agreement in shape, especially at low p_T , the inclusion of flavour-tagging efficiencies significantly improves the overall agreement in normalisation.

Although some minor differences remain, a good agreement is observed overall across the relevant kinematic distributions at loose preselection level. Most of the differences remaining between smeared truth-level and reconstruction-level distributions in individual bins are well within the MC statistical uncertainties arising from the relatively limited MC statistics available.

9.5.2 Validation in signal regions

As the expected signal rates in the signal regions are ultimately what is entering the statistical inference, it is important that the good agreement observed at preselection is still present in the kinematically tighter selections of the signal regions. Additionally, it is worth investigating the agreement across all signal models considered in the original analysis, as opposed to only validating specific benchmark points. A comparison of the reconstruction-level and truth-level event rates before and after smearing in the signal regions SR-LM, SR-MM and SR-HM for all signal models considered in the 1ℓ search is shown in fig. 9.6. For the sake of conciseness, only the cumulative m_{CT} bins are shown in each signal region in fig. 9.6. The agreement in the individual m_{CT} bins in each SR-LM, SR-MM and SR-HM is provided in figs. B.1 to B.3.

The truth smearing drastically improves the agreement in event rate estimates at truth- and reconstruction-level across all SR bins. While, compared to reconstruction-level, the event rates are generally overestimated at truth-level before smearing, both tend to agree well within statistical uncertainties after smearing.

9.5.3 Validation using likelihood

Using the nominal expected event rates at (smeared) truth-level for every signal model in the original signal grid considered in the 1ℓ search, expected and observed CL_s values can

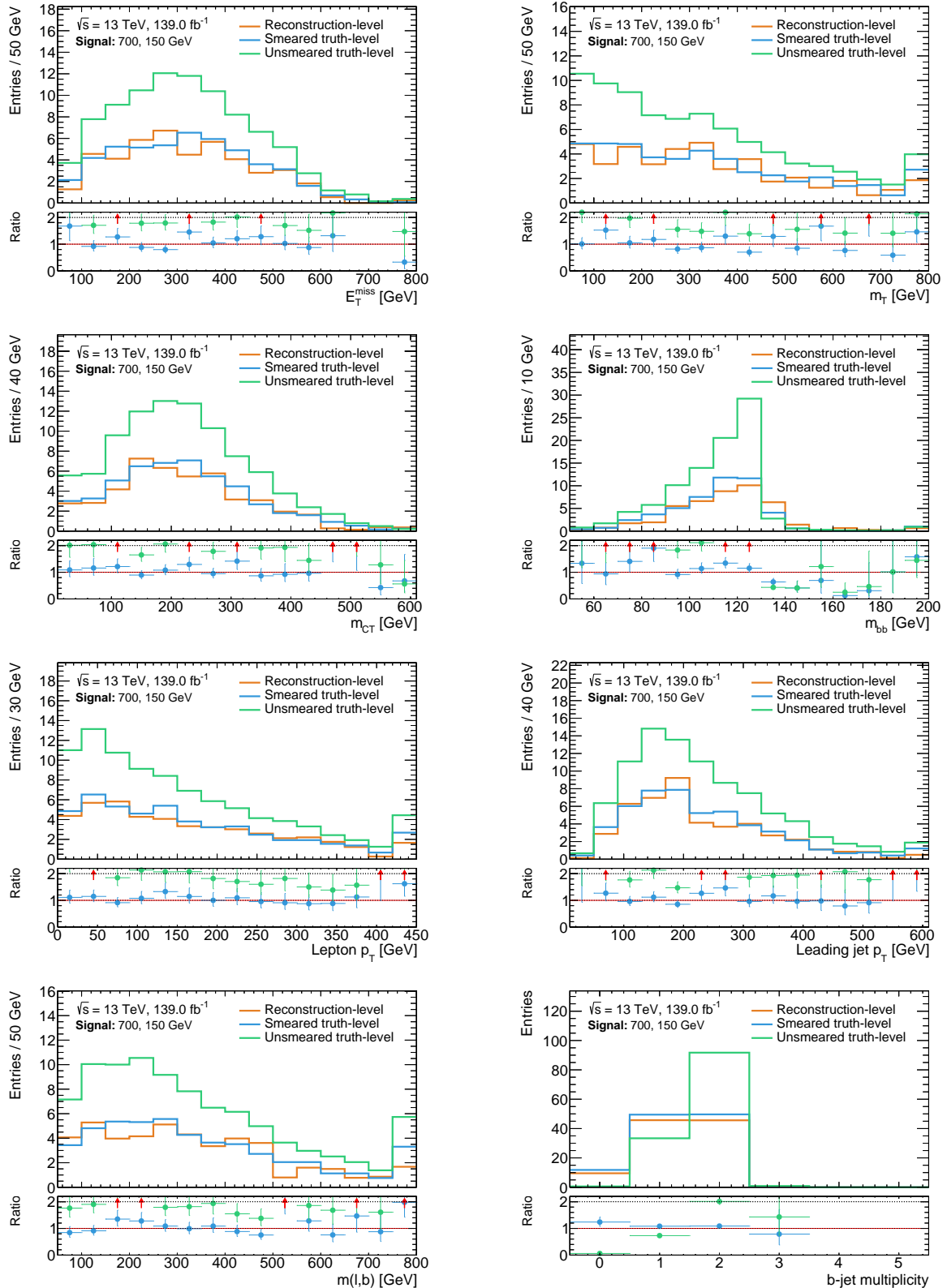


Figure 9.4: Comparisons of the kinematic distributions of key observables at (smeared) truth- and reconstruction-level. The exemplary benchmark signal point with mass parameters $m(\tilde{\chi}_1^\pm/\tilde{\chi}_2^0), m(\tilde{\chi}_1^0) = 700, 150 \text{ GeV}$ is shown. The ratio pad shows the ratio of smeared and unsmeared truth-level distributions (blue and green) to reconstruction-level distributions (orange). Only MC statistical uncertainty is included in the error bars. All distributions are shown in a loose preselection requiring exactly one lepton, $E_T^{\text{miss}} > 50 \text{ GeV}$, $m_T > 50 \text{ GeV}$, and 2–3 jets, two of which need to be b -tagged. The latter requirement is dropped for the b -jet multiplicity distribution.

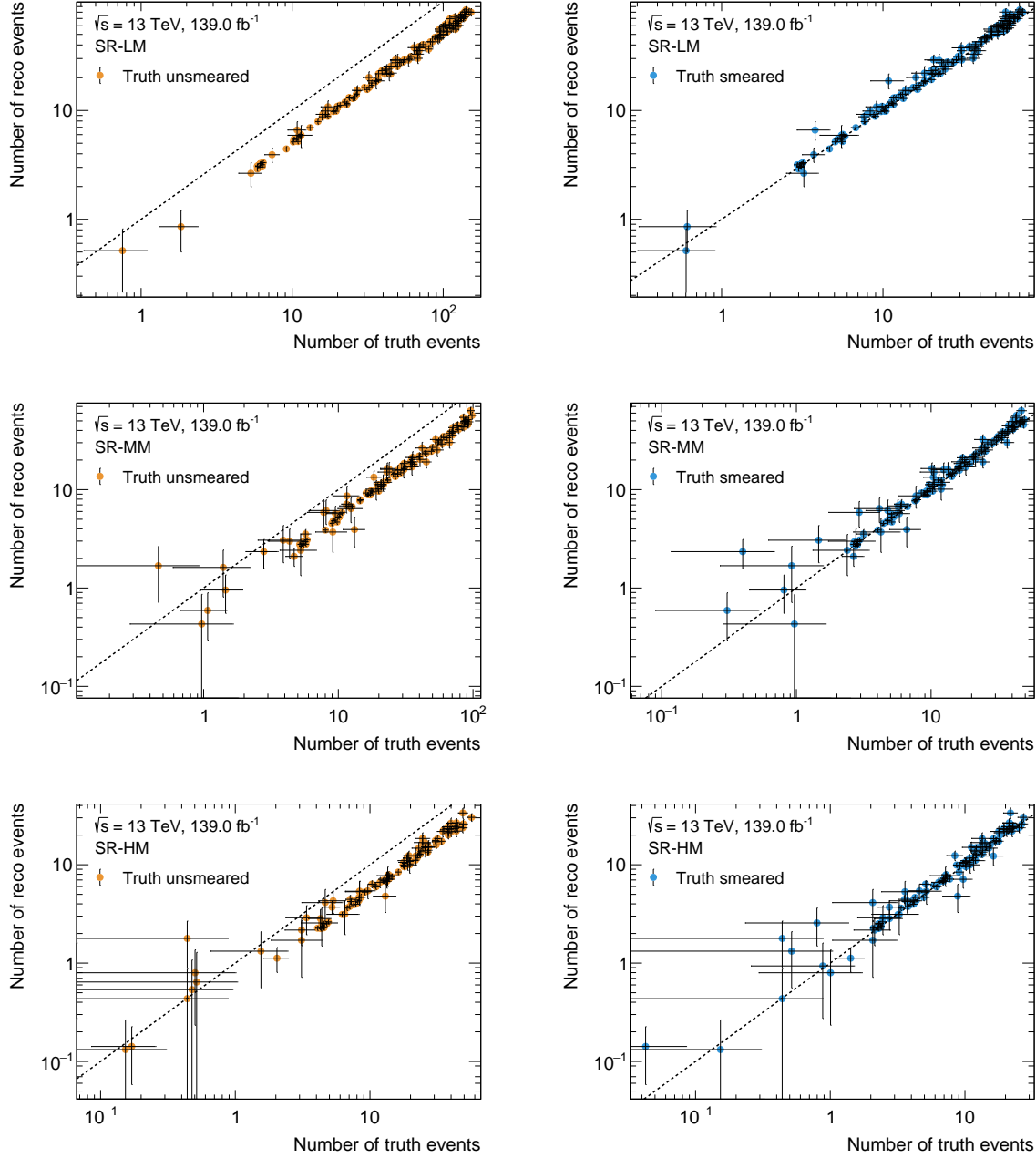


Figure 9.5: Comparison of the event rates at truth- and reconstruction-level before (left) and after (right) truth smearing. From top to bottom, the SR-LM, SR-MM and SR-HM signal regions are shown, with cumulative (integrated) m_{CT} bins. Every single point in the scatter plots represents a single signal model considered in the 1ℓ search. Uncertainty bars include MC statistical uncertainties.

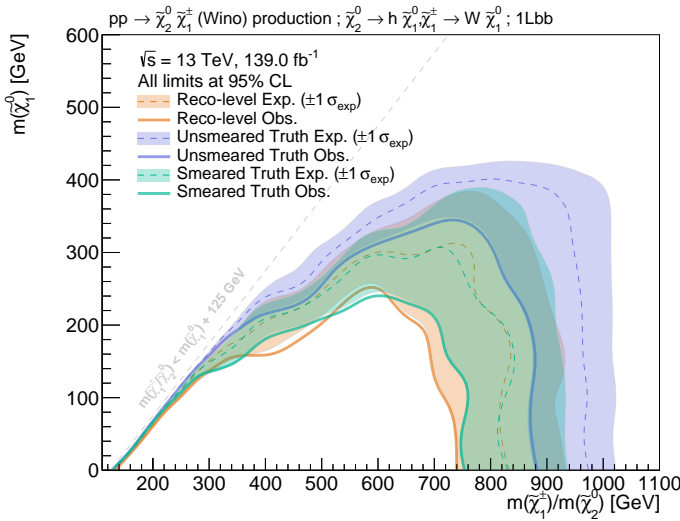


Figure 9.6: Expected and observed exclusion contours obtained with the full likelihood using reconstruction-level inputs (orange) as well as truth-level inputs before (purple) and after (green) smearing. Uncertainties include all statistical and systematic uncertainties on the background and signal for the reconstruction-level contours, but only statistical and systematic uncertainties on the background for truth-level signal inputs.

be computed and exclusion contours can be derived. Figure 9.6 compares the expected and observed exclusion contours obtained using the full likelihood and reconstruction-level signal inputs with those obtained using the full likelihood and truth-level signal inputs before and after truth smearing. While all systematic uncertainties on the signal are included in the reconstruction-level contours, no signal uncertainties are considered when obtaining both the smeared and unsmeared truth-level contours. As expected from the previous validation steps in the signal regions, the sensitivity using unsmeared truth-level signal inputs is significantly overestimated compared to the published analysis exclusion limit using reconstruction-level inputs. The smeared truth-level inputs, however, yield exclusion contours with an acceptable match compared to the reconstruction-level results.

In summary, the validation process performed at multiple selection levels of the analysis shows that the signal pipeline can be approximated reasonably well using a truth-level analysis and dedicated smearing functions. For signal models producing final states with kinematics close to those of the scenarios validated in the previous sections, this approach allows to determine the event rate estimates with high computational efficiency. In large-scale reinterpretations, the smeared truth-level analysis can be used as a basis for an efficient classification of models into two categories: models that are safely excluded or not excluded based on truth-level analysis only, and models where exclusion is in doubt and instead the precision of the full analysis pipeline using RECAST is required.

Chapter 10

Simplified likelihoods

In the previous chapter, the concept of preserving an analysis for the purpose of reinterpretations was introduced and a truth-level version of the signal pipeline was discussed. In large-scale reinterpretations involving a large number of SUSY models to be tested against, not only the signal pipeline, but also the statistical inference requires significant computational effort. This chapter therefore introduces the concept of *simplified likelihoods*, a method approximating the statistical model of an analysis using the HISTFACTORY template in order to achieve more efficient log-likelihood fits and, ultimately, hypothesis tests.

10.1 Motivation

Reinterpretations of ATLAS searches for SUSY in more complete and realistic SUSY scenarios (as opposed to simplified models) typically involve high-dimensional parameter spaces that are computationally extremely challenging to sample and compare to ATLAS data in an exhaustive manner. Large-scale reinterpretations of this type have already been performed in ATLAS after the Run 1 data-taking period in both the full 19-dimensional pMSSM [82] as well as a 5-dimensional representation of the pMSSM focussing on the electroweak sector [81]. Due to the complexity of the statistical models of today’s ATLAS searches for SUSY, originating from the large number[†] of channels and the sizeable set of nuisance parameters usually considered, the wall time needed for the statistical inference is usually not negligible. In a typical large-scale reinterpretation involving $\mathcal{O}(10^5\text{--}10^6)$ sampled models, an optimistic estimation of the wall time needed for the statistical inference per model of $\mathcal{O}(10\text{ s}\text{--}10^2\text{ s})$ is too computationally expensive, especially when more than just a single ATLAS search is included. It is thus crucial to reduce the number of models that need to be evaluated using the searches’ full statistical model.

One approach of alleviating this computational problem is to approximate the SUSY searches through their model-independent upper limits, often published in conjunction with the model-dependent exclusion limits. As discussed in section 5.3, the model-independent upper limits are derived using single-bin signal regions that do not rely on shape-fits but simply count the numbers of events after a set of selection cuts (so-called *cut-and-count* regions), thereby

[†] As an example, the full likelihood of the 1ℓ search using the exclusion signal regions has 8 channels with a total of 14 bins. Each channel gets event rates for 9 samples that depend on a total of 115 modifiers.

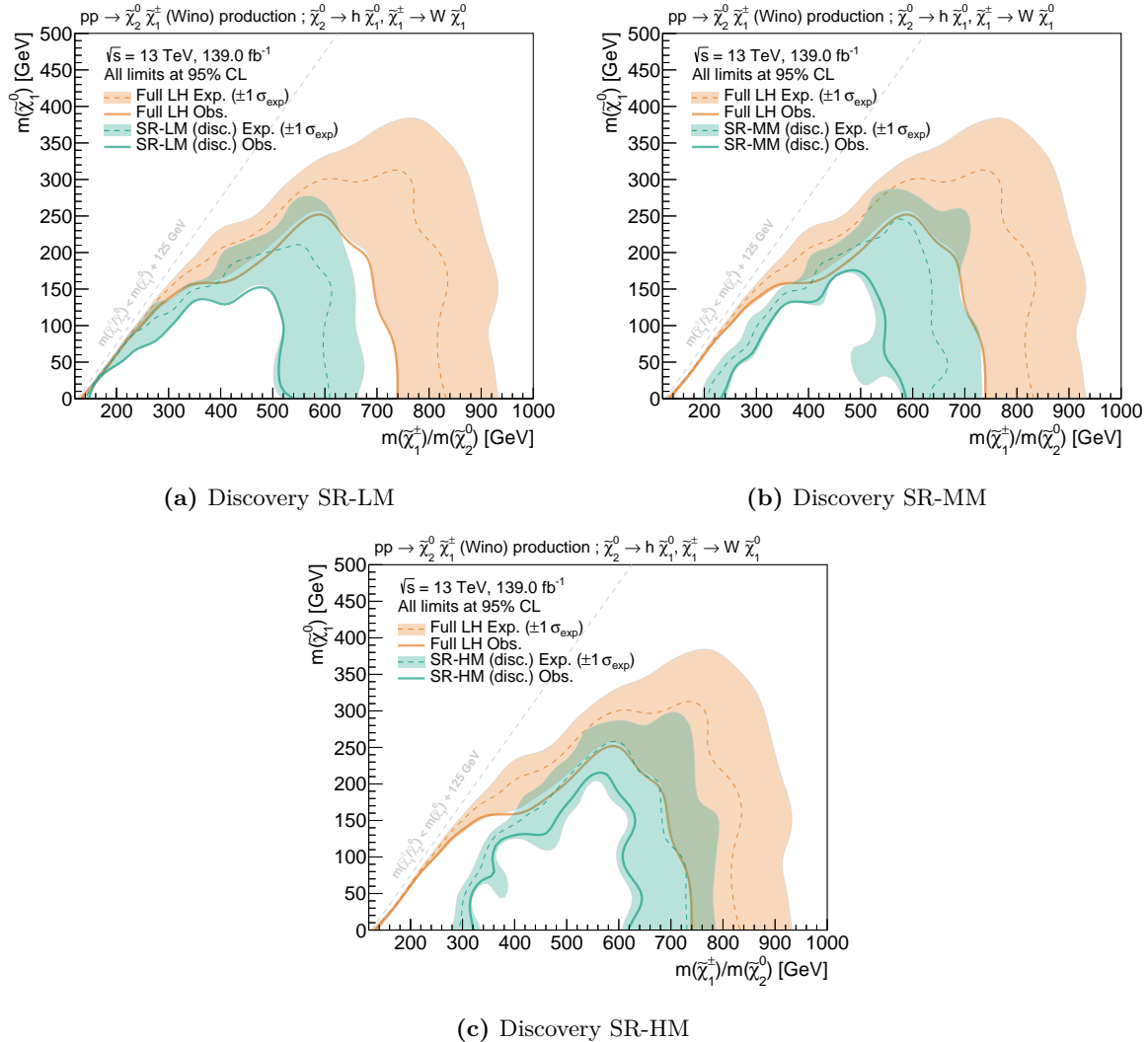


Figure 10.1: Comparison of exclusion limits obtained using a likelihood built from all nine exclusion signal regions (orange), and the discovery signal regions (green). As discussed in section 5.3, the discovery signal regions are simple *cut-and-count* regions making minimal model assumptions. As they are not mutually exclusive, they cannot be statistically combined, thus resulting in three separate exclusion contours. All statistical and systematic uncertainties on the background and the signal event rates are included in all regions.

making minimal model assumptions. In the case of searches using dedicated multi-bin signal regions that are statistically combined to derive exclusion limits on model parameters, this approach—while computationally very efficient—naturally underestimates the true exclusion power of the respective search since model-dependent signal shapes are not exploited.

Figure 10.1 illustrates this approach in the context of the 1ℓ search. The exclusion limits obtained with the exclusion signal regions implementing a two-dimensional shape-fit are compared to the exclusion contours obtained using the discovery signal regions, defined in table 5.3. As the discovery signal regions are not mutually exclusive, they cannot be statistically combined and thus three separate observed and expected contours need to be drawn. It can be observed that even a best-expected combination of the three discovery signal regions does not reach the sensitivity achieved using the two-dimensional shape-fit setup, resulting from the statistical combination of the nine exclusion signal regions. In the past, such approaches were used nonetheless in large-scale scans of the pMSSM using ATLAS data from Run 1 [82, 81], yielding conservative results and thus leaving substantial room for improvement.

Hence the motivation to introduce a method for approximating ATLAS searches for SUSY without disregarding their elaborate use of multi-bin signal regions exploiting the varying shapes of signal and SM background distributions. The method introduced hereafter targets ATLAS searches for SUSY using likelihoods built according to the HISTFACTORY template.

10.2 Building simplified likelihoods

In order to retain the full statistical combination of multiple signal region bins implemented in many SUSY searches, while still being able to achieve a sufficiently fast approximation, the statistical treatment of the background model including its uncertainties needs to be simplified. In the procedure presented in the following, this is achieved by first performing a background-only fit to data using the full likelihood in order to determine the best-fit values of all model parameters ϕ . The post-fit total background estimate as well as the total uncertainty on the estimate in every bin are subsequently computed from the best-fit values, and used to construct a simplified likelihood.

As the full likelihood in JSON format defines the full statistical model used for the statistical inference, the above background-only fit can be performed using `pyhf` and the preserved likelihood of the analysis. With the full likelihoods starting to become available on HEPDATA (see e.g. Ref. [274]) this procedure can rely on public information only and is therefore widely accessible to the HEP community. The simplified likelihoods introduced herein follow the same JSON specification used for the full likelihoods, described in Ref. [161]. The following description highlights the specification details relevant to the simplified likelihood.

Background model

In the simplified likelihood, the background model is approximated with a single background sample, called `total_bkg` in listing 10.1 and representing the total SM background estimate in the different analysis channels. The pre-fit sample rate of the total background sample is set to the total post-fit background estimate obtained in the background-only fit using the full likelihood (in listing 10.1 set to be 10.0). Furthermore, the complete set of nuisance

parameters in the original full likelihood is reduced to a single constrained parameter α with up and down variations corresponding to the post-fit uncertainties on the total SM background estimates in each bin. In listing 10.1, the single nuisance parameter is called `total_error` and is implemented as a rate modifier (introduced in section 3.1). It is constrained by a Gaussian of the form $\text{Gaus}(a = 0 | \alpha, \sigma = 1)$ and is correlated over all bins in each channel. The 1σ up and down evaluations of the rate modification, necessary for the interpolations during the log-likelihood fit to data, are given by the post-fit uncertainties on the total background estimate.

Although the final uncertainty is thus constrained by a simple Gaussian, the full treatment of the uncertainties including all correlations using the full likelihood in order to derive the in pre-fit values in the simplified likelihood, ensures that non-Gaussian effects are included to some extent.

```
{
    "name": "total_bkg",
    "data": [10.0],
    "modifiers": [
        {
            "data": {"hi_data": [12.0], "lo_data": [8.0]},
            "name": "total_error", "type": "histosys"
        }
    ]
}
```

Listing 10.1: Example of a total background sample with sample rate and total uncertainty as derived from a previous fit in the SRs and CRs. The ‘`histosys`’ type modifier in HISTFACTORY implements a shape uncertainty correlated over all bins.

Analysis channels

Each channel in the full likelihood with the original number of bins is also entering the simplified likelihood[†]. Each contains the total background sample as specified above. Apart from the total background sample, one additional sample is needed: the signal sample, an example of which is shown in listing 10.2. It introduces the unconstrained signal strength parameter μ as second and final parameter of the likelihood. For simplicity, the example shown in listing 10.2 does not introduce any additional uncertainties on the signal rates, thereby assuming them to be negligible. Depending on the BSM scenario, signal uncertainties can, however, be introduced through additional event rate modifiers.

```
{
    "name": "signal",
    "data": [7.0],
    "modifiers": [{"data": null, "name": "mu", "type": "normfactor"}]
}
```

Listing 10.2: Example of a signal sample with sample rate and unconstrained normalisation parameter that will be used as POI.

[†] Being able to reproduce the full statistical combination of all analysis regions is one of the main motivations for the introduction of the simplified likelihood.

Observations and measurements

According to the JSON specification defined in Ref. [161], the data observed by the analysis in each channel (and each bin) is introduced by means of an *observation*. In the case of the simplified likelihood, this is taken directly from the full likelihood and, by construction, does not need to be modified in any form. An example of an observation including several channels and bins is shown in listing 10.3.

```
{
    "observations": {
        {"name": "channel_A" : "data": [25.0]},
        {"name": "channel_B" : "data": [20.0]},
        {"name": "channel_C" : "data": [11.0, 13.0, 21.0]}
    }
}
```

Listing 10.3: Example of an observation in the simplified likelihood. It can be taken directly from the corresponding full likelihood. This example implements three channels, two with one bin, and one with three bins. The number of events observed in data are given for each channel and bin.

The only part of the JSON specification left to be defined is the *measurement*, specifying the name of the parameter of interest as well as parameter set configurations not already covered in the channel definitions. For the simplified likelihood, it is straightforward to write down, as the POI is the signal strength parameter and no additional parameters need further configuration. An example measurement is shown in listing 10.4.

```
{
    "measurements": {
        "name": "myMeasurement",
        "config": { "poi": "mu", "parameters": []}
    }
}
```

Listing 10.4: Example of a measurement in the simplified likelihood. The signal strength is the parameter of interest, no additional parameters need further configuration.

Put together, the above pieces result in a simplified likelihood for a given signal model, using a background model obtained from an initial background-only using the full likelihood, thus considering the full treatment of the systematic uncertainties. The simplified likelihood approach thus assumes the total background estimate to be fixed at the post-fit values obtained from the initial full likelihood fit, and only allowed to vary in a correlated way within the total uncertainty.

All simplified likelihoods used in the following have been produced using SIMPLIFY [284], a python tool written by the author. The background model of the simplified likelihood of the 1ℓ search in JSON format is available at Ref. [285]. By the means of JSON patches [286], any signal model, for which the nominal expected event rates in the analysis regions are known, can then be evaluated using this simplified likelihood.

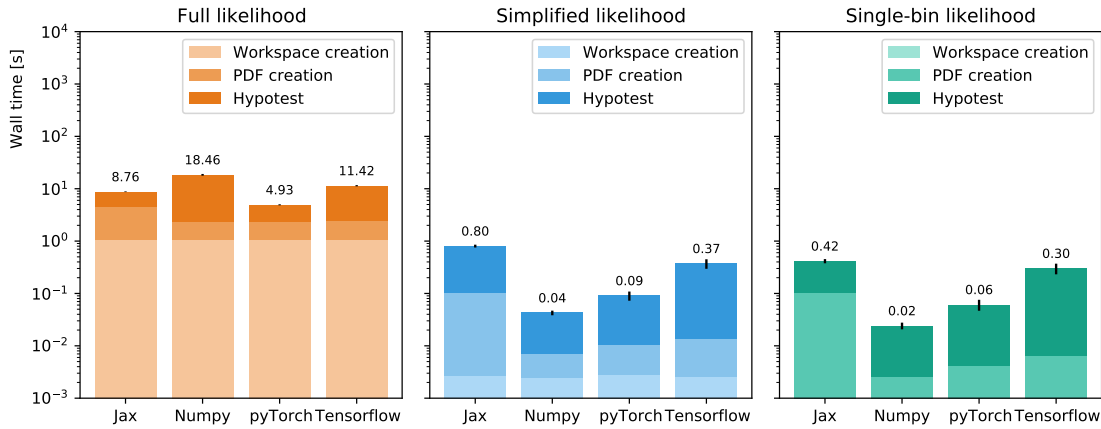


Figure 10.2: Benchmarks of the wall times necessary for hypothesis testing using different likelihoods and `pyhf` backends in the context of the 1ℓ search. Benchmark details are given in the text. The full likelihood (left) includes the full statistical implementation of the original analysis, the simplified likelihood (center) represents the simplified likelihood approach presented in this document, and the single-bin likelihood (right) represents the single-bin approximation using the discovery signal regions. The uncertainties represent the standard deviation of the benchmark test sample. The ‘workspace creation’ refers to I/O operations reading in the JSON file containing the likelihood. The ‘pdf creation’ step refers to the creation of the statistical model in a `pyhf`-internal structure, depending already on the computational backend. ‘Hypotest’ refers to the wall time of a single exclusion hypothesis test computing a CL_s value. Error bars correspond to the standard deviation of the benchmark sample.

10.3 Computational performance

One of the main figures of merit of an analysis approximation naturally is the reduction in computational wall time compared to the full analysis. Figure 10.2 shows a benchmark for different likelihood configurations in the context of the 1ℓ search. The wall times of hypothesis tests using the full analysis likelihood are compared with those using the simplified likelihood constructed following the previously introduced prescription. In addition, the wall time of the single-bin likelihood using the discovery SRs already used in fig. 10.1, is shown. For each likelihood, different computational backends are used for the tensor algebra operations in `pyhf`. All benchmarks have been performed on an Intel i7-4790 CPU with a nominal clock speed of 3.60 GHz, 4 cores and 8 threads. The CPU was not isolated, but under minimal load. The original 125 signal points of the 1ℓ search were used in each configuration.

The use of automatic differentiation of the full log-likelihood gradient, enabled by some of the tensor algebra backends to `pyhf`, offers an efficient minimisation of the negative log-likelihood, resulting in fast hypothesis tests of $\mathcal{O}(5\text{s})$ for the full likelihood. In large-scale reinterpretations, this is however still too computationally expensive. The simplified likelihood, on the other hand, yields minimum wall times for hypothesis tests of the order of 0.04 s per signal model. Compared to the naive single-bin approach using the discovery signal regions (the *single-bin*

Table 10.1: Benchmarks of the wall times needed for computing the CL_s value for a single signal model using the full and the simplified likelihoods. The signal models used for the benchmarks include all signal models originally considered in the respective searches. The uncertainty corresponds to the standard deviation of the wall times of the benchmark sample. The performance gain is stated as ratio between the wall times. The PYTORCH (NUMPY) backend of `pyhf` is used for the full (simplified) likelihood, in conjunction with the SCIPY optimiser. Searches without reference quoted are not yet public.

Analysis	Full likelihood [s]	Simplified likelihood [s]	Improvement
ATLAS compressed search [86]	16.49 ± 3.16	0.073 ± 0.012	$236\times$
ATLAS 3ℓ search	40.41 ± 15.7	0.082 ± 0.021	$495\times$
ATLAS 2ℓ search [258]	5.93 ± 0.16	0.079 ± 0.0082	$75\times$
ATLAS 1ℓ search [184]	4.93 ± 0.11	0.040 ± 0.0057	$123\times$
ATLAS direct stau search [287]	1.91 ± 0.090	0.039 ± 0.0055	$49\times$
ATLAS sbottom search [288]	1.36 ± 0.067	0.038 ± 0.0046	$36\times$
ATLAS stop search	2.27 ± 0.062	0.044 ± 0.011	$51\times$

likelihood), the simplified likelihood thus offers hypothesis tests with a similar wall time[†], but a significantly better approximation of the true analysis exclusion power.

Interestingly, the wall time of the simplified likelihood does not benefit from the usage of features like automatic differentiation, offered by backends like PYTORCH. This is due to the extreme simplicity of the simplified likelihood function, causing the computational benefits from features like automatic differentiation to not outweigh the sizeable overhead associated to the startup and execution times of libraries like PYTORCH.

In addition to the 1ℓ search, the simplified likelihood approach is validated a set of additional ATLAS searches for SUSY. Table 10.1 summarises the mean wall times of all ATLAS searches investigated. In all cases, PYTORCH offers the fastest backend for the full likelihood while NUMPY shows best performance for the simplified likelihood. The performance improvement of roughly two orders of magnitude, observed in the 1ℓ search, is confirmed in the other ATLAS SUSY searches investigated. The wall time of the simplified likelihoods appears to be bound from below at $\mathcal{O}(10^{-2}\text{ s})$, limiting the performance gain for some of the faster analyses whose full likelihoods are already relatively simple to begin with.

10.4 Physics performance

A comparison of the exclusion contours obtained with the full and simplified likelihoods in the context of the 1ℓ search is shown in fig. 10.3. The results obtained using the simplified likelihood are shown in blue, while the results obtained using the full likelihood are given in orange. Both the observed (without the usual theoretical up and down variations on the signal cross section) and expected exclusion limits including the uncertainty band are shown. In the case of the full likelihood, the complete set of MC statistical and systematic uncertainties introduced in chapter 7 are taken into account. As discussed in section 10.2, the uncertainty band on the

[†] In fact, the simplified likelihood is actually even faster than the single-bin approach, as the latter needs to be executed separately for each discovery SR and thus the numbers quoted need to be multiplied by the number of discovery SRs used in the analysis (three in the case of the 1ℓ search).

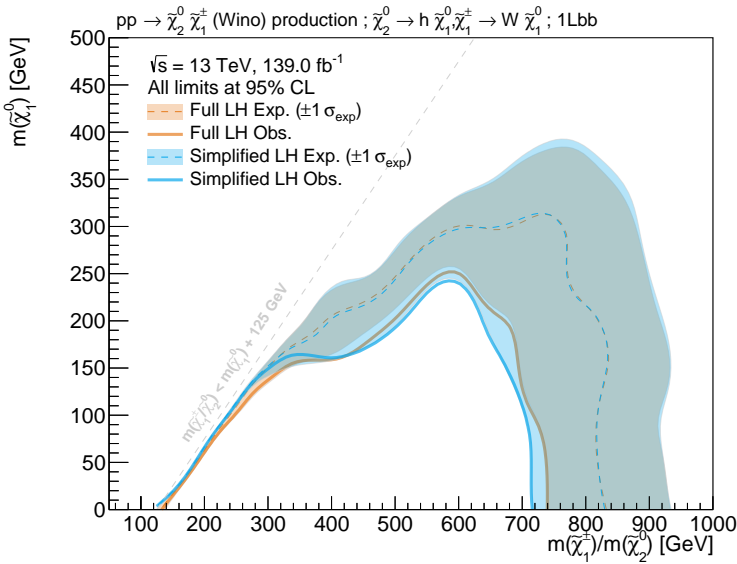


Figure 10.3: Comparison of the simplified likelihood (blue) and full likelihood (orange) exclusion contours for the 1ℓ search. The uncertainty band includes all MC statistical and systematic uncertainties in the case of the full likelihood, and only the simplified uncertainties in the case of the simplified likelihood.

simplified likelihood contour results from the single nuisance parameter built through reduction of the original nuisance parameters.

The observed and expected CL_s values obtained using both likelihoods are shown in fig. 10.4. As expected from the exclusion contour, both the simplified and the full likelihood agree reasonably well across the majority of the CL_s range. For signal models well within exclusion ($CL_s \ll 0.05$) based on the full likelihood, the simplified likelihood of the 1ℓ search tends to result in slightly lower CL_s values than the full likelihood, yielding a slightly too optimistic sensitivity estimate. In the range relevant to the exclusion contour at 95% CL ($CL_s \approx 0.05$), the results from the simplified likelihood agree however well with those from the full likelihood.

In addition to the 1ℓ search, the simplified likelihood approach has been tested on the ATLAS SUSY searches listed in table 10.1. An overview of the results can be seen in fig. 10.5, comparing the exclusion contours obtained with the simplified likelihood against the full analysis results. In some analyses, e.g., the ATLAS sbottom and ATLAS 3ℓ searches, the simplified likelihoods show excellent agreements. In other analyses, like e.g., the ATLAS direct stau search, the agreement is less good but overall still acceptable. In summary, this demonstrates that the method can, in many cases, offer a fast and reliable approximation of ATLAS searches for SUSY using the HistFactory template.

10.5 Limitations

Building a well-performing simplified likelihood is not always as straightforward as described in section 10.2, and some analyses require special care when approximated. For example, in the case of the ATLAS compressed search [86], shown in fig. 10.5(f), only a subset of the original analysis signal regions are entering the simplified likelihood, because studies showed this to yield an overall improvement in agreement between the two likelihoods. The straightforward structure of the simplified likelihood is, in this case, not able to reproduce the statistical behaviour of the background model of the full likelihood in the signal regions omitted. As these

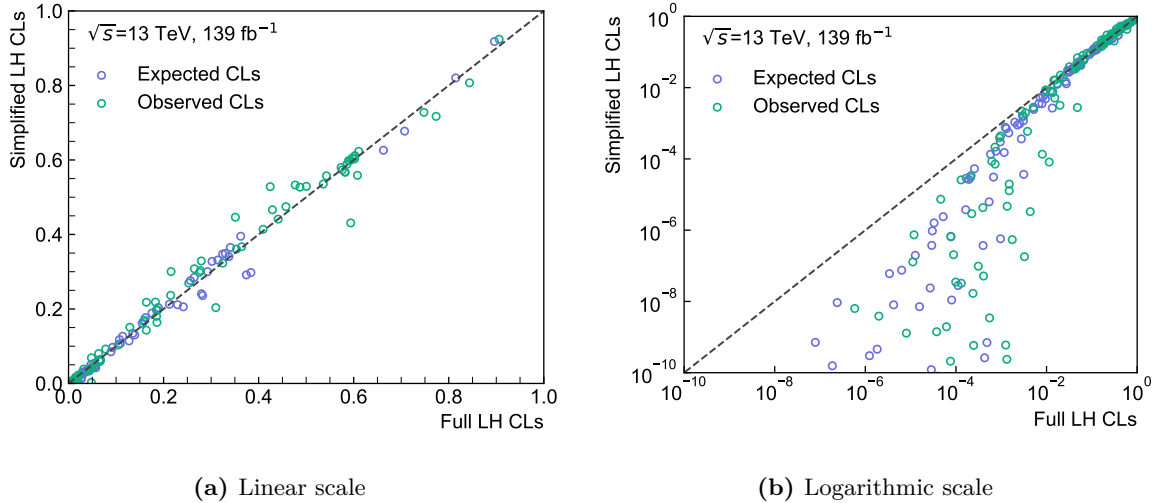


Figure 10.4: Scatter plots comparing the observed and expected CL_s values obtained using the simplified and the full likelihoods for the same set of signal models considered in the 1ℓ search. Both linear and logarithmic scale representations are shown to give an overview of the full range of CL_s values.

signal regions were found to only add limited sensitivity to the search, their removal in the simplified likelihood yields an overall improvement in agreement. Figure B.8 further illustrates the impact of removing these signal regions in the simplified likelihood.

It is worth highlighting again that the simplified likelihood assumes that the total background model can be described by a single sample with a single rate modifier, constrained by a Gaussian and correlated over all bins, with background event rates and uncertainties obtained from a background-only fit using the full likelihood. This, in particular, assumes that the background model is sufficiently constrained by the large statistics in the CRs and that the introduction of signal contributions—especially in the SRs—does not significantly change the background model in a way that cannot be replicated with a single background sample where the event rates only depend on a single, constrained nuisance parameter. Although to some extent tolerable in the full analysis likelihood, such a configuration, where the background model is no longer only mostly constrained by the large statistics in the control regions, is especially problematic for the simplified likelihood.

An additional limitation arises in cases of significant signal contamination in the CRs. In the full likelihood, significant signal contaminations in the CRs generally lead to smaller background estimates in the SRs, which, in turn, result in conservative exclusion limits given the observed data. In the simplified likelihood, even with the CRs included, the single constrained nuisance parameter does not offer enough degrees of freedom to scale down the background model enough in the $\mu = 1$ hypothesis, resulting in *fake* sensitivity in the CRs. Although it is generally important to limit signal contamination in the CRs for the sake of healthy statistical log-likelihood fits, this is especially true in the case of very simplified likelihoods as introduced herein. In the case of the ATLAS stop search shown in fig. 10.5(b), significant signal contamination of more than 30% appears for many signal models with $m(\tilde{t}_1) < m(\tilde{\chi}_1^0) + m(t)$,

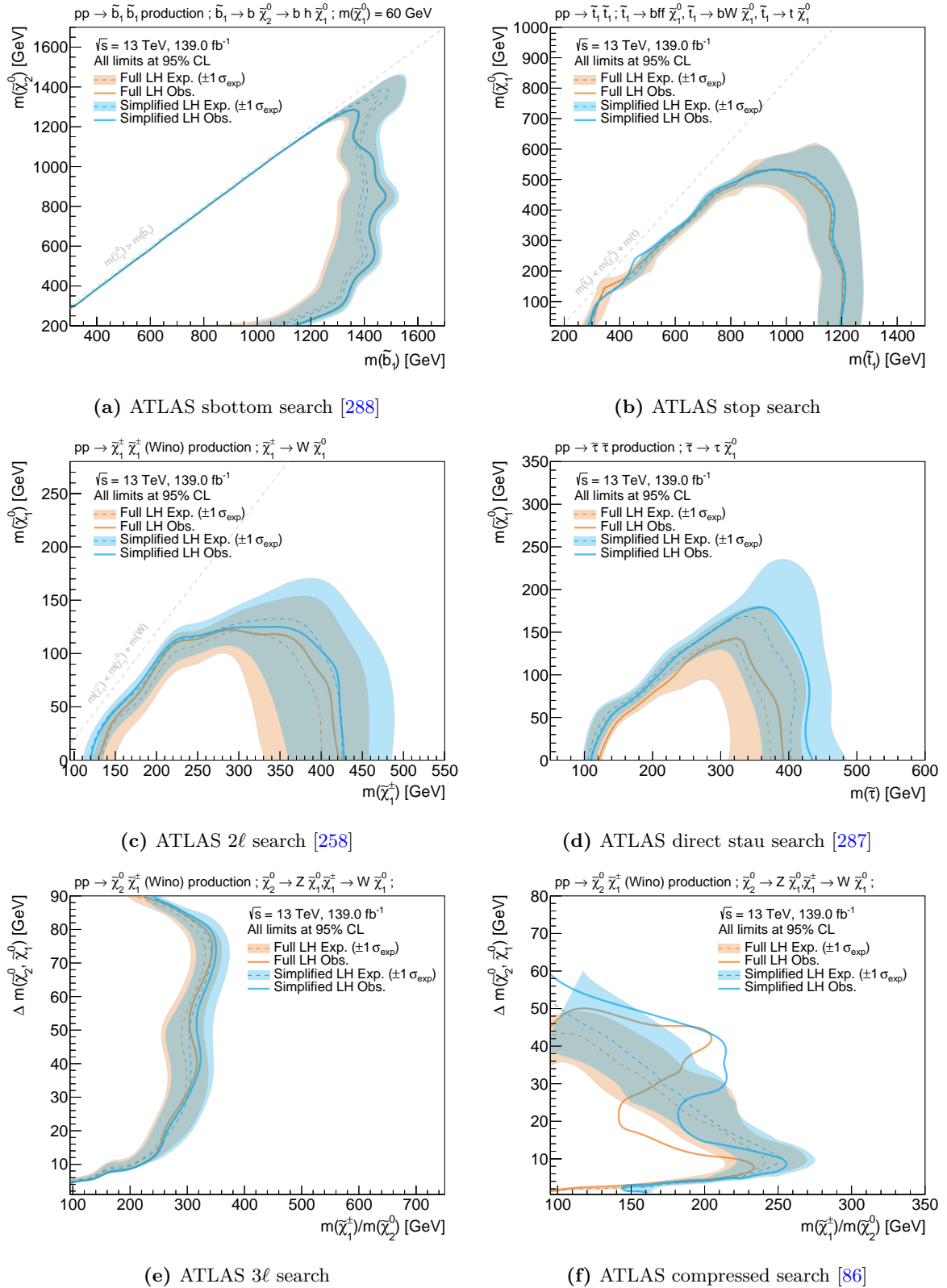


Figure 10.5: Simplified likelihood results for the different ATLAS searches studied. The results from the simplified likelihood (blue) are compared with the results of the full analysis likelihood (orange). The same reconstruction-level signal inputs are used in both cases. The shorthand notation ‘*LH*’ refers to likelihood.

which can thus not be evaluated using the simplified likelihood including control regions[†]. In fig. B.9, the impact of not applying the simplified likelihood on signal models with significant signal contamination in the region $m(\tilde{t}_1) < m(\tilde{\chi}_1^0) + m(t)$ is shown. In practice, this means that models need to be carefully checked for potential signal contamination in the control regions, and cannot be evaluated using the simplified likelihood in case the signal contamination is found to be too high[§].

10.6 Outlook and future prospects

The simplified likelihoods introduced in this chapter can offer precise and computationally efficient approximations of ATLAS SUSY searches for which the full likelihood in JSON format is available. A publicly available python tool has been developed for generic conversion of any full likelihood in JSON format into the simplified format introduced herein [284].

The procedure of approximating the statistical model of a search is orthogonal to the truth-level analysis discussed in section 9.4 in the sense that both approximations target a different part of the analysis workflow shown in fig. 9.1. As such, both approaches can be combined into a *simplified analysis* that runs a smeared truth-level analysis in order to determine an estimate for signal event rates, followed by a simplified statistical inference using the simplified likelihood instead of the full statistical model. Figure 10.6 compares the expected and observed exclusion contours obtained in the full 1ℓ search published with those obtained with the simplified version of the search, using smeared truth-level analysis and a simplified likelihood. The agreement observed between the exclusion contours obtained by both analysis versions is noteworthy, especially given the considerable scope of the two-fold approximation applied in the simplified analysis version. This very simplified analysis will be used in the following chapter to enable a computationally efficient reinterpretation of the 1ℓ search in the pMSSM.

As the full likelihood defines the full statistical model given the observed data in an analysis, other forms of likelihood simplifications can be thought of. One possible approach worth investigating is the construction of likelihood simplifications using a variable number of nuisance parameters, as opposed to reducing the full set of nuisance parameters to a single one. In such an approach, a principal components analysis could project the full N -dimensional nuisance parameter space onto a number $n \leq N$ principal components maximising the variance of the projected space, i.e. resulting in minimal loss in bin-by-bin correlation information. The n principal components can then be kept separate, while the $N - n$ remaining components can be combined in into a *residual* term[‡]. A similar approach was already introduced in chapter 7, where the large number of nuisance parameters related to the JER and JES uncertainties were reduced to a more manageable set of *effective* nuisance parameters with minimal loss in bin-by-bin correlation information.

[†] This is a kinematic region that the analysis is not designed to be sensitive in, hence the CRs are not guaranteed to be free of signal contamination.

[§] The exact amount of tolerable signal contamination should be explicitly checked on a per-analysis basis. For models exceeding the tolerated amount, the full likelihood can be used instead of the simplified one.

[‡] In a way, the simplified likelihood introduced in this thesis is the special case of this approach where $n = 0$ is chosen and none of the principal components are kept separate while all N nuisance parameters are combined into a single term.

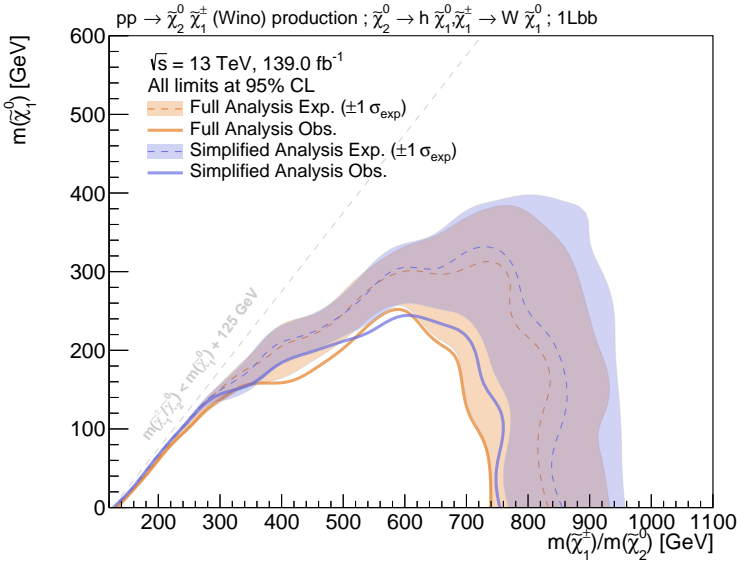


Figure 10.6: Expected and observed exclusion contours obtained with the full likelihood and reconstruction-level inputs (orange) and the simplified likelihood and smeared truth-level inputs (purple). All statistical and systematic uncertainties on the background and signal are considered for the reconstruction-level contours determined using the full likelihood.

Up until very recently, the only way for physicists outside the collaboration to re-use ATLAS searches for SUSY required building approximations of their statistical models based on lossy projections of the full likelihood. With ATLAS’ recent push to publish full analysis likelihoods, new approaches for approximation of the statistical models are becoming available. In principle, the full likelihood contains all information necessary for generating a simplified likelihood with a certain degree of compromise between statistical precision and computational efficiency, allowing to find an ideal approximation given constraints on available computing resources of the specific use-case.

Chapter 11

Reinterpretation in the pMSSM

After having discussed methods and approaches to reinterpret ATLAS searches for SUSY, this chapter presents a reinterpretation of the 1ℓ search in the pMSSM, relying on the analysis approximations previously discussed.

11.1 Motivation

In today's searches for SUSY, it is common to use simplified models as a way of avoiding the necessity of having to deal with high-dimensional parameter spaces that are extremely challenging to sample and compare to data. As has been discussed in sections 1.2.7 and 8.3, simplified models are however by no means complete SUSY models, but only serve as proxies for more complex and realistic SUSY scenarios. As such, simplified model limits cannot trivially be translated into limits on model parameters of a more complete SUSY model and large-scale reinterpretations are necessary to understand the constraints current SUSY searches set on realistic SUSY scenarios.

One class of more complete models, focussing on phenomenologically viable models, is the pMSSM, introduced in section 1.2.6. With its 19 parameters it offers much more complex SUSY scenarios while still being of somewhat manageable dimensionality. Still, large-scale reinterpretations in the pMSSM are computationally challenging and require a set of approximations as those introduced in chapters 9 and 10. In the following, the *simplified analysis* constructed using the smeared truth-level analysis and the simplified likelihood will be used as the sole method to evaluate a set of pMSSM models.

Although the following sections will be restricted to a reinterpretation of the 1ℓ search, efforts are ongoing within ATLAS to perform large-scale reinterpretations using a majority of the Run 2 ATLAS searches for SUSY, most likely resulting in one of the most comprehensive set of ATLAS constraints on SUSY yet.

Table 11.1: Scan ranges used for each of the 19 pMSSM parameters. For parameters written with a modulus sign, both the positive and negative values are allowed. The term ‘gen(s)’ refers to generation(s). Flat probability distributions are used to sample random values from the given ranges.

Parameter	min	max	Note
$m_{\tilde{L}_1}$ ($= m_{\tilde{L}_2}$)	10 TeV	10 TeV	Left-handed slepton (first two gens.) mass
$m_{\tilde{e}_1}$ ($= m_{\tilde{e}_2}$)	10 TeV	10 TeV	Right-handed slepton (first two gens.) mass
$m_{\tilde{L}_3}$	10 TeV	10 TeV	Left-handed stau doublet mass
$m_{\tilde{e}_3}$	10 TeV	10 TeV	Right-handed stau mass
$m_{\tilde{Q}_1}$ ($= m_{\tilde{Q}_2}$)	10 TeV	10 TeV	Left-handed squark (first two gens.) mass
$m_{\tilde{u}_1}$ ($= m_{\tilde{u}_2}$)	10 TeV	10 TeV	Right-handed up-type squark (first two gens.) mass
$m_{\tilde{d}_1}$ ($= m_{\tilde{d}_2}$)	10 TeV	10 TeV	Right-handed down-type squark (first two gens.) mass
$m_{\tilde{Q}_3}$	2 TeV	5 TeV	Left-handed squark (third gen.) mass
$m_{\tilde{u}_3}$	2 TeV	5 TeV	Right-handed top squark mass
$m_{\tilde{d}_3}$	2 TeV	5 TeV	Right-handed bottom squark mass
$ M_1 $	0 TeV	2 TeV	Bino mass parameter
$ M_2 $	0 TeV	2 TeV	Wino mass parameter
$ \mu $	0 TeV	2 TeV	Bilinear Higgs mass parameter
M_3	1 TeV	5 TeV	Gluino mass parameter
$ A_t $	0 TeV	8 TeV	Trilinear top coupling
$ A_b $	0 TeV	2 TeV	Trilinear bottom coupling
$ A_\tau $	0 TeV	2 TeV	Trilinear τ lepton coupling
M_A	0 TeV	5 TeV	Pseudoscalar Higgs boson mass
$\tan \beta$	1	60	Ratio of the Higgs vacuum expectation values

11.2 Model sampling and processing

11.2.1 Sampling

All signal models considered in the following are sampled from the pMSSM using the parameter ranges shown in table 11.1. Flat probability distributions are used to draw random values within the given ranges for each parameter and each unique set of pMSSM parameters generated that way is referred to as an independent pMSSM model.

As this work discusses a search for electroweakinos, the SUSY models drawn from the pMSSM are sampled with a special focus on the electroweak sector. This is achieved by setting the mass parameters of the first and second generation squarks as well as those of the sleptons to values much higher than those accessible at LHC energies, effectively decoupling them. For naturalness arguments, third generation squarks and the gluino are not strictly decoupled but set to sufficiently high values such as not to affect the electroweak sector too much. The lower and upper bounds on the 12 scanned parameters are chosen to yield a high density of models with electroweakino masses accessible at LHC energies while allowing the scan to be as general as possible.

Once a value for each of the 19 pMSSM parameters has been chosen for each point, a number of publicly available software packages are executed in order to compute the properties of each model. In a first step, SPHENO v4.0.5 [289, 290] is used to calculate the spectrum of the sparticles. It is used to determine the masses and branching fractions of the Higgs sector

using FEYNHIGGS v2.15.0 [291–293]. An additional SUSY spectrum calculation is performed using SOFTSUSY v4.1.8 [294]. Although the spectra obtained from SOFTSUSY will not be directly used in the following, the program is still required to complete successfully in order to reduce the number of pMSSM models with pathological properties. After the complete model spectrum has been calculated, the dark matter relic abundance of each model is determined with MICROMEGAs v5.0.8 [295, 296].

11.2.2 Selection and processing

In order to avoid models with pathological properties, all spectrum generators and additional programs are required to complete execution without error. The cross section for surviving models is computed at NLO using PROSPINO v2.1 [297, 298]. Models with an inclusive cross section for all electroweakino production processes below 0.07 fb are discarded as they would result in less than 10 expected signal events with an integrated luminosity of 139 fb^{-1} , not enough to be sensitive to with current electroweak SUSY searches. All models are further required to produce a lightest Higgs mass compatible within a $\pm 5\text{ GeV}$ range with the SM Higgs mass experimentally measured[†].

No constraints on the computed cosmological LSP abundance are applied at this stage in order to give a more general view after the models are evaluated using the 1ℓ search. Experimental constraints, like e.g., the lower limit on the chargino mass from LEP, are also not applied at this stage for the same reason.

Of the 10,000 unique models sampled from the pMSSM using the above prescription, 5152 models survive the constraints and requirements discussed in this section and are analysed using the simplified 1ℓ search. The majority of the models failing this selection step were rejected due to the cross section constraints.

11.2.3 Event generation

Event generation is performed using the software centrally provided by the ATLAS production system. The initial pair of sparticles with up to one additional parton in the matrix element (ME) are generated using the MADGRAPH5_AMC@NLO v2.6.1. [189, 190] generator. Next, PYTHIA8.230 [191] with the A14 [194] tune is used for the hadronisation and parton shower (PS), together with the NNPDF 2.3 LO [193] PDF set. The number of events N generated for each model is determined by

$$N = \sigma \times \mathcal{L}_{\text{eff}}, \quad (11.1)$$

where $\mathcal{L}_{\text{eff}} = 700\text{ fb}^{-1}$ is an effective integrated luminosity and σ is the total production cross section of the model. The number of events generated is capped at a minimum number of 10^4 and a maximum number of 10^6 truth-level events.

[†] The mass range is based on a conservative estimate of the theoretical uncertainties arising from the FEYNHIGGS calculation.

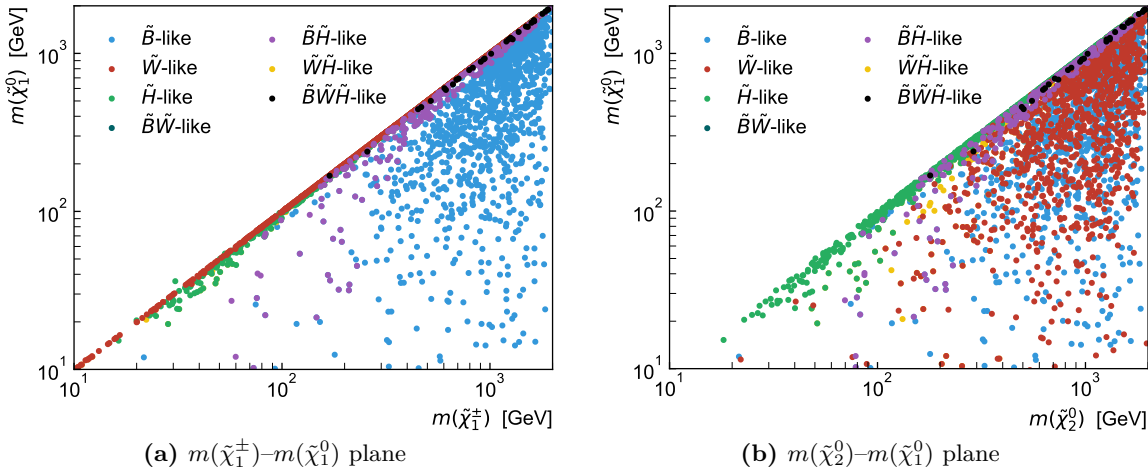


Figure 11.1: Projections of all models sampled onto the (a) $m(\tilde{\chi}_1^\pm)$ - $m(\tilde{\chi}_1^0)$ and (b) $m(\tilde{\chi}_2^0)$ - $m(\tilde{\chi}_1^0)$ planes. Each point represent a distinct pMSSM model. The colour encodes the composition of the $\tilde{\chi}_1^0$ in each model. Details on how the LSP type is defined are given in the text.

11.2.4 Truth-level analysis

All models passing event generation are evaluated using the simplified analysis comprised of truth-level inputs, four-vector smearing and the simplified likelihood. This is the only evaluation done for the models considered herein. A full scan over the pMSSM including multiple ATLAS searches would additionally include a processing step reverting back to the full analysis available through RECAST for model points where (non-)exclusion is uncertain based on the simplified analysis only.

11.3 Phenomenology of the LSP

The composition of the $\tilde{\chi}_1^0$ in each pMSSM model sampled is shown in projections onto the $m(\tilde{\chi}_1^\pm)$ - $m(\tilde{\chi}_1^0)$ and $m(\tilde{\chi}_2^0)$ - $m(\tilde{\chi}_1^0)$ planes in figs. 11.1(a) and 11.1(b), respectively. The $\tilde{\chi}_1^0$ is considered to be bino-like (\tilde{B} -like), wino-like (\tilde{W} -like) or higgsino-like (\tilde{H} -like) if the corresponding fraction from the neutralino mass mixing matrix is at least 80%. If more than one component has a fraction of more than 20%, then the $\tilde{\chi}_1^0$ is considered to be of mixed nature. For example, a $\tilde{\chi}_1^0$ with more than 20% bino-, wino- and higgsino-components is referred to as $\tilde{B}\tilde{W}\tilde{H}$ -like. The nature of the LSP as a function of the bino, wino and higgsino mass parameters (M_1 , M_2 and μ) is shown as a reference in fig. C.1.

In the bulk of the $m(\tilde{\chi}_1^\pm)$ - $m(\tilde{\chi}_1^0)$ plane, i.e. the parameter space targeted by the 1ℓ search using the simplified model, a large majority of the models produce a bino-like LSP with nearly mass-degenerate $\tilde{\chi}_1^\pm$ and $\tilde{\chi}_2^0$. These models correspond to cases where $M_1 \ll \mu$ and $M_1 < M_2$ and thus produce electroweakino spectra similar to the canonical simplified model considered in the 1ℓ search. Some sensitivity can therefore be expected towards these models in the context of the 1ℓ search, provided that the branching fractions of the decays $\tilde{\chi}_1^\pm \rightarrow W^\pm \tilde{\chi}_1^0$ and especially $\tilde{\chi}_2^0 \rightarrow h \tilde{\chi}_1^0$ are large enough and produce on-shell bosons.

Towards the diagonal of the $m(\tilde{\chi}_1^\pm)$ - $m(\tilde{\chi}_1^0)$ plane, i.e. for models where the $\tilde{\chi}_1^\pm$ and $\tilde{\chi}_1^0$ are nearly mass-degenerate, the nature of the LSP shows a larger variation. In a large set of models where M_2 is not too heavy and $M_2 \ll M_1$ as well as $M_2 \ll \mu$, the LSP has a significant wino component and is nearly mass-degenerate with the $\tilde{\chi}_1^\pm$, while the $\tilde{\chi}_2^0$ and other electroweakinos can be more massive. In models where the LSP has a large higgsino component, i.e. $\mu \ll M_1$ and $\mu \ll M_2$, the three electroweakinos $\tilde{\chi}_1^\pm$, $\tilde{\chi}_2^0$ and $\tilde{\chi}_1^0$ are nearly mass-degenerate and, if promptly decaying, result in very soft decay products, making these models inherently difficult to target.

11.4 Impact of the search on the pMSSM

In the following sections, the impact of the 1ℓ search on the pMSSM is discussed using one-dimensional and two-dimensional projections and distributions. A model is considered to be excluded if the observed CL_s value obtained with the simplified likelihood using the smeared truth-level inputs and the simplified likelihood is below 0.05. Of the 5152 models evaluated, the 1ℓ search excludes a total of 98, or about 1.9%, of the models.

For the one-dimensional distributions shown in the following, the total number of models is compared against the number of models excluded by the 1ℓ search. An additional pad indicates the ratio between models excluded and total models sampled in each bin of the distribution. In the two-dimensional projections, the numbers in the bins indicate the number of pMSSM models falling into each bin. In these projections, the fraction of models excluded with the 1ℓ search is encoded using the z -axis, represented by a colour bar. Bins in which all models are excluded are coloured in black, while bins without any excluded models are left white. Where applicable, the exclusion contour obtained by the 1ℓ search using the simplified model is overlaid.

11.4.1 Impact on electroweakino masses

Figures 11.2 and 11.3 show the bin-by-bin fractions of models excluded by the 1ℓ search as two- and one-dimensional distributions, respectively. From the $\tilde{\chi}_1^\pm$ - $\tilde{\chi}_1^0$ plane in fig. 11.2(a), it can be seen that the 1ℓ search is most sensitive to pMSSM models in mass ranges similar to those excluded in the context of the simplified model. Most of the models excluded have $\tilde{\chi}_1^\pm/\tilde{\chi}_2^0$ masses ranging from roughly 200 GeV to about 700 GeV, and LSP ranging masses from 0 GeV to about 300 GeV. The proportion of excluded models peaks at $m(\tilde{\chi}_1^\pm, \tilde{\chi}_2^0) \approx 450$ GeV and light LSPs with $\tilde{\chi}_1^0 < 150$ GeV, as visible in fig. 11.3.

The models excluded by the 1ℓ search can roughly be classified in two categories: models lying within the simplified model exclusion contour and models with nearly mass-degenerate $\tilde{\chi}_1^\pm$ and $\tilde{\chi}_2^0$. As discussed in section 11.3, most models within the simplified model exclusion contour produce a bino-like LSP and result in nearly mass-degenerate[†] $\tilde{\chi}_1^\pm$ and $\tilde{\chi}_2^0$. Expectedly, the 1ℓ search shows sensitivity to $\tilde{\chi}_1^\pm \tilde{\chi}_2^0$ production in models with wino-like electroweakinos and a bino-like $\tilde{\chi}_1^0$, resulting in spectra close to that of the canonical simplified model originally considered in the search. The mass spectrum of such a model, excluded by the 1ℓ search, is shown in fig. 11.4(a).

[†] Figure C.2 illustrates this behaviour further.

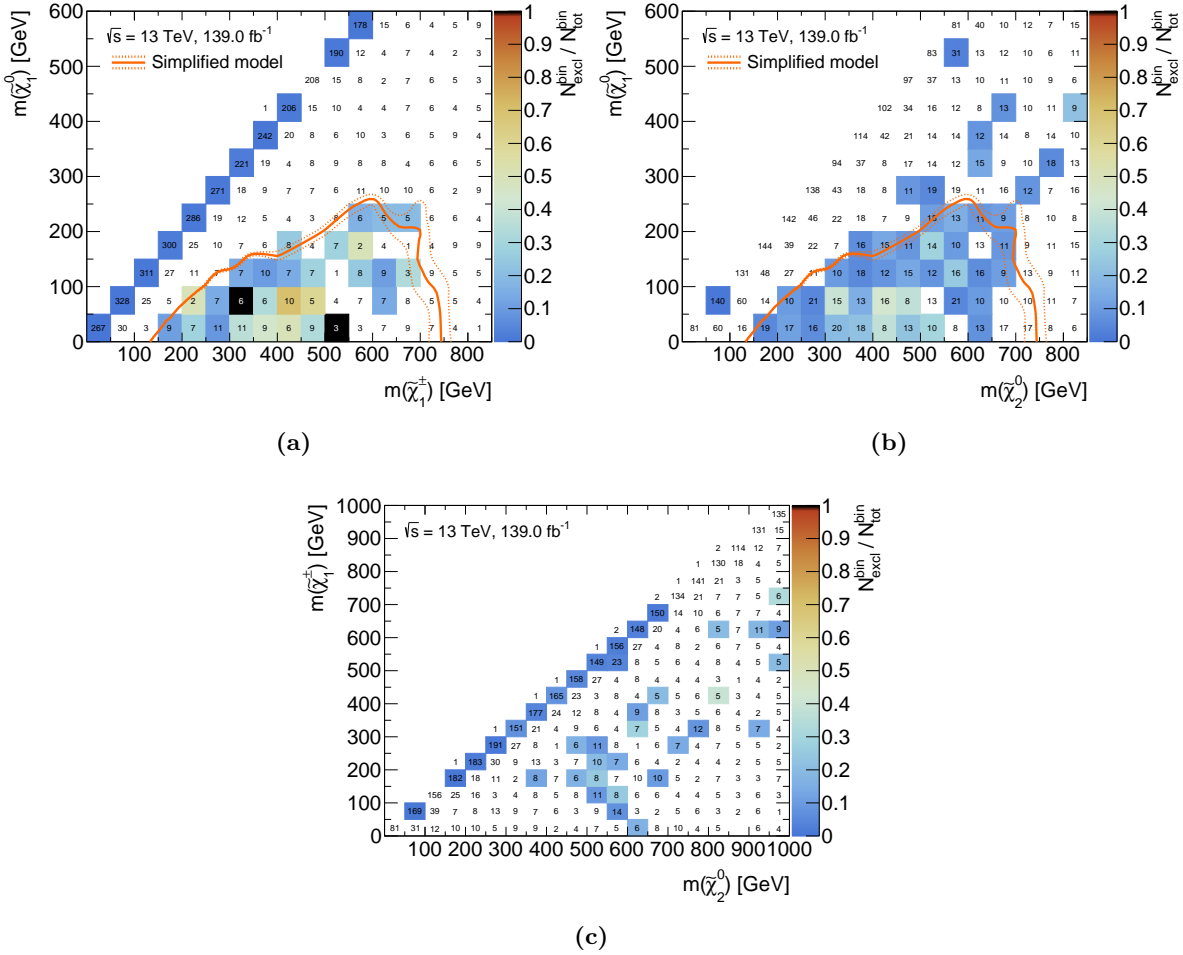


Figure 11.2: Bin-by-bin fraction of excluded models as a function of the relevant sparticle masses. The numbers in the bins correspond to the total number of models sampled falling into the respective bin. The number of models excluded by the 1ℓ search is encoded with a colour bar ranging from 0 to 1. Where all models in a given bin are excluded, the bin is coloured in black. Bins without any models excluded are left white. Models are evaluated using the simplified likelihood of the 1ℓ search. The simplified model contour is shown in orange.

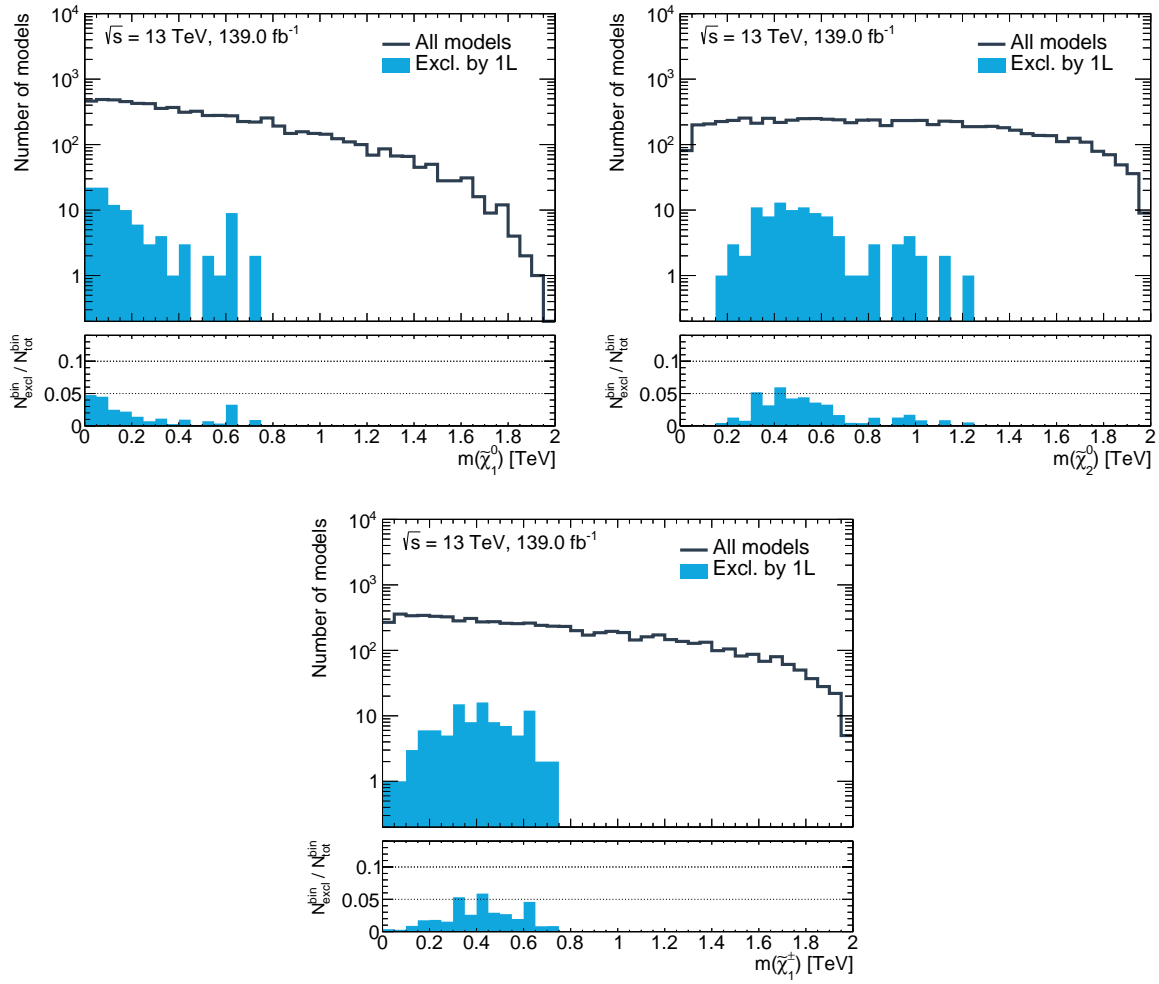


Figure 11.3: Bin-by-bin number of excluded models as a one-dimensional function of the electroweakino masses. The bin-wise fraction of excluded models, $N_{\text{excl}}^{\text{bin}} / N_{\text{tot}}^{\text{bin}}$, is shown in the lower pad. All models are evaluated using the simplified likelihood of the 1ℓ search.

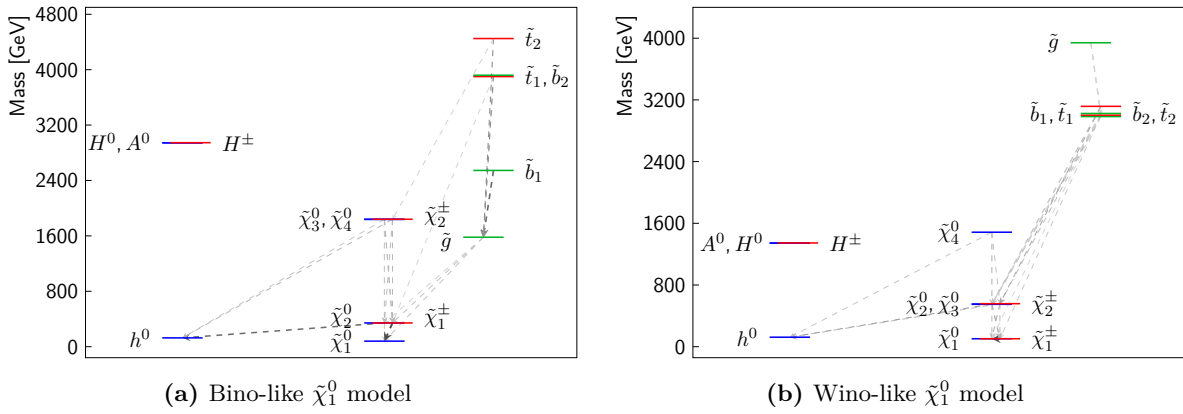


Figure 11.4: Mass spectra of two exemplary pMSSM models. Both models are excluded by the 1ℓ search. Fig. (a) represents a model with a bino-like LSP and nearly mass-degenerate $\tilde{\chi}_1^\pm$ and $\tilde{\chi}_1^0$. In fig. (b), a model with wino-like LSP and mass-degenerate $\tilde{\chi}_1^\pm$ and $\tilde{\chi}_2^0$ but comparably light $\tilde{\chi}_2^\pm$ (nearly mass-degenerate with the $\tilde{\chi}_2^0$) is shown. The branching fractions of the different decays are indicated through the width and and greyscale colour (pure black being 100%, pure white being 0%) of the arrows. Branching fractions below 10% are suppressed for the sake of visibility. Figures generated using `pyslha` [94].

The second category of models excluded comprises cases where the LSP is wino-like and nearly mass-degenerate with the $\tilde{\chi}_1^\pm$. These models correspond to the diagonal of the $m(\tilde{\chi}_1^\pm)$ – $m(\tilde{\chi}_1^0)$ plane in fig. 11.2(a). As the mass difference between the LSP and the $\tilde{\chi}_1^\pm$ is typically of the order of only a few 100 MeV, the $\tilde{\chi}_1^\pm$ can become long-lived, and primarily decays to a LSP and an off-shell W boson decaying into soft objects not reconstructed in the detector. If the $\tilde{\chi}_1^\pm$ is produced with large momentum, it can live long enough to traverse multiple layers of the ATLAS pixel detector before decaying, leading to a disappearing track signature. Searches targeting prompt electroweakino decays are not expected to be sensitive to these models, and instead dedicated disappearing track searches are developed within ATLAS (cf., for example, Ref. [299]). Even though no sensitivity to these models is expected from the 1ℓ search, a small set of models with a wino-like LSP can still be excluded. These models correspond to scenarios where the next-to-lightest chargino $\tilde{\chi}_2^\pm$ is not too heavy such that the 1ℓ search is sensitive to $\tilde{\chi}_2^\pm \tilde{\chi}_2^0$ production with cross sections of $\mathcal{O}(1\text{ fb})$. If the $\tilde{\chi}_2^\pm$ decays directly into the LSP via $\tilde{\chi}_2^\pm \rightarrow W^\pm \tilde{\chi}_1^0$, enough events with an isolated lepton can occur, allowing to exclude the model[†]. An exemplary mass spectrum of such a model, excluded by the 1ℓ search, is shown in fig. 11.4(b).

No sensitivity is observed for pMSSM models with higgsino-like electroweakinos, i.e. compressed mass spectra[§]. This is expected, as the electroweakino decays in such scenarios typically produce off-shell W , Z and h bosons, resulting in very soft final state objects the 1ℓ search is not optimised for. Dedicated searches (see, for example, Ref. [86]) exist in ATLAS to target such compressed scenarios and work is ongoing to include these in the large-scale scans of the pMSSM.

[†] Provided that the branching fraction of the $\tilde{\chi}_2^0 \rightarrow h \tilde{\chi}_1^0$ decay is also large enough, such that a final state with one lepton, E_T^{miss} and two b -jets from a Higgs decay can be realised often enough.

[§] The mass spectrum of an exemplary pMSSM model with higgsino-like LSP is shown in fig. C.4, highlighting that all three electroweakinos $\tilde{\chi}_1^\pm$, $\tilde{\chi}_2^0$ and $\tilde{\chi}_1^0$ are nearly mass-degenerate.

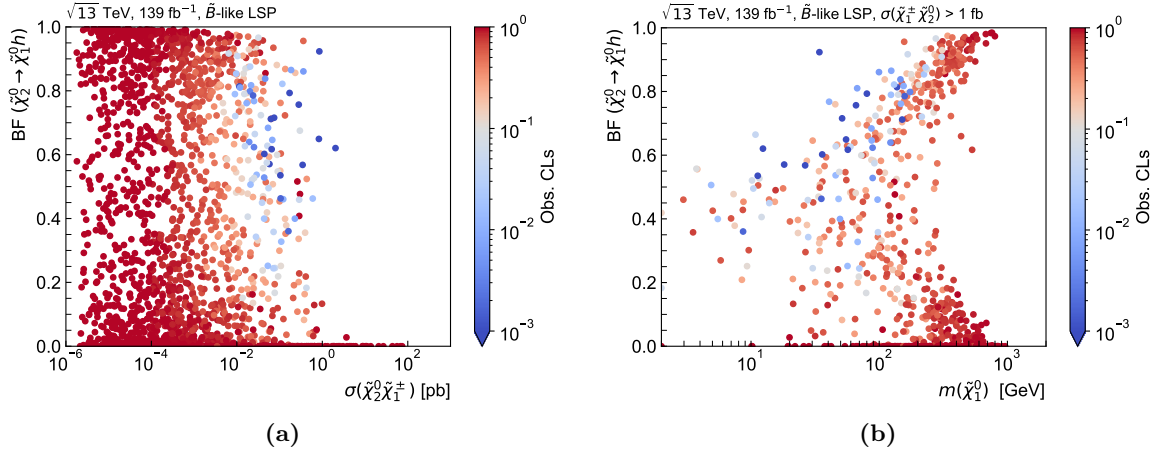


Figure 11.5: Density of the pMSSM models with bino-like $\tilde{\chi}_1^0$ projected onto the plane spanned by (a) $\tilde{\chi}_1^\pm\tilde{\chi}_2^0$ pair-production cross section and $\text{BF}(\tilde{\chi}_2^0 \rightarrow h\tilde{\chi}_1^0)$ and (b) $m(\tilde{\chi}_1^0)$ and $\text{BF}(\tilde{\chi}_2^0 \rightarrow h\tilde{\chi}_1^0)$. The observed CL_s value obtained for each model using the 1ℓ search is encoded using the colour-palette. Models with a red tint cannot be excluded, models with a neutral white tint are on the boundary of exclusion, and models with a blue tint can be excluded. Only models with a bino-like LSP are shown in both figures. Only models satisfying $\sigma(\tilde{\chi}_1^\pm\tilde{\chi}_2^0) > 1 \text{ fb}$ are shown in fig. (b).

In general, the sensitivity to pMSSM models is significantly reduced compared to the simplified model exclusion contour, even in the parameter space generating models with spectra similar to that of the simplified model. The crucial difference, responsible for the loss in sensitivity, is the fact that the simplified model assumes branching fractions of 100% of the $\tilde{\chi}_1^\pm \rightarrow W^\pm\tilde{\chi}_1^0$ and $\tilde{\chi}_2^0 \rightarrow h\tilde{\chi}_1^0$ decays (with on-shell W and h bosons). While the former is in general a good assumption in pMSSM models where $m(\tilde{\chi}_1^0) + m(W) \lesssim m(\tilde{\chi}_1^\pm) \lesssim m(\tilde{\chi}_2^0)$, the latter turns out not to be the dominant decay of the $\tilde{\chi}_2^0$ in many models where the competing decay $\tilde{\chi}_2^0 \rightarrow Z\tilde{\chi}_1^0$ dominates instead. The couplings of the $\tilde{\chi}_2^0$ to the Higgs boson are suppressed by powers of $|\mu|/M_2$ in the gaugino-like regions [300], meaning that the branching fraction of $\tilde{\chi}_2^0 \rightarrow h\tilde{\chi}_1^0$ takes on reasonably high values only in models with an LSP containing a substantial bino component[†].

As can be seen from fig. 11.2(a), even in the bulk of the $\tilde{\chi}_1^\pm\tilde{\chi}_2^0$ plane—containing mostly models with a bino-like LSP—not all models can be excluded by the simplified 1ℓ search. For a large majority of these models, no sensitivity is expected because the $\tilde{\chi}_1^\pm/\tilde{\chi}_2^0$ masses are too high, such that the $\tilde{\chi}_1^\pm\tilde{\chi}_2^0$ pair-production cross section is too low. Figure 11.5 shows a projection of the pMSSM models in a two-dimensional plane spanned by the $\tilde{\chi}_1^\pm\tilde{\chi}_2^0$ pair-production cross section and $\text{BF}(\tilde{\chi}_2^0 \rightarrow h\tilde{\chi}_1^0)$. This reveals that for many models, even if the $\tilde{\chi}_1^\pm\tilde{\chi}_2^0$ pair-production cross section is reasonably high, the branching fraction of the $\tilde{\chi}_2^0 \rightarrow h\tilde{\chi}_1^0$ is too low to produce enough events with Higgs candidates that could be reconstructed in the 1ℓ search. For the few non-excluded models with reasonably high $\tilde{\chi}_1^\pm\tilde{\chi}_2^0$ pair-production cross section of $\sigma(\tilde{\chi}_1^\pm\tilde{\chi}_2^0) \gtrsim 1 \text{ fb}$ and high enough Higgs coupling to $\tilde{\chi}_2^0$, the mass of the LSP turns out to be too high ($m(\tilde{\chi}_1^0) \gtrsim 300 \text{ GeV}$), typically resulting in final states with insufficient E_T^{miss} and soft objects that are not reconstructed in the context of the 1ℓ search. This behaviour

[†] The Higgs coupling suppression is illustrated in fig. C.3.

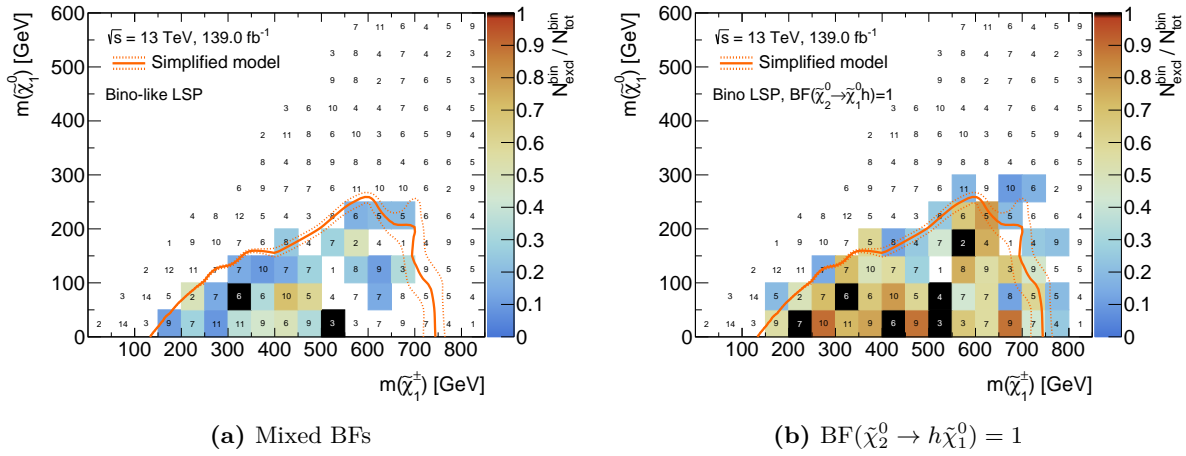


Figure 11.6: Bin-by-bin fraction of excluded models with a bino-like $\tilde{\chi}_1^0$ as a function of $m(\tilde{\chi}_1^\pm)$ and $m(\tilde{\chi}_1^0)$. In fig. (a) the pMSSM models originally sampled are shown. In fig (b), the branching fraction of the $\tilde{\chi}_2^0 \rightarrow h\tilde{\chi}_1^0$ decay is manually set to 100% after which event generation and 1ℓ analysis evaluation are re-executed. Only models with a bino-like LSP are shown in both figures.

is illustrated in fig. 11.5(b), where only models with a bino-like LSP and $\sigma(\tilde{\chi}_1^\pm \tilde{\chi}_2^0) > 1 \text{ fb}$ are shown.

As a cross-check, a sizeable portion of the models with a bino-like LSP were reprocessed with $\text{BF}(\tilde{\chi}_2^0 \rightarrow h\tilde{\chi}_1^0)$ fixed to unity (and $\text{BF}(\tilde{\chi}_2^0 \rightarrow Z\tilde{\chi}_1^0)$ consequently set to disappear) and subsequently reanalysed with the 1ℓ search. Figure 11.6(b) reveals that significantly more models can be excluded within the simplified model contour when the simplified model branching fraction assumption is restored. As the $\tilde{\chi}_2^0$ decay into a Z boson and $\tilde{\chi}_1^0$ is the competing decay to $\tilde{\chi}_2^0 \rightarrow h\tilde{\chi}_1^0$, statistically combining searches targeting these decay modes could therefore recover the loss in sensitivity originating from mixed branching fractions in realistic SUSY models. Likewise, the development of searches targeting both decay modes at the same time, would also recover the full sensitivity[†].

11.4.2 Impact on pMSSM parameters

The impact of the 1ℓ search on the pMSSM parameters relevant to the electroweak sector are shown in one-dimensional distributions in fig. 11.7. As already discussed in section 11.4.1, the 1ℓ search has the largest impact for small values in the bino mass parameter M_1 , leading to models with a bino-like LSP when $M_1 < M_2$ and $M_1 \ll \mu$. Consequently, the proportion of excluded models peaks at slightly higher values in the distribution of the wino mass parameter, $|M_2| \approx 400 \text{ GeV}$. As the search is not sensitive to compressed scenarios with a higgsino-like LSP, no models with small values in $|\mu|$ can be excluded.

Since the pseudoscalar Higgs boson does not directly enter the phenomenology of the models targeted by the 1ℓ search, only indirect constraints can be set on m_A , excluding models across the full range of the m_A distribution sampled. A similar behaviour is observed in $\tan \beta$ where

[†] Provided that they are targeted with statistically independent signal regions such that a combined likelihood can be built.

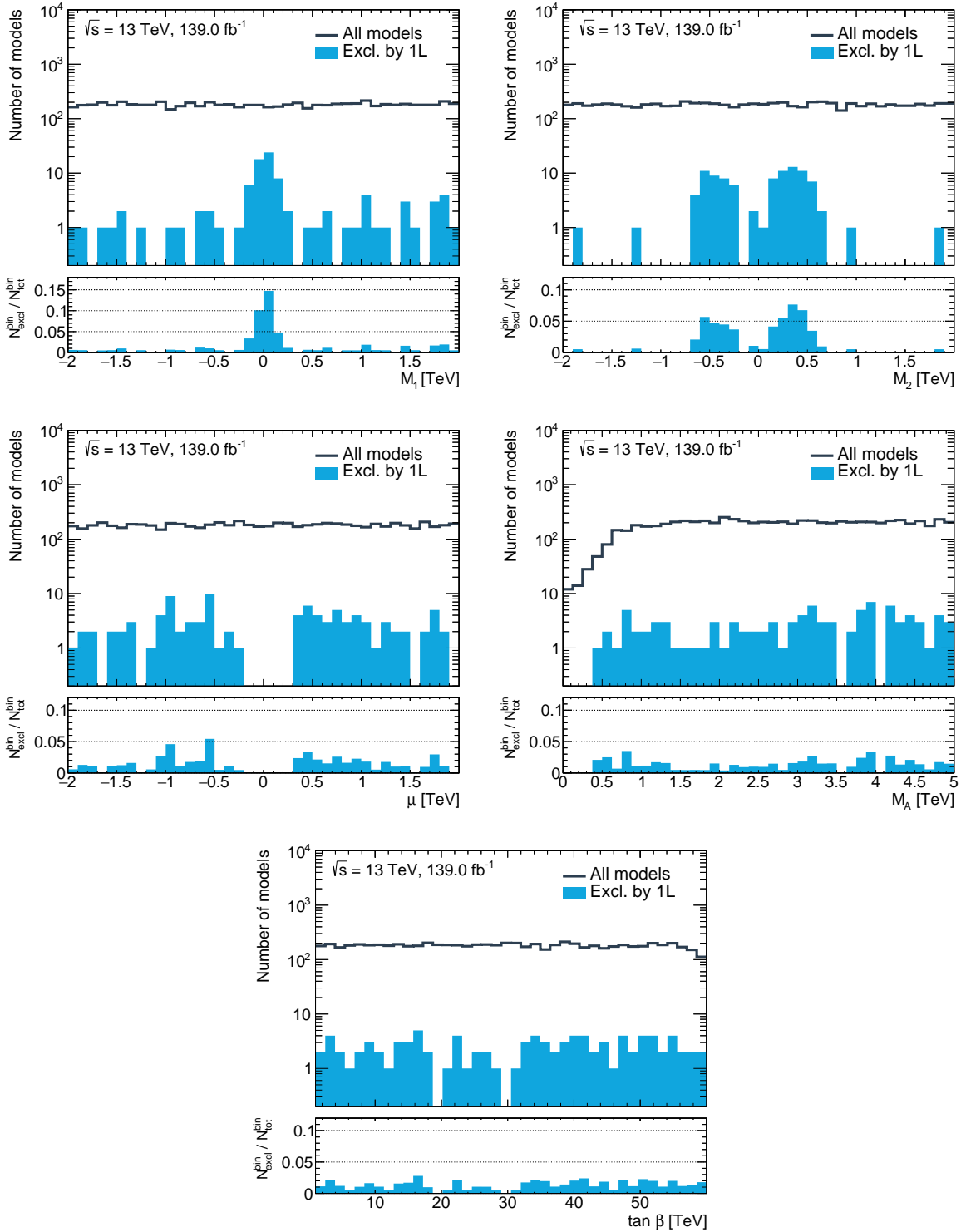


Figure 11.7: Bin-by-bin number of excluded models as a one-dimensional function of the pMSSM parameters sampled relevant to the electroweak sector. The bin-wise fraction of excluded models, $N_{\text{excl}}^{\text{bin}} / N_{\text{tot}}^{\text{bin}}$, is shown in the lower pad. All models are evaluated using the simplified likelihood of the 1ℓ search.

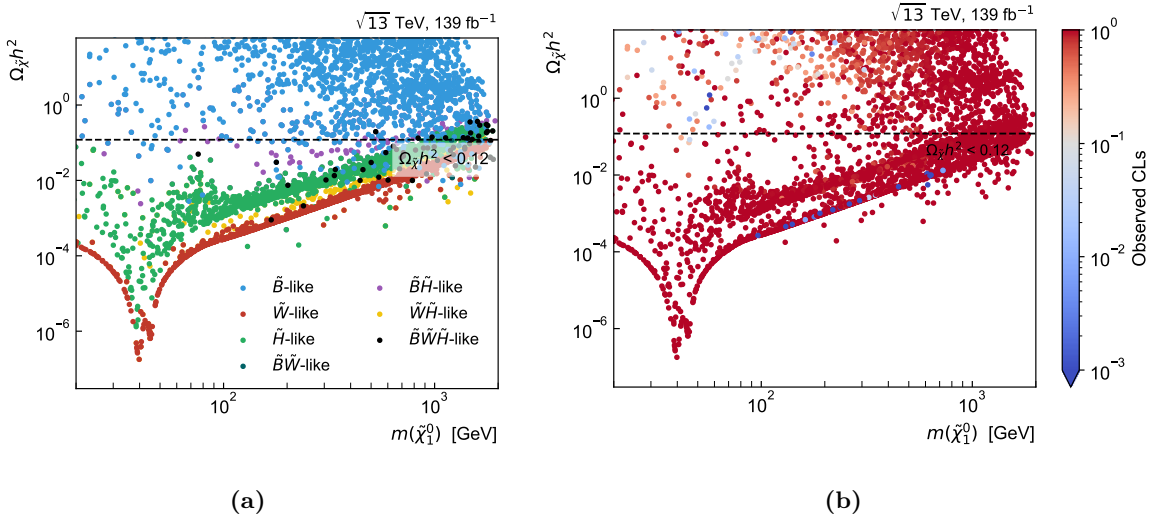


Figure 11.8: Density of the pMSSM model points sampled in the plane spanned by the relic density and the $\tilde{\chi}_1^0$ mass. The model points are additionally shown as a function of (a) the nature of their LSP and (b) the observed CL_s value obtained for 139 fb^{-1} of data using the 1ℓ search. The horizontal dashed line represents the DM relic density measurement by the Planck collaboration [47], interpreted as an upper limit $\Omega_{\tilde{\chi}} h^2 < 0.12$ such that the $\tilde{\chi}_1^0$ can be a sub-dominant DM component.

the excluded models have values of $\tan \beta$ spanning the full range from 1 to 60. Likewise, no direct constraints on the trilinear scalar couplings (A_t , A_b , A_τ), and the remaining gluino and third generation squark mass parameters (M_3 , $m_{\tilde{Q}_3}$, $m_{\tilde{u}_3}$, $m_{\tilde{d}_3}$) is observed[†].

11.4.3 Impact on dark matter relic density

The $\tilde{\chi}_1^0$ cosmological abundance, $\Omega_{\tilde{\chi}} h^2$, in dependence of its type and mass is shown in fig. 11.8(a). The value of the DM relic density measured by the Planck mission is also given [47]. The Planck measurement is interpreted as upper limit on the DM relic density, thus allowing the $\tilde{\chi}_1^0$ to be a sub-dominant DM component.

Some interesting features are worth highlighting. First, most of the models sampled with a bino-like $\tilde{\chi}_1^0$ result in a cosmological abundance too high to be compatible with the value measured by Planck. Of the pMSSM models sampled herein, only models with a $\tilde{\chi}_1^0$ containing a considerable wino or higgsino component consistently satisfy $\Omega_{\tilde{\chi}} h^2 < 0.12$ over a large range of $m(\tilde{\chi}_1^0)$. Models with $m(\tilde{\chi}_1^0) \simeq m(Z)/2$ produce especially low values in $\Omega_{\tilde{\chi}} h^2$ as the $\tilde{\chi}_1^0$ can resonantly annihilate through s -channel Z exchange. This is the so-called *Z-funnel*, a mechanism that becomes more efficient, the larger the higgsino component of the $\tilde{\chi}_1^0$ is [301]. Likewise, models with nearly mass-degenerate $\tilde{\chi}_1^\pm \tilde{\chi}_1^0$ pair at $m(W)/2$ can also produce low relic densities because of $\tilde{\chi}_1^\pm \tilde{\chi}_1^0$ co-annihilation through s -channel W exchange. A funnel similar to the *Z-funnel* but involving s -channel Higgs exchange exists around $m(\tilde{\chi}_1^0) \simeq m(h)/2$. It requires the $\tilde{\chi}_1^0$ to have a sizeable bino component [301] and is therefore not visible in fig. 11.8(a) because models with a bino-like LSP are underrepresented in the relevant mass range.

[†] Illustrated in fig. C.5.

In practice, the LEP limits[†] on the chargino mass of $\tilde{\chi}_1^\pm > 103.5 \text{ GeV}$ [85] rule out models with $|M_2| \lesssim 100 \text{ GeV}$ and $|\mu| \lesssim 100 \text{ GeV}$, leaving only models with a bino-like LSP in the region with $m(\tilde{\chi}_1^0) \lesssim 100 \text{ GeV}$.

Although theoretically models with a bino-like $\tilde{\chi}_1^0$ could produce low $\tilde{\chi}_1^0$ relic density values through the Z - and h -funnels, in practice such models are not sampled in this thesis due to the sampling technique used. In order to further study the impact of the 1ℓ search on models relevant to the DM phenomenology, i.e. models with a bino-like LSP in the Z - and h -funnels, a different sampling technique would need to be employed, including experimental constraints in the sampling priors in addition to oversampling models with a bino-like LSP in the relevant mass range.

Although of limited use due to the limited number of models in the relevant parameter space, the impact of the 1ℓ search on the DM relic density can still be investigated with the models available. Figure 11.8(b) shows the $\tilde{\chi}_1^0$ cosmological abundance in dependence of its mass. Instead of encoding the nature of the $\tilde{\chi}_1^0$, the colour now encodes the observed CL_s value obtained by the 1ℓ search. By comparing with fig. 11.8(a), it can be seen that the majority of the models with a bino-like $\tilde{\chi}_1^0$, excluded by the 1ℓ search, have a cosmological abundance not satisfying $\Omega_{\tilde{\chi}} h^2 < 0.12$. Through its limited sensitivity to some of the models with a wino-like $\tilde{\chi}_1^0$, the 1ℓ search is, however, still able to exclude some models with a compatible LSP relic density.

11.5 Discussion

Large-scale reinterpretations in high-dimensional SUSY model spaces are crucial in order to assess the sensitivity of SUSY searches in the context of realistic SUSY scenarios. The evaluation of signal models at smeared truth level, in combination with the simplified likelihoods introduced in chapter 10, offers a computationally efficient but still reliable approach for such reinterpretations.

A reinterpretation of the 1ℓ search in a limited number of models sampled from the pMSSM with a focus on the electroweak sector revealed that the search is sensitive to SUSY scenarios beyond the canonical simplified model originally considered. In general, the simplified model phenomenology maps reasonably well onto a portion of the pMSSM parameter space. The sensitivity of the 1ℓ search towards pMSSM models is, however, negatively impacted by the competing decays $\tilde{\chi}_2^0 \rightarrow Z\tilde{\chi}_1^0$ and $\tilde{\chi}_2^0 \rightarrow h\tilde{\chi}_1^0$, breaking one of the main assumptions of the simplified model. In order to maximise the sensitivity of future searches to $\tilde{\chi}_1^\pm\tilde{\chi}_2^0$ pair-production in more complete SUSY scenarios, it is therefore crucial to target both decay modes at the same time. In searches targeting final states with one lepton, multiple jets and missing transverse momentum, both the b -jet multiplicity as well as the invariant mass of the jets originating from the decays $h \rightarrow b\bar{b}$ and $Z \rightarrow q\bar{q}$ can easily be exploited to develop disjoint[§] signal regions targeting both decay modes.

Beyond the combination of single decay modes, it could be worth targeting not only $\tilde{\chi}_1^\pm\tilde{\chi}_2^0$ production, but also the $\tilde{\chi}_1^\pm\tilde{\chi}_1^\pm$ production mode at the same time in a single likelihood function.

[†] The impact of this limit in the $\Omega_{\tilde{\chi}} h^2 - m(\tilde{\chi}_1^0)$ projection is shown in fig. C.6.

[§] Building signal regions that are not orthogonal to each other prevents the construction of a single likelihood and thus does not allow statistical combination.

In ATLAS, work is for example ongoing to perform a search for electroweakinos in the 1ℓ final state using dedicated signal regions targeting both $\tilde{\chi}_1^\pm \tilde{\chi}_2^0 \rightarrow WZ \tilde{\chi}_1^0 \tilde{\chi}_1^0 \rightarrow \ell \nu_\ell q \bar{q} \tilde{\chi}_1^0 \tilde{\chi}_1^0$ and $\tilde{\chi}_1^\pm \tilde{\chi}_1^\pm \rightarrow WW \tilde{\chi}_1^0 \tilde{\chi}_1^0 \rightarrow \ell \nu_\ell q \bar{q} \tilde{\chi}_1^0 \tilde{\chi}_1^0$ at the same time.

Finally, the impact of the 1ℓ search on the DM relic density was discussed. The parameter ranges and sampling technique chosen were used to guarantee the scan to be as general as possible. For this reason, many models sampled are not directly relevant to the DM phenomenology. Only a small number of models with a bino-like $\tilde{\chi}_1^0$ are sampled from Z - and h -funnel region where $\Omega_{\tilde{\chi}} h^2 < 0.12$ can be expected to be satisfied for a sizeable fraction of such models. Outside of these two funnels, models with a bino-like $\tilde{\chi}_1^0$ only satisfy the relic density constraint for $\tilde{\chi}_1^\pm$ and $\tilde{\chi}_1^0$ masses outside of the parameter space that the 1ℓ search is sensitive to. In order to be able to further investigate the impact of the 1ℓ search on DM observables—especially in the Z and h -funnels—a different sampling technique would need to be adopted, including experimental constraints in the sampling priors and oversampling the relevant regions of the parameter space.

Part IV

Summary and Outlook

Chapter 12

Conclusions

This thesis presented a search for direct production of electroweakinos in events with one lepton, missing transverse momentum and a Higgs boson decaying into two b -jets. The full dataset of Run 2 of the LHC, amounting to 139 fb^{-1} of pp collisions at $\sqrt{s} = 13 \text{ TeV}$, recorded with the ATLAS experiment, was analysed. The search targets a simplified electroweakino ($\tilde{\chi}_1^\pm \tilde{\chi}_2^0$) pair-production model with subsequent decays into W and Higgs bosons together with two lightest neutralinos ($\tilde{\chi}_1^0$). The $\tilde{\chi}_1^0$ is the LSP of the model, is electrically neutral and stable, and thus could be a good candidate for DM. It escapes the detector without leaving a trace, resulting, in general, in a significant amount of missing transverse momentum that can be triggered on. The search further targets a W boson decay into a lepton–neutrino pair and a Higgs boson decay into a b -jet pair.

Both the lepton–neutrino and the b -jet pairs offer powerful discriminative handles, exploited through the use of a number of kinematic observables in order to maximise the signal-to-background ratio in the phase space targeted. Using a dedicated optimisation procedure, two sets of signal regions are defined, one targeting generic BSM scenarios (called *discovery* signal regions), and one optimised for the simplified model in question (called *exclusion* signal regions). The exclusion signal regions are designed to be mutually exclusive through their requirements on the transverse mass (m_T) and the contransverse mass (m_{CT}). Contributions from SM background processes in the signal regions originate primarily from $t\bar{t}$ and single top production, as well as $W + \text{jets}$ processes. Contributions from SM backgrounds are estimated either with a semi-data-driven technique using dedicated control regions, or directly from MC simulation. A binned likelihood is constructed, statistically combining all exclusion signal regions into a two-dimensional shape-fit that exploits the varying shapes of the m_T and m_{CT} distributions of SUSY signal and SM background processes. This approach allows to achieve sensitivity to a wide variety of kinematic regimes.

No significant excess has been observed in any of the signal regions, and thus model-dependent exclusion limits and model-independent upper limits on the visible cross section of BSM processes have been derived. Due to the introduction of the two-dimensional shape-fit and the unprecedented amount of 139 fb^{-1} of pp collision data analysed, the model-dependent exclusion limits set by previous searches targeting the same simplified model can be significantly extended. For a massless LSP, $\tilde{\chi}_1^\pm/\tilde{\chi}_2^0$ masses up to 740 GeV can be excluded at 95% CL. In the case of a heavier LSP with $m(\tilde{\chi}_1^0) \approx 250 \text{ GeV}$, the limits on the $\tilde{\chi}_1^\pm/\tilde{\chi}_2^0$ masses weaken to about

600 GeV. At the time of writing, the limits obtained by this search represent the most stringent constraints on $\tilde{\chi}_1^\pm \tilde{\chi}_2^0$ pair-production set by ATLAS in the context of the simplified model considered [256]. The model-independent 95% CL upper limits on the visible cross section of BSM processes vary between 0.26 fb and 0.11 fb, depending on the signal region considered.

The absence of physics beyond the SM in the Run 2 dataset of the LHC in the search presented herein, is in line with the results of other SUSY searches performed by ATLAS and CMS. While the existence of gluinos and squarks at the TeV-scale was already severely challenged by the end of Run 1 of the LHC, the limits on electroweakinos and sleptons were, in general, weaker because of their smaller production cross sections. Due to the large integrated luminosity available through the Run 2 dataset, and the improved analysis techniques and strategies developed over the last years, the limits on electroweakinos and sleptons are also significantly increasing, and in some cases start to approach the 1 TeV mark [256, 258].

Given these constraints, it might be tempting to discard the existence of SUSY at the LHC altogether. Such conclusions would, however, be drawn much too early. On the one hand, 139 fb^{-1} of pp collision data only corresponds to a fraction of the total integrated luminosity the LHC is designed to deliver. By the end of the lifetime of the high-luminosity LHC upgrade, a projected amount of 3000 fb^{-1} [259] will have been delivered to the particle physics experiments. Many supersymmetric models not accessible with the Run 2 dataset using today's analyses, will hence only come into reach in the upcoming runs of the LHC. On the other hand, most limits derived by SUSY searches assume specific simplified models and are thus only valid in the context of the assumptions made in these models. In any realistic SUSY scenario, assumptions like 100% branching ratios or small sets of participating, non-decoupled supersymmetric particles are, however, most likely not exactly fulfilled. Thus, simplified model limits can in general not be trivially interpreted as the true underlying constraints on the respective parameters of a realistic SUSY scenario.

Due to the rapidly changing landscape of models for physics beyond the SM and the limited scope of parameter limits quoted by the experiments, reinterpretations of searches for supersymmetry are highly desirable and see significant interest from both the experimental and theory communities. With this in mind, the search for SUSY presented herein was implemented to be fully reinterpretable in the light of new BSM models. This is achieved by using a cyber-infrastructure called RECAST [262], relying on containerised workflows orchestrating parametrised job templates. Additionally, the full likelihood of the search was made publicly available in a readily available format, allowing it to be incorporated in a number of reinterpretation efforts outside of ATLAS [275, 276].

Large-scale reinterpretations in high-dimensional model spaces are especially interesting, but computationally extremely challenging, and thus require suitable approximations. In this thesis, a method to generically approximate the likelihoods of SUSY searches using binned distributions was introduced and validated using a selection of ATLAS searches for SUSY. The search previously presented was reinterpreted in the pMSSM, a 19-dimensional parameter space containing more realistic SUSY scenarios (compared to simplified models). Due to the assumption of 100% branching fractions not being satisfied in many of these more complete SUSY scenarios, the sensitivity of the 1ℓ search was found to be noticeably reduced. A small fraction of models sampled could, however, still be excluded.

The impact of the 1ℓ search on electroweakino masses was investigated, revealing some sensitivity to $\tilde{\chi}_2^\pm \tilde{\chi}_2^0$ production with a wino-like LSP, in addition to sensitivity towards models phenomenologically close to the simplified model the search was optimised for. The impact of the 1ℓ search on the DM relic density was also investigated. While no conclusive statement could be made for models with a bino-like $\tilde{\chi}_1^0$ because of the limited number of such models sampled in the relevant parameter space, some models with a wino-like $\tilde{\chi}_1^0$ with cosmological abundance satisfying the Planck constraint could still be excluded.

Although hopes of quickly finding supersymmetric particles with the LHC have not materialised, there is still a possibility of finding hints for physics beyond the SM in the collision data recorded by the LHC experiments. Considerable regions of the parameter space of realistic SUSY scenarios are still largely unconstrained and offer ample space for SUSY to hide in. In order to provide a comprehensive overview of the constrained parameter space, it is not only important to optimise searches to be sensitive to the complex phenomenology of realistic supersymmetric scenarios, but also to design the searches to be systematically reinterpretable, especially in light of more complete and realistic scenarios. After all, searches for BSM physics are the tools that shine a light on the otherwise unilluminated landscapes of the parameter spaces of BSM theories. Allowing these tools to be reusable significantly increases the area of parameter space they can shine a light onto.

Part V

Appendix

Appendix A

A.1 Additional information on signal region optimisation

The following figures provide additional information on the signal region optimisation performed in chapter 5. Figure A.1 shows the results of the N -dimensional cut scan for the remaining benchmark signal points considered. As before, three different uncertainty configurations are used for computing the significance Z_B , and all values are computed for the two statistically independent subsets used during the N -dimensional scan. This approach allows to gauge the impact of statistical fluctuations on the cut combinations tested.

By choosing a well-performing cut combination for each benchmark point, the optimised selections in figs. A.2 to A.7 are found after a round of $N - 1$ plots. As discussed in section 5.2.2 the optimal cut combinations for each benchmark signal point are consolidated into multiple signal regions designed to be sensitive to different kinematic regions of the model parameter space.

Figure A.8 shows additional information on some of the investigated simplified shape-fit configurations. Two-dimensional shape-fits in $(m_T, m_{b\bar{b}})$, (m_T, E_T^{miss}) and (m_T, m_{CT}) with 3×3 bins each are compared. The configuration using bins in m_T and m_{CT} results in the best expected CL_s values throughout the entire signal grid. Adding a requirement on high values of $m_{\ell b_1}$ to SR-HM further increases the expected sensitivity. Overall, the expected sensitivity achieved through introduction of the two-dimensional shape fit significantly exceeds the sensitivity of the previous analysis iteration (using a one-dimensional shape-fit in m_T , scaled to 139 fb^{-1}).

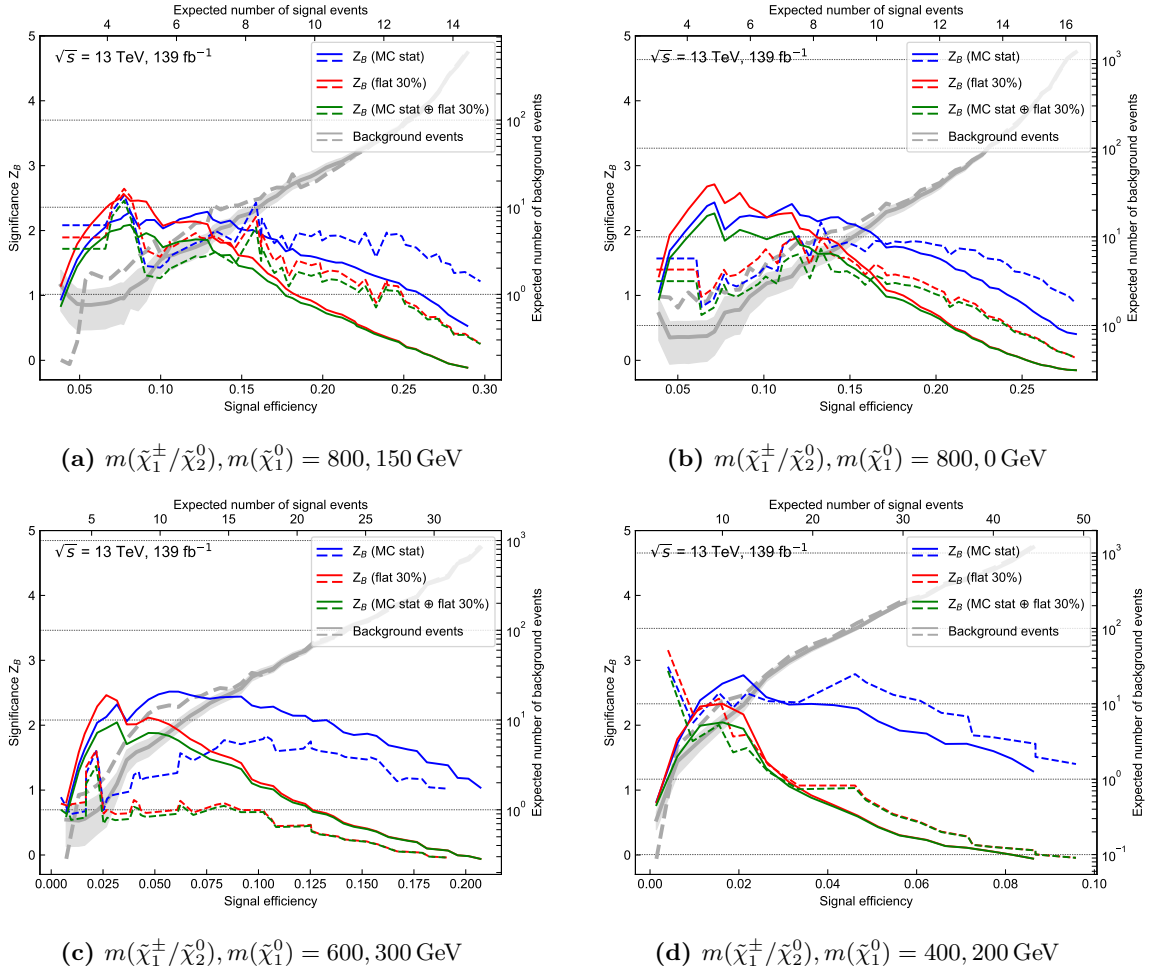


Figure A.1: Results of the N -dimensional cut scan for the remaining four benchmark points. The binomial discovery significance Z_B is plotted against the signal efficiency for varying uncertainty configurations. Additionally, the expected SM background rates are shown, including statistical uncertainty for one of the two statistically independent samples (shaded area). The solid and dashed lines represent the two statistically independent subset that the MC samples are split into.

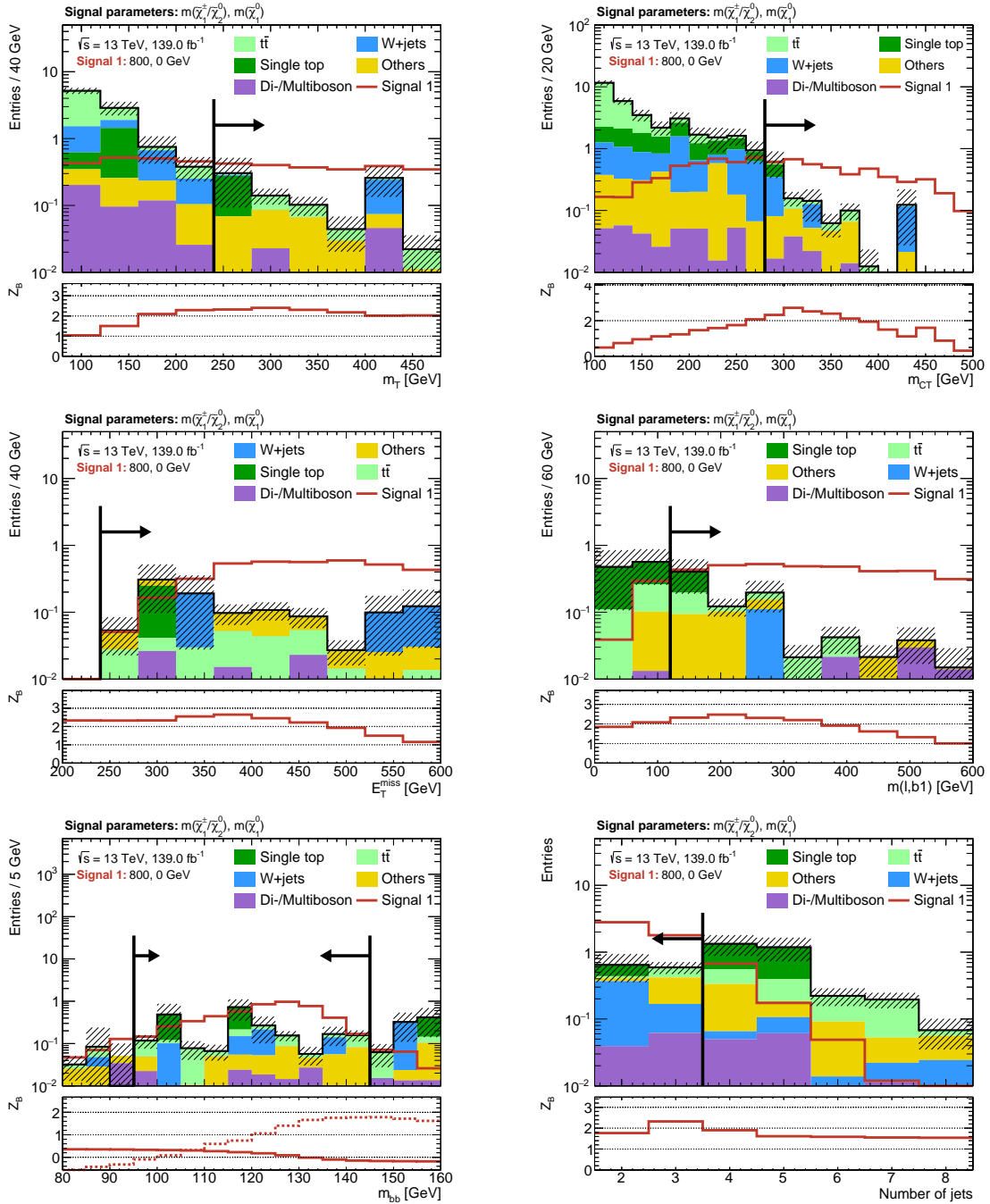


Figure A.2: N-1 plots for the chosen cut combination for the $(m(\tilde{\chi}_1^\pm/\tilde{\chi}_2^0), m(\tilde{\chi}_1^0)) = (800 \text{ GeV}, 0 \text{ GeV})$ signal point. The shaded region includes MC statistical uncertainty as well as 30% systematic uncertainty (added in quadrature) on the background. The significance is computed using the binomial discovery significance using the uncertainty on the background.

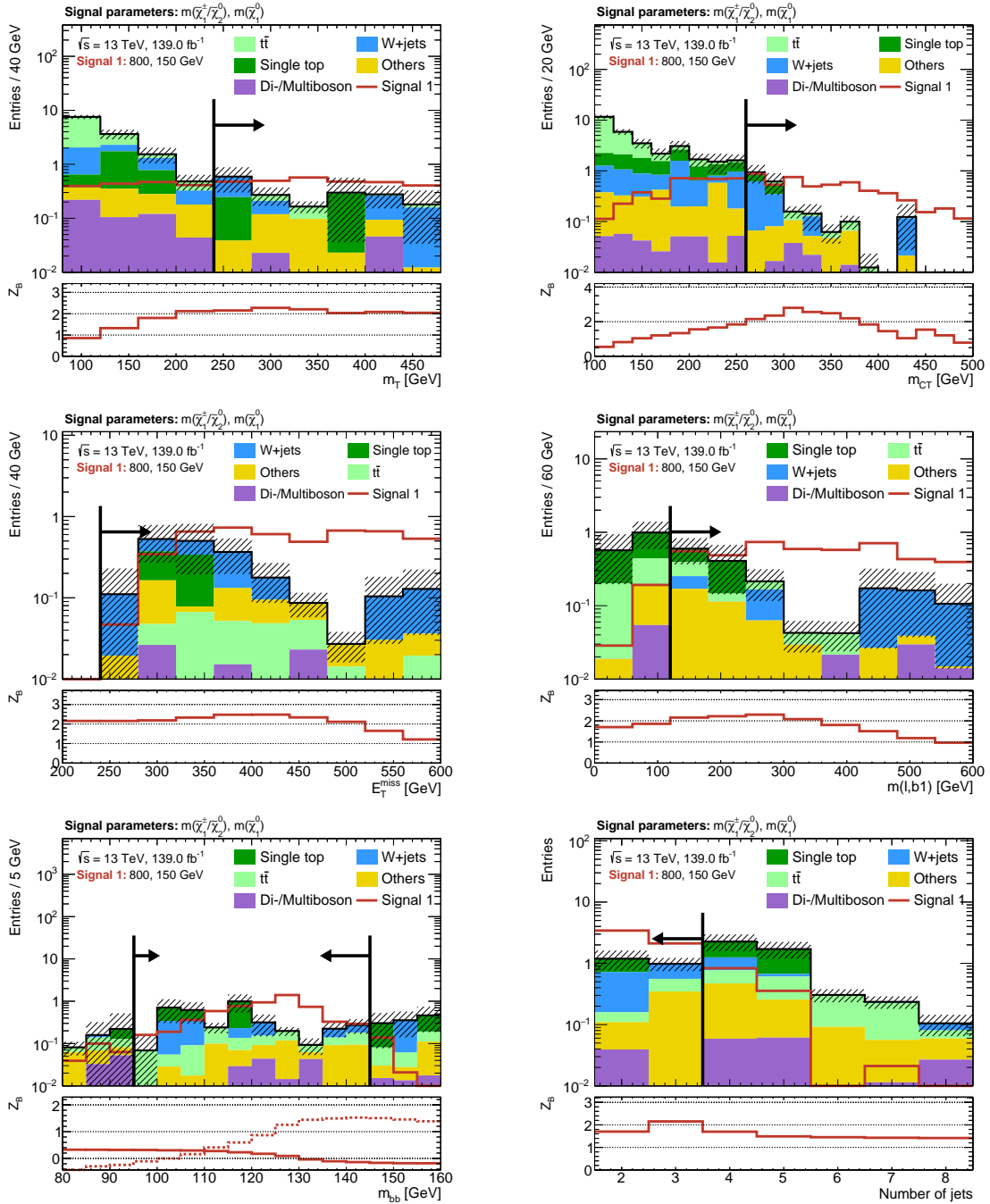


Figure A.3: N-1 plots for the chosen cut combination for the $(m(\tilde{\chi}_1^\pm/\tilde{\chi}_2^0), m(\tilde{\chi}_1^0)) = (800 \text{ GeV}, 150 \text{ GeV})$ signal point. The shaded region includes MC statistical uncertainty as well as 30% systematic uncertainty (added in quadrature) on the background. The significance is computed using the binomial discovery significance using the uncertainty on the background.

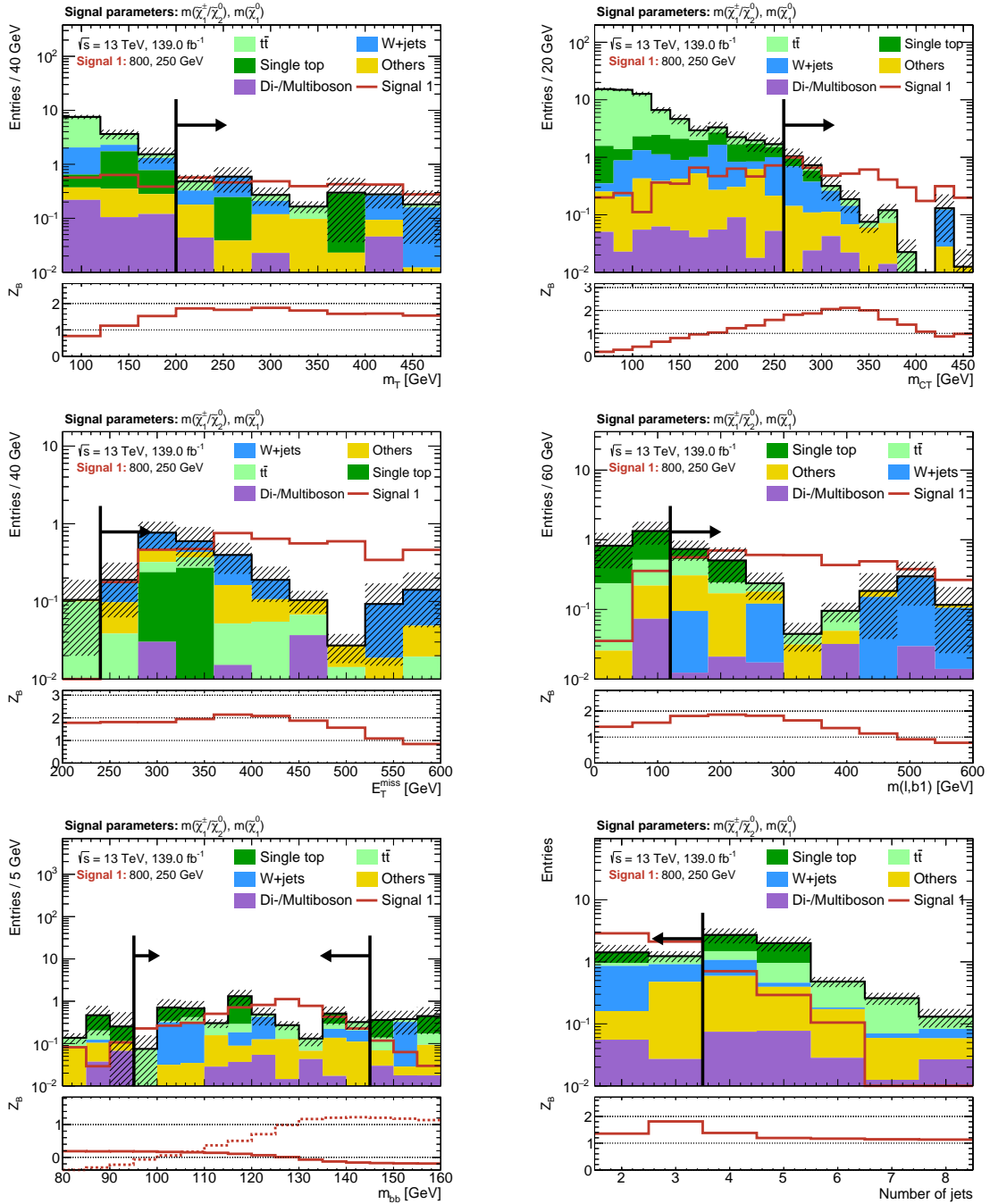


Figure A.4: N-1 plots for the chosen cut combination for the $(m(\tilde{\chi}_1^\pm/\tilde{\chi}_2^0), m(\tilde{\chi}_1^0)) = (800 \text{ GeV}, 250 \text{ GeV})$ signal point. The shaded region includes MC statistical uncertainty as well as 30% systematic uncertainty (added in quadrature) on the background. The significance is computed using the binomial discovery significance using the uncertainty on the background.

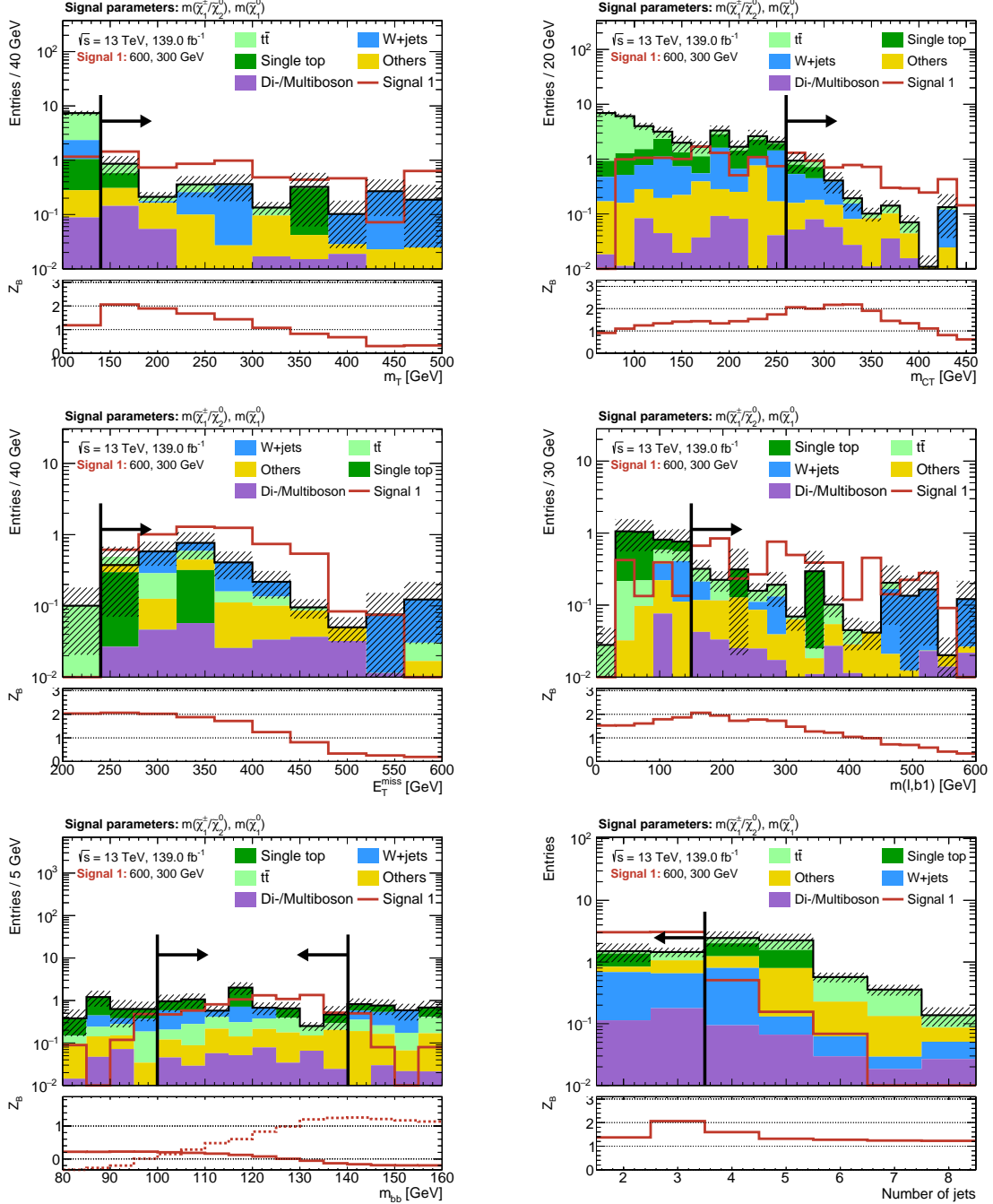


Figure A.5: N-1 plots for the chosen cut combination for the $(m(\tilde{\chi}_1^\pm/\tilde{\chi}_2^0), m(\tilde{\chi}_1^0)) = (600 \text{ GeV}, 300 \text{ GeV})$ signal point. The shaded region includes MC statistical uncertainty as well as 30% systematic uncertainty (added in quadrature) on the background. The significance is computed using the binomial discovery significance using the uncertainty on the background.

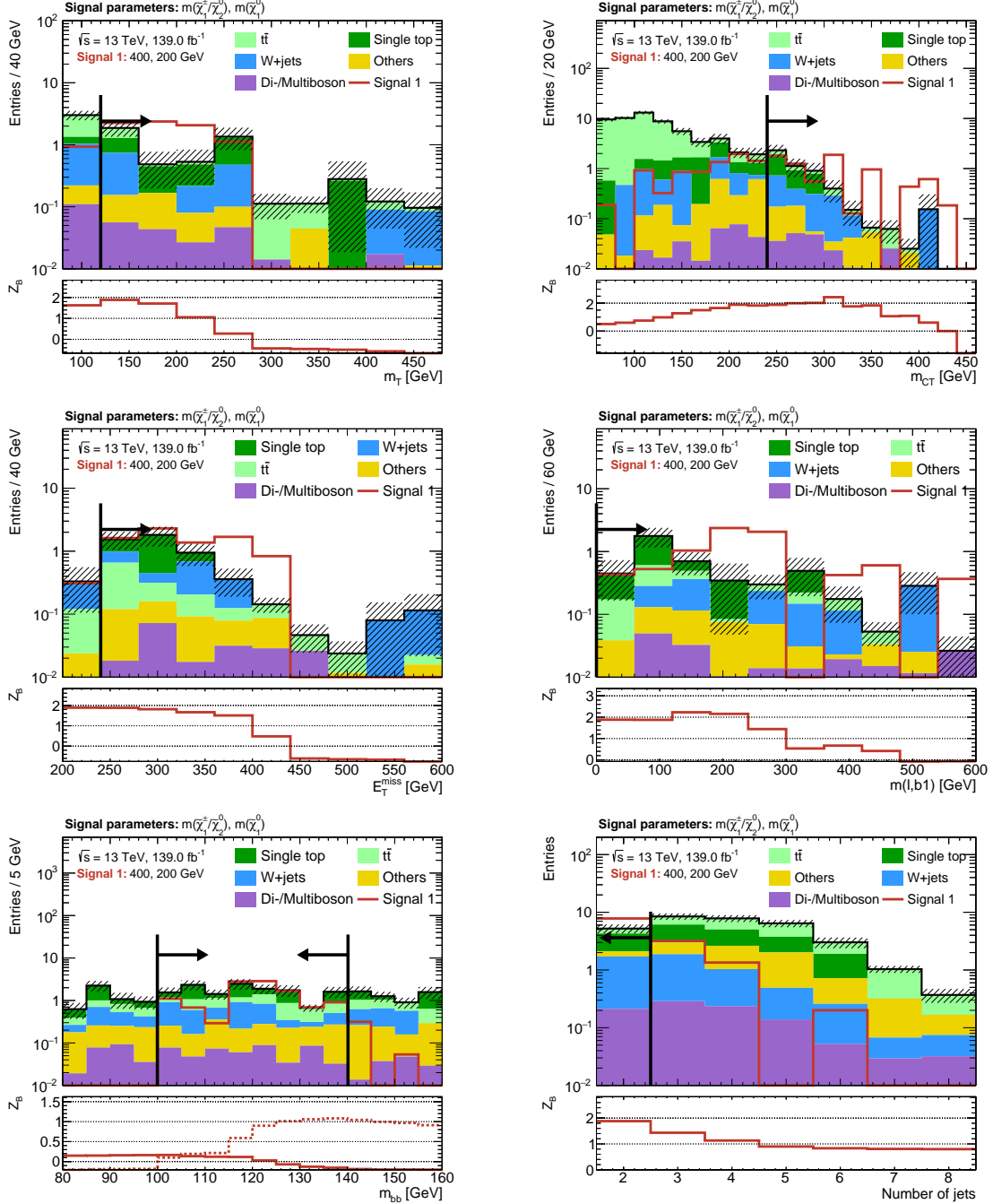


Figure A.6: N-1 plots for the chosen cut combination for the $(m(\tilde{\chi}_1^\pm/\tilde{\chi}_2^0), m(\tilde{\chi}_1^0)) = (400 \text{ GeV}, 200 \text{ GeV})$ signal point. The shaded region includes MC statistical uncertainty as well as 30% systematic uncertainty (added in quadrature) on the background. The significance is computed using the binomial discovery significance using the uncertainty on the background.

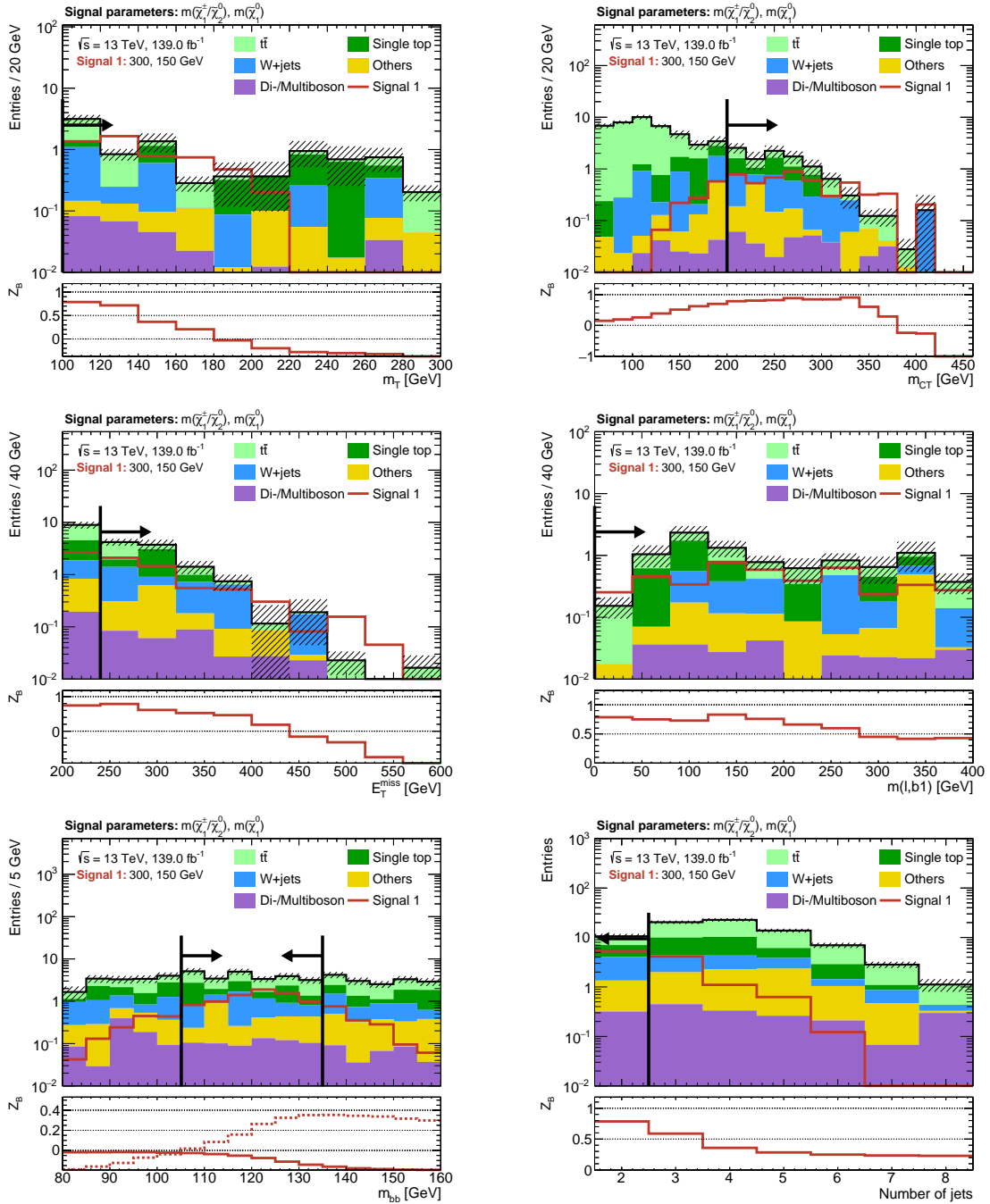


Figure A.7: N-1 plots for the chosen cut combination for the $(m(\tilde{\chi}_1^\pm/\tilde{\chi}_2^0), m(\tilde{\chi}_1^0)) = (300 \text{ GeV}, 150 \text{ GeV})$ signal point. The shaded region includes MC statistical uncertainty as well as 30% systematic uncertainty (added in quadrature) on the background. The significance is computed using the binomial discovery significance using the uncertainty on the background.

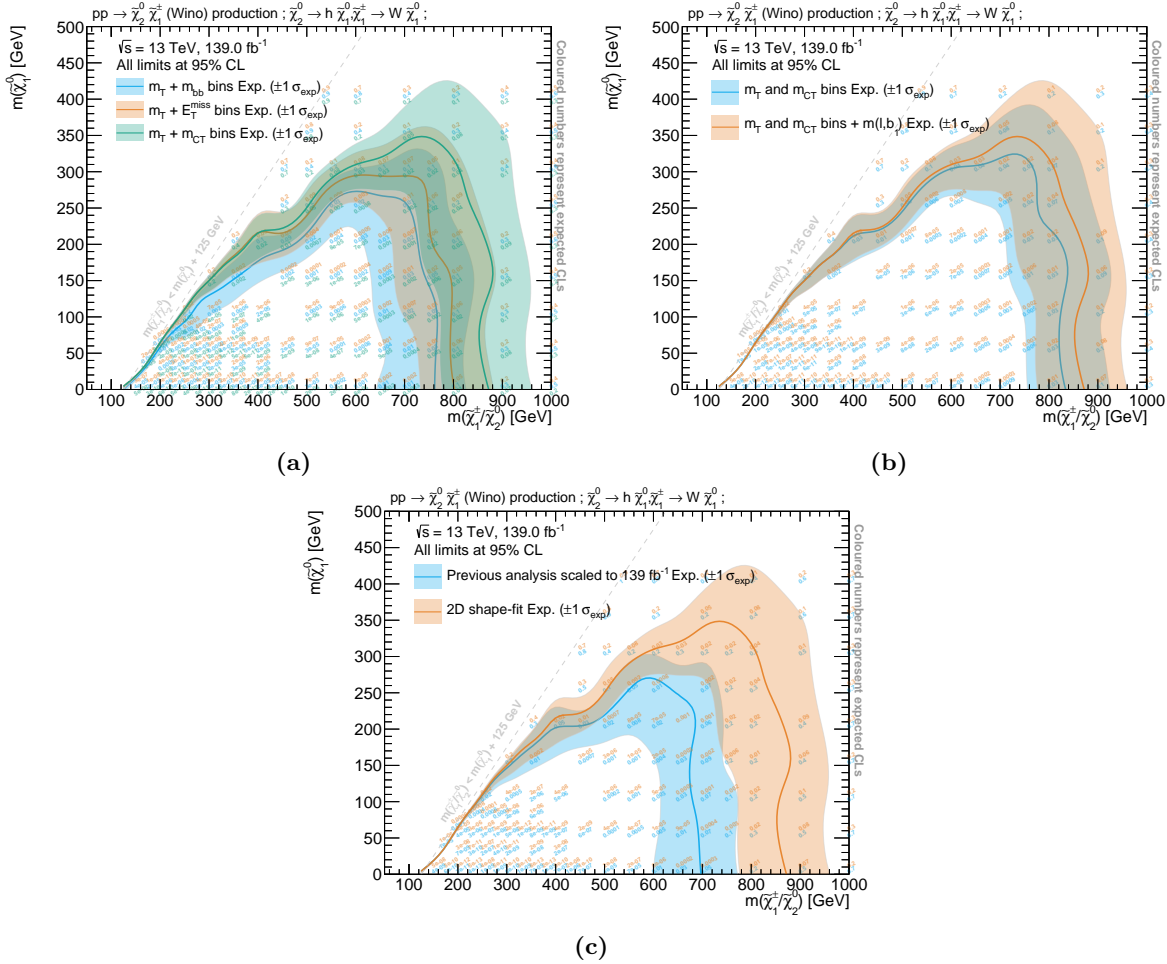


Figure A.8: Comparison of different shape-fit configurations. Fig. (a) compares three different two-dimensional shape-fit configurations using 3×3 bins in (m_T, E_T^{miss}) , (m_T, m_{bb}) and (m_T, m_{CT}) . Fig. (b) illustrates the sensitivity increase achieved through a requirement on high m_{elb_1} values in SR-HM on top of the two-dimensional shape-fit in m_T and m_{CT} . Fig. (c) compares the two-dimensional shape-fit in m_T and m_{CT} to the previous analysis iteration signal regions scaled to 139 fb^{-1} . All shown exclusion limits are expected limits at 95% CL, using MC statistical and 30% systematic uncertainty. Background estimation in the signal regions is taken directly from MC for all SM backgrounds.

A.2 Background estimation

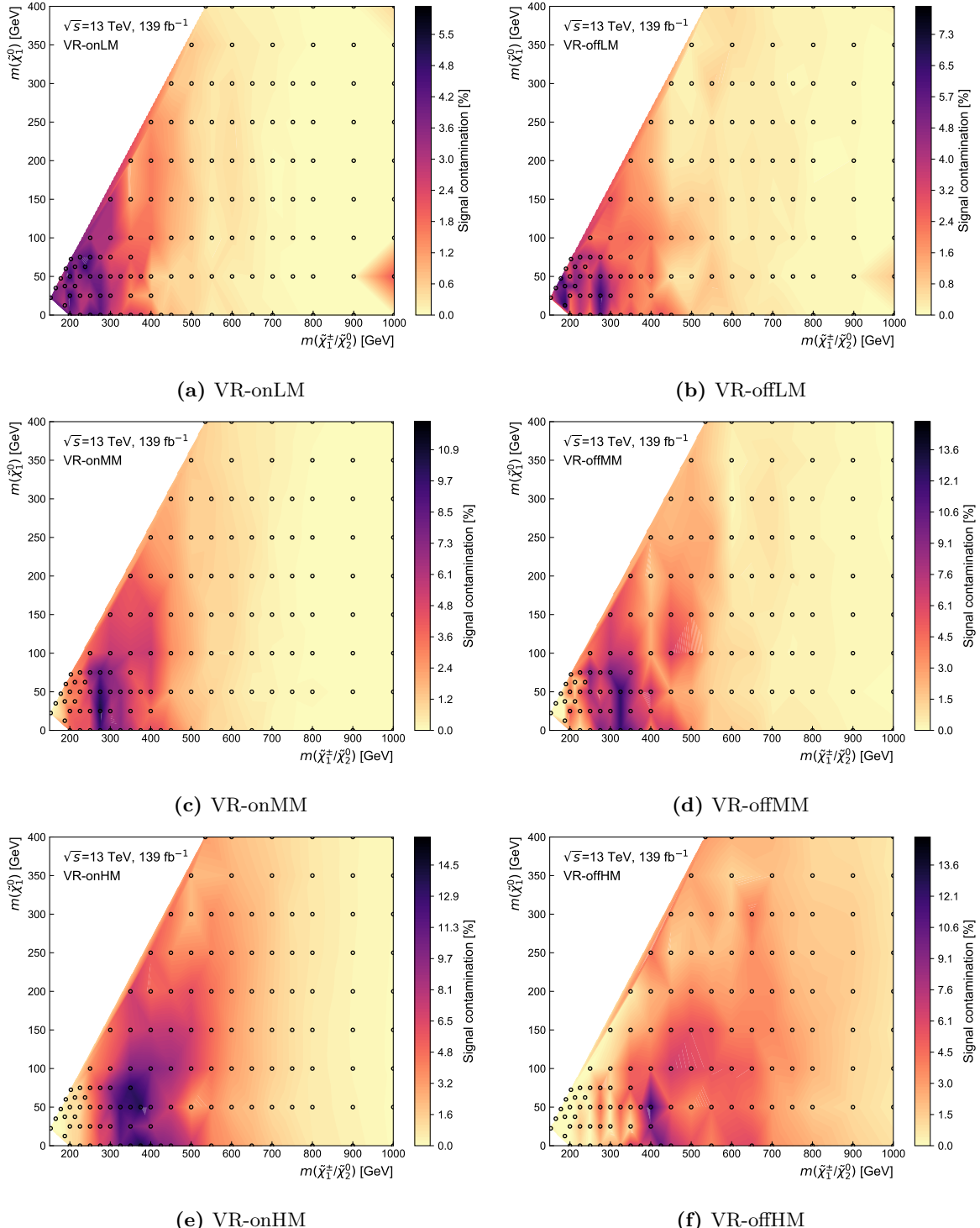


Figure A.9: Signal contamination (shown on the z -axis) for all VRs throughout the signal grid. The space between the signal points (indicated by the black circles) is interpolated using Delaunay triangles.

ATLAS SUSY Searches* - 95% CL Lower Limits									
Model	Signature	$f_{\mathcal{L}} dt$ [fb $^{-1}$]	Mass limit						Reference
$\tilde{q}\tilde{q}, \tilde{q} \rightarrow q\tilde{q}_1^0$	0 e, μ mono-jet	2-6 jets	E_T^{miss}	139	\tilde{q} [10× Digen.]	0.43	0.71	1.9	$m(\tilde{q})=400\text{ GeV}$ $m(\tilde{q})=m(\tilde{q}_1^0)=5\text{ GeV}$
$\tilde{q}\tilde{q}, \tilde{q} \rightarrow q\tilde{q}_1^0$	0 e, μ	2-6 jets	E_T^{miss}	139	\tilde{q} [1× Bkg Digen.]	0.43	0.71	2.35	ATLAS-CONF-2019-040 1711.03301
$\tilde{g}\tilde{g}, \tilde{g} \rightarrow q\tilde{q}_1^0 \chi_1^0$	1 e, μ	2-6 jets	E_T^{miss}	139	\tilde{q}	Forbidden	1.15-1.95	2.2	$m(\tilde{g})=100\text{ GeV}$
$\tilde{g}\tilde{g}, \tilde{g} \rightarrow q\tilde{q}_1^0 \chi_1^0$	ee, $\mu\mu$	2 jets	E_T^{miss}	36.1	\tilde{q}	1.2	1.2	2.2	ATLAS-CONF-2020-047 1805.11381
$\tilde{g}\tilde{g}, \tilde{g} \rightarrow q\tilde{q}_1^0 Z\chi_1^0$	0-1 e, μ	7-11 jets	E_T^{miss}	139	\tilde{q}	1.15	1.97	1.97	ATLAS-CONF-2020-022 1908.08457
$\tilde{g}\tilde{g}, \tilde{g} \rightarrow q\tilde{q}_1^0$	SS ee, $\mu\mu$	6 jets	E_T^{miss}	139	\tilde{q}	1.25	2.25	2.25	ATLAS-CONF-2018-041 1909.08457
Inclusive Searches	0-1 e, μ	3 jets	E_T^{miss}	79.8	\tilde{q}	1.25			
Inclusive Searches	SS ee, $\mu\mu$	6 jets	E_T^{miss}	139	\tilde{q}				
$b\tilde{b}, \tilde{b}_1\tilde{b}_1, \tilde{b}_1\rightarrow b\tilde{b}_1^0$	Multiple	Multiple	E_T^{miss}	36.1	\tilde{b}_1	Forbidden	0.9	0.9	$m(\tilde{b}_1)=300\text{ GeV}$ $BR(\tilde{b}_1^0)=1$
$b\tilde{b}, \tilde{b}_1\tilde{b}_1, \tilde{b}_1\rightarrow b\tilde{b}_1^0$	0 e, μ	6 jets	E_T^{miss}	139	\tilde{b}_1	Forbidden	0.74	0.74	1708.09266, 1711.03301 1909.08457
$b\tilde{b}, \tilde{b}_1\tilde{b}_1, \tilde{b}_1\rightarrow b\tilde{b}_1^0$	2 e, τ	2 jets	E_T^{miss}	139	\tilde{b}_1	Forbidden	0.13-0.85	0.23-1.35	1908.03122
$b\tilde{b}, \tilde{b}_1\tilde{b}_1, \tilde{b}_1\rightarrow b\tilde{b}_1^0$	0-1 e, μ	≥ 1 jet	E_T^{miss}	139	\tilde{b}_1	0.44-0.59	1.25	1.25	ATLAS-CONF-2020-033, 2004.14960 $\Delta m(\tilde{b}_1^0)=300\text{ GeV}$ $m(\tilde{b}_1^0)=1\text{ GeV}$
$b\tilde{b}, \tilde{b}_1\tilde{b}_1, \tilde{b}_1\rightarrow b\tilde{b}_1^0$	1 e, μ	3 jets	E_T^{miss}	139	\tilde{b}_1	0.44-0.59	1.16	1.16	ATLAS-CONF-2019-017 1803.10178
$b\tilde{b}, \tilde{b}_1\tilde{b}_1, \tilde{b}_1\rightarrow b\tilde{b}_1^0$	1 $\tau + e, \mu, \tau$	2 jets	E_T^{miss}	36.1	\tilde{b}_1	0.85	0.85	0.85	$m(\tilde{b}_1^0)=50\text{ GeV}$ $m(\tilde{b}_1^0)=50\text{ GeV}$ $m(\tilde{b}_1^0)=50\text{ GeV}$
$b\tilde{b}, \tilde{b}_1\tilde{b}_1, \tilde{b}_1\rightarrow b\tilde{b}_1^0$	0 e, μ	2 jets	E_T^{miss}	36.1	\tilde{b}_1	0.43	0.43	0.43	1805.01849 1711.03301
$b\tilde{b}, \tilde{b}_1\tilde{b}_1, \tilde{b}_1\rightarrow b\tilde{b}_1^0$	0 e, μ	mono-jet	E_T^{miss}	36.1	\tilde{b}_1	0.67-1.18	0.67-1.18	0.67-1.18	SUSY-2018-09 SUSY-2018-09
$b\tilde{b}, \tilde{b}_1\tilde{b}_1, \tilde{b}_1\rightarrow b\tilde{b}_1^0$	1-2 e, μ	1-2 jets	E_T^{miss}	139	\tilde{b}_1	0.66	0.66	0.66	$m(\tilde{b}_1^0)=360\text{ GeV}$ $m(\tilde{b}_1^0)=360\text{ GeV}$
$b\tilde{b}, \tilde{b}_1\tilde{b}_1, \tilde{b}_1\rightarrow b\tilde{b}_1^0$	3 e, μ	3 jets	E_T^{miss}	139	\tilde{b}_1	0.64	0.64	0.64	$m(\tilde{b}_1^0)=360\text{ GeV}$ $m(\tilde{b}_1^0)=360\text{ GeV}$
$\tilde{\chi}_{1,2}^{\pm 1,0}$ via WZ	3 e, μ	1 jet	E_T^{miss}	139	$\tilde{\chi}_{1,2}^{\pm 1,0}$	0.205	0.42	0.42	ATLAS-CONF-2020-015 1911.12056
$\tilde{\chi}_{1,2}^{\pm 1,\mp}$ via WW	2 e, μ	2 jets	E_T^{miss}	139	$\tilde{\chi}_{1,2}^{\pm 1,\mp}$	0.42	0.74	0.74	2004.10894, 1909.09228 $m(\tilde{\chi}_1^0)=0.5(m(\tilde{\chi}_1^0))^{0.5}$
$\tilde{\chi}_{1,2}^{\pm 1,0}$ via WW	0-1 e, μ	2 jets	E_T^{miss}	139	$\tilde{\chi}_{1,2}^{\pm 1,0}$	0.74	1.0	1.0	$m(\tilde{\chi}_1^0)=0.5(m(\tilde{\chi}_1^0))^{0.5}$
$\tilde{\chi}_{1,2}^{\pm 1,\mp}$ via \tilde{Z}_L/\tilde{B}	2 e, μ	2 jets	E_T^{miss}	139	$\tilde{\chi}_{1,2}^{\pm 1,\mp}$	0.16-0.3	0.12-0.39	0.12-0.39	$m(\tilde{\chi}_1^0)=0.5(m(\tilde{\chi}_1^0))^{0.5}$
$\tilde{\chi}_{1,2}^{\pm 1,\mp}$ via \tilde{Z}_L/\tilde{B}	2 τ	2 jets	E_T^{miss}	139	$\tilde{\chi}_{1,2}^{\pm 1,\mp}$	0.7	0.7	0.7	1908.09215 1911.06860
$\tilde{\chi}_{1,2}^{\pm 1,\mp}$ via \tilde{Z}_L/\tilde{B}	0 e, μ	1 jet	E_T^{miss}	139	$\tilde{\chi}_{1,2}^{\pm 1,\mp}$	0.256	0.256	0.256	1908.09215 1911.06860
$\tilde{\chi}_{1,2}^{\pm 1,\mp}$ via \tilde{Z}_L/\tilde{B}	0 e, μ	2 jets	E_T^{miss}	36.1	$\tilde{\chi}_{1,2}^{\pm 1,\mp}$	0.55	0.55	0.55	1806.04030 ATLAS-CONF-2020-040
$\tilde{\chi}_{1,2}^{\pm 1,\mp}$ via \tilde{Z}_L/\tilde{B}	4 e, μ	4 jets	E_T^{miss}	139	$\tilde{\chi}_{1,2}^{\pm 1,\mp}$	0.55	0.55	0.55	$BR(\tilde{\chi}_1^0 \rightarrow h)=1$ $BR(\tilde{\chi}_1^0 \rightarrow Z)=1$
Direct $\tilde{\chi}_1^{\pm 1}$ prod., long-lived $\tilde{\chi}_1^\pm$	Disapp. trk	1 jet	E_T^{miss}	36.1	$\tilde{\chi}_1^{\pm 1}$	0.46	0.46	0.46	Pure Wine Pure Higgsino
Stable \tilde{g} R-hadron	Multiple	Multiple	E_T^{miss}	36.1	\tilde{g}	2.0	2.0	2.0	ATL-PHYS-PUB-2017-019 1902.01636, 1808.04095
Metastable \tilde{g} , R-hadron, $\tilde{g} \rightarrow q\tilde{q}_1^0$	3 e, μ	0 jets	E_T^{miss}	139	\tilde{g}	0.625	1.05	1.05	$m(\tilde{g})=100\text{ GeV}$
Long-lived	4 e, μ	4 jets	E_T^{miss}	32	\tilde{g}	1.9	1.9	1.9	$\lambda_{\tilde{g}11}=0.11$ $m(\tilde{g})=0.07$
RPh	4 jets + R jets	0 jets	E_T^{miss}	36.1	\tilde{g}	0.82	1.33	1.33	ATLAS-CONF-2020-009 1607.08079
RPh	4 jets + R jets	Multiple	E_T^{miss}	36.1	\tilde{g}	1.05	1.3	1.3	1804.03602 $m(\tilde{g})=200\text{ GeV}$
RPh	Multiple	Multiple	E_T^{miss}	36.1	\tilde{g}	0.55	1.05	1.05	ATLAS-CONF-2019-003 $m(\tilde{g})=200\text{ GeV}$
RPh	2 jets + b	2 jets	E_T^{miss}	36.1	\tilde{g}	0.42	0.61	0.95	ATLAS-CONF-2020-016 1710.07171
RPh	2 jets + b	2 jets	E_T^{miss}	36.1	\tilde{g}	0.42	0.61	0.95	ATLAS-CONF-2020-040 170.05544
RPh	1 μ	2 jets	E_T^{miss}	136	\tilde{g}	1.0	1.6	1.6	2003.11956 $BR(\tilde{g} \rightarrow \mu\mu)=100\%$, $cos\theta_g=1$

*Only a selection of the available mass limits on new states or phenomena is shown. Many of the limits are based on simplified models, c.f. refs. for the assumptions made.

Figure A.10: Summary of the ATLAS searches for SUSY. A representative selection of the available search results is shown. Results are given with respect to the nominal cross section. In some cases these additional dependencies are indicated by darker bands showing different model parameters. Figure adapted from Ref. [256].

Appendix B

B.1 Truth smearing

The estimated event rates in the exclusion signal regions at truth-level before and after truth smearing are compared with the reconstruction-level event rates in figs. [B.1](#) to [B.3](#). Each one of the 125 signal models from the simplified model signal grid corresponds to one point in the scatter plots. The smearing significantly improves the agreement between truth- and reconstruction-level event rate estimates in all signal region bins.

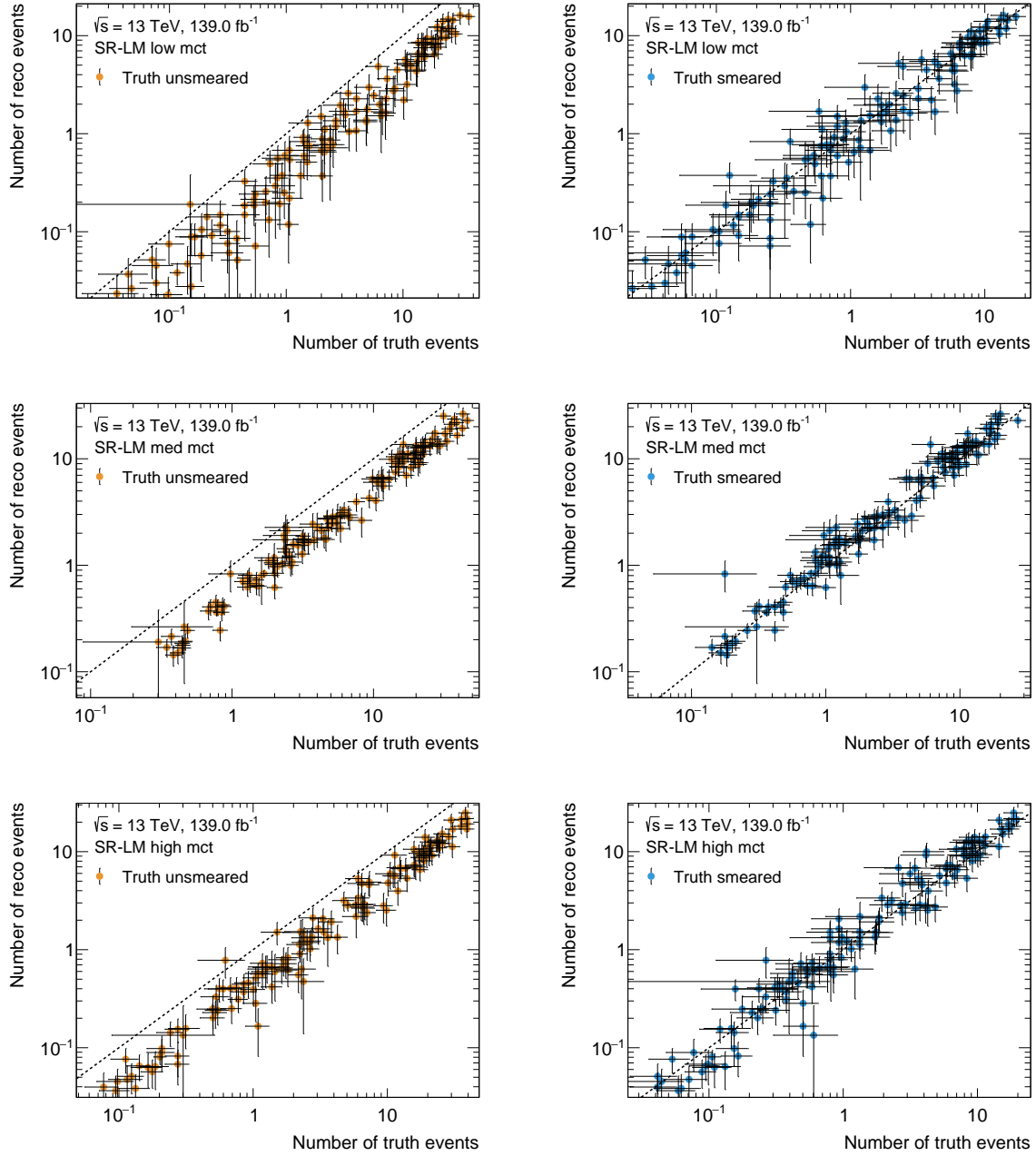


Figure B.1: Comparison of the event rates at truth- and reconstruction-level before (left) and after (right) truth smearing in SR-LM. From top to bottom, the low, medium and high m_{CT} bins are shown. Every single point in the scatter plots represents a single signal model considered in the original 1-lepton analysis. Uncertainties include only MC statistical uncertainties.

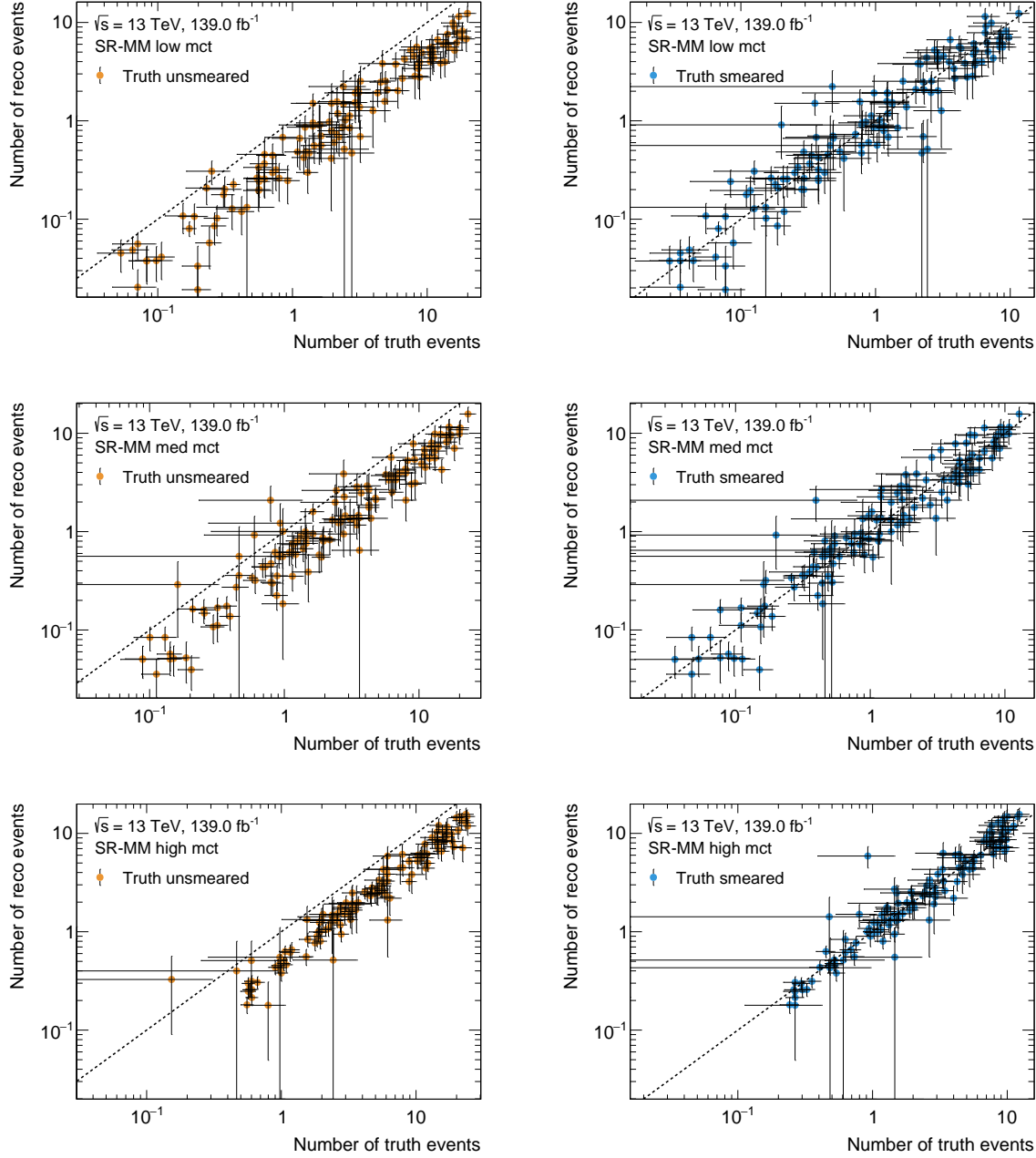


Figure B.2: Comparison of the event rates at truth- and reconstruction-level before (left) and after (right) truth smearing in SR-MM. From top to bottom, the low, medium and high m_{CT} bins are shown. Every single point in the scatter plots represents a single signal model considered in the original 1-lepton analysis. Uncertainties include only MC statistical uncertainties.

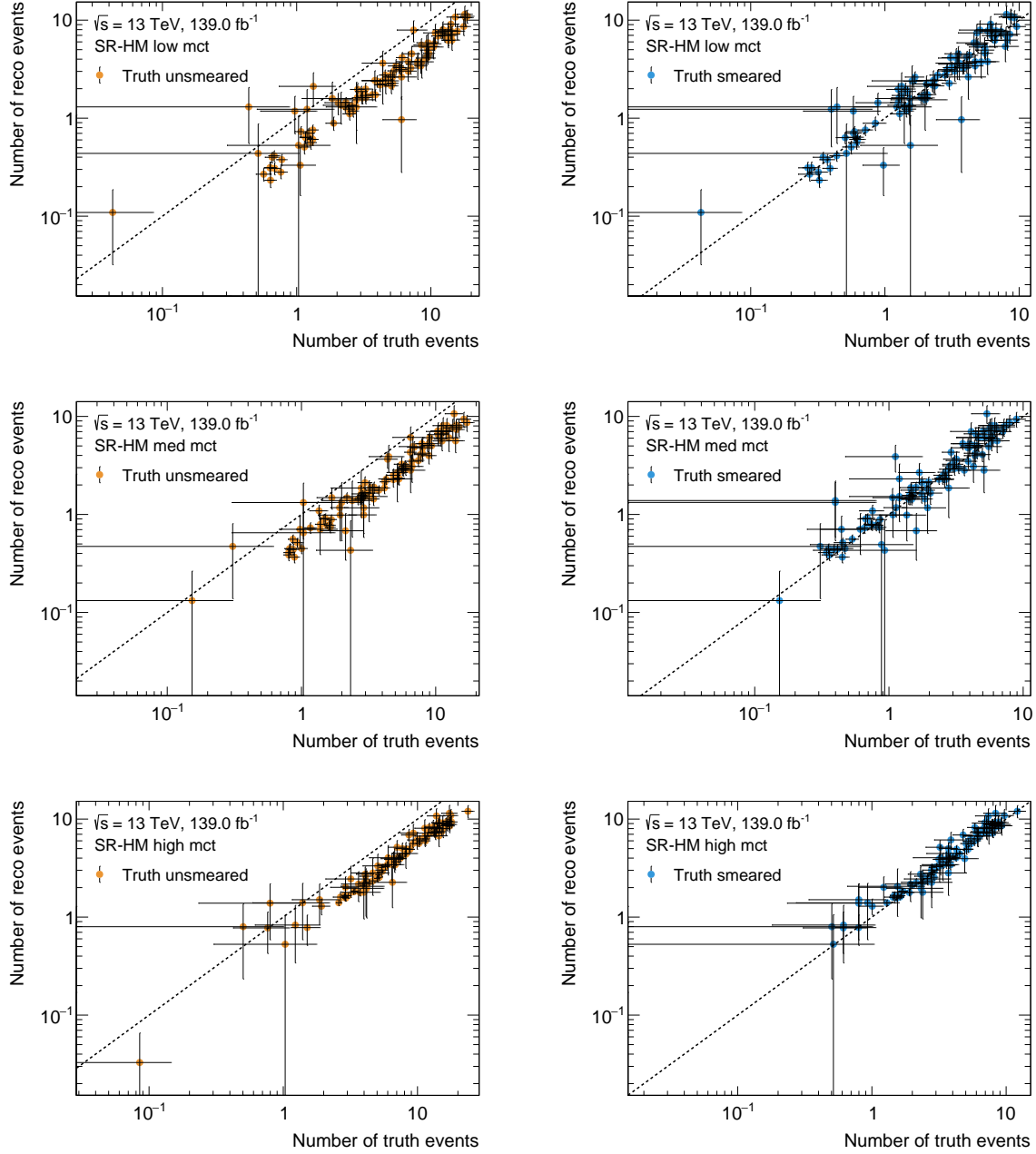


Figure B.3: Comparison of the event rates at truth- and reconstruction-level before (left) and after (right) truth smearing in SR-HM. From top to bottom, the low, medium and high m_{CT} bins are shown. Every single point in the scatter plots represents a single signal model considered in the original 1-lepton analysis. Uncertainties include only MC statistical uncertainties.

B.2 Simplified likelihood results

Figures B.4 and 10.5 show comparisons of the exclusion limits obtained using the full and simplified likelihoods for different ATLAS SUSY searches. In addition to the exclusion limits, the observed CL_s are given for every signal model tested. Although some likelihood simplifications needed special care (see section 10.5) and validation, a good agreement is observed throughout all analyses tested.

Figures B.6 and B.7 directly compare the expected and observed CL_s values obtained using both likelihood configurations for each ATLAS SUSY search considered. Both linear- and log-scale representations are shown, revealing that the simplified likelihood tends to lead to good agreement in the CL_s values around 0.05, while slightly overestimating sensitivity in the region with $CL_s \ll 0.05$, where signal models are in any case being excluded (and thus to some extent it is not important how small the CL_s value actually is).

Figures B.8 and B.9 highlight the limitations of the simplified likelihood approach using the ATLAS compressed and stop searches.

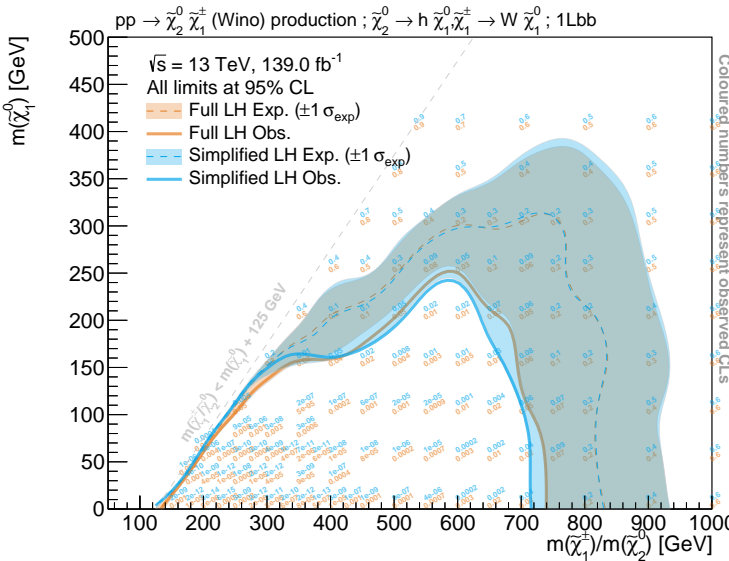


Figure B.4: Comparison of the simplified likelihood (blue contours) and full likelihood (orange contours) results for the search for electroweakinos presented previously. The observed contours are shown as solid lines, while the expected contours are shown as dashed lines. Observed CL_s values from both likelihoods are given. The uncertainty band includes all MC statistical and systematic uncertainties in the case of the full likelihood.

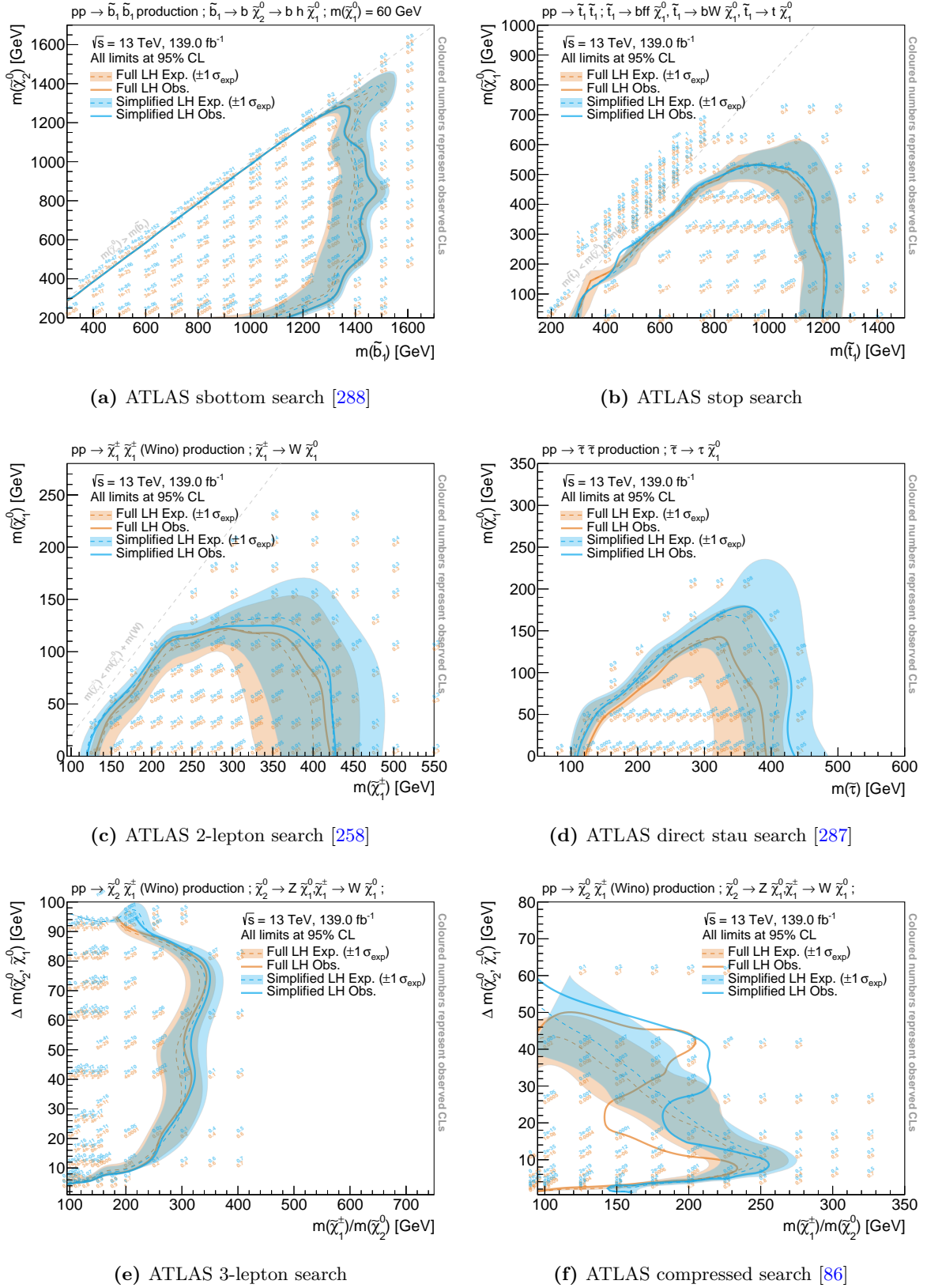


Figure B.5: Comparison of the simplified likelihood (blue contours) and full likelihood (orange contours) results for different ATLAS SUSY searches. The observed contours are shown as solid lines, while the expected contours are shown as dashed lines. Observed CL_s values from both likelihoods are given. The uncertainty band includes all MC statistical and systematic uncertainties in the case of the full likelihood, and the simplified uncertainties in the case of the simplified likelihood.

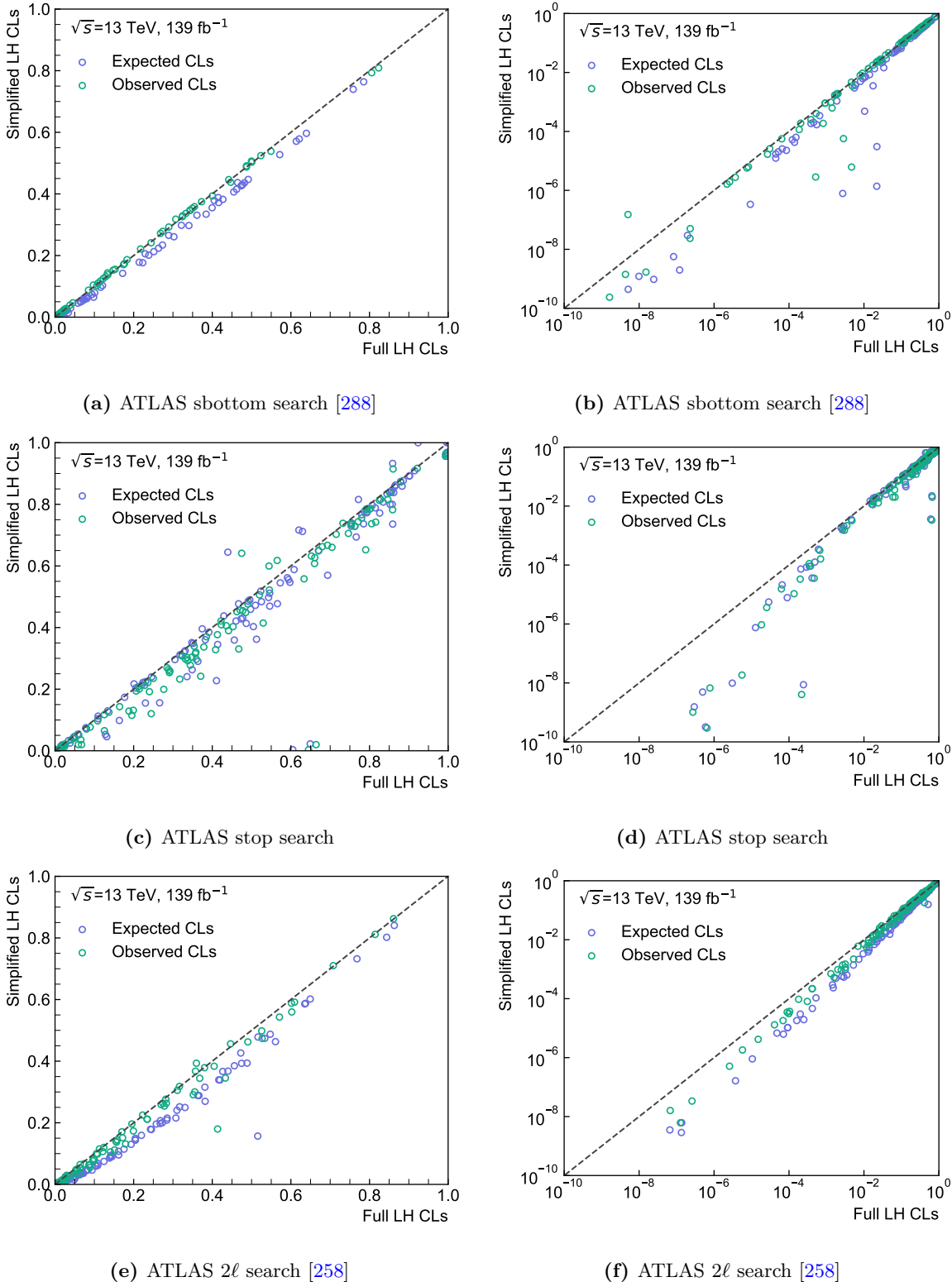


Figure B.6: Scatter plots comparing the observed and expected CL_s values obtained using the simplified and the full likelihoods for the same set of signal models originally considered in the various ATLAS SUSY searches. Both linear and logarithmic scale representations are shown on the left- and right-hand side, respectively, illustrating the full range of CL_s values. Apart from the scales, both columns show exactly the same results for each row of plots.

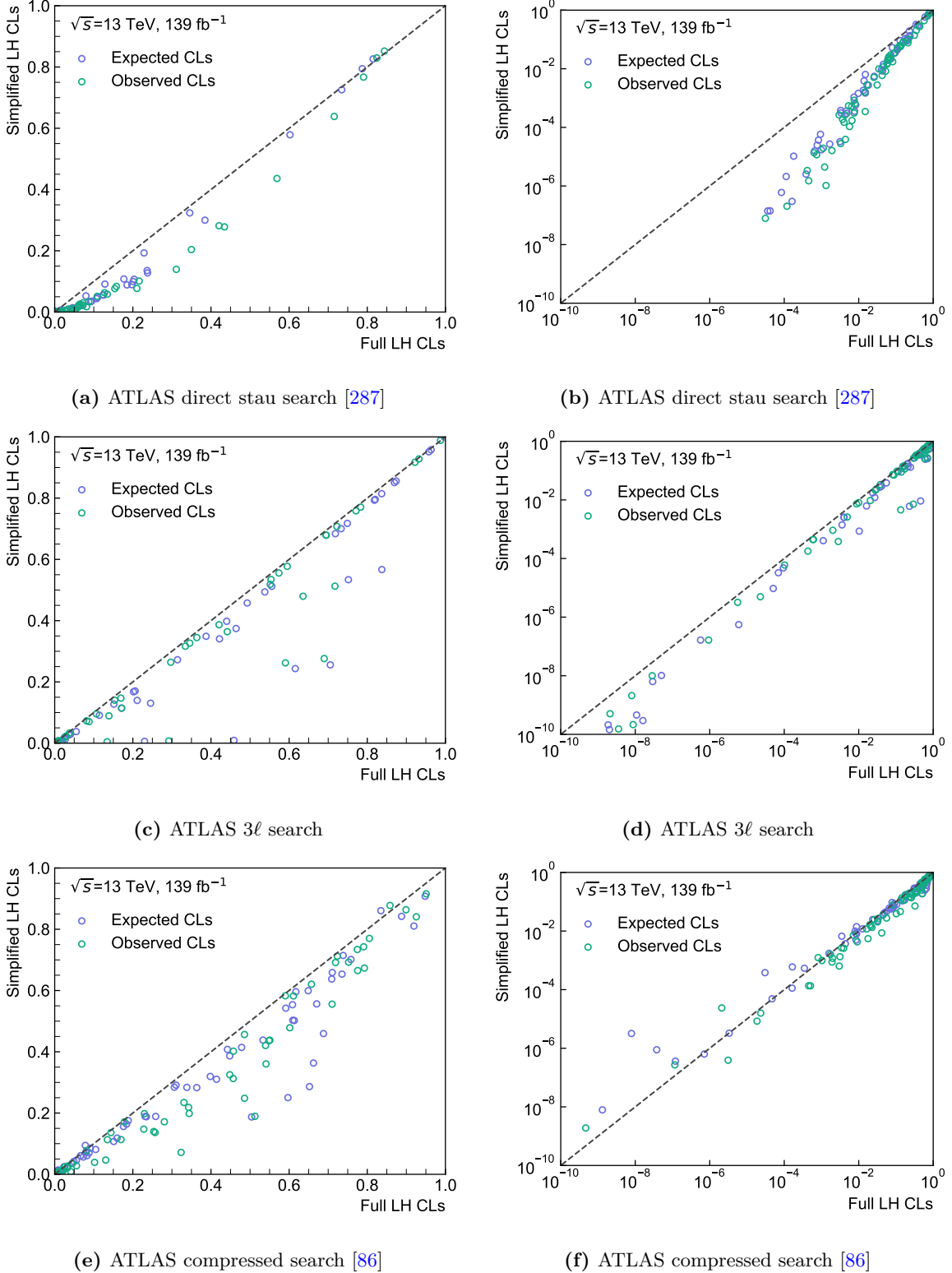


Figure B.7: Scatter plots comparing the observed and expected CL_s values obtained using the simplified and the full likelihoods for the same set of signal models originally considered in the various ATLAS SUSY searches. Both linear and logarithmic scale representations are shown on the left- and right-hand side, respectively, illustrating the full range of CL_s values. Apart from the scales, both columns show exactly the same results for each row of plots.

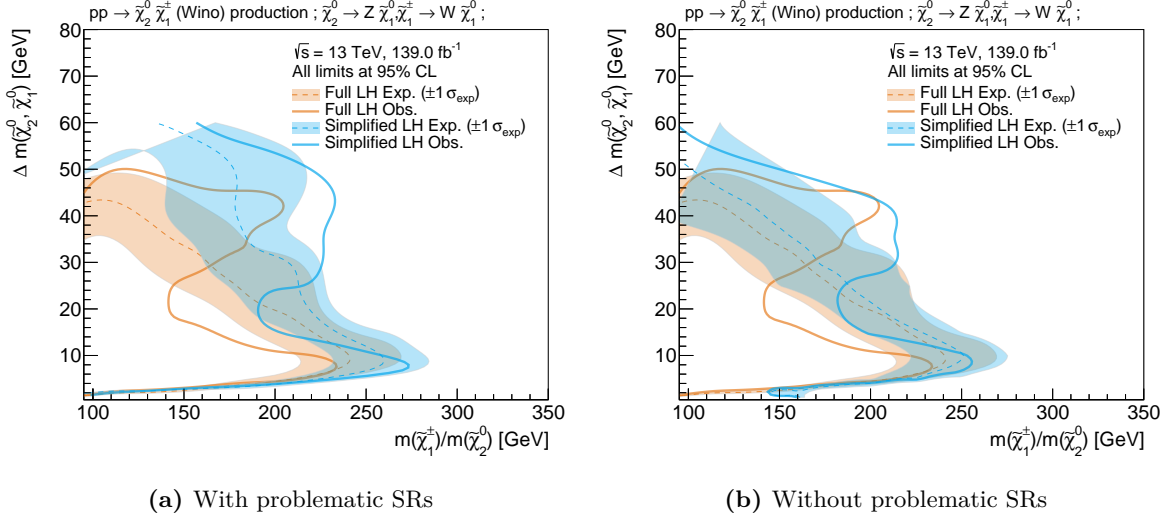


Figure B.8: The contours obtained with the full and simplified likelihoods of the ATLAS compressed search [86] are shown with the problematic signal regions (a) included and (b) removed. A noticeable improvement in agreement between the simplified and full likelihood contours is observed after removing the signal regions responsible for the instabilities discussed in section 10.5.

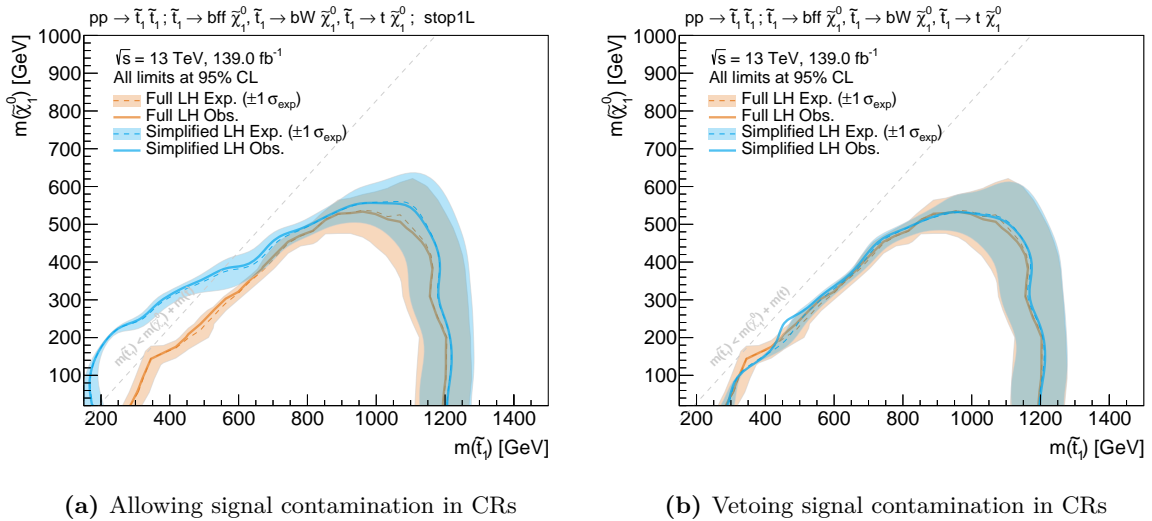


Figure B.9: The contours obtained with the full and simplified likelihoods of the ATLAS stop search. In fig. (a) the simplified likelihood is also applied on signal points with $m(\tilde{t}_1) < m(\tilde{\chi}_1^0) + m(t)$, where significant signal contamination in the CRs occurs. In fig. (b), such signal points are removed and thus not evaluated using the simplified likelihood.

Appendix C

C.1 Phenomenology of the LSP

In the following, various two-dimensional projections of the parameter space sampled in function of the LSP type are shown.

Figure C.1 shows the LSP type as a function of the pMSSM parameters M_1 , M_2 , μ and $\tan \beta$, illustrating the behaviour of the neutralino mass mixing matrix introduced in section 1.1.2. Models with $|M_1| < |M_2|$ and $|M_1| \ll |\mu|$ tend to have an LSP with dominant bino component, while, in models with $|M_2| < |M_1|$ and $|M_2| \ll |\mu|$, the LSP is mostly wino-like. Models where $|\mu| \ll |M_1|$ and $|\mu| \ll |M_2|$, the LSP is mostly higgsino-like. In models with mass parameters in between those edge cases, the LSP becomes a mixed state. The parameter $\tan \beta$ does not have a large impact on the LSP type within the ranges sampled.

Figure C.2 shows the fraction of models excluded by the 1ℓ search in different two-dimensional projections on the electroweakino masses. Only models with a bino-like or wino-like LSP are shown in order to highlight the different spectra. No models with a higgsino-like LSP are shown since the 1ℓ search is not sensitive to such scenarios. Models with a bino-like LSP tend to have nearly mass-degenerate $\tilde{\chi}_1^\pm$ and $\tilde{\chi}_2^0$ and are thus close to the canonical simplified model considered in the search. Models with a wino-like LSP have nearly mass-degenerate $\tilde{\chi}_1^\pm$ and $\tilde{\chi}_1^0$. In such models, the 1ℓ search can become sensitive to $\tilde{\chi}_2^\pm \tilde{\chi}_2^0$ production with subsequent decay $\tilde{\chi}_2^\pm \rightarrow h \tilde{\chi}_1^0$.

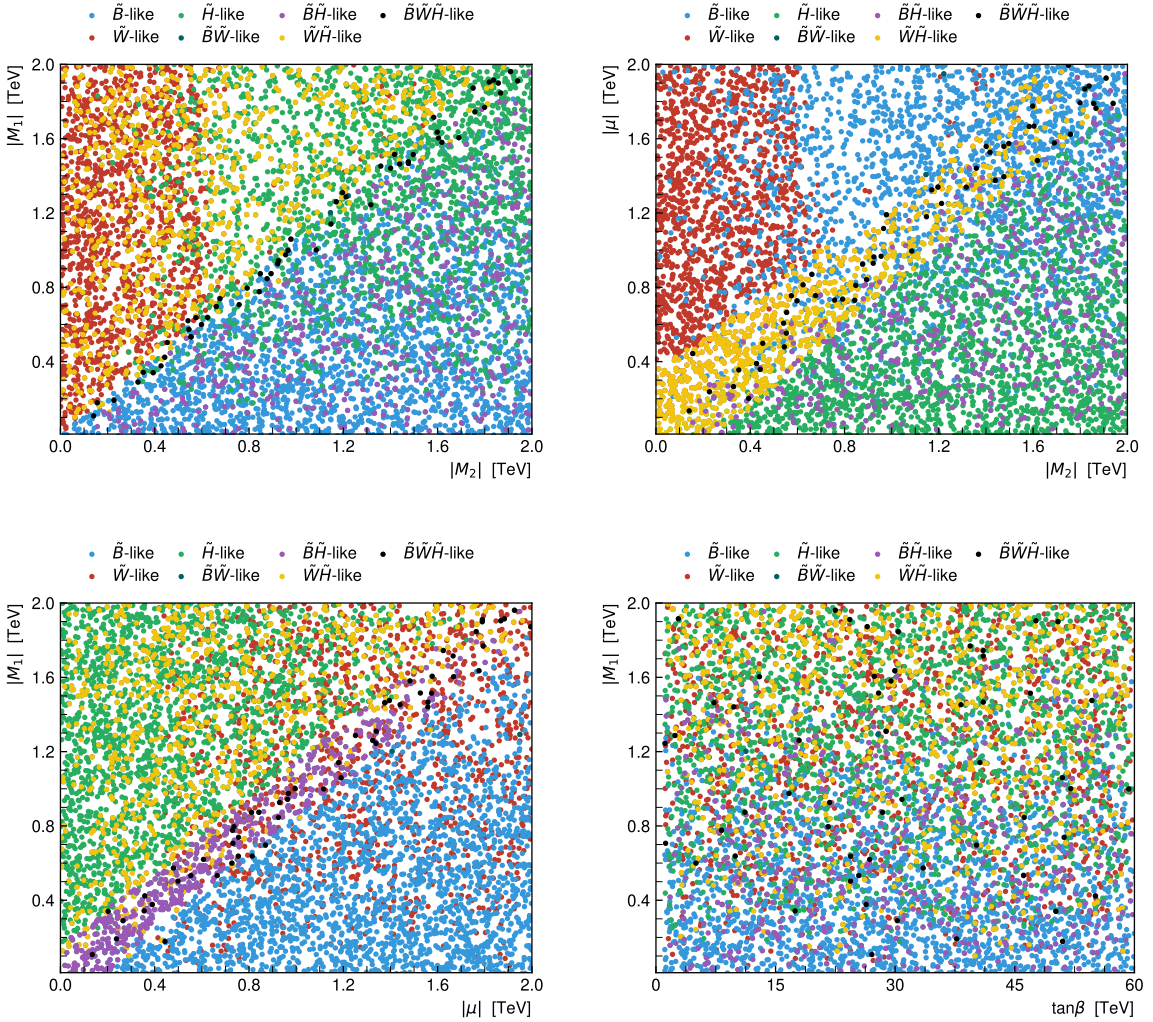


Figure C.1: Phenomenology of the LSP as a function of two-dimensional projections of the pMSSM parameter space. The parameters M_1 , M_2 , μ and $\tan\beta$ in various projections. Each point in the plots corresponds to a unique pMSSM model sampled. The colour codes the nature of the LSP using the definitions introduced in section 11.3.

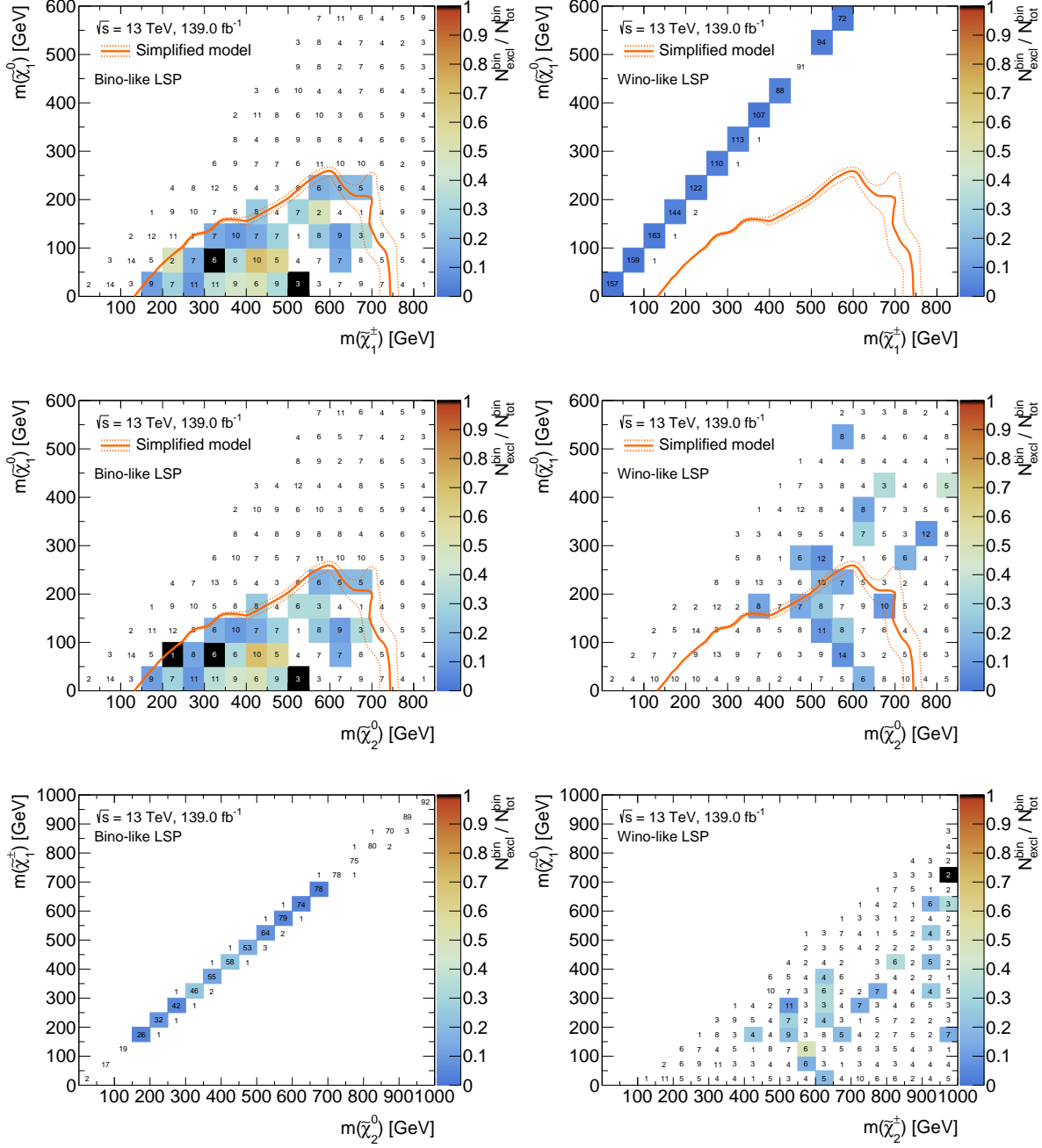


Figure C.2: Bin-by-bin fraction of excluded models as a two-dimensional function of the relevant sparticle masses. Only pMSSM models with a bino-like (wino-like) LSP are shown on the left (right). The numbers in the bins correspond to the total number of models sampled falling into the respective bin. The number of models excluded by the 1ℓ search is encoded with a colour bar ranging from 0 to 1. Where all models in a given bin are excluded, the bin is coloured in black. Bins without any models excluded are left white. Models are evaluated using the simplified likelihood of the 1-lepton analysis. The simplified model contour is shown in orange.

C.2 Impact on electroweakinos

As illustrated in fig. C.3, the couplings of the $\tilde{\chi}_2^0$ to the Higgs boson are suppressed by powers of $|\mu|/M_2$ in the wino-like and bino-like scenarios [300], meaning that the branching fraction of $\tilde{\chi}_2^0 \rightarrow h\tilde{\chi}_1^0$ takes on reasonably high values only in models with an LSP that is nearly pure bino.

Figure C.4 shows the compressed mass spectrum of an exemplary pMSSM model point with higgsino-like $\tilde{\chi}_1^0$.

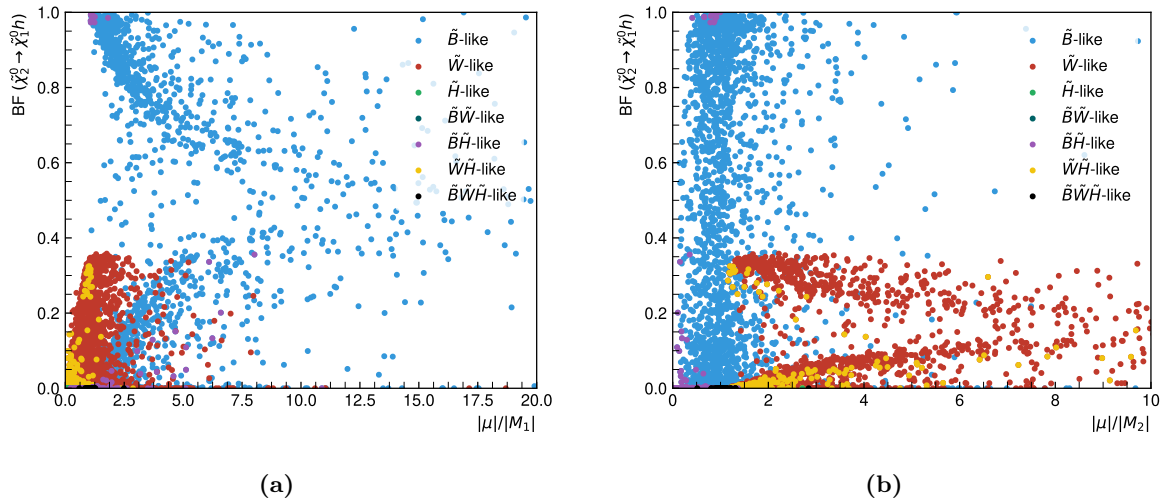


Figure C.3: Density of the pMSSM models projected onto the plane spanned by $\text{BF}(\tilde{\chi}_2^0 \rightarrow h\tilde{\chi}_1^0)$ and (a) $|\mu|/|M_1|$ or (b) $|\mu|/|M_2|$. Models are shown as a function of their $\tilde{\chi}_1^0$ type.

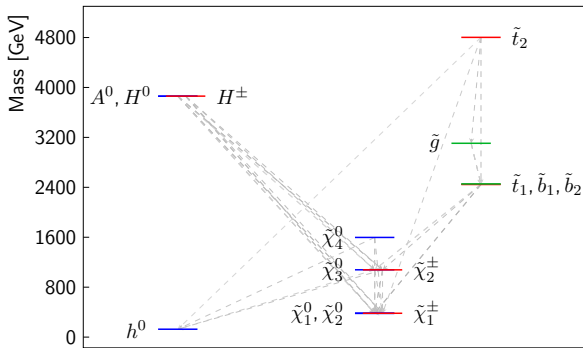


Figure C.4: Mass spectrum of an exemplary pMSSM model with a higgsino-like $\tilde{\chi}_1^0$. The branching fractions of the different decays are indicated through the width and and greyscale colour (pure black being 100%, pure white being 0%) of the arrows. Branching fractions below 10% are suppressed for the sake of visibility. Figure generated using `pyslha` [94].

C.3 Impact on pMSSM parameters

In fig. C.5, the impact of the 1ℓ search on the remaining pMSSM parameters sampled, not already shown in section 11.4.2, are provided. As before, the full set of models evaluated with the 1ℓ search is shown as black line, while the bin-wise number of models excluded by the search are indicated with the blue histogram. An additional pad indicates the fraction of models excluded in each bin.

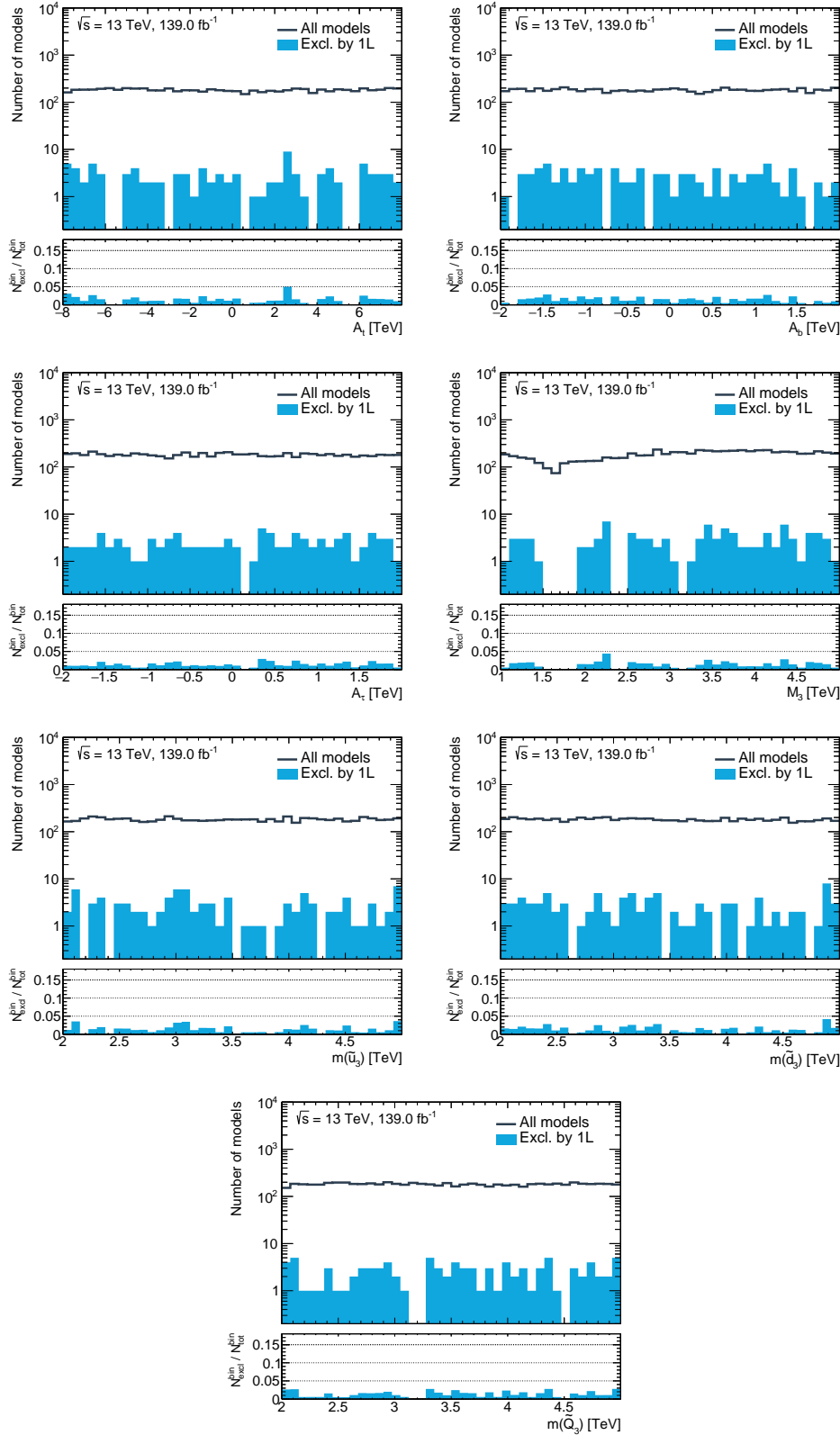


Figure C.5: Bin-by-bin number of excluded models as a one-dimensional function of the remaining scanned pMSSM parameters not already shown in fig. 11.7. The bin-wise fraction of excluded models, $N_{\text{excl}}^{\text{bin}} / N_{\text{tot}}^{\text{bin}}$, is shown in the lower pad. All models are evaluated using the simplified likelihood of the 1ℓ search.

C.4 Impact on dark matter relic density

Figure C.6 compares the density of pMSSM models in a two-dimensional projection on the $\Omega_{\tilde{\chi}} h^2$ – $m(\tilde{\chi}_1^0)$ plane before and after the LEP constraint on the chargino mass of $\tilde{\chi}_1^\pm > 103.5 \text{ GeV}$ [85] is applied.

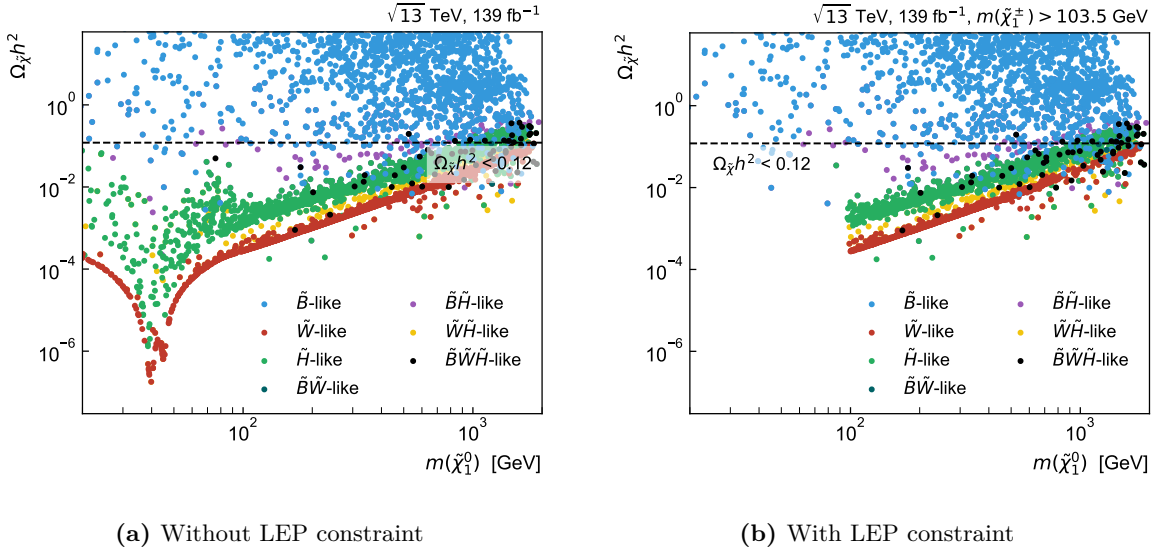


Figure C.6: Density of the pMSSM model points sampled in the plane spanned by the relic density and the $\tilde{\chi}_1^0$ mass. The model points are additionally shown as a function of the nature of their $\tilde{\chi}_1^0$. In fig. (a) all pMSSM models originally sampled and evaluated are shown. In fig. (b), only models satisfying the constraint $\tilde{\chi}_1^\pm > 103.5 \text{ GeV}$ set by LEP [85] are shown. The horizontal dashed line represents the DM relic density measurement by the Planck collaboration, interpreted as an upper limit $\Omega_{\tilde{\chi}} h^2 < 0.12$ such that the $\tilde{\chi}_1^0$ can be a sub-dominant DM component.

Abbreviations

Λ CDM Lambda Cold Dark Matter. 18

AFP ATLAS Forward Proton. 51

ALFA Absolute Luminosity for ATLAS. 51

BDT boosted decision tree. 77

BSM beyond the Standard Model. 1, 2, 18, 19, 41, 43, 49, 57, 64, 95, 124, 128, 135–137, 141, 152, 177–179

CKM Cabibbo–Kobayashi–Maskawa. 6, 17, 31, 77

CMB cosmic microwave background. 18

CMLE conditional maximum likelihood estimator. 61

CR control region. 65, 101–108, 112–114, 116, 119–121, 123, 152, 157, 159, 203

CSC Cathode Strip Chamber. 49, 50, 76

DAQ Data Acquisition System. 52

DM dark matter. 1, 18, 19, 28, 30, 32, 172–174, 177, 179, 210

DR diagram removal. 115

DS diagram subtraction. 115

EM Electromagnetic. 48, 49, 74–76

EMEC electromagnetic end-cap calorimeter. 48

FCal forward calorimeter. 49

FCNC flavour-changing neutral current. 31

FSR final state radiation. 53, 54, 79, 80, 115

ggF gluon–gluon fusion. 71

- GUT** grand unified theory. 19, 20
- HEC** hadronic end-cap calorimeter. 48
- HEP** high energy physics. 57, 60, 64, 131, 136, 151
- HF** heavy flavour. 70–72, 74–77, 79
- HL-LHC** High Luminosity LHC. 42
- HLT** High Level Trigger. 51, 52, 84
- HPC** high-performance computer. 138
- IBL** insertable B-layer. 46
- ID** inner detector. 45–47, 49, 55, 56, 73–76, 78, 85, 112, 144
- IP** interaction point. 43–45, 51, 75, 76
- ISR** initial state radiation. 53, 54, 80, 81, 115
- JER** jet energy resolution. 77, 112, 113, 117, 144, 159
- JES** jet energy scale. 77, 112, 113, 117, 159
- JVT** jet vertex tagger. 77, 79
- L1** Level 1. 51, 52, 83, 84
- L1Topo** Level-1 Topological Processor. 51
- LAr** liquid argon. 48, 49
- LEP** Large Electron Positron. 30, 33, 37, 163, 173, 210
- LHC** Large Hadron Collider. 1, 2, 37–39, 41–44, 69, 80, 83, 130, 131, 136, 137, 162, 177–179
- LO** leading order. 9, 53, 71, 115
- LSP** lightest supersymmetric particle. 34, 80, 81, 130, 163–165, 168–170, 172, 173, 177, 179, 205–208
- MC** Monte Carlo. 52, 53, 55, 56, 58, 59, 71–73, 77, 79, 84, 85, 87–89, 91, 93, 94, 97–99, 101–104, 106, 111–117, 119–127, 135, 138, 140, 142–147, 155, 156, 177, 184–191, 196–200
- MDT** Monitored Drift Tube. 49, 50, 76
- ME** matrix element. 53, 54, 71, 72, 115, 116, 163
- MLE** maximum likelihood estimator. 59, 60, 64
- MS** muon spectrometer. 49, 50, 56, 75–77, 85, 112, 144

MSSM Minimal Supersymmetric Standard Model. 20, 26–31

NLL next-to-leading logarithm. 72

NLO next-to-leading order. 9, 53, 72, 115, 163

PDF parton distribution function. 44, 53, 71, 72, 115, 163

pdf probability density function. 52, 57, 62, 63, 138

PMNS Pontecorvo–Maki–Nakagawa–Sakata. 6, 17

pMSSM phenomenological Minimal Supersymmetric Standard Model. 31, 32, 34, 35, 131, 141, 149, 151, 159, 161–165, 168–173, 178, 205–210

POI Parameter of Interest. 59, 62, 128, 152, 153

PS parton shower. 53, 54, 71, 72, 115, 116, 163

QCD quantum chromodynamics. 8, 11–13, 17, 22, 53–55, 69–71

QED quantum electrodynamics. 5, 9–12, 14, 21, 53, 54

QFT quantum field theory. 7, 8, 22

RF radio frequency. 39

ROC receiver operating characteristic. 88, 89

ROI region of interest. 51

RPC Resistive Plate Chamber. 49, 50

SCT silicon microstip tracker. 45–47, 73, 75

SM Standard Model of particle physics. 1, 2, 5–8, 14, 16–23, 26, 32, 34, 59, 60, 69–71, 73, 79–82, 88, 90, 91, 94, 95, 101, 104, 105, 116, 119, 121, 123, 124, 135, 151, 152, 163, 177–179, 184, 191

SR signal region. 64, 65, 87, 93–95, 101–105, 108, 116, 117, 121, 123–125, 128, 145, 152, 154, 155, 157, 203

SUSY Supersymmetry. 1, 2, 18, 23, 32, 33, 37, 41, 55, 60, 69, 70, 73, 80, 81, 83, 87, 88, 101, 103, 113, 116, 130, 131, 136–138, 141, 143, 149, 151, 155, 156, 159–163, 170, 173, 177–179, 193, 199–202

TGC Thin Gap Chamber. 49, 50

TRT transition radiation tracker. 45–47, 74

VBF vector boson fusion. 71

vdM van der Meer. [42](#), [111](#)

VEV vacuum expectation value. [15](#), [17](#), [29](#), [31](#)

VR validation region. [102–104](#), [108](#), [116](#), [121–123](#), [192](#)

WIMP weakly interacting massive particle. [19](#)

ZDC Zero-Degree Calorimeter. [51](#)

Bibliography

- [1] ATLAS Collaboration, “Observation of a new particle in the search for the Standard Model Higgs boson with the ATLAS detector at the LHC,” *Phys. Lett. B* **716** (2012) 1, [arXiv:1207.7214 \[hep-ex\]](https://arxiv.org/abs/1207.7214).
- [2] CMS Collaboration, “Observation of a new boson at a mass of 125 GeV with the CMS experiment at the LHC,” *Phys. Lett. B* **716** (2012) 30, [arXiv:1207.7235 \[hep-ex\]](https://arxiv.org/abs/1207.7235).
- [3] I. C. Brock and T. Schorner-Sadenius, *Physics at the terascale*. Wiley, Weinheim, 2011. <https://cds.cern.ch/record/1354959>.
- [4] M. E. Peskin and D. V. Schroeder, *An Introduction to quantum field theory*. Addison-Wesley, Reading, USA, 1995. <http://www.slac.stanford.edu/~mpeskin/QFT.html>.
- [5] S. P. Martin, “A Supersymmetry primer,” [arXiv:hep-ph/9709356v7 \[hep-ph\]](https://arxiv.org/abs/hep-ph/9709356v7). [Adv. Ser. Direct. High Energy Phys.18,1(1998)].
- [6] M. Bustamante, L. Cieri, and J. Ellis, “Beyond the Standard Model for Montaneros,” in *5th CERN - Latin American School of High-Energy Physics*. 11, 2009. [arXiv:0911.4409 \[hep-ph\]](https://arxiv.org/abs/0911.4409).
- [7] L. Brown, *The Birth of particle physics*. Cambridge University Press, Cambridge Cambridgeshire New York, 1986.
- [8] P. J. Mohr, D. B. Newell, and B. N. Taylor, “CODATA Recommended Values of the Fundamental Physical Constants: 2014,” *Rev. Mod. Phys.* **88** no. 3, (2016) 035009, [arXiv:1507.07956 \[physics.atom-ph\]](https://arxiv.org/abs/1507.07956).
- [9] P. D. Group, “Review of Particle Physics,” *Progress of Theoretical and Experimental Physics* **2020** no. 8, (08, 2020) , <https://academic.oup.com/ptep/article-pdf/2020/8/083C01/34673722/ptaa104.pdf>. <https://doi.org/10.1093/ptep/ptaa104>. 083C01.
- [10] **Super-Kamiokande** Collaboration, Y. Fukuda *et al.*, “Evidence for oscillation of atmospheric neutrinos,” *Phys. Rev. Lett.* **81** (1998) 1562–1567, [arXiv:hep-ex/9807003 \[hep-ex\]](https://arxiv.org/abs/hep-ex/9807003).
- [11] Z. Maki, M. Nakagawa, and S. Sakata, “Remarks on the unified model of elementary particles,” *Prog. Theor. Phys.* **28** (1962) 870–880. [,34(1962)].
- [12] N. Cabibbo, “Unitary symmetry and leptonic decays,” *Phys. Rev. Lett.* **10** (Jun, 1963) 531–533. <https://link.aps.org/doi/10.1103/PhysRevLett.10.531>.

- [13] M. Kobayashi and T. Maskawa, “CP Violation in the Renormalizable Theory of Weak Interaction,” *Prog. Theor. Phys.* **49** (1973) 652–657.
- [14] E. Noether and M. A. Tavel, “Invariant variation problems,” [arXiv:physics/0503066](https://arxiv.org/abs/physics/0503066).
- [15] J. C. Ward, “An identity in quantum electrodynamics,” *Phys. Rev.* **78** (Apr, 1950) 182–182. <https://link.aps.org/doi/10.1103/PhysRev.78.182>.
- [16] Y. Takahashi, “On the generalized ward identity,” *Il Nuovo Cimento (1955-1965)* **6** no. 2, (Aug, 1957) 371–375. <https://doi.org/10.1007/BF02832514>.
- [17] G. ’tHooft, “Renormalization of massless yang-mills fields,” *Nuclear Physics B* **33** no. 1, (1971) 173 – 199. <http://www.sciencedirect.com/science/article/pii/0550321371903956>.
- [18] J. Taylor, “Ward identities and charge renormalization of the yang-mills field,” *Nuclear Physics B* **33** no. 2, (1971) 436 – 444. <http://www.sciencedirect.com/science/article/pii/0550321371902975>.
- [19] A. A. Slavnov, “Ward identities in gauge theories,” *Theoretical and Mathematical Physics* **10** no. 2, (Feb, 1972) 99–104. <https://doi.org/10.1007/BF01090719>.
- [20] C. N. Yang and R. L. Mills, “Conservation of isotopic spin and isotopic gauge invariance,” *Phys. Rev.* **96** (Oct, 1954) 191–195. <https://link.aps.org/doi/10.1103/PhysRev.96.191>.
- [21] K. G. Wilson, “Confinement of quarks,” *Phys. Rev. D* **10** (Oct, 1974) 2445–2459. <https://link.aps.org/doi/10.1103/PhysRevD.10.2445>.
- [22] T. DeGrand and C. DeTar, *Lattice Methods for Quantum Chromodynamics*. World Scientific, Singapore, 2006. <https://cds.cern.ch/record/1055545>.
- [23] S. L. Glashow, “Partial-symmetries of weak interactions,” *Nuclear Physics* **22** no. 4, (1961) 579 – 588. <http://www.sciencedirect.com/science/article/pii/0029558261904692>.
- [24] S. Weinberg, “A model of leptons,” *Phys. Rev. Lett.* **19** (Nov, 1967) 1264–1266. <https://link.aps.org/doi/10.1103/PhysRevLett.19.1264>.
- [25] A. Salam and J. C. Ward, “Weak and electromagnetic interactions,” *Il Nuovo Cimento (1955-1965)* **11** no. 4, (Feb, 1959) 568–577. <https://doi.org/10.1007/BF02726525>.
- [26] C. S. Wu, E. Ambler, R. W. Hayward, D. D. Hoppes, and R. P. Hudson, “Experimental test of parity conservation in beta decay,” *Phys. Rev.* **105** (Feb, 1957) 1413–1415. <https://link.aps.org/doi/10.1103/PhysRev.105.1413>.
- [27] M. Gell-Mann, “The interpretation of the new particles as displaced charge multiplets,” *Il Nuovo Cimento (1955-1965)* **4** no. 2, (Apr, 1956) 848–866. <https://doi.org/10.1007/BF02748000>.
- [28] K. Nishijima, “Charge Independence Theory of V Particles*,” *Progress of Theoretical Physics* **13** no. 3, (03, 1955) 285–304, <https://academic.oup.com/ptp/article-pdf/13/3/285/5425869/13-3-285.pdf>. <https://doi.org/10.1143/PTP.13.285>.
- [29] T. Nakano and K. Nishijima, “Charge Independence for V-particles*,” *Progress of Theoretical Physics* **10** no. 5, (11, 1953) 581–582, <https://academic.oup.com/ptp/article-pdf/10/5/581/5364926/10-5-581.pdf>. <https://doi.org/10.1143/PTP.10.581>.

- [30] F. Englert and R. Brout, “Broken symmetry and the mass of gauge vector mesons,” *Phys. Rev. Lett.* **13** (Aug, 1964) 321–323.
<https://link.aps.org/doi/10.1103/PhysRevLett.13.321>.
- [31] P. W. Higgs, “Broken symmetries and the masses of gauge bosons,” *Phys. Rev. Lett.* **13** (Oct, 1964) 508–509. <https://link.aps.org/doi/10.1103/PhysRevLett.13.508>.
- [32] P. W. Higgs, “Spontaneous symmetry breakdown without massless bosons,” *Phys. Rev.* **145** (May, 1966) 1156–1163. <https://link.aps.org/doi/10.1103/PhysRev.145.1156>.
- [33] Y. Nambu, “Quasiparticles and Gauge Invariance in the Theory of Superconductivity,” *Phys. Rev.* **117** (1960) 648–663. [,132(1960)].
- [34] J. Goldstone, “Field Theories with Superconductor Solutions,” *Nuovo Cim.* **19** (1961) 154–164.
- [35] V. Brdar, A. J. Helmboldt, S. Iwamoto, and K. Schmitz, “Type-I Seesaw as the Common Origin of Neutrino Mass, Baryon Asymmetry, and the Electroweak Scale,” *Phys. Rev. D* **100** (2019) 075029, [arXiv:1905.12634 \[hep-ph\]](https://arxiv.org/abs/1905.12634).
- [36] G. ’t Hooft and M. Veltman, “Regularization and renormalization of gauge fields,” *Nuclear Physics B* **44** no. 1, (1972) 189 – 213.
<http://www.sciencedirect.com/science/article/pii/0550321372902799>.
- [37] G. L. Kane, *The supersymmetric world : the beginnings of the theory*. World Scientific, Singapore River Edge, N.J, 2000.
- [38] F. Zwicky, “Die Rotverschiebung von extragalaktischen Nebeln,” *Helv. Phys. Acta* **6** (1933) 110–127. <https://cds.cern.ch/record/437297>.
- [39] V. C. Rubin and W. K. Ford, Jr., “Rotation of the Andromeda Nebula from a Spectroscopic Survey of Emission Regions,” *Astrophys. J.* **159** (1970) 379–403.
- [40] G. Bertone, D. Hooper, and J. Silk, “Particle dark matter: Evidence, candidates and constraints,” *Phys. Rept.* **405** (2005) 279–390, [arXiv:hep-ph/0404175](https://arxiv.org/abs/hep-ph/0404175).
- [41] D. Clowe, M. Bradac, A. H. Gonzalez, M. Markevitch, S. W. Randall, C. Jones, and D. Zaritsky, “A direct empirical proof of the existence of dark matter,” *Astrophys. J.* **648** (2006) L109–L113, [arXiv:astro-ph/0608407 \[astro-ph\]](https://arxiv.org/abs/astro-ph/0608407).
- [42] A. Taylor, S. Dye, T. J. Broadhurst, N. Benitez, and E. van Kampen, “Gravitational lens magnification and the mass of abell 1689,” *Astrophys. J.* **501** (1998) 539, [arXiv:astro-ph/9801158](https://arxiv.org/abs/astro-ph/9801158).
- [43] C. Bennett *et al.*, “Four year COBE DMR cosmic microwave background observations: Maps and basic results,” *Astrophys. J. Lett.* **464** (1996) L1–L4, [arXiv:astro-ph/9601067](https://arxiv.org/abs/astro-ph/9601067).
- [44] G. F. Smoot *et al.*, “Structure in the COBE Differential Microwave Radiometer First-Year Maps,” *ApJS* **396** (September, 1992) L1.
- [45] **WMAP** Collaboration, “Nine-year Wilkinson Microwave Anisotropy Probe (WMAP) Observations: Final Maps and Results,” *ApJS* **208** no. 2, (October, 2013) 20, [arXiv:1212.5225 \[astro-ph.CO\]](https://arxiv.org/abs/1212.5225).

- [46] **WMAP** Collaboration, “Nine-year Wilkinson Microwave Anisotropy Probe (WMAP) Observations: Cosmological Parameter Results,” *ApJS* **208** no. 2, (October, 2013) 19, [arXiv:1212.5226 \[astro-ph.CO\]](https://arxiv.org/abs/1212.5226).
- [47] **Planck** Collaboration, “Planck 2018 results. I. Overview and the cosmological legacy of Planck,” *Astron. Astrophys.* **641** (2020) A1, [arXiv:1807.06205 \[astro-ph.CO\]](https://arxiv.org/abs/1807.06205).
- [48] A. Liddle, *An introduction to modern cosmology; 3rd ed.* Wiley, Chichester, Mar, 2015. <https://cds.cern.ch/record/1976476>.
- [49] **Planck** Collaboration, “Planck 2018 results. VI. Cosmological parameters,” *Astron. Astrophys.* **641** (2020) A6, [arXiv:1807.06209 \[astro-ph.CO\]](https://arxiv.org/abs/1807.06209).
- [50] H. Georgi and S. L. Glashow, “Unity of all elementary-particle forces,” *Phys. Rev. Lett.* **32** (Feb, 1974) 438–441. <https://link.aps.org/doi/10.1103/PhysRevLett.32.438>.
- [51] I. Aitchison, *Supersymmetry in Particle Physics. An Elementary Introduction.* Cambridge University Press, Cambridge, 2007.
- [52] **Muon g-2** Collaboration, G. Bennett *et al.*, “Final Report of the Muon E821 Anomalous Magnetic Moment Measurement at BNL,” *Phys. Rev. D* **73** (2006) 072003, [arXiv:hep-ex/0602035](https://arxiv.org/abs/hep-ex/0602035).
- [53] H. Baer and X. Tata, *Weak Scale Supersymmetry: From Superfields to Scattering Events.* Cambridge University Press, 2006.
- [54] T. Aoyama *et al.*, “The anomalous magnetic moment of the muon in the Standard Model,” *Phys. Rept.* **887** (2020) 1–166, [arXiv:2006.04822 \[hep-ph\]](https://arxiv.org/abs/2006.04822).
- [55] **Muon g-2** Collaboration, B. Abi *et al.*, “Measurement of the Positive Muon Anomalous Magnetic Moment to 0.46 ppm,” *Phys. Rev. Lett.* **126** no. 14, (2021) 141801, [arXiv:2104.03281 \[hep-ex\]](https://arxiv.org/abs/2104.03281).
- [56] A. Czarnecki and W. J. Marciano, “The Muon anomalous magnetic moment: A Harbinger for ‘new physics’,” *Phys. Rev. D* **64** (2001) 013014, [arXiv:hep-ph/0102122](https://arxiv.org/abs/hep-ph/0102122).
- [57] J. L. Feng and K. T. Matchev, “Supersymmetry and the anomalous magnetic moment of the muon,” *Phys. Rev. Lett.* **86** (2001) 3480–3483, [arXiv:hep-ph/0102146](https://arxiv.org/abs/hep-ph/0102146).
- [58] S. Coleman and J. Mandula, “All possible symmetries of the s matrix,” *Phys. Rev.* **159** (Jul, 1967) 1251–1256. <https://link.aps.org/doi/10.1103/PhysRev.159.1251>.
- [59] R. Haag, J. T. Lopuszanski, and M. Sohnius, “All Possible Generators of Supersymmetries of the s Matrix,” *Nucl. Phys.* **B88** (1975) 257. [,257(1974)].
- [60] J. Wess and B. Zumino, “Supergauge transformations in four dimensions,” *Nucl. Phys. B* **70** (1974) 39.
- [61] H. Georgi and S. L. Glashow, “Gauge theories without anomalies,” *Phys. Rev. D* **6** (Jul, 1972) 429–431. <https://link.aps.org/doi/10.1103/PhysRevD.6.429>.
- [62] S. Dimopoulos and D. W. Sutter, “The Supersymmetric flavor problem,” *Nucl. Phys. B* **452** (1995) 496–512, [arXiv:hep-ph/9504415](https://arxiv.org/abs/hep-ph/9504415).
- [63] **MEG** Collaboration, T. Mori, “Final Results of the MEG Experiment,” *Nuovo Cim. C* **39** no. 4, (2017) 325, [arXiv:1606.08168 \[hep-ex\]](https://arxiv.org/abs/1606.08168).

- [64] H. P. Nilles, “Supersymmetry, Supergravity and Particle Physics,” *Phys. Rept.* **110** (1984) 1–162.
- [65] A. Lahanas and D. Nanopoulos, “The road to no-scale supergravity,” *Physics Reports* **145** no. 1, (1987) 1 – 139.
<http://www.sciencedirect.com/science/article/pii/0370157387900342>.
- [66] J. L. Feng, A. Rajaraman, and F. Takayama, “Superweakly interacting massive particles,” *Phys. Rev. Lett.* **91** (2003) 011302, [arXiv:hep-ph/0302215](https://arxiv.org/abs/hep-ph/0302215).
- [67] S. Y. Choi, J. Kalinowski, G. A. Moortgat-Pick, and P. M. Zerwas, “Analysis of the neutralino system in supersymmetric theories,” *Eur. Phys. J. C* **22** (2001) 563–579, [arXiv:hep-ph/0108117](https://arxiv.org/abs/hep-ph/0108117). [Addendum: Eur.Phys.J.C 23, 769–772 (2002)].
- [68] **Super-Kamiokande** Collaboration, K. Abe *et al.*, “Search for proton decay via $p \rightarrow e^+ \pi^0$ and $p \rightarrow \mu^+ \pi^0$ in 0.31 megaton-years exposure of the Super-Kamiokande water Cherenkov detector,” *Phys. Rev. D* **95** no. 1, (2017) 012004, [arXiv:1610.03597](https://arxiv.org/abs/1610.03597) [[hep-ex](#)].
- [69] J. R. Ellis, “Beyond the standard model for hill walkers,” in *1998 European School of High-Energy Physics*, pp. 133–196. 8, 1998. [arXiv:hep-ph/9812235](https://arxiv.org/abs/hep-ph/9812235).
- [70] J. R. Ellis, J. Hagelin, D. V. Nanopoulos, K. A. Olive, and M. Srednicki, “Supersymmetric Relics from the Big Bang,” *Nucl. Phys. B* **238** (1984) 453–476.
- [71] D. O. Caldwell, R. M. Eisberg, D. M. Grumm, M. S. Witherell, B. Sadoulet, F. S. Goulding, and A. R. Smith, “Laboratory limits on galactic cold dark matter,” *Phys. Rev. Lett.* **61** (Aug, 1988) 510–513. <https://doi.org/10.1103/PhysRevLett.61.510>.
- [72] M. Mori, M. M. Nojiri, K. S. Hirata, K. Kihara, Y. Oyama, A. Suzuki, K. Takahashi, M. Yamada, H. Takei, M. Koga, K. Miyano, H. Miyata, Y. Fukuda, T. Hayakawa, K. Inoue, T. Ishida, T. Kajita, Y. Koshio, M. Nakahata, K. Nakamura, A. Sakai, N. Sato, M. Shiozawa, J. Suzuki, Y. Suzuki, Y. Totsuka, M. Koshiba, K. Nishijima, T. Kajimura, T. Suda, A. T. Suzuki, T. Hara, Y. Nagashima, M. Takita, H. Yokoyama, A. Yoshimoto, K. Kaneyuki, Y. Takeuchi, T. Tanimori, S. Tasaka, and K. Nishikawa, “Search for neutralino dark matter heavier than the w boson at kamiokande,” *Phys. Rev. D* **48** (Dec, 1993) 5505–5518. <https://doi.org/10.1103/PhysRevD.48.5505>.
- [73] **CDMS** Collaboration, D. S. Akerib *et al.*, “Exclusion limits on the WIMP-nucleon cross section from the first run of the Cryogenic Dark Matter Search in the Soudan Underground Laboratory,” *Phys. Rev. D* **72** (2005) 052009, [arXiv:astro-ph/0507190](https://arxiv.org/abs/astro-ph/0507190).
- [74] A. Djouadi, J.-L. Kneur, and G. Moultaka, “SuSpect: A Fortran code for the supersymmetric and Higgs particle spectrum in the MSSM,” *Comput. Phys. Commun.* **176** (2007) 426–455, [arXiv:hep-ph/0211331](https://arxiv.org/abs/hep-ph/0211331).
- [75] C. F. Berger, J. S. Gainer, J. L. Hewett, and T. G. Rizzo, “Supersymmetry without prejudice,” *Journal of High Energy Physics* **2009** no. 02, (Feb, 2009) 023–023.
[http://dx.doi.org/10.1088/1126-6708/2009/02/023](https://dx.doi.org/10.1088/1126-6708/2009/02/023).
- [76] J. Alwall, P. Schuster, and N. Toro, “Simplified Models for a First Characterization of New Physics at the LHC,” *Phys. Rev. D* **79** (2009) 075020, [arXiv:0810.3921](https://arxiv.org/abs/0810.3921) [[hep-ph](#)].
- [77] **LHC New Physics Working Group** Collaboration, D. Alves, “Simplified Models for LHC New Physics Searches,” *J. Phys. G* **39** (2012) 105005, [arXiv:1105.2838](https://arxiv.org/abs/1105.2838) [[hep-ph](#)].

- [78] D. S. Alves, E. Izaguirre, and J. G. Wacker, “Where the Sidewalk Ends: Jets and Missing Energy Search Strategies for the 7 TeV LHC,” *JHEP* **10** (2011) 012, [arXiv:1102.5338 \[hep-ph\]](https://arxiv.org/abs/1102.5338).
- [79] F. Ambrogi, S. Kraml, S. Kulkarni, U. Laa, A. Lessa, and W. Waltenberger, “On the coverage of the pMSSM by simplified model results,” *Eur. Phys. J. C* **78** no. 3, (2018) 215, [arXiv:1707.09036 \[hep-ph\]](https://arxiv.org/abs/1707.09036).
- [80] O. Buchmueller and J. Marrouche, “Universal mass limits on gluino and third-generation squarks in the context of Natural-like SUSY spectra,” *Int. J. Mod. Phys. A* **29** no. 06, (2014) 1450032, [arXiv:1304.2185 \[hep-ph\]](https://arxiv.org/abs/1304.2185).
- [81] **ATLAS** Collaboration, M. Aaboud *et al.*, “Dark matter interpretations of ATLAS searches for the electroweak production of supersymmetric particles in $\sqrt{s} = 8$ TeV proton-proton collisions,” *JHEP* **09** (2016) 175, [arXiv:1608.00872 \[hep-ex\]](https://arxiv.org/abs/1608.00872).
- [82] **ATLAS** Collaboration, “Summary of the ATLAS experiment’s sensitivity to supersymmetry after LHC Run 1 — interpreted in the phenomenological MSSM,” *JHEP* **10** (2015) 134, [arXiv:1508.06608 \[hep-ex\]](https://arxiv.org/abs/1508.06608).
- [83] **ATLAS** Collaboration, “Mass reach of the atlas searches for supersymmetry.” https://atlas.web.cern.ch/Atlas/GROUPS/PHYSICS/PUBNOTES/ATL-PHYS-PUB-2020-020/fig_23.png, 2020.
- [84] **CMS** Collaboration, “Summary plot moriond 2017.” https://twiki.cern.ch/twiki/pub/CMSPublic/SUSYSummary2017/Moriond2017_BarPlot.pdf, 2017.
- [85] L. S. W. Group, “Notes lepsusywg/02-04.1 and lepsusywg/01-03.1.” <http://lepsusy.web.cern.ch/lepsusy/>, 2004. Accessed: 2021-02-11.
- [86] ATLAS Collaboration, “Searches for electroweak production of supersymmetric particles with compressed mass spectra in $\sqrt{s} = 13$ TeV pp collisions with the ATLAS detector,” *Phys. Rev. D* **101** (2020) 052005, [arXiv:1911.12606 \[hep-ex\]](https://arxiv.org/abs/1911.12606).
- [87] W. Beenakker, C. Borschensky, M. Krämer, A. Kulesza, and E. Laenen, “NNLL-fast: predictions for coloured supersymmetric particle production at the LHC with threshold and Coulomb resummation,” *JHEP* **12** (2016) 133, [arXiv:1607.07741 \[hep-ph\]](https://arxiv.org/abs/1607.07741).
- [88] M. Beneke, M. Czakon, P. Falgari, A. Mitov, and C. Schwinn, “Threshold expansion of the $gg(q\bar{q}) \rightarrow Q\bar{Q} + X$ cross section at $\mathcal{O}(\alpha_s^4)$,” *Phys. Lett. B* **690** (2010) 483, [arXiv:0911.5166 \[hep-ph\]](https://arxiv.org/abs/0911.5166).
- [89] J. Fiaschi and M. Klasen, “Neutralino-chargino pair production at NLO+NLL with resummation-improved parton density functions for LHC Run II,” *Phys. Rev. D* **98** no. 5, (2018) 055014, [arXiv:1805.11322 \[hep-ph\]](https://arxiv.org/abs/1805.11322).
- [90] B. Fuks, M. Klasen, D. R. Lamprea, and M. Roethering, “Gaugino production in proton-proton collisions at a center-of-mass energy of 8 TeV,” *JHEP* **10** (2012) 081, [arXiv:1207.2159 \[hep-ph\]](https://arxiv.org/abs/1207.2159).
- [91] J. Fiaschi and M. Klasen, “Slepton pair production at the LHC in NLO+NLL with resummation-improved parton densities,” *JHEP* **03** (2018) 094, [arXiv:1801.10357 \[hep-ph\]](https://arxiv.org/abs/1801.10357).

- [92] **ATLAS** Collaboration, G. Aad *et al.*, “Observation of a new particle in the search for the Standard Model Higgs boson with the ATLAS detector at the LHC,” *Phys. Lett. B* **716** (2012) 1–29, [arXiv:1207.7214 \[hep-ex\]](https://arxiv.org/abs/1207.7214).
- [93] **CMS** Collaboration, S. Chatrchyan *et al.*, “Observation of a New Boson at a Mass of 125 GeV with the CMS Experiment at the LHC,” *Phys. Lett. B* **716** (2012) 30–61, [arXiv:1207.7235 \[hep-ex\]](https://arxiv.org/abs/1207.7235).
- [94] A. Buckley, “PySLHA: a Pythonic interface to SUSY Les Houches Accord data,” *Eur. Phys. J. C* **75** no. 10, (2015) 467, [arXiv:1305.4194 \[hep-ph\]](https://arxiv.org/abs/1305.4194).
- [95] CERN, “About cern.” <https://home.cern/about>. Accessed: 2021-01-21.
- [96] CERN, “CERN Annual report 2019,” tech. rep., CERN, Geneva, 2020. <https://cds.cern.ch/record/2723123>.
- [97] O. S. Bruning, P. Collier, P. Lebrun, S. Myers, R. Ostojic, J. Poole, and P. Proudlock, *LHC Design Report*. CERN Yellow Reports: Monographs. CERN, Geneva, 2004. <https://cds.cern.ch/record/782076>.
- [98] M. Blewett and N. Vogt-Nilsen, “Proceedings of the 8th international conference on high-energy accelerators, cern 1971. conference held at geneva, 20–24 september 1971.,” tech. rep., 1971, 1971.
- [99] L. R. Evans and P. Bryant, “LHC Machine,” *JINST* **3** (2008) S08001. 164 p. [http://cds.cern.ch/record/1129806](https://cds.cern.ch/record/1129806). This report is an abridged version of the LHC Design Report (CERN-2004-003).
- [100] R. Scrivens, M. Kronberger, D. Küchler, J. Lettry, C. Mastrostefano, O. Midttun, M. O’Neil, H. Pereira, and C. Schmitzer, “Overview of the status and developments on primary ion sources at CERN*.”, <https://cds.cern.ch/record/1382102>.
- [101] M. Vretenar, J. Vollaire, R. Scrivens, C. Rossi, F. Roncarolo, S. Ramberger, U. Raich, B. Puccio, D. Nisbet, R. Mompo, S. Mathot, C. Martin, L. A. Lopez-Hernandez, A. Lombardi, J. Lettry, J. B. Lallement, I. Kozsar, J. Hansen, F. Gerigk, A. Funken, J. F. Fuchs, N. Dos Santos, M. Calviani, M. Buzio, O. Brunner, Y. Body, P. Baudrenghien, J. Bauche, and T. Zickler, *Linac4 design report*, vol. 6 of *CERN Yellow Reports: Monographs*. CERN, Geneva, 2020. <https://cds.cern.ch/record/2736208>.
- [102] E. Mobs, “The CERN accelerator complex - 2019. Complexe des accélérateurs du CERN - 2019.”, <https://cds.cern.ch/record/2684277>. General Photo.
- [103] **ATLAS** Collaboration, “The ATLAS Experiment at the CERN Large Hadron Collider,” *JINST* **3** (2008) S08003.
- [104] **CMS** Collaboration, S. Chatrchyan *et al.*, “The CMS Experiment at the CERN LHC,” *JINST* **3** (2008) S08004.
- [105] **ALICE** Collaboration, K. Aamodt *et al.*, “The ALICE experiment at the CERN LHC,” *JINST* **3** (2008) S08002.
- [106] **LHCb** Collaboration, J. Alves, A. Augusto *et al.*, “The LHCb Detector at the LHC,” *JINST* **3** (2008) S08005.
- [107] **TOTEM** Collaboration, G. Anelli *et al.*, “The TOTEM experiment at the CERN Large Hadron Collider,” *JINST* **3** (2008) S08007.

- [108] **LHCf** Collaboration, O. Adriani *et al.*, “Technical design report of the LHCf experiment: Measurement of photons and neutral pions in the very forward region of LHC,”.
- [109] **MoEDAL** Collaboration, J. Pinfold *et al.*, “Technical Design Report of the MoEDAL Experiment,”.
- [110] **ATLAS** Collaboration, “ATLAS Public Results - Luminosity Public Results Run 2.”, <https://twiki.cern.ch/twiki/bin/view/AtlasPublic/LuminosityPublicResultsRun2>. Accessed: 2021-01-17.
- [111] **ATLAS** Collaboration, Z. Marshall, “Simulation of Pile-up in the ATLAS Experiment,” *J. Phys. Conf. Ser.* **513** (2014) 022024.
- [112] “First beam in the LHC - accelerating science,”, <https://home.cern/news/news/accelerators/record-luminosity-well-done-lhc>. Accessed: 2021-01-10.
- [113] **ATLAS Collaboration** Collaboration, “Luminosity determination in pp collisions at $\sqrt{s} = 13$ TeV using the ATLAS detector at the LHC,” Tech. Rep. ATLAS-CONF-2019-021, CERN, Geneva, Jun, 2019. <https://cds.cern.ch/record/2677054>.
- [114] **ATLAS** Collaboration, M. Aaboud *et al.*, “Luminosity determination in pp collisions at $\sqrt{s} = 8$ TeV using the ATLAS detector at the LHC,” *Eur. Phys. J. C* **76** no. 12, (2016) 653, [arXiv:1608.03953 \[hep-ex\]](https://arxiv.org/abs/1608.03953).
- [115] G. Avoni, M. Bruschi, G. Cabras, D. Caforio, N. Dehghanian, A. Floderus, B. Giacobbe, F. Giannuzzi, F. Giorgi, P. Grafström, V. Hedberg, F. L. Manghi, S. Meneghini, J. Pinfold, E. Richards, C. Sbarra, N. S. Cesari, A. Sbrizzi, R. Soluk, G. Ucchielli, S. Valentinetto, O. Viazlo, M. Villa, C. Vittori, R. Vuillermet, and A. Zoccoli, “The new LUCID-2 detector for luminosity measurement and monitoring in ATLAS,” *Journal of Instrumentation* **13** no. 07, (Jul, 2018) P07017–P07017. <https://doi.org/10.1088/1748-0221/13/07/p07017>.
- [116] S. van der Meer, “Calibration of the effective beam height in the ISR,” Tech. Rep. CERN-ISR-PO-68-31. ISR-PO-68-31, CERN, Geneva, 1968. <https://cds.cern.ch/record/296752>.
- [117] P. Grafström and W. Kozanecki, “Luminosity determination at proton colliders,” *Progress in Particle and Nuclear Physics* **81** (2015) 97 – 148. <http://www.sciencedirect.com/science/article/pii/S0146641014000878>.
- [118] M. Bajko *et al.*, “Report of the Task Force on the Incident of 19th September 2008 at the LHC,” Tech. Rep. LHC-PROJECT-Report-1168. CERN-LHC-PROJECT-Report-1168, CERN, Geneva, Mar, 2009. <https://cds.cern.ch/record/1168025>.
- [119] “New schedule for CERN’s accelerators and experiments,”. <https://home.cern/news/press-release/cern/first-beam-lhc-accelerating-science>. Accessed: 2021-01-10.
- [120] **ATLAS** Collaboration, G. Aad *et al.*, “Luminosity Determination in pp Collisions at $\sqrt{s} = 7$ TeV Using the ATLAS Detector at the LHC,” *Eur. Phys. J. C* **71** (2011) 1630, [arXiv:1101.2185 \[hep-ex\]](https://arxiv.org/abs/1101.2185).

- [121] **ATLAS Collaboration** Collaboration, G. Aad *et al.*, “Improved luminosity determination in pp collisions at $\sqrt{s} = 7$ TeV using the ATLAS detector at the LHC. Improved luminosity determination in pp collisions at $\text{sqrt}(s) = 7$ TeV using the ATLAS detector at the LHC,” *Eur. Phys. J. C* **73** no. CERN-PH-EP-2013-026. CERN-PH-EP-2013-026, (Feb, 2013) 2518. 27 p. <https://cds.cern.ch/record/1517411>. Comments: 26 pages plus author list (39 pages total), 17 figures, 9 tables, submitted to EPJC, All figures are available at <a href=.
- [122] “Record luminosity: well done LHC.” <https://home.cern/news/news/accelerators/new-schedule-cerns-accelerators-and-experiments>. Accessed: 2021-01-10.
- [123] A. G., B. A. I., B. O., F. P., L. M., R. L., and T. L., *High-Luminosity Large Hadron Collider (HL-LHC): Technical Design Report V. 0.1*. CERN Yellow Reports: Monographs. CERN, Geneva, 2017. <https://cds.cern.ch/record/2284929>.
- [124] J. Pequenao, “Computer generated image of the whole ATLAS detector.” Mar, 2008.
- [125] **ATLAS** Collaboration, “ATLAS: Detector and physics performance technical design report. Volume 1.”
- [126] J. Pequenao, “Computer generated image of the ATLAS inner detector.” Mar, 2008.
- [127] **ATLAS Collaboration** Collaboration, K. Potamianos, “The upgraded Pixel detector and the commissioning of the Inner Detector tracking of the ATLAS experiment for Run-2 at the Large Hadron Collider,” Tech. Rep. ATL-PHYS-PROC-2016-104, CERN, Geneva, Aug, 2016. <https://cds.cern.ch/record/2209070>. 15 pages, EPS-HEP 2015 Proceedings.
- [128] **ATLAS IBL** Collaboration, B. Abbott *et al.*, “Production and Integration of the ATLAS Insertable B-Layer,” *JINST* **13** no. 05, (2018) T05008, [arXiv:1803.00844 \[physics.ins-det\]](https://arxiv.org/abs/1803.00844).
- [129] **ATLAS** Collaboration, “ATLAS Insertable B-Layer Technical Design Report,” Tech. Rep. CERN-LHCC-2010-013. ATLAS-TDR-19, Sep, 2010. [http://cds.cern.ch/record/1291633](https://cds.cern.ch/record/1291633).
- [130] **ATLAS** Collaboration, G. Aad *et al.*, “ATLAS b-jet identification performance and efficiency measurement with $t\bar{t}$ events in pp collisions at $\sqrt{s} = 13$ TeV,” *Eur. Phys. J. C* **79** no. 11, (2019) 970, [arXiv:1907.05120 \[hep-ex\]](https://arxiv.org/abs/1907.05120).
- [131] ATLAS Collaboration, “Particle Identification Performance of the ATLAS Transition Radiation Tracker.” ATLAS-CONF-2011-128, 2011. <https://cds.cern.ch/record/1383793>.
- [132] J. Pequenao, “Computer Generated image of the ATLAS calorimeter.” Mar, 2008.
- [133] J. Pequenao, “Computer generated image of the ATLAS Muons subsystem.” Mar, 2008.
- [134] S. Lee, M. Livan, and R. Wigmans, “Dual-Readout Calorimetry,” *Rev. Mod. Phys.* **90** no. arXiv:1712.05494. 2, (Dec, 2017) 025002. 40 p. <https://cds.cern.ch/record/2637852>. 44 pages, 53 figures, accepted for publication in Review of Modern Physics.
- [135] M. Leite, “Performance of the ATLAS Zero Degree Calorimeter,” Tech. Rep. ATL-FWD-PROC-2013-001, CERN, Geneva, Nov, 2013. <https://cds.cern.ch/record/1628749>.

- [136] S. Abdel Khalek *et al.*, “The ALFA Roman Pot Detectors of ATLAS,” *JINST* **11** no. 11, (2016) P11013, [arXiv:1609.00249 \[physics.ins-det\]](https://arxiv.org/abs/1609.00249).
- [137] U. Amaldi, G. Cocconi, A. Diddens, R. Dobinson, J. Dorenbosch, W. Duinker, D. Gustavson, J. Meyer, K. Potter, A. Wetherell, A. Baroncelli, and C. Bosio, “The real part of the forward proton proton scattering amplitude measured at the cern intersecting storage rings,” *Physics Letters B* **66** no. 4, (1977) 390 – 394.
<http://www.sciencedirect.com/science/article/pii/0370269377900223>.
- [138] L. Adamczyk, E. Banaś, A. Brandt, M. Bruschi, S. Grinstein, J. Lange, M. Rijssenbeek, P. Sicho, R. Staszewski, T. Sykora, M. Trzebiński, J. Chwastowski, and K. Korcyl, “Technical Design Report for the ATLAS Forward Proton Detector,” Tech. Rep. CERN-LHCC-2015-009. ATLAS-TDR-024, May, 2015.
<https://cds.cern.ch/record/2017378>.
- [139] **ATLAS** Collaboration, A. R. Martínez, “The Run-2 ATLAS Trigger System,” *J. Phys. Conf. Ser.* **762** no. 1, (2016) 012003.
- [140] **ATLAS Collaboration** Collaboration, *ATLAS level-1 trigger: Technical Design Report*. Technical Design Report ATLAS. CERN, Geneva, 1998.
<https://cds.cern.ch/record/381429>.
- [141] **ATLAS** Collaboration, G. Aad *et al.*, “Operation of the ATLAS trigger system in Run 2,” *JINST* **15** no. 10, (2020) P10004, [arXiv:2007.12539 \[physics.ins-det\]](https://arxiv.org/abs/2007.12539).
- [142] **ATLAS Collaboration** Collaboration, P. Jenni, M. Nessi, M. Nordberg, and K. Smith, *ATLAS high-level trigger, data-acquisition and controls: Technical Design Report*. Technical Design Report ATLAS. CERN, Geneva, 2003.
<https://cds.cern.ch/record/616089>.
- [143] **ATLAS** Collaboration, G. Aad *et al.*, “The ATLAS Simulation Infrastructure,” *Eur. Phys. J. C* **70** (2010) 823–874, [arXiv:1005.4568 \[physics.ins-det\]](https://arxiv.org/abs/1005.4568).
- [144] T. Gleisberg, S. Hoeche, F. Krauss, M. Schonherr, S. Schumann, F. Siegert, and J. Winter, “Event generation with SHERPA 1.1,” *JHEP* **02** (2009) 007, [arXiv:0811.4622 \[hep-ph\]](https://arxiv.org/abs/0811.4622).
- [145] A. Buckley *et al.*, “General-purpose event generators for LHC physics,” *Phys. Rept.* **504** (2011) 145–233, [arXiv:1101.2599 \[hep-ph\]](https://arxiv.org/abs/1101.2599).
- [146] V. N. Gribov and L. N. Lipatov, “Deep inelastic e p scattering in perturbation theory,” *Sov. J. Nucl. Phys.* **15** (1972) 438–450.
- [147] J. Blumlein, T. Doyle, F. Hautmann, M. Klein, and A. Vogt, “Structure functions in deep inelastic scattering at HERA,” in *Workshop on Future Physics at HERA (To be followed by meetings 7-9 Feb and 30-31 May 1996 at DESY)*. 9, 1996. [arXiv:hep-ph/9609425](https://arxiv.org/abs/hep-ph/9609425).
- [148] A. Buckley, J. Ferrando, S. Lloyd, K. Nordström, B. Page, M. Rüfenacht, M. Schönher, and G. Watt, “LHAPDF6: parton density access in the LHC precision era,” *Eur. Phys. J. C* **75** (2015) 132, [arXiv:1412.7420 \[hep-ph\]](https://arxiv.org/abs/1412.7420).
- [149] M. Bengtsson and T. Sjostrand, “Coherent Parton Showers Versus Matrix Elements: Implications of PETRA - PEP Data,” *Phys. Lett. B* **185** (1987) 435.
- [150] S. Catani, F. Krauss, R. Kuhn, and B. R. Webber, “QCD matrix elements + parton showers,” *JHEP* **11** (2001) 063, [arXiv:hep-ph/0109231](https://arxiv.org/abs/hep-ph/0109231).

- [151] L. Lonnblad, “Correcting the color dipole cascade model with fixed order matrix elements,” *JHEP* **05** (2002) 046, [arXiv:hep-ph/0112284](https://arxiv.org/abs/hep-ph/0112284).
- [152] B. Andersson, G. Gustafson, G. Ingelman, and T. Sjostrand, “Parton Fragmentation and String Dynamics,” *Phys. Rept.* **97** (1983) 31–145.
- [153] B. Andersson, *The Lund Model*. Cambridge Monographs on Particle Physics, Nuclear Physics and Cosmology. Cambridge University Press, 1998.
- [154] D. Amati and G. Veneziano, “Preconfinement as a Property of Perturbative QCD,” *Phys. Lett. B* **83** (1979) 87–92.
- [155] D. Yennie, S. Frautschi, and H. Suura, “The infrared divergence phenomena and high-energy processes,” *Annals of Physics* **13** no. 3, (1961) 379–452.
<https://www.sciencedirect.com/science/article/pii/0003491661901518>.
- [156] M. Dobbs and J. B. Hansen, “The HepMC C++ Monte Carlo event record for High Energy Physics,” *Comput. Phys. Commun.* **134** (2001) 41–46.
- [157] **GEANT4** Collaboration, S. Agostinelli *et al.*, “GEANT4: A Simulation toolkit,” *Nucl. Instrum. Meth.* **A506** (2003) 250–303.
- [158] **ATLAS Collaboration** Collaboration, “The new Fast Calorimeter Simulation in ATLAS,” Tech. Rep. ATL-SOFT-PUB-2018-002, CERN, Geneva, Jul, 2018.
<https://cds.cern.ch/record/2630434>.
- [159] K. Cranmer, “Practical Statistics for the LHC,” in *2011 European School of High-Energy Physics*, pp. 267–308. 2014. [arXiv:1503.07622 \[physics.data-an\]](https://arxiv.org/abs/1503.07622).
- [160] G. Cowan, K. Cranmer, E. Gross, and O. Vitells, “Asymptotic formulae for likelihood-based tests of new physics,” *Eur. Phys. J.* **C71** (2011) 1554, [arXiv:1007.1727 \[physics.data-an\]](https://arxiv.org/abs/1007.1727). [Erratum: Eur. Phys. J.C73,2501(2013)].
- [161] ATLAS Collaboration, “Reproduction searches for new physics with the ATLAS experiment through publication of full statistical likelihoods.” ATL-PHYS-PUB-2019-029, 2019. <https://cds.cern.ch/record/2684863>.
- [162] **ROOT Collaboration** Collaboration, K. Cranmer, G. Lewis, L. Moneta, A. Shibata, and W. Verkerke, “HistFactory: A tool for creating statistical models for use with RooFit and RooStats,” Tech. Rep. CERN-OPEN-2012-016, New York U., New York, Jan, 2012.
<https://cds.cern.ch/record/1456844>.
- [163] W. Verkerke and D. P. Kirkby, “The RooFit toolkit for data modeling,” *eConf C0303241* (2003) MOLT007, [arXiv:physics/0306116 \[physics\]](https://arxiv.org/abs/physics/0306116). [,186(2003)].
- [164] F. James and M. Roos, “MINUIT: a system for function minimization and analysis of the parameter errors and corrections,” *Comput. Phys. Commun.* **10** no. CERN-DD-75-20, (Jul, 1975) 343–367. 38 p. <https://cds.cern.ch/record/310399>.
- [165] L. Moneta, K. Belasco, K. S. Cranmer, S. Kreiss, A. Lazzaro, D. Piparo, G. Schott, W. Verkerke, and M. Wolf, “The RooStats Project,” *PoS ACAT2010* (2010) 057, [arXiv:1009.1003 \[physics.data-an\]](https://arxiv.org/abs/1009.1003).
- [166] R. Brun and F. Rademakers, “ROOT: An object oriented data analysis framework,” *Nucl. Instrum. Meth.* **A389** (1997) 81–86.

- [167] I. Antcheva *et al.*, “Root — a c++ framework for petabyte data storage, statistical analysis and visualization,” *Computer Physics Communications* **182** no. 6, (2011) 1384 – 1385. <http://www.sciencedirect.com/science/article/pii/S0010465511000701>.
- [168] M. Baak, G. J. Besjes, D. Côte, A. Koutsman, J. Lorenz, and D. Short, “HistFitter software framework for statistical data analysis,” *Eur. Phys. J. C* **75** (2015) 153, [arXiv:1410.1280 \[hep-ex\]](https://arxiv.org/abs/1410.1280).
- [169] L. Heinrich, M. Feickert, G. Stark, and K. Cranmer, “pyhf: pure-python implementation of histfactory statistical models,” *Journal of Open Source Software* **6** no. 58, (2021) 2823. <https://doi.org/10.21105/joss.02823>.
- [170] L. Heinrich, M. Feickert, and G. Stark, “pyhf: v0.6.0,” Version 0.6.0. <https://github.com/scikit-hep/pyhf>.
- [171] C. R. Harris, K. J. Millman, S. J. van der Walt, R. Gommers, P. Virtanen, D. Cournapeau, E. Wieser, J. Taylor, S. Berg, N. J. Smith, R. Kern, M. Picus, S. Hoyer, M. H. van Kerkwijk, M. Brett, A. Haldane, J. F. del R’io, M. Wiebe, P. Peterson, P. G’erard-Marchant, K. Sheppard, T. Reddy, W. Weckesser, H. Abbasi, C. Gohlke, and T. E. Oliphant, “Array programming with NumPy,” *Nature* **585** no. 7825, (Sept., 2020) 357–362. <https://doi.org/10.1038/s41586-020-2649-2>.
- [172] A. Paszke, S. Gross, F. Massa, A. Lerer, J. Bradbury, G. Chanan, T. Killeen, Z. Lin, N. Gimelshein, L. Antiga, A. Desmaison, A. Kopf, E. Yang, Z. DeVito, M. Raison, A. Tejani, S. Chilamkurthy, B. Steiner, L. Fang, J. Bai, and S. Chintala, “Pytorch: An imperative style, high-performance deep learning library,” in *Advances in Neural Information Processing Systems 32*, H. Wallach, H. Larochelle, A. Beygelzimer, F. d’Alché-Buc, E. Fox, and R. Garnett, eds., pp. 8024–8035. Curran Associates, Inc., 2019. <http://papers.neurips.cc/paper/9015-pytorch-an-imperative-style-high-performance-deep-learning-library.pdf>.
- [173] M. Abadi, A. Agarwal, P. Barham, E. Brevdo, Z. Chen, C. Citro, G. S. Corrado, A. Davis, J. Dean, M. Devin, S. Ghemawat, I. Goodfellow, A. Harp, G. Irving, M. Isard, Y. Jia, R. Jozefowicz, L. Kaiser, M. Kudlur, J. Levenberg, D. Mané, R. Monga, S. Moore, D. Murray, C. Olah, M. Schuster, J. Shlens, B. Steiner, I. Sutskever, K. Talwar, P. Tucker, V. Vanhoucke, V. Vasudevan, F. Viégas, O. Vinyals, P. Warden, M. Wattenberg, M. Wicke, Y. Yu, and X. Zheng, “TensorFlow: Large-scale machine learning on heterogeneous systems,” 2015. <https://www.tensorflow.org/>. Software available from tensorflow.org.
- [174] J. Bradbury, R. Frostig, P. Hawkins, M. J. Johnson, C. Leary, D. Maclaurin, and S. Wanderman-Milne, “JAX: composable transformations of Python+NumPy programs,” Version 0.1.46, 2018. [http://github.com/google/jax](https://github.com/google/jax).
- [175] S. S. Wilks, “The large-sample distribution of the likelihood ratio for testing composite hypotheses,” *Ann. Math. Statist.* **9** no. 1, (03, 1938) 60–62. <https://doi.org/10.1214/aoms/1177732360>.
- [176] A. Wald, “Tests of statistical hypotheses concerning several parameters when the number of observations is large,” *Transactions of the American Mathematical Society* **54** no. 3, (1943) 426–482. <https://doi.org/10.1090/S0002-9947-1943-0012401-3>.
- [177] G. Cowan, “Statistics for Searches at the LHC,” in *69th Scottish Universities Summer School in Physics: LHC Physics*, pp. 321–355. 7, 2013. [arXiv:1307.2487 \[hep-ex\]](https://arxiv.org/abs/1307.2487).

- [178] A. L. Read, “Presentation of search results: the CL_S technique,” *J. Phys. G* **28** (2002) 2693.
- [179] R. D. Cousins, J. T. Linnemann, and J. Tucker, “Evaluation of three methods for calculating statistical significance when incorporating a systematic uncertainty into a test of the background-only hypothesis for a Poisson process,” *Nucl. Instrum. Meth. A* **595** no. 2, (2008) 480, [arXiv:physics/0702156](https://arxiv.org/abs/physics/0702156) [physics.data-an].
- [180] K. CRANMER, “Statistical challenges for searches for new physics at the lhc,” *Statistical Problems in Particle Physics, Astrophysics and Cosmology* (May, 2006) .
http://dx.doi.org/10.1142/9781860948985_0026.
- [181] ATLAS Collaboration, “Search for direct pair production of a chargino and a neutralino decaying to the 125 GeV Higgs boson in $\sqrt{s} = 8$ TeV pp collisions with the ATLAS detector,” *Eur. Phys. J. C* **75** (2015) 208, [arXiv:1501.07110](https://arxiv.org/abs/1501.07110) [hep-ex].
- [182] ATLAS Collaboration, “Search for chargino and neutralino production in final states with a Higgs boson and missing transverse momentum at $\sqrt{s} = 13$ TeV with the ATLAS detector,” *Phys. Rev. D* **100** (2019) 012006, [arXiv:1812.09432](https://arxiv.org/abs/1812.09432) [hep-ex].
- [183] CMS Collaboration, “Search for electroweak production of charginos and neutralinos in WH events in proton–proton collisions at $\sqrt{s} = 13$ TeV,” *JHEP* **11** (2017) 029, [arXiv:1706.09933](https://arxiv.org/abs/1706.09933) [hep-ex].
- [184] ATLAS Collaboration, “Search for direct production of electroweakinos in final states with one lepton, missing transverse momentum and a Higgs boson decaying into two b -jets in pp collisions at $\sqrt{s} = 13$ TeV with the ATLAS detector,” *Eur. Phys. J. C* **80** (2020) 691, [arXiv:1909.09226](https://arxiv.org/abs/1909.09226) [hep-ex].
- [185] ATLAS Collaboration, “Improvements in $t\bar{t}$ modelling using NLO+PS Monte Carlo generators for Run 2.” ATL-PHYS-PUB-2018-009, 2018.
<https://cds.cern.ch/record/2630327>.
- [186] ATLAS Collaboration, “Modelling of the $t\bar{t}H$ and $t\bar{t}V(V = W, Z)$ processes for $\sqrt{s} = 13$ TeV ATLAS analyses.” ATL-PHYS-PUB-2016-005, 2016.
<https://cds.cern.ch/record/2120826>.
- [187] ATLAS Collaboration, “ATLAS simulation of boson plus jets processes in Run 2.” ATL-PHYS-PUB-2017-006, 2017. <https://cds.cern.ch/record/2261937>.
- [188] ATLAS Collaboration, “Multi-Boson Simulation for 13 TeV ATLAS Analyses.” ATL-PHYS-PUB-2017-005, 2017. <https://cds.cern.ch/record/2261933>.
- [189] J. Alwall, R. Frederix, S. Frixione, V. Hirschi, F. Maltoni, O. Mattelaer, H. S. Shao, T. Stelzer, P. Torrielli, and M. Zaro, “The automated computation of tree-level and next-to-leading order differential cross sections, and their matching to parton shower simulations,” *JHEP* **07** (2014) 079, [arXiv:1405.0301](https://arxiv.org/abs/1405.0301) [hep-ph].
- [190] R. Frederix and S. Frixione, “Merging meets matching in MC@NLO,” *JHEP* **12** (2012) 061, [arXiv:1209.6215](https://arxiv.org/abs/1209.6215) [hep-ph].
- [191] T. Sjöstrand, S. Ask, J. R. Christiansen, R. Corke, N. Desai, P. Ilten, S. Mrenna, S. Prestel, C. O. Rasmussen, and P. Z. Skands, “An Introduction to PYTHIA 8.2,” *Comput. Phys. Commun.* **191** (2015) 159–177, [arXiv:1410.3012](https://arxiv.org/abs/1410.3012) [hep-ph].

- [192] L. Lönnblad and S. Prestel, “Matching tree-level matrix elements with interleaved showers,” *JHEP* **03** (2012) 019, [arXiv:1109.4829 \[hep-ph\]](https://arxiv.org/abs/1109.4829).
- [193] R. D. Ball *et al.*, “Parton distributions with LHC data,” *Nucl. Phys. B* **867** (2013) 244, [arXiv:1207.1303 \[hep-ph\]](https://arxiv.org/abs/1207.1303).
- [194] ATLAS Collaboration, “ATLAS Pythia 8 tunes to 7 TeV data.” ATL-PHYS-PUB-2014-021, 2014. <https://cds.cern.ch/record/1966419>.
- [195] D. J. Lange, “The EvtGen particle decay simulation package,” *Nucl. Instrum. Meth. A* **462** (2001) 152.
- [196] ATLAS Collaboration, “The Pythia 8 A3 tune description of ATLAS minimum bias and inelastic measurements incorporating the Donnachie–Landshoff diffractive model.” ATL-PHYS-PUB-2016-017, 2016. <https://cds.cern.ch/record/2206965>.
- [197] B. Fuks, M. Klasen, D. R. Lamprea, and M. Rothberg, “Precision predictions for electroweak superpartner production at hadron colliders with RESUMMINO,” *Eur. Phys. J. C* **73** (2013) 2480, [arXiv:1304.0790 \[hep-ph\]](https://arxiv.org/abs/1304.0790).
- [198] S. Alioli, P. Nason, C. Oleari, and E. Re, “A general framework for implementing NLO calculations in shower Monte Carlo programs: the POWHEG BOX,” *JHEP* **06** (2010) 043, [arXiv:1002.2581 \[hep-ph\]](https://arxiv.org/abs/1002.2581).
- [199] S. Frixione, P. Nason, and G. Ridolfi, “A Positive-weight next-to-leading-order Monte Carlo for heavy flavour hadroproduction,” *JHEP* **09** (2007) 126, [arXiv:0707.3088 \[hep-ph\]](https://arxiv.org/abs/0707.3088).
- [200] P. Nason, “A New method for combining NLO QCD with shower Monte Carlo algorithms,” *JHEP* **11** (2004) 040, [arXiv:hep-ph/0409146](https://arxiv.org/abs/hep-ph/0409146).
- [201] E. Bothmann *et al.*, “Event generation with Sherpa 2.2,” *SciPost Phys.* **7** no. 3, (2019) 034, [arXiv:1905.09127 \[hep-ph\]](https://arxiv.org/abs/1905.09127).
- [202] S. Höche, F. Krauss, S. Schumann, and F. Siegert, “QCD matrix elements and truncated showers,” *JHEP* **05** (2009) 053, [arXiv:0903.1219 \[hep-ph\]](https://arxiv.org/abs/0903.1219).
- [203] S. Höche, F. Krauss, M. Schönher, and F. Siegert, “QCD matrix elements + parton showers. The NLO case,” *JHEP* **04** (2013) 027, [arXiv:1207.5030 \[hep-ph\]](https://arxiv.org/abs/1207.5030).
- [204] NNPDF Collaboration, R. D. Ball *et al.*, “Parton distributions for the LHC run II,” *JHEP* **04** (2015) 040, [arXiv:1410.8849 \[hep-ph\]](https://arxiv.org/abs/1410.8849).
- [205] ATLAS Collaboration, “Example ATLAS tunes of PYTHIA8, PYTHIA6 and POWHEG to an observable sensitive to Z boson transverse momentum.” ATL-PHYS-PUB-2013-017, 2013. <https://cds.cern.ch/record/1629317>.
- [206] M. Czakon and A. Mitov, “Top++: A program for the calculation of the top-pair cross-section at hadron colliders,” *Comput. Phys. Commun.* **185** (2014) 2930, [arXiv:1112.5675 \[hep-ph\]](https://arxiv.org/abs/1112.5675).
- [207] M. Cacciari, M. Czakon, M. Mangano, A. Mitov, and P. Nason, “Top-pair production at hadron colliders with next-to-next-to-leading logarithmic soft-gluon resummation,” *Phys. Lett. B* **710** (2012) 612–622, [arXiv:1111.5869 \[hep-ph\]](https://arxiv.org/abs/1111.5869).

- [208] P. Kant, O. M. Kind, T. Kintscher, T. Lohse, T. Martini, S. Mölbitz, P. Rieck, and P. Uwer, “HatHor for single top-quark production: Updated predictions and uncertainty estimates for single top-quark production in hadronic collisions,” *Comput. Phys. Commun.* **191** (2015) 74–89, [arXiv:1406.4403 \[hep-ph\]](https://arxiv.org/abs/1406.4403).
- [209] N. Kidonakis, “Two-loop soft anomalous dimensions for single top quark associated production with a W^- or H^- ,” *Phys. Rev. D* **82** (2010) 054018, [arXiv:1005.4451 \[hep-ph\]](https://arxiv.org/abs/1005.4451).
- [210] J. M. Campbell and R. K. Ellis, “ $t\bar{t}W^{+-}$ production and decay at NLO,” *JHEP* **07** (2012) 052, [arXiv:1204.5678 \[hep-ph\]](https://arxiv.org/abs/1204.5678).
- [211] A. Lazopoulos, T. McElmurry, K. Melnikov, and F. Petriello, “Next-to-leading order QCD corrections to $t\bar{t}Z$ production at the LHC,” *Phys. Lett. B* **666** (2008) 62–65, [arXiv:0804.2220 \[hep-ph\]](https://arxiv.org/abs/0804.2220).
- [212] R. Gavin, Y. Li, F. Petriello, and S. Quackenbush, “FEWZ 2.0: A code for hadronic Z production at next-to-next-to-leading order,” [arXiv:1011.3540 \[hep-ph\]](https://arxiv.org/abs/1011.3540).
- [213] **LHC Higgs Cross Section Working Group** Collaboration, D. de Florian *et al.*, “Handbook of LHC Higgs Cross Sections: 4. Deciphering the Nature of the Higgs Sector,” [arXiv:1610.07922 \[hep-ph\]](https://arxiv.org/abs/1610.07922).
- [214] ATLAS Collaboration, “Performance of the ATLAS track reconstruction algorithms in dense environments in LHC Run 2,” *Eur. Phys. J. C* **77** (2017) 673, [arXiv:1704.07983 \[hep-ex\]](https://arxiv.org/abs/1704.07983).
- [215] R. Frühwirth, “Application of Kalman filtering to track and vertex fitting,” *Nucl. Instrum. Methods Phys. Res., A* **262** no. HEPHY-PUB-503, (Jun, 1987) 444. 19 p. <https://cds.cern.ch/record/178627>.
- [216] T. Cornelissen, M. Elsing, I. Gavrilenco, W. Liebig, E. Moyse, and A. Salzburger, “The new ATLAS track reconstruction (NEWT),” *J. Phys.: Conf. Ser.* **119** (2008) 032014. <https://cds.cern.ch/record/1176900>.
- [217] ATLAS Collaboration, “Vertex Reconstruction Performance of the ATLAS Detector at $\sqrt{s} = 13$ TeV.” ATL-PHYS-PUB-2015-026, 2015. <https://cds.cern.ch/record/2037717>.
- [218] ATLAS Collaboration, “Reconstruction of primary vertices at the ATLAS experiment in Run 1 proton–proton collisions at the LHC,” *Eur. Phys. J. C* **77** (2017) 332, [arXiv:1611.10235 \[hep-ex\]](https://arxiv.org/abs/1611.10235).
- [219] ATLAS Collaboration, “Topological cell clustering in the ATLAS calorimeters and its performance in LHC Run 1,” *Eur. Phys. J. C* **77** (2017) 490, [arXiv:1603.02934 \[hep-ex\]](https://arxiv.org/abs/1603.02934).
- [220] ATLAS Collaboration, “Electron and photon performance measurements with the ATLAS detector using the 2015–2017 LHC proton–proton collision data,” *JINST* **14** (2019) P12006, [arXiv:1908.00005 \[hep-ex\]](https://arxiv.org/abs/1908.00005).
- [221] ATLAS Collaboration, “Measurement of the photon identification efficiencies with the ATLAS detector using LHC Run 2 data collected in 2015 and 2016,” *Eur. Phys. J. C* **79** (2019) 205, [arXiv:1810.05087 \[hep-ex\]](https://arxiv.org/abs/1810.05087).

- [222] ATLAS Collaboration, “Electron reconstruction and identification in the ATLAS experiment using the 2015 and 2016 LHC proton–proton collision data at $\sqrt{s} = 13$ TeV,” *Eur. Phys. J. C* **79** (2019) 639, [arXiv:1902.04655 \[hep-ex\]](https://arxiv.org/abs/1902.04655).
- [223] ATLAS Collaboration, “Muon reconstruction performance of the ATLAS detector in proton–proton collision data at $\sqrt{s} = 13$ TeV,” *Eur. Phys. J. C* **76** (2016) 292, [arXiv:1603.05598 \[hep-ex\]](https://arxiv.org/abs/1603.05598).
- [224] ATLAS Collaboration, “Muon reconstruction and identification efficiency in ATLAS using the full Run 2 pp collision data set at $\sqrt{s} = 13$ TeV,” [arXiv:2012.00578 \[hep-ex\]](https://arxiv.org/abs/2012.00578).
- [225] M. Cacciari, G. P. Salam, and G. Soyez, “The anti- k_t jet clustering algorithm,” *JHEP* **04** (2008) 063, [arXiv:0802.1189 \[hep-ph\]](https://arxiv.org/abs/0802.1189).
- [226] M. Cacciari, G. P. Salam, and G. Soyez, “FastJet user manual,” *Eur. Phys. J. C* **72** (2012) 1896, [arXiv:1111.6097 \[hep-ph\]](https://arxiv.org/abs/1111.6097).
- [227] M. Cacciari, “FastJet: A Code for fast k_t clustering, and more,” in *Deep inelastic scattering. Proceedings, 14th International Workshop, DIS 2006, Tsukuba, Japan, April 20-24, 2006*, pp. 487–490. 2006. [arXiv:hep-ph/0607071 \[hep-ph\]](https://arxiv.org/abs/hep-ph/0607071). [,125(2006)].
- [228] ATLAS Collaboration, G. Aad *et al.*, “Jet energy scale and resolution measured in proton-proton collisions at $\sqrt{s} = 13$ TeV with the ATLAS detector,” [arXiv:2007.02645 \[hep-ex\]](https://arxiv.org/abs/2007.02645).
- [229] M. Cacciari and G. P. Salam, “Pileup subtraction using jet areas,” *Phys. Lett. B* **659** (2008) 119–126, [arXiv:0707.1378 \[hep-ph\]](https://arxiv.org/abs/0707.1378).
- [230] ATLAS Collaboration, “Jet energy measurement with the ATLAS detector in proton–proton collisions at $\sqrt{s} = 7$ TeV,” *Eur. Phys. J. C* **73** (2013) 2304, [arXiv:1112.6426 \[hep-ex\]](https://arxiv.org/abs/1112.6426).
- [231] ATLAS Collaboration, “Determination of jet calibration and energy resolution in proton–proton collisions at $\sqrt{s} = 8$ TeV using the ATLAS detector,” [arXiv:1910.04482 \[hep-ex\]](https://arxiv.org/abs/1910.04482).
- [232] ATLAS Collaboration, “Performance of pile-up mitigation techniques for jets in pp collisions at $\sqrt{s} = 8$ TeV using the ATLAS detector,” *Eur. Phys. J. C* **76** (2016) 581, [arXiv:1510.03823 \[hep-ex\]](https://arxiv.org/abs/1510.03823).
- [233] ATLAS Collaboration, “Optimisation and performance studies of the ATLAS b -tagging algorithms for the 2017-18 LHC run.” ATL-PHYS-PUB-2017-013, 2017. <https://cds.cern.ch/record/2273281>.
- [234] ATLAS Collaboration, “ATLAS b -jet identification performance and efficiency measurement with $t\bar{t}$ events in pp collisions at $\sqrt{s} = 13$ TeV,” *Eur. Phys. J. C* **79** (2019) 970, [arXiv:1907.05120 \[hep-ex\]](https://arxiv.org/abs/1907.05120).
- [235] ATLAS Collaboration, “Measurements of b -jet tagging efficiency with the ATLAS detector using $t\bar{t}$ events at $\sqrt{s} = 13$ TeV,” *JHEP* **08** (2018) 089, [arXiv:1805.01845 \[hep-ex\]](https://arxiv.org/abs/1805.01845).
- [236] ATLAS Collaboration, “Performance of missing transverse momentum reconstruction with the ATLAS detector using proton–proton collisions at $\sqrt{s} = 13$ TeV,” *Eur. Phys. J. C* **78** (2018) 903, [arXiv:1802.08168 \[hep-ex\]](https://arxiv.org/abs/1802.08168).

- [237] **ATLAS Collaboration** Collaboration, “ E_T^{miss} performance in the ATLAS detector using 2015–2016 LHC p-p collisions,” Tech. Rep. ATLAS-CONF-2018-023, CERN, Geneva, Jun, 2018. <http://cds.cern.ch/record/2625233>.
- [238] D. Adams *et al.*, “Recommendations of the Physics Objects and Analysis Harmonisation Study Groups 2014,” Tech. Rep. ATL-PHYS-INT-2014-018, CERN, Geneva, Jul, 2014. <https://cds.cern.ch/record/1743654>.
- [239] M. Cacciari, G. P. Salam, and G. Soyez, “The Catchment Area of Jets,” *JHEP* **04** (2008) 005, [arXiv:0802.1188 \[hep-ph\]](arXiv:0802.1188 [hep-ph]).
- [240] **UA1** Collaboration, G. Arnison *et al.*, “Experimental Observation of Isolated Large Transverse Energy Electrons with Associated Missing Energy at $\sqrt{s} = 540$ GeV,” *Phys. Lett. B* **122** (1983) 103–116.
- [241] **Aachen-Annecy-Birmingham-CERN-Helsinki-London(QMC)-Paris(CdF)-Riverside-Rome-Rutherford-Saclay(CEN)-Vienna** Collaboration, G. Arnison *et al.*, “Further evidence for charged intermediate vector bosons at the SPS collider,” *Phys. Lett. B* **129** no. CERN-EP-83-111, (Jun, 1985) 273–282. 17 p. <https://cds.cern.ch/record/163856>.
- [242] D. R. Tovey, “On measuring the masses of pair-produced semi-invisibly decaying particles at hadron colliders,” *JHEP* **04** (2008) 034, [arXiv:0802.2879 \[hep-ph\]](arXiv:0802.2879 [hep-ph]).
- [243] G. Polesello and D. R. Tovey, “Supersymmetric particle mass measurement with the boost-corrected contransverse mass,” *JHEP* **03** (2010) 030, [arXiv:0910.0174 \[hep-ph\]](arXiv:0910.0174 [hep-ph]).
- [244] **ATLAS** Collaboration, G. Aad *et al.*, “Performance of the missing transverse momentum triggers for the ATLAS detector during Run-2 data taking,” *JHEP* **08** (2020) 080, [arXiv:2005.09554 \[hep-ex\]](arXiv:2005.09554 [hep-ex]).
- [245] **ATLAS** Collaboration, G. Aad *et al.*, “Performance of algorithms that reconstruct missing transverse momentum in $\sqrt{s} = 8$ TeV proton-proton collisions in the ATLAS detector,” *Eur. Phys. J. C* **77** no. 4, (2017) 241, [arXiv:1609.09324 \[hep-ex\]](arXiv:1609.09324 [hep-ex]).
- [246] ATLAS Collaboration, “ATLAS data quality operations and performance for 2015–2018 data-taking,” *JINST* **15** (2020) P04003, [arXiv:1911.04632 \[physics.ins-det\]](arXiv:1911.04632 [physics.ins-det]).
- [247] ATLAS Collaboration, “Selection of jets produced in 13 TeV proton–proton collisions with the ATLAS detector.” ATLAS-CONF-2015-029, 2015. <https://cds.cern.ch/record/2037702>.
- [248] N. Hartmann, “ahoi.” <https://gitlab.com/nikoladze/ahoi>, 2018.
- [249] **ATLAS** Collaboration, “Object-based missing transverse momentum significance in the ATLAS detector,” Tech. Rep. ATLAS-CONF-2018-038, CERN, Geneva, Jul, 2018. <https://cds.cern.ch/record/2630948>.
- [250] A. Roodman, “Blind analysis in particle physics,” *eConf* **C030908** (2003) TUIT001, <arXiv:physics/0312102>.
- [251] ATLAS Collaboration, “Measurement of the Inelastic Proton–Proton Cross Section at $\sqrt{s} = 13$ TeV with the ATLAS Detector at the LHC,” *Phys. Rev. Lett.* **117** (2016) 182002, [arXiv:1606.02625 \[hep-ex\]](arXiv:1606.02625 [hep-ex]).

- [252] ATLAS Collaboration, “A method for the construction of strongly reduced representations of ATLAS experimental uncertainties and the application thereof to the jet energy scale.” ATL-PHYS-PUB-2015-014, 2015. <https://cds.cern.ch/record/2037436>.
- [253] J. Bellm *et al.*, “Herwig 7.0/Herwig++ 3.0 release note,” *Eur. Phys. J. C* **76** no. 4, (2016) 196, [arXiv:1512.01178 \[hep-ph\]](https://arxiv.org/abs/1512.01178).
- [254] ATLAS Collaboration, “Simulation of top-quark production for the ATLAS experiment at $\sqrt{s} = 13$ TeV.” ATL-PHYS-PUB-2016-004, 2016. <https://cds.cern.ch/record/2120417>.
- [255] S. Frixione, E. Laenen, P. Motylinski, C. White, and B. R. Webber, “Single-top hadroproduction in association with a W boson,” *JHEP* **07** (2008) 029, [arXiv:0805.3067 \[hep-ph\]](https://arxiv.org/abs/0805.3067).
- [256] **ATLAS Collaboration** Collaboration, “SUSY July 2020 Summary Plot Update,” Tech. Rep. ATL-PHYS-PUB-2020-020, CERN, Geneva, Jul, 2020. [http://cds.cern.ch/record/2725258](https://cds.cern.ch/record/2725258).
- [257] **CMS Collaboration** Collaboration, “Search for chargino-neutralino production in final states with a Higgs boson and a W boson,” Tech. Rep. CMS-PAS-SUS-20-003, CERN, Geneva, 2021. <https://cds.cern.ch/record/2758360>.
- [258] ATLAS Collaboration, “Search for electroweak production of charginos and sleptons decaying into final states with two leptons and missing transverse momentum in $\sqrt{s} = 13$ TeV pp collisions using the ATLAS detector,” *Eur. Phys. J. C* **80** (2020) 123, [arXiv:1908.08215 \[hep-ex\]](https://arxiv.org/abs/1908.08215).
- [259] G. Apollinari, I. Béjar Alonso, O. Brüning, M. Lamont, and L. Rossi, *High-Luminosity Large Hadron Collider (HL-LHC): Preliminary Design Report*. CERN Yellow Reports: Monographs. CERN, Geneva, 2015. <https://cds.cern.ch/record/2116337>.
- [260] **LHC Reinterpretation Forum** Collaboration, W. Abdallah *et al.*, “Reinterpretation of LHC Results for New Physics: Status and Recommendations after Run 2,” *SciPost Phys.* **9** no. 2, (2020) 022, [arXiv:2003.07868 \[hep-ph\]](https://arxiv.org/abs/2003.07868).
- [261] ATLAS Collaboration, “RECAST framework reinterpretation of an ATLAS Dark Matter Search constraining a model of a dark Higgs boson decaying to two b -quarks.” ATL-PHYS-PUB-2019-032, 2019. <https://cds.cern.ch/record/2686290>.
- [262] K. Cranmer and I. Yavin, “RECAST: Extending the Impact of Existing Analyses,” *JHEP* **04** (2011) 038, [arXiv:1010.2506 \[hep-ex\]](https://arxiv.org/abs/1010.2506).
- [263] D. Dercks, N. Desai, J. S. Kim, K. Rolbiecki, J. Tattersall, and T. Weber, “CheckMATE 2: From the model to the limit,” *Comput. Phys. Commun.* **221** (2017) 383–418, [arXiv:1611.09856 \[hep-ph\]](https://arxiv.org/abs/1611.09856).
- [264] M. Drees, H. Dreiner, D. Schmeier, J. Tattersall, and J. S. Kim, “CheckMATE: Confronting your Favourite New Physics Model with LHC Data,” *Comput. Phys. Commun.* **187** (2015) 227–265, [arXiv:1312.2591 \[hep-ph\]](https://arxiv.org/abs/1312.2591).
- [265] E. Conte, B. Fuks, and G. Serret, “MadAnalysis 5, A User-Friendly Framework for Collider Phenomenology,” *Comput. Phys. Commun.* **184** (2013) 222–256, [arXiv:1206.1599 \[hep-ph\]](https://arxiv.org/abs/1206.1599).
- [266] E. Maguire, L. Heinrich, and G. Watt, “HEPData: a repository for high energy physics data,” *J. Phys. Conf. Ser.* **898** no. 10, (2017) 102006, [arXiv:1704.05473 \[hep-ex\]](https://arxiv.org/abs/1704.05473).

- [267] **ATLAS** Collaboration, “Simpleanalysis.” <https://gitlab.cern.ch/atlas-sa/simple-analysis>, 2021.
- [268] S. Ovyn, X. Rouby, and V. Lemaitre, “DELPHES, a framework for fast simulation of a generic collider experiment,” [arXiv:0903.2225 \[hep-ph\]](https://arxiv.org/abs/0903.2225).
- [269] A. Buckley, J. Butterworth, D. Grellscheid, H. Hoeth, L. Lonnblad, J. Monk, H. Schulz, and F. Siegert, “Rivet user manual,” *Comput. Phys. Commun.* **184** (2013) 2803–2819, [arXiv:1003.0694 \[hep-ph\]](https://arxiv.org/abs/1003.0694).
- [270] A. Buckley, D. Kar, and K. Nordström, “Fast simulation of detector effects in Rivet,” *SciPost Phys.* **8** (2020) 025, [arXiv:1910.01637 \[hep-ph\]](https://arxiv.org/abs/1910.01637).
- [271] S. Kraml, S. Kulkarni, U. Laa, A. Lessa, W. Magerl, D. Proschofsky-Spindler, and W. Waltenberger, “SModelS: a tool for interpreting simplified-model results from the LHC and its application to supersymmetry,” *Eur. Phys. J. C* **74** (2014) 2868, [arXiv:1312.4175 \[hep-ph\]](https://arxiv.org/abs/1312.4175).
- [272] F. Ambrogi, S. Kraml, S. Kulkarni, U. Laa, A. Lessa, V. Magerl, J. Sonneveld, M. Traub, and W. Waltenberger, “SModelS v1.1 user manual: Improving simplified model constraints with efficiency maps,” *Comput. Phys. Commun.* **227** (2018) 72–98, [arXiv:1701.06586 \[hep-ph\]](https://arxiv.org/abs/1701.06586).
- [273] **ATLAS** Collaboration, “Search for direct production of electroweakinos in final states with one lepton, missing transverse momentum and a higgs boson decaying into two b -jets in pp collisions at $\sqrt{s} = 13$ tev with the atlas detector,” 2021.
<https://www.hepdata.net/record/ins1755298?version=4>.
- [274] **ATLAS** Collaboration, “1lbb-likelihoods-hepdata.tar.gz,” 2020.
<https://www.hepdata.net/record/resource/1408476?view=true>.
- [275] G. Alguero, S. Kraml, and W. Waltenberger, “A SModelS interface for pyhf likelihoods,” [arXiv:2009.01809 \[hep-ph\]](https://arxiv.org/abs/2009.01809).
- [276] M. D. Goodsell, “Implementation of the ATLAS-SUSY-2019-08 analysis in the MadAnalysis 5 framework (electroweakinos with a Higgs decay into a $b\bar{b}$ pair, one lepton and missing transverse energy; 139 fb^{-1}),” *Mod. Phys. Lett. A* **36** no. 01, (2021) 2141006.
- [277] J. Y. Araz *et al.*, “Proceedings of the second MadAnalysis 5 workshop on LHC recasting in Korea,” *Mod. Phys. Lett. A* **36** no. 01, (2021) 2102001, [arXiv:2101.02245 \[hep-ph\]](https://arxiv.org/abs/2101.02245).
- [278] M. Feickert, L. Heinrich, G. Stark, and B. Galewsky, “Distributed statistical inference with pyhf enabled through funcX,” in *25th International Conference on Computing in High-Energy and Nuclear Physics*. 3, 2021. [arXiv:2103.02182 \[cs.DC\]](https://arxiv.org/abs/2103.02182).
- [279] R. Chard, Y. Babuji, Z. Li, T. Skluzacek, A. Woodard, B. Blaiszik, I. Foster, and K. Chard, “funcx: A federated function serving fabric for science,” ACM, Jun, 2020.
<http://dx.doi.org/10.1145/3369583.3392683>.
- [280] D. Merkel, “Docker: Lightweight linux containers for consistent development and deployment,” *Linux J.* **2014** no. 239, (Mar., 2014) .
- [281] S. Binet and B. Couturier, “docker & HEP: Containerization of applications for development, distribution and preservation,” *J. Phys.: Conf. Ser.* **664** no. 2, (2015) 022007. 8 p. <https://cds.cern.ch/record/2134524>.

- [282] K. Cranmer and L. Heinrich, “Yadage and Packtivity - analysis preservation using parametrized workflows,” *J. Phys. Conf. Ser.* **898** no. 10, (2017) 102019, [arXiv:1706.01878 \[physics.data-an\]](https://arxiv.org/abs/1706.01878).
- [283] ATLAS Collaboration, “Electron and photon energy calibration with the ATLAS detector using 2015–2016 LHC proton–proton collision data,” *JINST* **14** (2019) P03017, [arXiv:1812.03848 \[hep-ex\]](https://arxiv.org/abs/1812.03848).
- [284] Schanet, Eric, “simplify,” Version 0.1.5. <https://github.com/eschanet/simplify>.
- [285] Schanet, Eric, “SUSY-2019-08 simplified likelihood,” Version 0.0.1. https://github.com/eschanet/simplify/blob/master/examples/ANA-SUSY-2019-08/simplify_BkgOnly.json.
- [286] P. C. Bryan and M. Nottingham, “Javascript object notation (json) patch,” Version RFC 6902, Apr, 2013. <https://www.rfc-editor.org/rfc/rfc6902.txt>.
- [287] ATLAS Collaboration, “Search for direct stau production in events with two hadronic τ -leptons in $\sqrt{s} = 13$ TeV pp collisions with the ATLAS detector,” *Phys. Rev. D* **101** (2020) 032009, [arXiv:1911.06660 \[hep-ex\]](https://arxiv.org/abs/1911.06660).
- [288] ATLAS Collaboration, “Search for bottom-squark pair production with the ATLAS detector in final states containing Higgs bosons, b -jets and missing transverse momentum,” *JHEP* **12** (2019) 060, [arXiv:1908.03122 \[hep-ex\]](https://arxiv.org/abs/1908.03122).
- [289] W. Porod, “SPheno, a program for calculating supersymmetric spectra, SUSY particle decays and SUSY particle production at e+ e- colliders,” *Comput. Phys. Commun.* **153** (2003) 275–315, [arXiv:hep-ph/0301101](https://arxiv.org/abs/hep-ph/0301101).
- [290] W. Porod and F. Staub, “SPheno 3.1: Extensions including flavour, CP-phases and models beyond the MSSM,” *Comput. Phys. Commun.* **183** (2012) 2458–2469, [arXiv:1104.1573 \[hep-ph\]](https://arxiv.org/abs/1104.1573).
- [291] S. Heinemeyer, W. Hollik, and G. Weiglein, “FeynHiggs: A Program for the calculation of the masses of the neutral CP even Higgs bosons in the MSSM,” *Comput. Phys. Commun.* **124** (2000) 76–89, [arXiv:hep-ph/9812320](https://arxiv.org/abs/hep-ph/9812320).
- [292] H. Bahl, T. Hahn, S. Heinemeyer, W. Hollik, S. Paßehr, H. Rzehak, and G. Weiglein, “Precision calculations in the MSSM Higgs-boson sector with FeynHiggs 2.14,” *Comput. Phys. Commun.* **249** (2020) 107099, [arXiv:1811.09073 \[hep-ph\]](https://arxiv.org/abs/1811.09073).
- [293] T. Hahn, S. Heinemeyer, W. Hollik, H. Rzehak, and G. Weiglein, “High-Precision Predictions for the Light CP -Even Higgs Boson Mass of the Minimal Supersymmetric Standard Model,” *Phys. Rev. Lett.* **112** no. 14, (2014) 141801, [arXiv:1312.4937 \[hep-ph\]](https://arxiv.org/abs/1312.4937).
- [294] B. C. Allanach, “SOFTSUSY: a program for calculating supersymmetric spectra,” *Comput. Phys. Commun.* **143** (2002) 305–331, [arXiv:hep-ph/0104145 \[hep-ph\]](https://arxiv.org/abs/hep-ph/0104145).
- [295] G. Belanger, F. Boudjema, A. Pukhov, and A. Semenov, “MicrOMEGAs 2.0: A Program to calculate the relic density of dark matter in a generic model,” *Comput. Phys. Commun.* **176** (2007) 367–382, [arXiv:hep-ph/0607059](https://arxiv.org/abs/hep-ph/0607059).
- [296] G. Belanger, F. Boudjema, A. Pukhov, and A. Semenov, “micrOMEGAs: A Tool for dark matter studies,” *Nuovo Cim. C* **033N2** (2010) 111–116, [arXiv:1005.4133 \[hep-ph\]](https://arxiv.org/abs/1005.4133).

- [297] W. Beenakker, R. Hopker, and M. Spira, “PROSPINO: A Program for the Production of Supersymmetric Particles in Next-to-leading Order QCD,” Tech. Rep. hep-ph/9611232, Nov, 1996. <https://cds.cern.ch/record/314229>. 12 pages, latex, no figures, Complete postscript file and FORTRAN source codes available from <http://wwwcn.cern.ch/mspira/prospino/>.
- [298] W. Beenakker, M. Klasen, M. Kramer, T. Plehn, M. Spira, and P. M. Zerwas, “The Production of charginos / neutralinos and sleptons at hadron colliders,” *Phys. Rev. Lett.* **83** (1999) 3780–3783, [arXiv:hep-ph/9906298](https://arxiv.org/abs/hep-ph/9906298). [Erratum: Phys.Rev.Lett. 100, 029901 (2008)].
- [299] **ATLAS Collaboration** Collaboration, “Search for long-lived charginos based on a disappearing-track signature using 136 fb^{-1} of pp collisions at $\sqrt{s} = 13 \text{ TeV}$ with the ATLAS detector,” Tech. Rep. ATLAS-CONF-2021-015, CERN, Geneva, Mar, 2021. <https://cds.cern.ch/record/2759676>.
- [300] A. Arbey, M. Battaglia, and F. Mahmoudi, “Higgs Production in Neutralino Decays in the MSSM - The LHC and a Future e^+e^- Collider,” *Eur. Phys. J. C* **75** no. 3, (2015) 108, [arXiv:1212.6865 \[hep-ph\]](https://arxiv.org/abs/1212.6865).
- [301] M. E. Cabrera, J. A. Casas, A. Delgado, S. Robles, and R. Ruiz de Austri, “Naturalness of MSSM dark matter,” *JHEP* **08** (2016) 058, [arXiv:1604.02102 \[hep-ph\]](https://arxiv.org/abs/1604.02102).

Acknowledgements

An dieser Stelle möchte ich mich herzlich bei allen bedanken, die mich bei der Anfertigung dieser Arbeit unterstützt haben. Insbesondere danke ich herzlich

- Prof. Dr. Dorothee Schaile für die Möglichkeit, diese Arbeit an ihrem Lehrstuhl durchzuführen sowie das Korrekturlesen der Arbeit.
- Dr. Jeanette Lorenz für die ausgezeichnete Betreuung, die vielen Anregungen, sowie die ehrliche und konstruktive Kritik beim Korrekturlesen dieser Arbeit. Sie hat es mir ermöglicht aktiv im 1-Lepton Analyseteam an der Suche nach Supersymmetrie mitwirken zu können.
- Dr. Nikolai Hartmann für die unzähligen Diskussionen über den Sinn und Unsinn der Datenanalyse mit und ohne ATLAS Software. Vielen Dank für die stets geduldige und ausführliche Beantwortung meiner Fragen, sowie das Bereitstellen unzähliger Zeilen Code, ohne die vieles schwieriger gewesen wäre.
- Allen Mitgliedern des Lehrstuhls Schaile für die angenehme und freundliche Arbeitsatmosphäre.
- Allen Freunden, die stets da waren, wenn ich sie gebraucht habe.

I also want to thank the entire 1-lepton analysis team, especially the coordinators Jeanette Lorenz, Da Xu and Alberto Cervelli. Thank you for the always supportive and enjoyable work environment. Many thanks also to Valentina Tudorache for patiently answering all my questions as well as all the entertaining conversations.

I would further like to thank Dr. Brian Petersen without whom the presented pMSSM studies would not have been possible.

En léiwen Merci och dem Yannick Erpelding fir d'Korrekturlesen—och wann en net alles verstanen huet—an dem Nick Beffort, fir all déi domm Reddit Posts, d'Korrekturlesen, an dei onzähleg Stonnen zesummen mat enger Spezi an der Hand.

Zu gudden Läschte, wëll ech op dëser Platz menger ganzer Famill merci soen, virun allem mengan léiwen Elteren an menger wonnerbarer Schwëster. Merci dass dir mëch bei allem waat ech maachen énnerstëtzzt an dass ech émmer op iech zielen kann, och wann ech weit fort sin. Ouni iech wier daat heiten net méiglech gewiescht. Besonneschen Merci och dem Nathalie Münster, dofir dass et mech seit Joren émmer énnerstëtzzt an émmer fir mech do as, och wann ech heiansdo depriméiert oder duercherneen sin.

Selbstständigkeitserklärung

Hiermit erkläre ich, die vorliegende Arbeit mit dem Titel

Search for electroweakinos using the ATLAS detector

Suche nach Elektroweakinos mit dem ATLAS Detektor

selbstständig verfasst zu haben und keine anderen als die in der Arbeit angegebenen Quellen und Hilfsmittel benutzt zu haben.

Eric Schanet

München, den 01. Mai 2021